Final Report

DEVELOPMENT AND EVALUATION OF TEST METHODS TO EVALUATE WATER DAMAGE AND EFFECTIVENESS OF ANTISTRIPPING AGENTS

UF Project No.: 4910-4504-722-12

New UF No.: 00026632

Contract No.: BC-354, RPWO #11

Submitted to:

Florida Department of Transportation
605 Suwannee Street
Tallahassee, FL 32399

Bjorn Birgisson, Associate Professor
Reynaldo Roque, Professor
Mang Tia, Professor
and
Eyad Masad*, Assistant Professor

Department of Civil and Coastal Engineering
College of Engineering
365 Weil Hall, P.O. Box 116580
Gainesville, FL 32611-6580
Tel: (352) 392-9537 SunCom: 622-9537
Fax: (352) 392-3394

*Texas A&M University
College Station, TX

June 2005

1. Report No.	2. Government Accession No.	3. Recipient's Catalog No.
al Report		

4. Title and Subtitle	5. Report Date
DEVELOPMENT AND EVALUATION OF TEST METHODS TO EVALUATE WATER DAMAGE AND EFFECTIVENESS OF ANTISTRIPPING AGENTS	June 2005
	6. Performing Organization Code
7. Author(s)	8. Performing Organization Report No.
Bjorn Birgisson, Reynaldo Roque, Mang Tia, and Eyad Masad	Initial UF #4910-4504-722-12 New UF #00026632
9. Performing Organization Name and Address	10. Work Unit No. (TRAIS)
University of Florida Department of Civil and Coastal Engineering 365 Weil Hall / P.O. Box 116580 Gainesville, FL 32611-6580	
	11. Contract or Grant No.
	BC 354, RPWO #11
12. Sponsoring Agency Name and Address	13. Type of Report and Period Covered
Florida Department of Transportation Research Management Center 605 Suwannee Street, MS 30 Tallahassee, FL 32399	Draft Final Report September 22, 1999 – April 30, 2005
	14. Sponsoring Agency Code

15. Supplementary Notes

Prepared in cooperation with the Federal Highway Administration

16. Abstract

Moisture damage in hot-mix asphalt (HMA) mixtures occurs when water can infiltrate the pavement system. Pore water in mixtures can cause premature failure of hot-mix asphalt pavements, primarily through loss of adhesion between the asphalt binder and the aggregates or the loss of cohesion in the asphalt binder. Loss of adhesion can lead to stripping and raveling. The stripping of asphalt films from the surface of aggregate particles may occur as a result of poor adhesion of the asphalt to aggregate surfaces or displacement of the asphalt films by water which is attracted by hydrophilic aggregates, the latter being considered as true stripping. Siliceous aggregates are generally considered as the source of the problem since forms of crystalline quartz often inhibit the development of good adhesion, and in some cases cannot be coated with asphalt. Liquid antistrip agents are often added to asphalt cements to promote adhesion and prevent stripping. Lime treatment of aggregate prior to production of hot-mix asphalt is considered as an alternative measure in the prevention of stripping. Currently available laboratory testing procedures available all evaluate the effects of water damage in the laboratory by measuring the relative change of a single parameter before and after conditioning (i.e., tensile strength ratio, resilient modulus ratio). These parameters do not distinguish between the different mechanisms present in a conditioned mixture, including the identification of the effects of pore water versus actual moisture damage. The current Superpave mixture design specification uses the AASHTO T-283 moisture susceptibility test for determining moisture sensitive mixtures. Most state agencies use AASHTO T-283 test, although there have been questions by the community at large about the accuracy of the test. Frequent false positives and/or negatives have been reported, leading to the initiation of this current study.

This report developed test methods and criteria needed to relate mixture characteristics with the potential severity of moisture damage. The results showed that no single mixture property can be used to consistently monitor the effects of moisture damage in mixtures. Therefore, a fundamental theoretical framework for the evaluation of moisture damage in mixtures was developed, along with associated specification parameters. The new theoretical framework is based on the Florida HMA fracture model, developed at the University of Florida. A new moisture conditioning procedure using cyclic pore pressures was also developed based on fundamental considerations. The new conditioning and evaluation method were tested on mixtures of varying aggregate types and gradations. The results presented show that the Florida HMA fracture mechanics model provides highly consistent evaluation of the level of moisture damage in mixtures. These test methods are also shown to be capable of evaluating the effectiveness of antistripping agents, considered to enhance the adhesion of asphalt binders to aggregate surfaces.

17. Key Words	18. Distribution Statement
Moisture damage, Hot Mix Asphalt, Stripping, Moisture Conditioning, Pore Pressures, Flexible Pavements, Fracture Mechanics	No restrictions. This document is available to the public through the National Technical Information Service, Springfield, VA, 22161

19. Security Classif. (of this report)	20. Security Classif. (of this page)	21. No. of Pages	22. Price
Unclassified	Unclassified	337	

DISCLAIMER

"The opinions, findings and conclusions expressed in this publication are those of the authors and not necessarily those of the Florida Department of Transportation or the U.S. Department of Transportation.

Prepared in cooperation with the State of Florida Department of Transportation and the U.S. Department of Transportation."

SI* (MODERN METRIC) CONVERSION FACTORS

APPROXIMATE CONVERSIONS TO SI UNITS

Symbol	When You Know	Multiply By	To Find	Symbol
	LENGTH			
in	inches	25.4	millimeters	mm
ft	feet	0.305	meters	m
yd	yards	0.914	meters	m
mi	miles	1.61	kilometers	km
	AREA			
in^2	square inches	645.2	square millimeters	mm^2
ft^2	square feet	0.093	square meters	m^2
yd^2	square yards	0.836	square meters	m^2
ac	acres	0.405	hectares	ha
mi^2	square miles	2.59	square kilometers	km^2
	VOLUME			
fl oz	fluid ounces	29.57	milliliters	ml
gal	gallons	3.785	liters	l
ft^3	cubic feet	0.028	cubic meters	m^3
yd^3	cubic yards	0.765	cubic meters	m^3
NOTE: Volumes greater than 1000 l shall be shown in m^3.				
	MASS			
oz	ounces	28.35	grams	g
lb	pounds	0.454	kilograms	kg
T	short tons (2000 lb)	0.907	megagrams	Mg
	TEMPERATURE (exact)			
°F	Fahrenheit temperature	5(F-32)/9 or (F-32)/1.8	Celcius temperature	°C
	ILLUMINATION			
fc	foot-candles	10.76	lux	l
fl	foot-Lamberts	3.426	candela/m^2	cd/m^2
	FORCE and PRESSURE or STRESS			
lbf	poundforce	4.45	newtons	N
psi	poundforce per square inch	6.89	kilopascals	kPa

APPROXIMATE CONVERSIONS FROM SI UNITS

Symbol	When You Know	Multiply By	To Find	Symbol
	LENGTH			
mm	millimeters	0.039	inches	in
m	meters	3.28	feet	ft
m	meters	1.09	yards	yd
km	kilometers	0.621	miles	mi
	AREA			
mm^2	square millimeters	0.0016	square inches	in^2
m^2	square meters	10.764	square feet	ft^2
m^2	square meters	1.195	square yards	yd^2
ha	hectares	2.47	acres	ac
km^2	square kilometers	0.386	square miles	mi^2
	VOLUME			
ml	milliliters	0.034	fluid ounces	fl oz
l	liters	0.264	gallons	gal
m^3	cubic meters	35.71	cubic feet	ft^3
m^3	cubic meters	1.307	cubic yards	yd^3
	MASS			
g	grams	0.035	ounces	oz
kg	kilograms	2.202	pounds	lb
Mg	megagrams	1.103	short tons (2000 lb)	T
	TEMPERATURE (exact)			
°C	Celcius temperature	1.8C + 32	Fahrenheit temperature	°F
	ILLUMINATION			
lx	lux	0.0929	foot-candles	fc
cd/m^2	candela/m^2	0.2919	foot-Lamberts	fl
	FORCE and PRESSURE or STRESS			
N	newtons	0.225	poundforce	lbf
kPa	kilopascals	0.145	poundforce per square inch	psi

* SI is the symbol for the International System of Units. Appropriate rounding should be made to comply with Section 4 of ASTM E380.

(Revised August 1992)

TABLE OF CONTENTS

LIST OF TABLES

LIST OF FIGURES

EXECUTIVE SUMMARY

The displacement of asphalt films from the surface of aggregate particles may occur as a result of poor adhesion of the asphalt to aggregate surfaces or displacement of the asphalt films by water which is attracted by hydrophilic aggregates, the latter being considered as true stripping. Siliceous aggregates are generally considered as the source of the problem since forms of crystalline quartz often inhibit the development of good adhesion, and in some cases cannot be coated with asphalt. Liquid antistrip agents are often added to asphalt cements to promote adhesion and prevent stripping. Lime treatment of aggregate prior to production of hot-mix asphalt is considered as an alternative measure in the prevention of stripping. The current laboratory testing procedures currently available for testing HMA moisture susceptibility were primarily developed to determine the degree of resistance to moisture damage by a particular combination of asphalt and aggregate, compare mixes composed of different types and quantities of aggregate, or to evaluate the effectiveness of antistripping agents. These moisture susceptibility tests all evaluate the effects of water damage in the laboratory by measuring the relative change of a single parameter before and after conditioning (i.e., tensile strength ratio, resilient modulus ratio). These parameters do not distinguish between the different mechanisms present in a conditioned mixture, including the identification of the effects of pore water versus actual moisture damage. The current Superpave mixture design specification uses the American Association of State Highway Transportation Officials (AASHTO) T-283 moisture susceptibility test for determining moisture sensitive mixtures. Most state agencies use AASHTO T-283 test, although there have been questions by the community at large about the accuracy of the test. Frequent false positives and/or negatives have been reported, leading to the initiation of this current study, as well as a larger national study sponsored by the National Cooperative Highway

Research Program (NCHRP) and entitled "NCHRP Project 9-34: Improved Conditioning Procedure for Predicting the Moisture Susceptibility of HMA Pavements."

This report documents developed test methods and criteria needed to relate mixture characteristics with the potential severity of moisture damage. A fundamental theoretical framework for the evaluation of moisture damage in mixtures was developed, along with associated specification parameters. A new moisture conditioning procedure using cyclic pore pressures was developed based on fundamental considerations. The new condition and evaluation method were tested on mixtures of varying aggregate types and gradations and was shown to result in consistent evaluation of the moisture damage potential of mixtures. These test methods are also shown to be capable of evaluating the effectiveness of antistripping agents, considered to enhance the adhesion of asphalt binders to aggregate surfaces. This summary provides a brief description of accomplishments, key findings, and recommendations resulting from this work.

The primary accomplishments and findings may be summarized as follows:

- The current AASHTO T-283 procedure was performed on 15 mixtures with known moisture damage potential consisting of varying gradations and aggregate types. The results showed a lack of correlation of trends observed from the AASHTO T-283 procedure with those based on field experience in Florida. This led to the conclusion that other effects were occurring that may not be captured by the tensile strength ratio.
- The results obtained from the evaluation of the AASHTO T-283 procedure show that the requirement of a minimum saturation level for all mixtures may be questionable. High permeability coarse-graded mixtures had to be subjected to repeated rounds of saturation conditioning in order to meet the saturation requirements. This may have resulted in these coarse-graded mixtures having experienced further damage due to the saturation

conditioning. It may be better and more reasonable to allow each mixture to find its own level of saturation after a single vacuum saturation cycle. This would more closely account for the natural resistance of mixtures in the field.

- A possible relationship between tensile strength ratio and mixture permeability was explored. The findings indicated no apparent relationship between mixture permeability and tensile strength ratio, which may be due to both high variability in the TSR measurements and the effects of microstructure on the void continuity and void distribution of mixtures.
- Three distinct nondestructive approaches were studied for use in the evaluation of moisture damage in mixtures. These testing methods are: 1) the ultrasonic pulse wave velocity test, 2) the resonant frequency test, and 3) the acoustic hammer test combined with higher order modal analysis. The ultrasonic pulse wave velocity test and the resonant frequency test were found to work well in monitoring changes over time in mixtures. However, the results also indicated that these two tests may not be suitable for measuring absolute values of modulus that can be used in a specification framework. A preliminary evaluation of the modal hammer test with high order modal analysis was shown to consistently detect the presence of moisture damage within fine-graded hot-mix asphalt mixtures. However, the ability of the modal hammer test to obtain consistent values of parameters that are suitable for use in specifications still needs further study.
- The results from the evaluation of nondestructive tests also showed that once moisture is introduced into both coarse-graded and fine-graded mixtures, it tends to stay in the mixture for a long time (greater than 6 days). The presence of moisture is shown to greatly affect the small-strain modulus from the ultrasonic pulse wave velocity test and

the resonant frequency test. Therefore, it is recommended that all specimens be conditioned to a consistent moisture/humidity level before any type of performance testing.

- A fundamental evaluation of pore pressure effects in mixtures in the laboratory was performed. Pore pressures were measured during static triaxial testing and dynamic modulus testing. The results showed clearly that mixtures can generate considerable pore pressures under loading.
- The dynamic modulus is currently being proposed as a potential parameter for evaluating the moisture damage potential of mixtures by NCHRP Project 9-34. Therefore, in this report, the dynamic modulus test was evaluated under a variety of saturation/drainage conditions. The results showed that the dynamic modulus test is very sensitive to the presence of moisture in mixtures, making the use of the dynamic modulus test very difficult for consistent evaluation of moisture damage in mixtures, unless each specimen is dried out to a consistent moisture/humidity level before testing. Unfortunately, this procedure on large specimens would likely take days.
- The use of the Florida cracking model (HMA fracture mechanics) was evaluated for use as a fundamental model for evaluating moisture damage in mixtures. The following properties were evaluated: indirect tensile strength, resilient modulus, creep compliance, creep rate, fracture energy limit, and dissipated creep strain energy limit. The results showed that no single engineering property consistently reflects the effects of moisture damage on all mixtures. However, the Florida cracking model was shown to result in consistent evaluation of moisture damage potential of all mixtures tested.

- The Energy Ratio, which is a fundamental parameter based on the Florida cracking model was introduced as a specification parameter for the evaluation of moisture damage in mixtures. An evaluation of the use of the Energy Ratio for a number of mixtures showed that the Energy Ratio consistently ranked damaged and undamaged mixtures correctly.
- The Energy Ratio parameter was also shown to consistently identify the presence of liquid antistripping agents in mixtures.
- In order to develop an understanding of appropriate conditioning systems for the acceleration of moisture damage in mixtures, a fundamental study was undertaken of mixture microstructure and associate pore pressures. Using digital X-ray tomographic imaging techniques, the microstructure of 12 mixtures of varying gradations was studied. The results showed that in addition to aggregate type effects, the distribution of air voids plays in mixtures plays a significant role in determining moisture damage potential of mixtures. Limestone and granite mixtures were also shown to result in different air void distributions. The results also identified that there are "pessimum" air void size and permeability values at which each mixture has the least resistance to moisture damage. This concept can be used to design mixes outside the "pessimum" range in order to improve the resistance to moisture damage.
- The micromechanics-study also showed that the difference in moisture damage between limestone and granite specimens with similar gradations was related to their respective values of cohesive and adhesive bond energies under dry and wet conditions. The asphalt showed a better healing ability when water was present but a decrease in its fracture resistance. Also, the granite mix exhibited more susceptibility to moisture damage as it had less resistance to fracture and less ability to heal than the limestone mix under wet

conditions. The current asphalt mix design methods need to account for the cohesive and adhesive properties of asphalt mixtures as well as for the air void structure, which are highly related to moisture damage.

- The micromechanics-based study also showed that field mixtures of varying gradations and aggregate structure have a characteristic hourglass distribution of air voids through the compacted layer, with higher air voids at the top and the bottom of the layer. These results were used as inputs into a finite element-based flow model that showed that water will generally flow horizontally out to the sides of the pavement in the top part of a compacted layer, rather than penetrating and saturating underlying layers. However, the permeability of the top part of the compacted layer was shown to be large enough to saturate the pavement during and immediately after rain.
- A fundamental evaluation of ranges of expected pore pressures in pavements was performed using a micromechanics-based finite element approach that employs the theory of mixtures. As such, the asphalt pavement is considered to consist of an aggregate/mastic component and air voids. The results showed that significant pore pressures can be expected in pavements during and immediately after a rain event. Typical ranges of expected pore pressures in the upper part of the compacted layer range from 100 kPa (14.5 psi) to 600 kPa (88 psi). These pore pressures may play an important role in the premature aging, scouring, and breakdown of mixtures. The inclusion of pore pressures in the moisture conditioning of mixtures should better reflect the mechanism(s) of water damage present in an actual pavement.
- A new pore pressure-based moisture conditioning system was developed. The initial concept was based on a modified triaxial cell, with closed-loop servo controlled pore

pressure pumps. This conditioning system can be greatly simplified to result in a simple table-top system that can condition a number of specimens at the same time.

- An evaluation of the new cyclic pore pressure conditioning system was performed, using four combinations of cyclic pore pressure ranges and temperatures. The results showed that conditioning mixtures at cyclic pore pressures as low as 5-15 psi at a conditioning temperature of 40° C resulted in moisture damage consistent with previous experience with the mixtures tested. For example, oolitic limestone mixtures from South Florida were shown to have high resistance to moisture damage, which is consistent with FDOT experience. In contrast, mixtures consisting of Georgia granite were shown to strip, which is again consistent with previous FDOT experience.
- The results from the evaluation of the new cyclic pore pressure conditioning system showed for mixtures with the same aggregate type and with the highest predicted interstitial void pore pressures obtained from the micromechanical analysis resulted in the greatest moisture damage.

The following conclusions may be derived from the accomplishments and findings summarized above:

- Based on the evaluation of the new cyclic pore pressure conditioning system in which four combinations of cyclic pore pressures and conditioning temperatures were evaluated, it can be concluded that moisture conditioning of mixtures can be effectively performed with cyclic pore pressures in the range of 5-15 psi at a conditioning temperature of 40° C.
- The evaluation of the resulting moisture damage should be performed with the Superpave IDT test, using the Florida cracking model and the Energy Ratio. A moisture conditioned mixture with an Energy Ratio less than one should be rejected, or antistripping additives

should be added and the mixture retested. Similarly, a conditioned mixture with an Energy Ratio greater than one, but a ratio of conditioned to unconditioned Energy Ratio values of less than 0.6 should result in the automatic requirement for the addition of antistripping agents.

- Before testing conditioned mixtures in the Superpave IDT test, it is important to follow the Superpave IDT test preparation protocol and cut pills into specimens that are no wider than 2 inches, in order to enhance the drying of the specimens. These specimens should be placed in a dehumidifying chamber for 48 hours prior to testing to ensure that the mixture has been dried to a constant humidity level before the performance testing.
- In lieu of the Superpave IDT test and the Florida cracking model, the new cyclic pore pressure conditioning system should be used for conditioning mixtures irrespective of the performance test used. The results presented show clearly that pore pressures may play an important role in the physics of moisture damage in mixtures.

CHAPTER 1
INTRODUCTION

1.1 Background

The displacement of asphalt films from the surface of aggregate particles may occur as a result of poor adhesion of the asphalt to aggregate surfaces or displacement of the asphalt films by water which is attracted by hydrophilic aggregates, the latter being considered as true stripping. Siliceous aggregates are generally considered as the source of the problem since forms of crystalline quartz often inhibit the development of good adhesion, and in some cases can not be coated with asphalt. Liquid antistrip agents are often added to asphalt cements to promote adhesion and prevent stripping. Lime treatment of aggregate prior to production of hot-mix asphalt is considered as an alternative in the prevention of stripping. Although the term "stripping" is generally used to define any form of water damage, the mechanisms that promote distress in asphalt pavements can be entirely different. For example, pore pressures produced under the tires of vehicles can cause the dislodging of asphalt film from the aggregate surface as well as hydrofracturing of the asphalt pavement mixture when its permeability is insufficient to adequately dissipate water and prevent high pore pressures. Pavement surfaces that have very low or extremely high permeability will not develop this problem. Consequently, the mix design, level of compaction, and degree of traffic densification will affect the permeability and the mixtures potential for hydrofracturing.

The laboratory testing procedures currently available for testing HMA moisture susceptibility were primarily developed to determine the degree of resistance to moisture damage by a particular combination of asphalt and aggregate, compare mixes composed of different types and quantities of aggregate, or to evaluate the effectiveness of antistripping agents (4, 5, 6, 7, 8). These moisture susceptibility tests all evaluate the effects of water damage in the laboratory by

measuring the relative change of a single parameter before and after conditioning (i.e., Tensile Strength Ratio, Resilient Modulus Ratio).

The current Superpave specification uses the Modified Lottman Method (AASHTO T-283) moisture susceptibility test for determining moisture sensitive mixtures. Asphalt concrete mixture specimens are compacted to about 7 percent air void content, vacuum saturated, processed and then tested by the indirect tension test. Low tensile strength ratios (e.g. less than 80 percent) are considered to be indicative of excessive water damage. However, tensile strength ratios greater than 1.0 are sometimes obtained which either reflects the variability of the test method or that sample conditioning actually improved the tensile strength of the mixture. Generally, there have been questions by the community at large about the accuracy of the Modified Lottman test. Frequent false positives and/or negatives have been reported, leading to the initiation of this study as well as a larger national study sponsored by the National Cooperative Highway Research Program (NCHRP) and entitled "NCHRP Project 9-34: Improved Conditioning Procedure for Predicting the Moisture Susceptibility of HMA Pavements."

Depending on materials, loading, and environment, it may be that one or all of the mechanisms of water damage are present and dominant in an actual pavement. However, for a proper evaluation of any given mixture and testing procedure, it is necessary to isolate and quantify the effects of each of the predominant mechanisms contributing to moisture damage. In fact, the lack of delineation between pore water effects and actual moisture damage may lead to erroneous conclusions. Water damage effects in HMA pavements may be bracketed by two extreme conditions: 1) the rapid application of cyclic pore pressures under saturated conditions that correspond

to critical field conditions, and 2) the longer term continuous low level exposure to water without pore pressures.

1.2 Problem Statement

Fine aggregate for asphalt mixtures often contain crystalline quartz particles that will not retain asphalt coatings and strip readily in the presence of water. This condition can reduce the durability of asphalt pavements resulting in raveling and/or cracking. There are five major potential mechanisms for moisture damage reported in the literature (e.g., Stuart 1990; Kandhal 1994; Kandhal and Rickards 2001):

- Detachment;
- Displacement;
- Spontaneous emulsification;
- Pore pressure; and
- Hydraulic scouring.

None of these mechanisms have been proven by connecting theoretical considerations to observed field behavior. Rather, these mechanisms are hypothesized based on field observation, along with limited basic laboratory characterization.

Depending on materials, loading, and environment, it may be that one or all of the mechanisms of water damage are present and dominant in an actual pavement. For a proper evaluation of any given mixture and testing procedure, it is necessary to isolate and quantify the effects of each of the predominant mechanisms contributing to moisture damage.

Water damage effects in HMA pavements may be bracketed by two extreme conditions: 1) the rapid application of cyclic pore pressures under saturated conditions that correspond to critical field conditions, and 2) the longer term continuous low level exposure to water without

pore pressures. No reported research has been conducted to identify which extreme condition is most important in causing moisture damage in mixtures, i.e., cyclic pore pressures or long term continuous low-level exposure.

There are currently no performance-based methods available for evaluating moisture damage in mixtures that have been widely accepted by state agencies. The methods used to evaluate moisture susceptibility of mixtures tend to be either qualitative in nature, like the boil test, or crude quantitative techniques that may neither include the appropriate mechanism of moisture damage nor the appropriate framework for analyzing the effects of moisture damage on mixtures.

In summary, there is a clear need to identify the most likely mechanism(s) of moisture damage in pavements. The identification of the key mechanism(s) of moisture damage will allow for the development of an appropriate laboratory-based conditioning system, along with the development of a robust performance-based framework for the evaluation of mixture moisture damage susceptibility. These new conditioning and evaluation methods should be capable of quantifying the effectiveness of liquid antistripping agents, lime, and/or other additives considered to enhance the adhesion of asphalt binders to aggregate surfaces.

1.3 Objectives

The primary objective of the proposed research is to define the effect that interacting mixture and mineralogical properties have on moisture damage in mixtures. Specific objectives include:

1) Identification of key mechanism(s) of moisture damage in pavements;
2) Development of test equipment and procedures;

3) Determination of permeability limits to minimize moisture damage, as well as aggregate mineralogical properties that affect moisture damage.
4) Development of a new conditioning, which is based on the most likely mechanism(s) of water damage.
5) Development of a new laboratory-based protocol for the evaluation of moisture damage in mixtures. This new evaluation protocol should be based on a theoretical framework that defines the interactive damage effects of variables.

1.4 Scope

To meet the numerous objectives of this research project, multiple studies were performed. The summary of results for each study is presented at the end of each chapter.

Chapter 1 provides background, objectives, and scope for this research project. Chapter 2 deals with a literature review of the key mechanisms of moisture damage, along with a review of available conditioning and evaluation systems. Chapter 3 provides an evaluation of the AASHTO T-283 procedure (i.e., the Modified Lottman Method). Chapter 4 reviews and evaluates three distinct nondestructive testing approaches for use in the quantification of moisture damage in mixtures, including the ultrasonic pulse wave velocity test, the resonant frequency test, and the acoustic hammer test combined with higher order modal analysis. Chapter 5 studies pore pressure effects on performance-based mixture properties, including the complex dynamic modulus. Chapter 6 evaluates the use of the Superpave Indirect Tension Test and the Florida HMA fracture mechanics framework for the measurement and quantification of moisture damage in mixtures. Chapter 7 introduces a specification parameter, entitled the Energy Ratio (ER), based on the Florida HMA fracture mechanics framework, for use in the evaluation of moisture damage in mixtures. Chapter 8 studies fundamental mixture properties

that affect moisture damage in mixtures, including the influence of air void size, air void distribution, permeability, and bond energy. Chapter 9 presents the results of a number of finite element-based numerical simulations of saturated flexible pavements using typical mixture properties, pavement configurations, and vehicle tire loads. Based on the results presented, a range of pore pressures for use in a laboratory-based conditioning procedure is identified. Chapter 10 presents the design of a new cyclic pore pressure-based moisture conditioning system for mixtures. Finally, Chapter 11 provides an evaluation of the new cyclic pore pressure conditioning system, using the Florida HMA fracture mechanics framework with the Energy Ratio parameter from Chapter 7.

CHAPTER 2
LITERATURE REVIEW

A major objective with this research project is to either identify or develop new methods evaluating the potential for moisture damage in mixtures. In order to determine optimal ways to condition and test mixtures, it is important to include the most likely mechanism(s) that cause moisture damage in the field and use that mechanism for conditioning in the laboratory. It is equally as important to develop a strong understanding of the key mixture properties that are affected by moisture damage, so that the evaluation and quantification of the effects of moisture damage can be robust and effective. In this chapter, the current state of knowledge about moisture damage in mixtures is reviewed. In particular, the focus is on: 1) review of key mechanisms of moisture damage; and 2) methods and evaluation protocols that have been either proposed or used recently for conditioning of mixtures.

In the following, the chemistry of the asphalt-aggregate bond is discussed, with a focus on factors that may contribute to stripping. Then, the mechanisms of stripping are reviewed, followed by a discussion of existing test methods and evaluation protocols.

2.1 Adhesion and Stripping

The phenomenon of stripping is directly related to the sensitivity of the bond between aggregates and asphalt in an asphalt mixture. Therefore, to determine why this adhesive bond is broken, it is first necessary to understand the physics of how aggregates and asphalt combine and adhere to each other to form an asphalt mixture. Numerous theories have been proposed to explain the adhesion. Rice (1958) classified these theories as mechanical interlocking, chemical reaction, and molecular orientation or surface energy. Chemical interactions are believed to be

the best explanation of the adhesive bond (Curtis et al. 1993). Furthermore, all theories assume that the bond is influenced by the composition and surface chemistry of the aggregates.

A discussion of the chemistry of the asphalt-aggregate bond, as well as the aggregate properties that promote adhesion follows. In addition, some others factors that contribute are commented.

2.1.1 Chemistry of the Asphalt-Aggregate Bond

The asphalt-aggregate bond arises due to the presence of acidic and basic components in an asphalt mixture that react forming water-insoluble compounds. The adhesion of asphalt to aggregate must occur and be maintained for a good pavement performance result. To investigate and control stripping problems, it is necessary to understand the chemistry of both the asphalt and aggregate at the asphalt-aggregate interface, and the effects of moisture on this bonding.

Asphalt is composed of a mixture of hydrocarbons that contain some polar functionalities, as well as constituents that contain metals such as nickel, vanadium, and iron. The aggregate provides a surface that is heterogeneous and has a variety of sites of different composition and levels of activity. These active sites are frequently charged or contain partial charges that attract and orient the polar constituents of asphalt. Curtis et al. (1993), in an investigation of the chemical and physical processes that govern adhesion between aggregates and asphalt, stated that the polar functionalities present at the point of contact between the asphalt film and the aggregate surface adhere to the surface through electrostatic forces, hydrogen bonding, or Van der Waals interactions.

When hot asphalt coats the aggregates particles, it tends to enter any available pores. Short-range chemical interactions in asphalt molecule are feasible because of electrostatic interactions that occur between the charged surface and the molecules attracted to the surface.

Adamson (1976) pointed out that "unsymmetrical molecules will be oriented at an interface." A charged aggregate surface attracts an oppositely charged or partially charged species or functional group contained in the species. The part of the attracted molecule that is available for interaction with other asphalt molecules would then be the charge of the aggregate and hence would have electrostatic interaction with other oppositely charged or partially charged asphalt molecules.

The intrusion of water or moisture may substantially affect the pH of the local environment. According to Scott (1978), changes in the pH of the microscopic water accumulations at the aggregate surface can alter the type of polar groups adsorbed, as well as their state of ionization/dissociation, leading to the build-up of opposing, negatively charged, electrical double layers on the aggregate and asphalt surfaces. The drive to reach equilibrium attracts more water and leads to physical separation of the asphalt from the aggregate.

In short, the bond that develops between asphalt and aggregate is primarily due to relatively weak dispersion forces that cause molecular orientation to occur. Water molecules, on the other hand, are highly polar and then are attracted to aggregates by much stronger orientation forces.

Therefore, if a three-phase interface consisting of aggregate, asphalt, and water exists, water is better than asphalt for reducing the free surface energy of the system to a thermodynamically stable condition of minimum surface energy (Figure 2-1). According to Fromm (1974), once the asphalt film is breached and water enters under the asphalt, surface tensions may force the water between the remaining asphalt-aggregate interface, causing stripping.

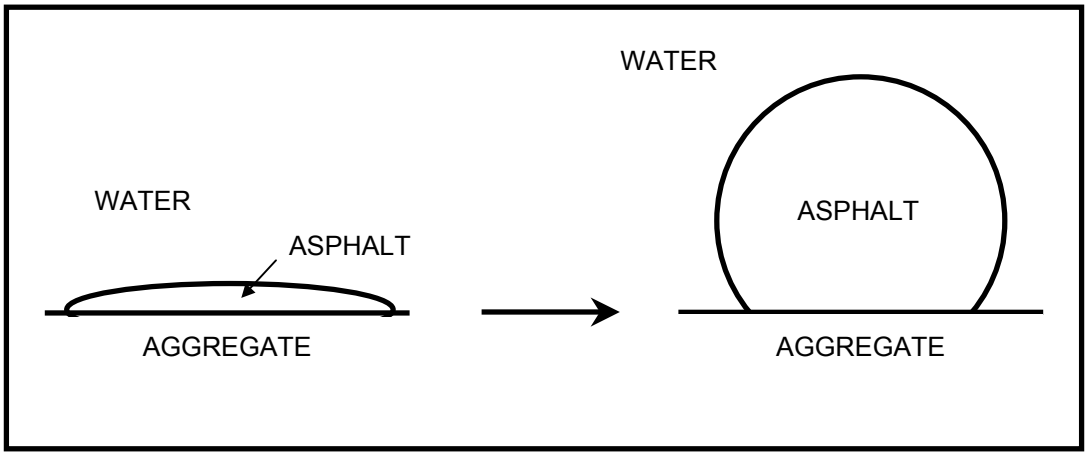

Figure 2-1. Surface energy theory of adhesion.

According to Thelen (1958), the surface or interfacial tensions (χ)between these phases are approximately as follows:

$\chi_{ab.}$ = interfacial tension between aggregate and asphalt = 17 ±3 ergs/cm^2

χ_{wb} = interfacial tension between water and asphalt = 30 ±5 ergs/cm^2

$\chi_{aw.}$ = interfacial tension between aggregate and water = 0 ergs/cm^2 (since under usual ambient temperature the aggregate surface is approximately a free water surface).

The energy potential to cause stripping is calculated as shown in Equation 2.1:

$$\Delta F = \chi_{ab} + \chi_{wb} - \chi_{aw} = 47 \text{ ergs} / \text{cm}^2 \quad (2.1)$$

Thus usual asphalt and normal organic materials will voluntarily spread over water films on aggregate, and will also tend to be stripped from these films by water. The rate at which these processes occur no doubt depends somewhat on the magnitude of the free energy evolved (ΔF), but in practice probably is controlled chiefly by the viscosity of the asphalt.

2.1.2 Aggregate Properties

Failure of the bond can fail at the interface, within the asphalt as a cohesive failure, or within the aggregate as a structural failure. Curtis et al. (1993) showed that the physicochemical surface properties of mineral aggregate are more important for moisture induced stripping compared to the properties of asphalt cement binder.

The surface charge of the aggregate determines, to some degree, the extent of attraction and adsorption of the asphalt. This surface charge can be quantified by measuring the streaming potential or Zeta potential of the aggregate. Consequently, the aggregate surface can be modified to effect favorable attraction between the asphalt and aggregate.

Electron transfer from the asphalt at the interface relies on the ability of aggregates to accept or donate these electrons. Scott (1978) observed that pH value varies depending on whether the aggregates are siliceous or calcareous. In addition, Curtis et al. (1993) concluded, from studies of the electron donor and electron acceptor properties of four aggregates, ranging from quartz, to silicate, to calcite-based, that aggregates composed of quartz exhibit the strongest acceptor character, while silicate materials are less strong. The carbonate rocks show a range of donor-acceptor properties.

Some mineral aggregates are inherently very susceptible to stripping. Interlocking properties of the aggregate particles, which include individual crystal faces, porosity, angularity, absorption, and surface coating are also believed to improve the bond strength in an asphalt mixture. Kiggundu and Roberts (1988) postulated that the absence of a sound interlocking network of these properties might induce stripping.

It is often observed that siliceous aggregates have slick, smooth areas, which may give rise to stripping, while roughness may help to promote bonding. Besides, some limestone and

lime-treated aggregates tend to form stronger, more robust, and durable bonds with asphalt. This is believed to be caused by the insensitivity of these bonds to the action of water. The bonds formed in this case are strong, insoluble bonds. Curtis et al. (1993) observed, from reactivity measurements with model carboxylic acids, that even within limestone samples, their ability to form insoluble salts varies substantially, depending on the availability of the surface calcium to enter into bond formation.

2.2 Other Causative Factors

Tunnicliff and Root (1984) performed a survey to summarize and analyze the use of antistripping additives in asphalt mixtures in the United States by submitting a questionnaire to members of the American Association of State Highway Transportation Officials (AASHTO) subcommittee on materials, agencies, asphalt cement producers, trade associations, and antistripping additive producers. Responses from the questionnaire imply that other factors contribute to stripping, such as asphalt cement characteristics, and construction practice.

On the other hand, Taylor and Khosla (1983) concluded, from a comprehensive survey of the literature regarding moisture damage in asphalt pavements, that stripping is a complex problem related to a large number of variables, including also the type and use of mix, environment, and traffic.

Based on an evaluation of the factors responsible for inducing stripping, Kandhal (1994) listed and discussed external factors and/or in-place properties of asphalt pavements, dealing basically with the same factors stated before.

A proper knowledge of these factors is essential in identifying and solving the stripping problem. A discussion of the most frequently listed factors identified by Taylor and Khosla (1983) and Kandhal (1994) follows.

2.2.1 Type and Use of Mix

The type and use of an asphalt mixture has been found to be related to the likelihood of stripping of the mix. The majority of pavement failures caused by stripping occur in open-graded mixes, base courses, and surface treatments, all of which are relatively permeable to water when compared with dense-graded mixes. Surface treatments have been noted to be particularly vulnerable to stripping. Stripping in dense-graded, hot-mix paving mixtures is generally not considered a large problem unless the mixtures exhibit excessive air voids, insufficient bitumen, inadequate compaction, or aggregate with adsorbed coatings. The practice of adding antistripping agents to the mixture may be improving the field performance of these mixtures. The inherent resistance to stripping exhibited by dense-graded, hot-mix paving mixtures may be caused, in part, by the use of hot, dry aggregate in those mixtures. However, there is a need to evaluate all mixtures for their susceptibility to moisture damage. In particular, since the use of antistripping agents is common in mixtures, it is important to evaluate mixtures that contain antistripping agents in an accurate and robust manner.

The small percentage of normally present air voids and the common presence of antistripping agents in well-compacted, dense-graded hot mixes is probably largely responsible for their excellent moisture resistance because the virtual absence of voids renders the mixes much less permeable. Full-depth (deep strength) asphalt pavements, as proposed by The Asphalt Institute, have been shown to provide excellent resistance to stripping. The dense-graded asphalt bases often used in full-depth pavements are observed to act as a vapor barrier so that little or no free moisture accumulates beneath the pavements.

2.2.2. Asphalt Characteristics

The mostly referenced relationship between the characteristics of the asphalt in a paving mixture and the tendency of the mix to strip relates stripping resistance to the viscosity of the binder in service. Binders of high viscosity have been observed to resist displacement by water much better than those of low viscosity, although even 60-penetration bitumen has been observed to strip. Fromm (1974) observed that high viscosity asphalt resisted pulling along an air-water interface and that the pulling of the asphalt film increased as asphalt viscosity decreased.

Low viscosity, however, is desirable during mixing operations because a low viscosity fluid has more wetting power than one of high viscosity. Observations made by Schmidt and Graf (1972) indicate that most asphalt appears to behave similarly with respect to moisture, provided they are of the same viscosity; i.e., the effect of asphalt composition is negligible. In contrast, Fromm (1974) observed that the rate of emulsion formation in asphalt submerged in water depends on the nature of the asphalt rather than its viscosity. Logically, emulsified asphalt may be more prone to stripping by spontaneous emulsification if some concentration of emulsifier remains in the binder after mixing. The presence of paraffin in asphalt is believed to be detrimental to stripping resistance.

Moreover, high viscosity asphalt cements cannot be used in many instances because of other considerations such as low-temperature cracking in cold regions and potential reduction in fatigue life of the surface courses. There is a need to understand the fundamentals of aggregate-asphalt adhesion so that the problem can be minimized by other means rather than increasing the asphalt cement viscosity, which is not effective in all cases and which may result in other performance problems.

Asphalt is composed of such a variety of chemical species that it most likely will also have a continuum of electron donor and acceptor behavior, the exact range of which is dependent on its chemistry. The matching of the electron donation and accepting abilities of the aggregates and asphalts, respectively, may lead to improvements in road performance.

One factor affecting the wetting of the aggregate surface by asphalt depends on the interfacial tension, promoting wetting, and facilitating close contact between the asphalt and the aggregate surface. However, the effectiveness of an additive, particularly an antistripping agent, varies with the type of the additive, as well as with the asphalt and aggregate.

After the asphalt has wetted the aggregate surface, some of its organic chemical functionalities enter into bond formation with the aggregate constituents. Frequently, these functional groups, such as carboxylic acid and phenolic, combine with alkali metals present on the aggregate surface to form water-insoluble salts (e.g., sodium salts). Consequently, these asphalt-aggregate bonds are ionic bonds that weaken or solubilize over time with exposure to moisture susceptible because of their inability to withstand solubilization and disbonding over extended time. Thus, even though tensile strength ratio (TSR) measurements may exhibit high values, these are reflective of only the physical strength of the bonds and do not measure their ability to withstand exposure or weathering.

2.2.3 Construction Practice

Inadequate surface and/or subsurface drainage provides water or moisture vapor, which is the necessary ingredient for inducing stripping. If excessive water or moisture is present in the pavement system the HMA pavement can strip prematurely. Kandhal et al. (1989) have reported case histories where the stripping was not a general phenomenon occurring on the entire project

but rather a localized phenomenon in areas of the project saturated with water and/or water vapor due to inadequate subsurface drainage conditions.

Water can enter the HMA pavement layers in different ways. It can enter as run-off through the road surface, primarily through surface cracks. It can enter from the sides and bottom as seepage from ditches and high water table in the cut areas.

The most common water movement is upward by capillarity under a pavement. Above the capillary fringe, water moves as a vapor. Many subbases or subgrades in the existing highway system lack the desired permeability; therefore, are saturated with the capillary moisture. The construction of multilane highways (or widening) to greater widths, gentler slopes and milder curves in all kinds of terrain has compounded the subsurface drainage problem. Quite often, a four-lane highway is rehabilitated by paving the median and shoulders with HMA resulting in a fully paved width of 72-78 feet, which is equivalent to a six-lane highway without any increase in the subsurface drainage capability.

Air voids in the HMA pavement may become saturated with water even from vapor condensation due to water in the subgrade or subbase. A temperature rise after this saturation can cause expansion of the water trapped in the mixture voids resulting in significant void pressure when the voids are saturated. The pore pressure from stresses induced by traffic can also cause the failure of the binder-aggregate bond. Initially, the traffic stresses may further compact the mixture and trap or greatly reduce the internal water drainage. Therefore, the internal pore water is in frequent motion (cyclic) and considerable pore pressure may be built up under the traffic action.

Tell-tale signs of water damage to HMA overlays (over concrete pavements) have been described by Kandhal (1994). He observed wet spots on the HMA overlay surface scattered

throughout the project. Usually at these wet spots water oozed out during hot afternoons. Some of the wet spots contained fines suspended in the water which were tracked on and turned into fatty areas (resulting from asphalt stripping and migrating to the surface) which usually preceded the formation of potholes.

Usually stripping in a four-lane highway facility occurs first in the slow traffic lane because it carries more and heavier traffic compared to the passing lane. Typically, but not always, stripping starts at the bottom of HMA layer, or a layer interface, and progresses upwards. It is evident from the preceding discussion that inadequate subsurface drainage is one of the primary factors inducing premature stripping in HMA pavements.

Other construction factors that may cause or enhance stripping include:

- inadequate compaction;
- excessive dust coating on aggregate;
- use of open-graded asphalt friction course;
- inadequate drying of aggregates;
- use of weak and friable aggregate;
- placement of overlays on deteriorated concrete pavements; and
- use of waterproof membranes and seal coats.

2.3 Mechanisms of Stripping

Despite the fact that several factors have been associated with stripping, there is a consensus that this phenomenon is principally caused by water. For this to occur, however, water has to penetrate the asphalt film. This can occur under various conditions and by several mechanisms.

There may be as many as five different mechanisms by which stripping of asphalt cement from an aggregate surface may occur. Those five mechanisms include (e.g., Stuart 1990; Kandhal 1994; Kandhal and Rickards 2001):

- detachment;
- displacement;
- spontaneous emulsification;
- pore pressure; and
- hydraulic scouring.

It appears that these mechanisms may act individually or together to cause adhesion failure in bituminous mixtures. In addition to these mechanisms outlined, other less likely, but potential mechanisms for stripping have been suggested such as osmosis due to presence of salts or salt solution in the aggregate pores that creates an osmotic pressure gradient that sucks water through the asphalt film. A discussion of each of the five mechanisms follows.

2.3.1 Detachment

The most likely mechanism occurs when there is a discontinuity and, hence, a line of juncture where asphalt, free water and aggregate are all in contact. In other words, detachment is the separation of an asphalt film from an aggregate surface by a thin layer of water, with no obvious break in the asphalt film (Figure 2-2).

In this case, the aggregates are completely uncoated in the presence of moisture, indicating a complete loss of adhesion. The theory of interfacial energy provides the rationale for explaining the detachment mechanism.

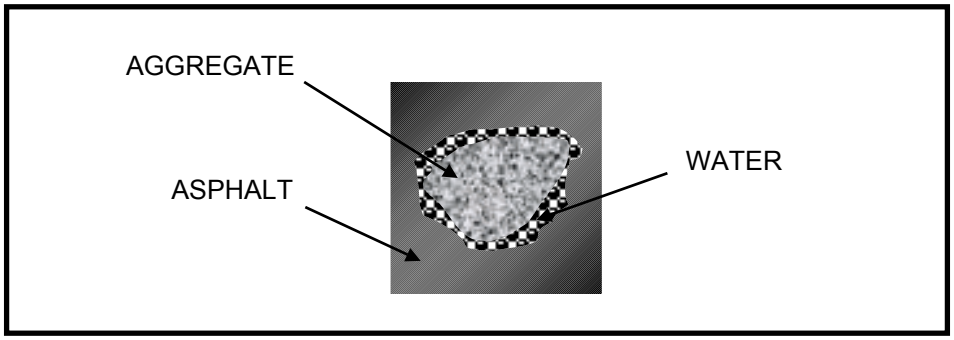

Figure 2-2. Stripping by detachment.

2.3.2 Displacement

Stripping by displacement results from the penetration of water to the aggregate surface through a break in the asphalt film. This break can be caused by incomplete coating of the aggregate initially or by film rupture. Because the asphalt film at these locations is generally thinner and under tension, rupture of the asphalt film is probable at the sharp edges and corners of angular aggregate pieces as a result of traffic loading. Stripping by displacement can result from pinholes in the asphalt film, which can form soon after coating of a dusty aggregate. Both the surface energy and the chemical reaction theory of adhesion can be used to explain stripping by displacement.

2.3.3 Spontaneous Emulsification

In spontaneous emulsification, water and asphalt combine to form an inverted emulsion, where asphalt represents the continuous phase and water represents the discontinuous phase. When such an emulsion is formed, the adhesive bond between the asphalt and the aggregate is broken. This can be further aggravated by the presence of emulsifiers such as mineral clays and some asphalt additives. The chemical reaction theory of adhesion can be used to explain stripping by spontaneous emulsification.

Fromm (1974) investigating how water penetrates asphalt films, observed that spontaneous emulsification occurs whenever asphalt films were immersed in water. The rate of emulsification depended, however, on the nature of the asphalt and the presence of additives. The fact that stripping has been observed to be reversible lends support to the spontaneous emulsification mechanism because evaporation of the water from the emulsion returns the asphalt to its original condition.

2.3.4 Pore Pressure

The effects of pore pressure take place when the air voids in the HMA pavement are reduced due to loading and the water in the voids is compressed to create pressure against the asphalt film. Once the pore pressure increases to a high level, the asphalt film on the aggregate will rupture under the pressure and create a break in the film where water can infiltrate to the surface of the aggregate. Pore pressure usually affects newly placed HMA pavements because the pavement is placed at a higher than designed air void content with the assumption that traffic loadings will decrease the air void content over time. The voids are interconnected and allow the water to move through the pavement. Once the pavement starts to densify, the interconnected voids close and traps water in the voids. Further densification causes the pores to collapse and increase the pressure on the water. Several reasons are attributed to the increase in pore pressure including traffic loadings, thermal expansion, freezing expansion, and thermal shock (Lottman 1982a). Once the asphalt film ruptures, then the displacement mechanism removes the asphalt film.

The pore pressure can affect the pavement system even when the pavement is not fully saturated. The unsaturated voids can create a capillary tension within the pavement, causing the pore pressure to become negative. This can cause the effective stresses to increase beyond the

effective stresses when the pavement is saturated. However, when a load is applied to the pavement, the total stress and the pore pressures will increase according to the load intensity. In turn, the effective stresses within the pavement will decrease. This will cause a cycling of compression and tension within the voids. This is illustrated in Figure 2-3.

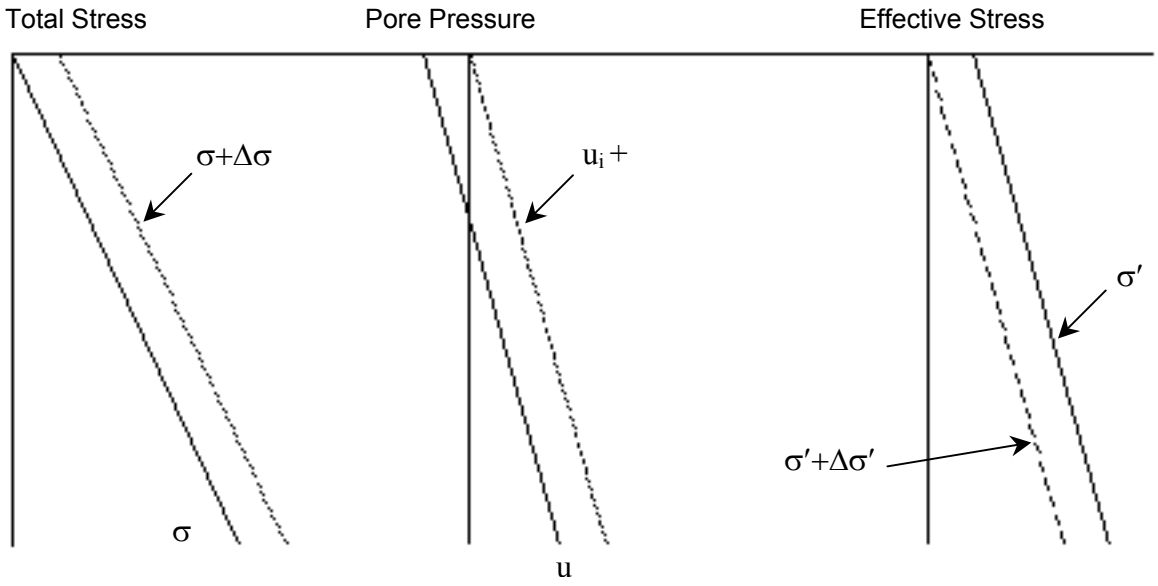

Figure 2-3. Effects of pore pressures on the effective stresses.

Inspection of field specimens of stripped pavements has revealed that stripping begins at the bottom of layer interfaces and works its way up, stripping mostly the coarse aggregate. This behavior can be explained both by the pore pressure mechanism, because:

- The asphalt at the bottom of a pavement layer is in tension upon the application of load and is often subject to prolonged exposure to moisture from water trapped within a granular base course above the subgrade.
- The observed hourglass distribution of air voids in compacted field mixtures, where the top and the bottom of the layer have larger air voids and higher permeability, but the middle of the layer has lower air voids and less permeability (Masad et al. 2005). The

higher permeability parts of the compacted layer are more likely to contain moisture, thus resulting in pore pressures due to vehicle loadings. For pavements with "wet feet," where there is a source of moisture underneath the pavement, stripping from the bottom more permeable part of the asphalt layer is therefore more likely.

2.3.5 Hydraulic Scouring

Hydraulic scouring is a mechanism of stripping that is applicable only to surface courses. Stripping due to hydraulic scouring results from the action of vehicle tires on a saturated pavement surface. This causes water to be pressed down into the pavement in front of the tire and immediately sucked away from the pavement behind the tire (Figure 2-4). This compression-tension cycle is believed to contribute to the stripping of the asphalt film from the aggregate.

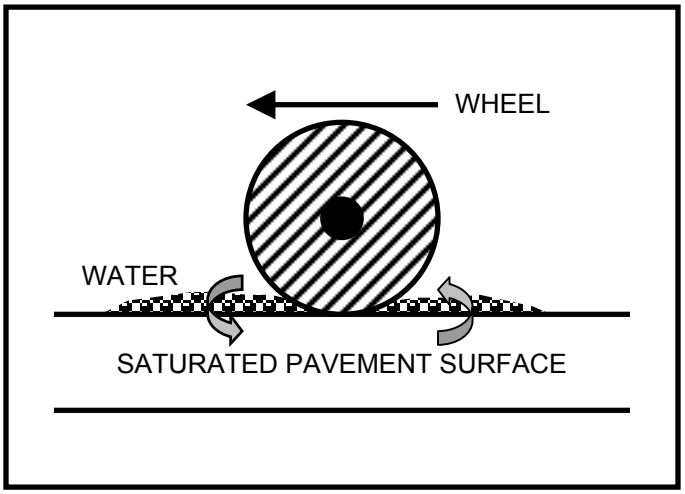

Figure 2-4. Stripping by hydraulic scouring.

2.4 Antistripping Additives

It is common practice to use antistripping (AS) additives to prevent stripping and improve the asphalt pavement performance. Tunnicliff and Root (1984) defined antistripping

additives as substances that convert the aggregate surface to one that is more easily wetted with asphalt than water. Both liquids and lime additives are effective to resist stripping.

2.4.1 Liquid Additives

Most of the liquid AS agents are surface-active agents, which, when mixed with asphalt cement, reduce surface tension and, therefore, promote increased adhesion to aggregate. The chemical composition of most commercially produced AS agents is proprietary. However, the majority of AS agents currently in use are chemical compounds that contain amines (Kandhal 1992; Tunnicliff and Root 1982). These AS agents must be " heat stable," that is, they should not lose their effectiveness when the modified asphalt cement is stored at high temperatures for a prolonged period of time.

The simplest and most economical way is to mix the AS agent with the asphalt cement in a liquid state prior to mixing the asphalt cement with the aggregate. Although this method is most commonly used, it is inefficient because only a portion of the AS agent reaches the aggregate-asphalt cement interface. Direct application of the AS agent to the aggregate surface is undoubtedly the most efficient way to ensure high quality bonding between the asphalt and the aggregate. However, this is generally not practical because of cost considerations in ensuring full coating of all aggregates, including the dust component. Normally, only small amounts of AS agents (for example 0.5 percent by weight of asphalt cement) are used in the binder.

The amount of AS agent to be used is important. Too little may not be effective and too much may be detrimental to the HMA mix. The long-term effectiveness of liquid AS agents during the service life of the HMA pavements has not been fully established.

Some agencies maintain an approved list of AS agents and require the contractors to use an AS agent in all HMA mixes without conducting any moisture-susceptibility test (Kandhal 1994).

2.4.2 Lime Additives

Unlike liquid AS agents, which are added to the asphalt cement, lime is added to the aggregate prior to mixing with asphalt cement. Many studies indicate that lime is a very effective antistripping agent (e.g., Kandhal 1994; Hicks 1991). However, its antistripping mechanism is not well understood. Various mechanisms have been postulated: (a) lime interacts with acids in the asphalt cement that are readily absorbed on the aggregate surface; (b) lime provides calcium ions which can replace hydrogen, sodium, potassium and other cations on the aggregate surface; and (c) lime reacts with most silicate aggregates to form a calcium silicate crust which has a strong bond to the aggregate and has sufficient porosity to allow penetration of the asphalt cement to form another strong bond.

Both hydrated lime $Ca(OH)_2$ and quick lime CaO (in slurry form) are effective, although the former is most commonly used. Dolomitic limes have also been used as antistripping additives. However, as a carbonate $CaCO_3$, lime is not as effective. Generally, 1 to 1½ percent of lime by weight of dry aggregate is used. Finer aggregates may require higher percentages because of increased aggregate surface area.

Aggregates have been treated with lime by the following four methods (Hicks 1991):

1) Dry hydrated lime: The main problem in using dry lime is to maintain its coating on the aggregate surface until it is coated with asphalt cement. It is more critical in drum mixers, which tend to pick up some of the lime in the exhaust gas flow. However, Georgia DOT has successfully instituted the use of dry hydrated lime in drum mixers by

injecting lime into the drum just ahead of the asphalt cement. The pick up of lime by the gas stream is prevented by modifications of the flights and providing suitable baffles inside the drum (Kennedy 1984). Some asphalt-paving technologists believe that the use of dry lime is not consistently effective, although many agencies including Georgia DOT report satisfactory results with dry lime.

2) Hydrated lime slurry: This method requires additional water to be added to the aggregates which results in increased fuel costs and reduced HMA production rates.
3) Dry hydrated lime to wet aggregate: In this method dry hydrated lime is added to wet aggregate, usually containing 3-5 percent water, and then mixed in a pugmill or tumble mixer to obtain a homogeneous mix.
4) Hot (quicklime) slurry: The use of quicklime (CaO) slurry has at least two advantages: (a) its cost is equal to that of hydrated lime, but when slaked the yield is 25 percent greater; and (b) the heat from slaking results in an elevated temperature which helps in the evaporation of the added moisture. However, quicklime should be handled with caution because it can cause skin burns.

The relative effectiveness of the preceding four treatments based on comparative laboratory and field studies have been generally inconclusive and, therefore, increased fuel and equipment costs and decreased HMA production rates associated with the wet process may not be justified at the present time.

2.5 Moisture Susceptibility Tests and Conditioning Systems

To combat stripping, proper mixture design is absolutely essential; however, it is possible for a properly designed mix to strip if field if water enters into the HMA layer. Therefore, each mixture must be evaluated to determine if it is susceptible to moisture damage.

Numerous test methods have been proposed and used in the past to predict the moisture susceptibility of HMA mixes (Lottman 1982a; Tunnicliff and Root 1984; Stuart 1986; Stuart 1990; Coplantz and Newcomb 1988; Hicks 1991; Kandhal 1992; Kandhal 1994; Al-Swailmi and Terrel 1992; Terrel and Al-Swailmi 1994). However, no single test has a wide acceptance, with the possible exception of the Modified Lottman Test (AASHTO 1986), which is now a part of the Superpave mixture design protocol. This is due to their overall recognized low reliability and lack of satisfactory relationship between laboratory and field conditions. Only selected test methods, which are commonly used by agencies, will be discussed briefly.

2.5.1 Quantitative or Subjective Tests

A) *Boiling Water Test*: Loose HMA mix is added to boiling water. ASTM D3625 specifies a 10-minute boiling period. The percentage of the total visible area of the aggregate that retains its original coating after boiling is estimated as above or below 95 percent. This test can be used for initial screening of HMA mixtures. Some agencies use it for quality control during production to determine the presence of an antistripping agent. This test method does not involve any strength analysis. Also, determining the stripping of fine aggregate is very difficult. This test method generally favors liquid antistripping agents over lime.

B) *Static-Immersion Test* (AASHTO T-182): A sample of HMA mix is immersed in distilled water at 77° F (25° C) for 16 to 18 hours. The sample is then observed through water to estimate the percentage of total visible area of the aggregate, which remains coated as above or below 95 percent. Again, this method does not involve any strength test.

2.5.2 Quantitative Strength Tests

A) *Lottman Test*: This method was developed by Lottman (1982a; 1984). Nine specimens, 4 inches (102 mm) in diameter and 2 ½ inches (64 mm) high, are compacted to expected field air void content. Specimens are divided into three groups of three specimens each. Group 1 is treated as control without any conditioning. Group 2 specimens are vacuum saturated (26 inches or 660 mm Hg) with water for 30 minutes. Group 3 specimens are vacuum saturated like Group 2 and then subjected to a freeze (0° F or –18° C for 15 hours) and a thaw (140° F or 60° C for 24 hours) cycle. All 9 specimens are tested for resilient modulus (M_R) and/or indirect tensile strength (ITS) at 55° F (13° C) or 73° F (23° C). A loading rate of 0.065 inch/minute (1.65 mm/minute) is used for the ITS test. Group 2 reflects field performance up to 4 years. Group 3 reflects field performance from 4 to 12 years. Retained tensile strength (TSR) is calculated for Group 2 and Group three specimens as follows:

TSR = ITS of conditioned specimens / ITS of control specimens

A minimum TSR of 0.70 is recommended by Lottman (1982a) and Maupin (1982) who reported values between 0.70 and 0.75 differentiated between stripping and nonstripping HMA mixtures. It has been argued that the Lottman procedure is too severe because the warm water soak of the vacuum saturated and frozen specimen can develop internal water pressure. However, Stuart (1986) and Parker and Gharaybeh (1987) generally found a good correlation between the laboratory and field results. Oregon has successfully used this test with a resilient modulus ratio in lieu of tensile strength ratio (TSR).

B) *Tunnicliff and Root Method*: This method was proposed by Tunnicliff and Root (1984) under NCHRP Project 274. They proposed six specimens to be compacted to 6-8 percent air void content and divided into two groups of three specimens each. Group 1 is treated as control without any conditioning. Group 2 specimens are vacuum saturated (20 inches or 508 mm Hg for about 5 minutes) with water to attain a saturation level of 55 to 80 percent. Specimens saturated more than 80 percent are discarded. The saturated specimens are then soaked in water at 140° F (60° C) using a loading rate of 2 inches/minute (51 mm/minute). A minimum TSR of 0.7 to 0.8 is usually specified. The use of a freeze-thaw cycle is not mandated in ASTM D4867-88, which is based on this method. The freeze-thaw cycle is optional. The primary emphasis is on saturation of the specimen, which for a short duration of about 24 hours has been reported to be insufficient to induce moisture-related damage (Coplantz and Newcomb 1988).

C) *Modified Lottman Test* (AASHTO T-283): This method was initially adopted by AASHTO in 1985 (AASHTO 1986). It combines the good features of Lottman Test (Lottman 1982a) and the Tunnicliff and Root Test (Tunnicliff and Root 1984). Six specimens are compacted to 6-8 percent air void content. Group 1 of three specimens is used as a control. Group 2 specimens are vacuum saturated (55 to 80 percent saturation) with water, and then subjected to one freeze-thaw cycle as proposed by Lottman. All specimens are tested for ITS at 77° F (25° C) using a loading rate of 2 inches/minute (51 mm/minute), and the TSR is determined. A minimum TSR of 0.7 is usually specified. This method is gaining acceptance by the specifying agencies.

D) *Immersion-Compression Test* (AASHTO T-165): Six specimens, 4 inches (102 mm) in diameter × 4 inches (102 mm) high, are compacted with a double plunger with a pressure of 3000 psi (20.7 MPa) for 2 minutes to about 6 percent air void content. Group 1 of three specimens is treated as control. Group 2 specimens are placed in water at 120° F (49° C) for 4 days or at 140° F (60° C) for 1 one. All specimens are tested for unconfined compressive strength at 77° F (25° C) using 0.2 inch/minute) loading rate. The retained compressive strength is determined. Many agencies specify at least 70 percent retained strength. This test has produced retained strengths near 100 percent even when stripping is evident. Stuart (1986) has attributed this to the internal pore water pressure and the insensitivity of the compression test to measure the moisture-induced damage properly. Lack of satisfactory precision has been a major problem with this test.

E) *Other Tests*: Moisture-vapor susceptibility, swell test, and a film-stripping test are used by California DOT. Retained Marshall stability is used in Puerto Rico and some other states.

Evidently, a wide variety of test methods are being used by various agencies. However, no test has proven to be "superior" and can correctly identify a moisture-susceptible mix in all cases. This means that many HMA mixes, which might otherwise perform satisfactory in the field, are likely to be rendered unacceptable if these tests and criteria are used. Also, mixtures that may pass these tests may not perform well in the field. The lack of robust evaluation and test systems has simply encouraged the increased use of antistripping agents in many states.

There are still many concerns and requirements related to the test methods, which need to be addressed:

1. Proliferation of test procedures and criteria.
2. Reproducibility of most test methods is not satisfactory. For example, small variations in air void content of the specimens can significantly affect the TSR results in the AASHTO T-283 test (Coplantz and Newcomb 1988).
3. Need to consider minimum wet strength (if the desired value can be established) of the conditioned specimens rather than relying solely on the TSR value. For example, some additives increase both dry and wet strengths but might have a low TSR value.
4. Lack of satisfactory correlation between laboratory and field performance.

However, based on a survey of states (Kandhal 1992) it appears that the Modified Lottman Test (AASHTO T-283) is the most widely used test method available at the present time to detect moisture damage in HMA mixes. AASHTO T-283 has been included in Superpave mix design procedures. A minimum TSR of 0.70 is recommended when using this test method. This criterion should be applied to the field-produced rather than laboratory-produced mixes.

According to Choubane et al. (2000), the AASHTO T-283 specified range of moisture saturation may not be appropriate because TSRs of asphalt samples saturated to the lower limit of the range may be significantly different than those saturated to the upper limit. On the other hand, this procedure shows more promise for predicting stripping potential in the laboratory when the saturation level is above 90 percent and a freeze-thaw cycle is considered. A modified AASHTO T-283 procedure is proposed, including a vacuum saturation for 30 minutes with 610 mm of mercury, which represents a level of saturation between 85 to 95 percent, and a freeze-thaw cycle.

2.5.3 Mixture Performance Testing for the Evaluation of Moisture Damage

The Strategic Highway Research Program (SHRP) had two research contracts dealing with moisture susceptibility of HMA mixes. SHRP Project A-003A "Performance Related Testing and Measuring of Asphalt-Aggregate Interactions and Mixtures" attempted to develop an improved test method to evaluate moisture susceptibility. SHRP Project A-003B "Fundamental Properties of Asphalt-Aggregate Interactions Including Adhesion and Adsorption" studied the fundamental aspects of asphalt-aggregate bond.

Net Adsorption Test (NAT) was developed under SHRP A-003B completed by the National Center for Asphalt Technology (NCAT). It is a preliminary screening test for matching mineral aggregates and asphalt cement (e.g., Kandhal 1994) and is based on the principles of adsorption and desorption. A solution of asphalt cement and toluene is introduced and circulated in a reaction column containing the aggregate sample. Once the solution temperature has been stabilized, 4 ml of solution is removed and the absorbance is determined with a spectrophotometer. Fifty grams of minus No. 4 (4.75 mm) aggregate is then added to the column, and the solution is circulated through the aggregate bed for 6.5 hours. A second 4-ml sample of the solution then is removed from the column and the absorbance is again determined. The difference in the absorbance readings is used to determine the amount of asphalt that has been removed from the solution (adsorption) because of the chemical attraction of the aggregate for the molecular components of the asphalt cement. Immediately after the second solution sample is taken, 575 m of water is added to the column. The solution is then circulated through the system for another 2 hours. A final 4 ml of solution is taken from the column at the end of this time. The increase in the adsorptivity is a measure of the amount of asphalt cement that is displaced by water molecules (desorption). Additional validation data are needed for the NAT.

The Environmental Conditioning System (ECS) was developed under SHRP Project A-003A "Performance Related Testing and Measuring of Asphalt-Aggregate Interactions and Mixtures" (Al-Swailmi and Terrel 1992; Terrel and Al-Swailmi 1994), and updated by researchers at the University of Texas, El Paso (Alam et al. 1998). This system was designed specifically to evaluate the moisture susceptibility of HMA specimens by resilient modulus testing. To saturate the specimen, the Environmental Conditioning System uses a vacuum-based control panel that draws water through the specimen from a storage reservoir. Simultaneously, temperature conditioned water was cycled around the specimen to get it to a proper temperature for testing. The disadvantage with this configuration is that by flowing ambient temperature water through the specimen, adequate conductance was prevented between the permeant and the confining water. As a result, the actual temperature of the specimen was unknown during testing. The well-known sensitivity of HMA to temperature makes this approach to control questionable. Additionally, the conditioning system is inefficient relying upon a copper coil, which runs through a heated water bath. The pressurized water running through the coil relies upon conductance through the copper to condition it. This configuration required up to 16 hours before the system was stabilized at temperature precluding it from use as a production capable system. Also, the system is limited to testing at temperatures above ambient. The specificity of purpose limited the Environmental Conditioning System's design to resilient modulus testing. Despite the significant research effort during the SHRP project, the Environmental Conditioning System has never reached acceptance by state agencies.

2.5.4 Other Developments of Interest

Based on the assumption that pore pressures were a major cause of moisture damage in mixtures, Jimenez (1974) developed a test procedure and a device to determine the stripping

susceptibility of asphalt. Specimens were vacuum-saturated in a 50° C (122° F) water bath and then conditioned by applying a sinusoidal load from 35 to 207 kPa (5 – 30 psi) at a rate of 580 times per minute for 10 minutes. The basic premise of the loading was to induce cyclic pore pressures in the specimen that were believed to be similar to those caused by traffic loads. After conditioning, the samples were placed in a 25° C water bath for 45 minutes before being tested for the indirect tensile strength which was compared to the indirect tensile strength of an equivalent unconditioned sample. Jimenez (1974) concluded that the new procedure was simple and repeatable but needed field-testing before it could be implemented.

Hydraulic scouring, as a result of repeated generation of pore water pressure, is considered to be the primary cause of moisture-induced damage in asphalt paving mixtures in a paper written by Mallick et al. (2003). A new process was developed for this research. Also, InstroTek, Inc., created a new piece of equipment in order to carry out this procedure (Mallick et al. 2003). Specimens were placed in a chamber that was positioned in a water bath. The water temperature was maintained by an immersion heater at either 40° or 60º C depending on the specimen's group. Compressed air was forced into the chamber so that the water is forced out of and below the sample surface. Next, a vacuum was applied that pulled the water back into the chamber. Depending on the specimen's group, this procedure was cycled 2,000, 3,000, 4,000, or 6,000 times. The tensile strength of the conditioned samples was then compared to the unconditioned samples to determine the retained strength. Mallick et al. (2003) concluded that this procedure gave comparable results with AASHTO T-283 but needed further refinement. Finally, because of problems with current tests, many have been looking at empirical "torture" tests such as the Hanburg test device to predict moisture susceptibility of HMH.

2.6 Conclusions

Based on the literature review, the following conclusions can be reached:

1. Of the five major potential mechanisms for moisture damage reported in the literature, none have been proven by connecting theoretical considerations to observed field behavior. Rather, these mechanisms are hypothesized based on field observation, along with limited basic laboratory characterization.
2. There are currently no performance-based methods for evaluating moisture damage available that have been widely accepted by state agencies.
3. The methods used to evaluate moisture susceptibility of mixtures tend to be either qualitative in nature, like the boil test, or crude quantitative techniques that may neither include the appropriate mechanism of moisture damage nor the appropriate framework for analyzing the effects of moisture damage on mixtures. These current laboratory testing procedures currently available, including the AASHTO T-283 procedure, were primarily developed to determine the degree of resistance to moisture damage by a particular combination of asphalt and aggregate, compare mixes composed of different types and quantities of aggregate, or to evaluate the effectiveness of antistripping agents (Lottman 1982b; Tunnicliff and Root 1984; Curtis et al. 1992; Al-Swailmi and Terrel 1992; Terrel and Al-Swailmi 1994). These moisture susceptibility tests all evaluate the effects of water damage in the laboratory by measuring the relative change of a single parameter before and after conditioning (i.e., tensile strength ratio, resilient modulus ratio). These parameters do not distinguish between the different mechanisms present in a conditioned mixture, including the identification of the effects of pore water versus actual moisture damage.

4. The current Superpave specification uses the AASHTO T-283 moisture susceptibility test for determining moisture sensitive mixtures. Most state agencies use AASHTO T-283 test, although there have been questions by the community at large about the accuracy of the test. Frequent false positives and/or negatives have been reported, leading to the initiation of this current study, as well as a larger national study sponsored by the National Cooperative Highway Research Program (NCHRP) and entitled "NCHRP Project 9-34: Improved Conditioning Procedure for Predicting the Moisture Susceptibility of HMA Pavements."
5. Depending on materials, loading, and environment, it may be that one or all of the mechanisms of water damage are present and dominant in an actual pavement. However, for a proper evaluation of any given mixture and testing procedure, it is necessary to isolate and quantify the effects of each of the predominant mechanisms contributing to moisture damage. Water damage effects in HMA pavements may be bracketed by two extreme conditions: a) the rapid application of cyclic pore pressures under saturated conditions that correspond to critical field conditions; and b) the longer term continuous low level exposure to water without pore pressures. However, little research has been conducted to further clarify the most important condition – i.e., pore pressures or long-term continuous low level exposure.

In summary, there is a clear need to develop a robust performance-based framework for the evaluation of mixture moisture damage susceptibility, as well as identifying the most likely basic mechanisms of moisture damage in pavements, and finally developing an appropriate conditioning system based on this mechanism.

2.7 References

AASHTO (American Association of State Highway Transportation Officials), "Resistance of Compacted Bituminous Mixture to Moisture Induced Damage," *AASHTO T283-86, Part II–Methods of Sampling and Testing*, August 1986.

Adamson, A.W., *Physical Chemistry of Surfaces*, *Third Edition*, John Wiley & Sons, New York, 1976.

Alam, M.M., Vemuri, N., Tandon, V., Nazarian, S., and Picornell, M., "A Test Method for Identifying Moisture Susceptible Asphalt Concrete Mixes," University of Texas at El Paso, El Paso, 1998.

Al-Swailmi, S., and Terrel, R.L., "Evaluation of Water Damage of Asphalt Concrete Mixtures Using the Environmental Conditioning System (ECS)," *Proceedings*, Association of Asphalt Paving Technologists (AAPT), Vol. 61, 1992.

Choubane, B., Page, G.C., and Musselman, J.A., "Effects of Different Water Saturation Levels on the Resistance of Compacted HMA Samples to Moisture Induced Damage," presented at the 80th Annual Transportation Research Board Meeting, Washington, D.C., 2000.

Coplantz, J.S., and Newcomb, D.E., "Water Sensibility Test Methods for Asphalt Concrete Mixtures–A Laboratory Comparison," *Transportation Research Record 1171*, Transportation Research Board (TRB), National Research Council (NRC), Washington, D.C., 1988.

Curtis, C.W., Stroup-Gardiner, M., Brannan, C.J., and Jones, D.R., "Adsorption of Asphalt on Aggregate to Evaluate Water Sensitivity," *Transportation Research Record #1362*, TRB, NRC, Washington, D.C., 1992.

Curtis, C.W., Ensley, K., and Epps, J., "Fundamental Properties of Asphalt-Aggregate Interactions Including Adhesion and Absorption," *SHRP-A-341*, Strategic Highway Research Program (SHRP), NRC, Washington, DC, 1993.

Curtis, C.W., Einsley, K., and Epps, J., "Fundamental Properties of Asphalt-Aggregate Interactions Including Adhesion and Absorption," *Final Report SHRP A-003B*, SHRP, 1993.

Fromm, H.J., "The Mechanisms of Asphalt Stripping from Aggregate Surfaces," *Proceedings*, AAPT, Vol. 43, 1974, pp. 191-223.

Hicks, R.G., "Moisture Damage in Asphalt Concrete," *NCHRP Synthesis of Highway Practice No. 175*, National Cooperative Highway Research Program (NCHRP), TRB, October 1991.

Jimenz, R.A., "Testing for Debonding of Asphalts from Aggregates," *Transportation Research Record 515*, TRB, NRC, Washington, D.C., 1974, pp. 1-17.

Kandhal, P.S., Lubold, C.W., and Roberts, F.L., "Water Damage to Asphalt Overlays: Case Histories," *Proceedings*, AAPT, Vol. 58, 1989.

Kandhal, P.S., "Moisture Susceptibility of HMA Mixes: Identification of Problem and Recommended Solutions," *NAPA Quality Improvement Publication 119*, December 1992.

Kandhal, P.S., "Field and Laboratory Investigation of Stripping in Asphalt Pavement: State of the Art Report," *Transportation Research Record 1454*, TRB, NRC, Washington, D.C., 1994, pp. 114-124.

Kandhal, P.S., and Rickards, I.S., "Premature Failure of Asphalt Overlays from Stripping: Case Histories," *Proceedings*, AAPT, Vol. 72, 2001, pp. 102-123.

Kennedy, T.W., "Use of Hydrated Lime in Asphalt Paving Mixtures," *Bulletin 325*, National Lime Association, 1984.

Kiggungu, B.M., and Roberts, F.R., "Stripping in HMA Mixtures: State-of-the-Art and Critical Review of Test Methods," *NCAT Report No. 88-2*, National Center for Asphalt Technology (NCAT), 1988.

Lottman, R.P., "Laboratory Test Method for predicting Moisture-Induced Damage to Asphalt Concrete," *Transportation Research Record #843*, TRB, NRC, Washington, D.C., 1982a.

Lottman, R.P., "Predicting Moisture-Induced Damage to Asphaltic Concrete–Field Evaluation," *NCHRP Report 246*, NCHRP, TRB, 1982b.

Majidzadeh, K., and Brovold, F.N., "State-of-Art: Effect of Water on Bitumen-Aggregate Mixtures," *HRB Special Report 98*, Highway Research Board (HRB), Washington, D.C., 1968.

Mallick, R.B., Gould, J.S., Bhattacharjee, S., Regimand, A., James, L.H., and Brown, E.R., "Development of a Rational Procedure for Evaluation of Moisture Susceptibility of Asphalt Paving Mixes," Presented at the Transportation Research Board Meeting, Washington, D.C., 2003.

Masad, E., Birgisson, B., Al-Omari, A., and Cooley, A., "Analysis of Permeability and Fluid Flow in Asphalt Mixes," *ASCE Journal of Materials in Civil Engineering*, American Society of Civil Engineers (ASCE), 2005.

Maupin, Jr., G.W., "The Use of Antistripping Additives in Virginia," *Proceedings*, AAPT, Vol. 51, 1982.

Parker, F., and Gharaybeh, F., "Evaluation of Indirect Tensile Tests for Assessing Stripping of Alabama Asphalt Concrete Mixtures," *Transportation Research Record 1115*, TRB, NRC, Washington, D.C., 1987.

Rice, J.M., "Relationship of Aggregate Characteristics to the Effect of Water on Bituminous Paving Mixtures. Symposium on Effect of Water on Bituminous Paving Mixtures," *ASTM STP No. 240*, American Society for Testing and Materials (ASTM), 1958, pp. 17-34.

Schmidt, R.J., and Graf, P.E., "The Effect of Water on the Resilient Modulus of Asphalt-Treated Mixes," *Proceedings*, AAPT, Vol. 41, 1972.

Scott, J.A.N., "Adhesion and Disbonding Mechanisms of Asphalt Used in Highway Construction and Maintenance," *Proceedings*, AAPT, Vol. 47, 1978, pp. 19-48.

Stuart, K.D., "Evaluation of Procedures Used to Predict Moisture Damage in Asphalt Mixtures," *FHWA Report FHWA/RD-86/091*, Federal Highway Administration (FHWA), 1986.

Stuart, K.D., "Moisture Damage in Asphalt Mixtures–A-State-of-the-Art Report," *Report FHWA-RD-90-019*, FHWA, August 1990.

Taylor, M.A., and Khosla, N.P., "Stripping of Asphalt Pavements: State of the Art," *Transportation Research Record 911*, TRB, NRC, Washington, D.C., 1983.

Terrel, R.L., and Al-Swailmi, S., "Water Sensitivity of Asphalt Aggregate Mixes: Test Selection," *SHRP-A-403*, SHRP, NRC, Washington, D.C., 1994.

Thelen, E., "Surface Energy and Adhesion Properties in Asphalt-Aggregate Systems," *HRB Bulletin 192*, HRB, Washington D.C., 1958.

Tunnicliff, D.G., and Root, R.E., "Antistripping Additives in Asphalt Concrete: State-of-the-Art Report," *Proceedings*, AAPT, Vol. 51, 1982.

Tunnicliff, D.G., and Root, R.E., "Use of Antistripping Additives in Asphaltic Concrete Mixtures," *NCHRP Report 274*, NCHRP, TRB, 1984.

CHAPTER 3
EVALUATION OF AASHTO T-283 TESTING RESULTS

3.1 Introduction

The laboratory testing procedures currently available for testing HMA moisture susceptibility, including the AASHTO T-283 procedure, were primarily developed to determine the degree of resistance to moisture damage by a particular combination of asphalt and aggregate, compare mixes composed of different types and quantities of aggregate, or to evaluate the effectiveness of antistripping agents (Lottman 1982; Tunnicliff and Root 1984; Curtis et al. 1992; Al-Swailmi and Terrel 1992; Terrel and Al-Swailmi 1994). These moisture susceptibility tests all evaluate the effects of water damage in the laboratory by measuring the relative change of a single parameter before and after conditioning (i.e., tensile strength ratio, resilient modulus ratio). These parameters do not distinguish between the different mechanisms present in a conditioned mixture, including the identification of the effects of pore water versus actual moisture damage.

The current Superpave specification uses the AASHTO T-283 moisture susceptibility test for determining moisture sensitive mixtures. Most state agencies use AASHTO T-283 test, although there have been questions by the community at large about the accuracy of the test. Frequent false positives and/or negatives have been reported, leading to the initiation of this current study, as well as a larger national study sponsored by the National Cooperative Highway Research Program (NCHRP) and entitled "NCHRP Project 9-34: Improved Conditioning Procedure for Predicting the Moisture Susceptibility of HMA Pavements." However, in view of the widespread use of the AASHTO T-283 test procedure for evaluating the potential for moisture damage in mixtures, it is necessary to evaluate the mixtures used in this study with the

AASHTO T-283 procedure. It is not anticipated that the results presented in this chapter should compare well or parallel trends in data observed from other test results.

3.2 Objectives

The main objective with this chapter is to establish a baseline test response database using the AASHTO T-283 test. A total of 15 mixtures of varying aggregate types and gradations are tested. Understanding that these test results are not necessarily expected to show trends that parallel results obtained from more refined conditioning and performance testing procedures, it is still felt that all mixtures used in this study should be tested by the AASHTO T-283 test.

3.3 Scope

In the following, the aggregates, gradations, and binder used in the testing in this chapter are presented, followed by a presentation of the AASHTO T-283 test results. In addition to comparison of the tensile strength ratio obtained from the AASHTO T-283 procedure between 15 mixtures of known aggregate sources and known performance, the potential relationship between permeability and the tensile strength ratio are also evaluated. Visual observations are made of different failure patterns obtained for limestone mixtures and granite mixtures, and the possible effects of microstructure are discussed.

3.4 Materials and Testing Methods

Two groups of aggregates were used. The first consisted of crushed granite from Georgia that has shown potential for stripping. The second consisted of an oolitic limestone aggregate from South Florida that has in the past not shown significant stripping potential. Both aggregate groups are used extensively in Florida and are considered to be excellent materials resulting in well-performing mixtures.

Six limestone and six granite mixtures were made up of four components: coarse aggregate, fine aggregate, screenings, and mineral filler. They were blended together in different proportions to provide six 12.5-mm nominal maximum aggregate size mixtures of coarse and fine gradations. The limestone mixtures are denoted as: WR-C1, WR-C2, WR-C3, WR-F1, WR-F2, WR-F3/C4, and the Georgia granite mixtures are denoted as: GA-C1, GA-C2, GA-C3, GA-F1, GA-F2, GA-F3/C4, with the letters C and F denoting coarse-graded and fine-graded mixtures according to whether the gradation passes below or above the Superpave™ restricted zone. The purpose of selecting granite mixtures of varying gradation was to ensure that the mixtures tested were of different permeability, and other volumetric properties, but with of the same aggregate type. The oolitic limestone and the Georgia granite mixtures are designed to be volumetrically equivalent. This allows the limestone mixtures to be used for comparison purposes, since it is known to be highly resistant to stripping. Finally, three additional granite mixtures were also evaluated. These mixtures are also commonly used by the FDOT. The first two mixtures consisted of Georgia granite, Florida limestone, and recycled asphalt pavement (RAP). One mixture was a coarse 12.5-mm nominal maximum aggregate size (SP2) and the other was a coarse 19-mm nominal maximum aggregate size (SP3). The third granite mixture (NS315) is a coarse 19-mm nominal maximum aggregate size mixture consisting of Nova Scotia granite. The resulting gradations for all mixtures are shown in Table 3-1 (a) and (b). The mixtures ranged from what could be described as fine uniformly-graded and fine dense-graded to coarse uniformly-graded and coarse gap-graded.

All mixtures were designed according to the Superpave volumetric mix design method. Design asphalt contents for all the mixtures were determined such that each mixture had 4 percent air voids at N_{design} = 109 gyrations. PG 67-22 (AC-30) asphalt was used for all limestone

Table 3-1. Mixture Gradations

(a) Volumetrically Equivalent Limestone and Granite Mixtures

Sieve Size	Limestone: Percent Passing					
	WR-C1	WR-C2	WR-C3	WR-F1	WR-F2	WR-F3/C4
19 mm (3/4)	100.0	100.0	100.0	100.0	100.0	100.0
12.5 mm (1/2)	97.0	91.0	98.0	96.0	91.0	95.0
9.5 mm (3/8)	90.0	74.0	89.0	85.0	78.0	85.0
4.75 mm (#4)	60.0	47.0	57.0	69.0	61.0	67.0
2.36 mm (#8)	33.0	30.0	36.0	53.0	44.0	37.0
1.18 mm (#16)	20.0	20.0	24.0	34.0	35.0	26.0
600 μm (#30)	15.0	14.0	18.0	23.0	24.0	20.0
300 μm (#50)	11.0	10.0	13.0	15.0	16.0	14.0
150 μm (#100)	7.6	6.7	9.2	9.6	9.1	8.6
75 μm (#200)	4.8	4.8	6.3	4.8	6.3	5.8
Sieve Size	Granite: Percent Passing					
	GA-C1	GAR-C2	GA-C3	GA-F1	GA-F2	GA-F3/C4
19 mm (3/4)	100.0	100.0	100.0	100.0	100.0	100.0
12.5 mm (1/2)	97.4	90.9	97.3	94.7	90.5	94.6
9.5 mm (3/8)	89.0	72.9	89.5	84.0	77.4	85.1
4.75 mm (#4)	55.5	45.9	55.4	66.4	60.3	65.1
2.36 mm (#8)	29.6	28.1	33.9	49.2	43.2	34.8
1.18 mm (#16)	19.2	18.9	23.0	32.7	34.0	26.0
600 μm (#30)	13.3	13.2	16.0	21.0	23.0	18.1
300 μm (#50)	9.3	9.2	11.2	12.9	15.3	12.5
150 μm (#100)	5.4	5.6	6.8	5.9	8.7	7.7
75 μm (#200)	3.5	3.9	4.7	3.3	5.4	5.8

(b) Additional Granite Mixtures Used

Sieve Size	SP-2	SP-3	NS315
25 mm (1)	100	100	100
19 mm (3/4)	98	100	97
12.5 mm (1/2)	89	98	83
9.5 mm (3/8)	84	89	66
4.75 mm (#4)	41	47	38
2.36 mm (#8)	31	25	23
1.18 mm (#16)	24	18	18
600 μm (#30)	17	15	14
300 μm (#50)	13	11	10
150 μm (#100)	9	7	6.5
75 μm (#200)	4	4	3.5

and granite mixtures in this study. Also, consistent with FDOT practice, an additional set of granite mixtures were also prepared with PG 67-22 asphalt containing 0.5 percent liquid antistripping agent by weight of total asphalt. The liquid antistripping agent used was ARR-MAZ AD-HERE LOF 65-00, which is commonly used in Florida. Table 3-2 (a) and (b) shows the volumetric properties for the mixtures used.

The following tests and analyses were performed:

- Mixtures were designed according to the Superpave™ volumetric mix design method.
- Mixtures were produced in the laboratory following the procedure outlined in AASHTO T-283. First, the aggregates and asphalt binder were heated to 150° C (300° F) for three hours prior to mixing. Once the mixing was completed, the mixture was allowed to cool to room temperature for two hours. After the cooling period, the loose mixture was long-term aged for 16 hours at 60° C (140° F). After the mixture was aged for 16 hours, it was reheated to 135° C (275° F) for two hours before compaction. The specimens were then compacted on the IPC Servopac Superpave™ gyratory compactor to 7-8 percent air voids. A total of nine samples of each mix were prepared.
- For each mixture, three samples were then subjected to saturation according to the AASHTO T-283 procedure. Throughout the testing, a target saturation level of 55 and 80 percent was maintained, which is the saturation required in AASHTO T-283 prior to 2003 changes. The saturation procedure called for a vacuum saturation for 15 minutes and then 15 minutes in a water bath without vacuum. If the minimum saturation was not achieved, then another cycle was used until the minimum saturation was achieved.
- After the target saturation level was achieved, the specimens were placed in a 60° C (140° F) hot water bath for 24 hours. After the hot bath, the conditioned specimens were

Table 3-2. Volumetric Properties of Mixtures Used

(a) Volumetrics for Volumetrically Equivalent Limestone and Granite Mixtures

Volumetric Property	Limestone						Granite					
	WR-C1	WR-C2	WR-C3	WR-F1	WR-F2	WR-F3/ C4	GA-C1	GA-C2	GA-C3	GA-F1	GA-F2	GA-F3/C4
Max. Specific Gravity (G_{mm})	2.328	2.347	2.349	2.338	2.375	2.347	2.442	2.500	2.492	2.473	2.532	2.505
Binder Specific Gravity (G_b)	1.035	1.035	1.035	1.035	1.035	1.035	1.035	1.035	1.035	1.035	1.035	1.035
Bulk Specific Gravity (G_{mb})	2.235	2.255	2.254	2.244	2.281	2.254	2.442	2.399	2.391	2.473	2.433	2.404
Percent Binder (P_b)	6.5	5.8	5.3	6.3	5.4	5.6	6.63	5.26	5.25	5.68	4.56	5.14
Aggregate Bulk Specific Gravity (G_{sb})	2.469	2.465	2.474	2.488	2.489	2.468	2.687	2.687	2.686	2.686	2.687	2.687
Aggregate Effective Specific Gravity (G_{se})	2.549	2.545	2.528	2.554	2.565	2.537	2.710	2.719	2.709	2.706	2.725	2.720
Absorbed Percent Binder (P_{ba})	1.1	1.3	0.9	1.1	1.2	1.1	0.37	0.43	0.31	0.28	0.53	0.46
Effective Percent Binder (P_{be})	5.3	4.6	4.5	5.3	4.2	4.5	6.32	4.85	4.96	5.42	4.06	4.70
Voids in Mineral Aggregates VMA (%)	15.4	13.8	13.6	15.6	13.2	14.0	18.5	15.4	15.7	16.6	13.6	15.1
Design Percent Air Voids Va (%)	4.0	3.9	4.0	4.0	3.9	3.9	4.0	4.0	4.1	4.0	3.9	4.0
Voids Filled with Asphalt VFA (%)	74.0	71.6	70.2	74.2	70.1	71.8	78.5	73.8	74.2	75.9	71.2	73.3
Dust to Asphalt Ratio (D/A)	1.0	0.8	1.2	0.8	1.4	1.0	0.6	0.8	0.9	0.6	1.2	1.2

Table 3-2. Volumetric Properties of Mixtures Used–continued

(b) Volumetrics for Additional Granite Mixtures Used

Volumetric Property	Granite		
	SP-2	SP-3	NS-315
Max. Specific Gravity (G_{mm})	2.470	2.496	2.455
Binder Specific Gravity (G_b)	1.035	1.035	1.035
Bulk Specific Gravity (G_{mb})	2.372	2.419	2.342
Percent Binder (P_b)	5.7	4.9	5.0
Aggregate Bulk Specific Gravity (G_{sb})	2.606	2.692	2.608
Aggregate Effective Specific Gravity (G_{se})	2.702	2.697	2.651
Absorbed Percent Binder (P_{ba})	0.701	0.702	0.610
Effective Percent Binder (P_{be})	5.03	4.18	4.420
Voids in Mineral Aggregates VMA (%)	13.3	13.5	15.9
Design Percent Air Voids Va (%)	3.97	3.08	4.6
Voids Filled with Asphalt VFA (%)	70.3	77.2	71.1
Dust to Asphalt Ratio (D/A)	0.614	0.816	0.7

split up into groups of two. The first batch of conditioned mixtures was split using the AASHTO T-283 indirect tensile test procedure and the effects of water conditioning on the mixes were also observed visually from the split pieces.

- The three unconditioned specimens for each mixture were also split using the AASHTO T-283 indirect tensile test procedure, and the resulting tensile strength ratio (TSR) was calculated as the ratio of the average tensile strength of the conditioned specimens over the average tensile strength of the unconditioned specimens.
- Finally, three more specimens of each mixture each were prepared to conduct falling head water permeability testing to evaluate the effects of void structure and access of water to the specimen. Test method and apparatus designation FM 5-565 was designed by FDOT (Choubane et al. 1998; 2000). The test method covers the laboratory determination of the water conductivity of a compacted asphalt mixture. The method gives a comparison of water permeability between asphalt samples tested in the same

manner. The method can be used to test both laboratory compacted cylindrical samples and field core samples. Table 3-3 lists the measured permeability for each mixture tested.

Table 3-3. Mixture Permeability and Average Percent Saturation

Mixture	Permeability (10^{-5} cm/s)	Saturation (percent)
WR-C1	72.4	72.3
WR-C2	64.2	61.8
WR-C3	29.4	77.6
WR-F3/C4	69.6	75.8
WR-F1	17.8	84.2
WR-F2	9.7	80.1
SP-2	102.0	58.9
SP-3	111.0	74.2
NS315	113.0	60.9
GA-C1	67.5	64.6
GA-C2	59.0	56.8
GA-C3	56.0	66.3
GA-F1	25.3	72.1
GA-F2	9.3	60.2
GA-F3/C4	34.2	58.1

3.5 Analysis of Test Results

Most agencies now require a TSR below 0.8 for determining a moisture susceptible mixture. For the purpose of this research, a TSR of less than 0.8 indicates a moisture sensitive mixture. The reason a TSR of 0.8 was selected was because the FDOT specifications call for a TSR of greater than 0.8 for all of the mixtures placed on a roadway.

The first step in examining the mixtures was to perform AASHTO T-283 on all the mixtures and to develop a baseline for the mixtures in respect to the tensile strength ratio (TSR). Figure 3-1 shows the TSR for the limestone mixtures. The hypothesis was made that the limestone mixtures should perform well in regard to moisture damage. However, as seen in the figure, only one of the six mixtures (i.e., WR-F1) passed the required TSR of 0.8. Also, the fine-graded mixtures seemed to perform better than the coarse-graded mixtures. The granite mixtures

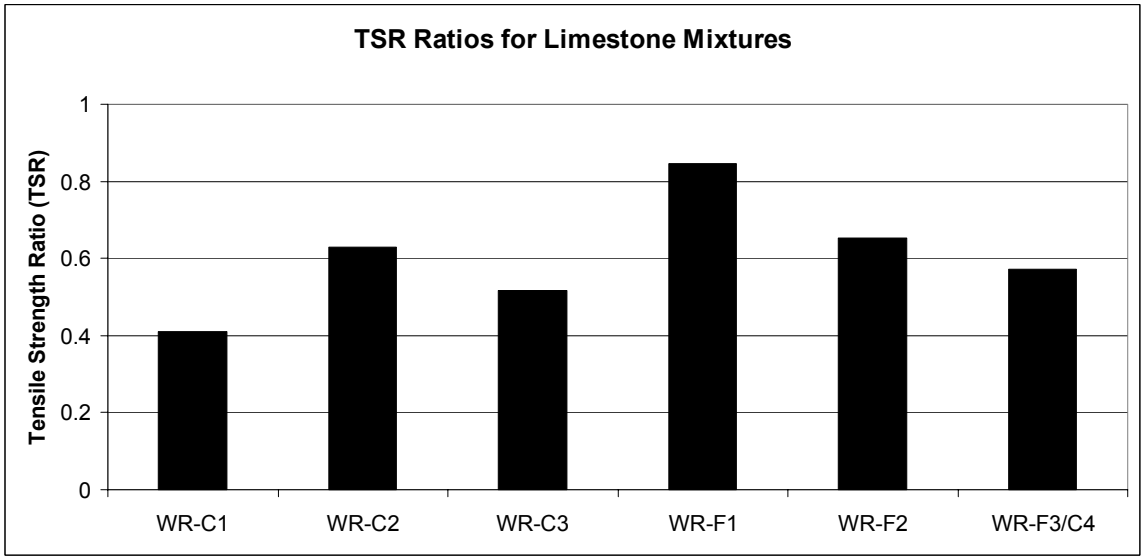

Figure 3-1. Tensile strength ratio for limestone mixtures.

were expected to perform poorly because the granite for two of the mixtures, SP-2 and SP-3, contains mica. The TSR for the granite mixtures is shown in Figure 3-2. Two of the mixtures did perform poorly, but the SP-2 mixture passed the TSR requirement. Figures 3-3 and 3-4 show the TSR results for the Georgia granite mixtures without and with antistripping agents, respectively.

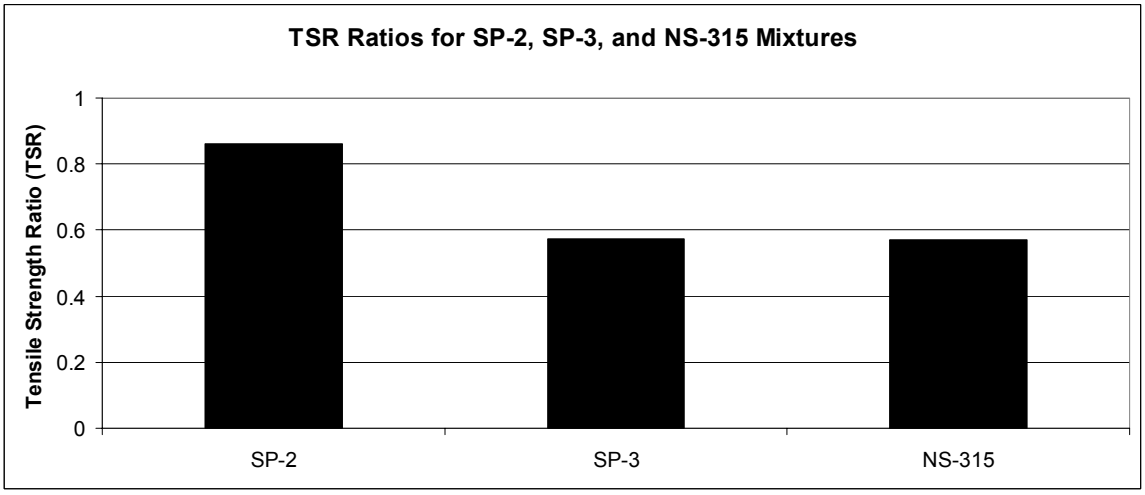

Figure 3-2. Tensile strength ratio for SP-2, SP-3, and NS-315 mixtures.

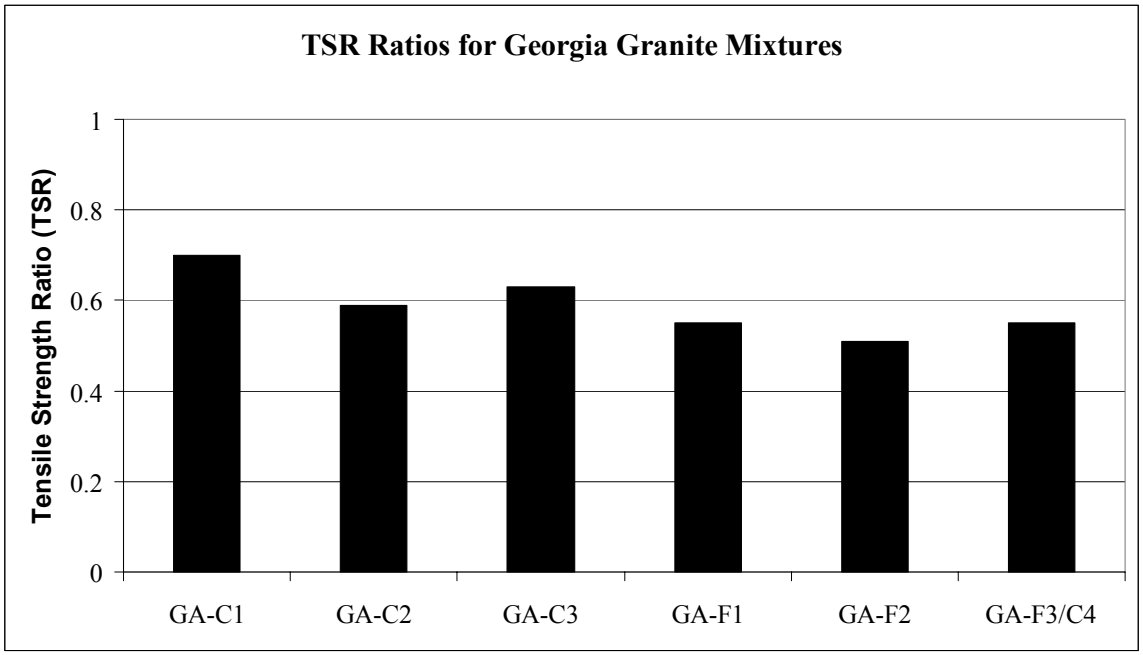

Figure 3-3. Tensile strength ratio for Georgia granite mixtures without antistripping agent.

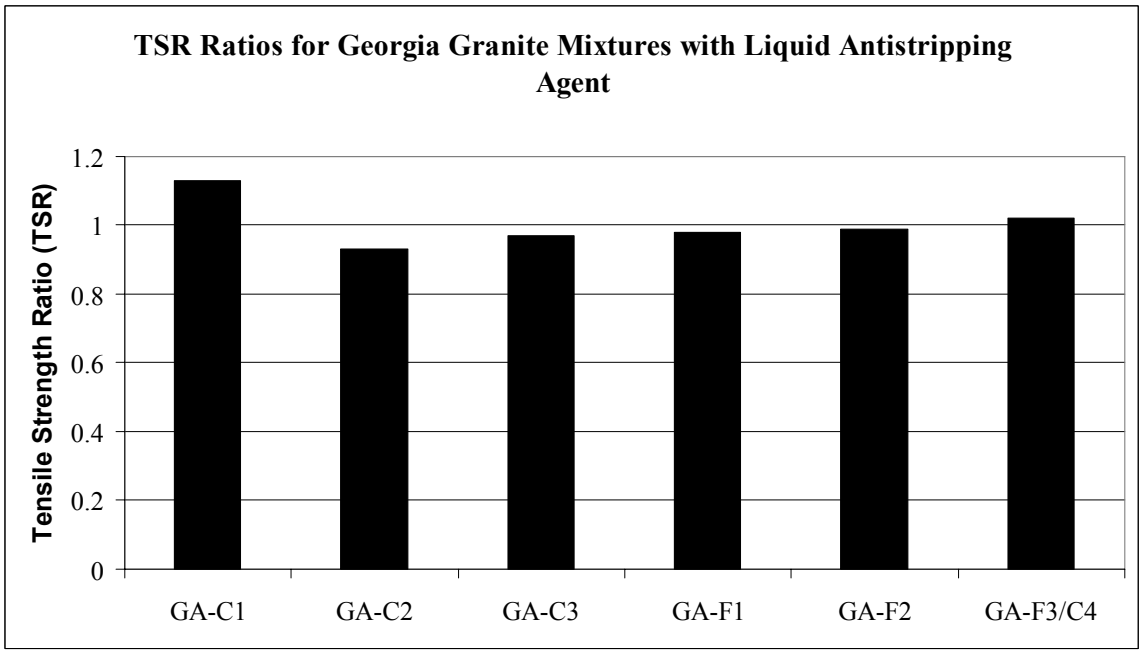

Figure 3-4. Tensile strength ratio and permeability for Georgia granite mixtures with antistripping agent.

As expected, all of the mixtures containing antistripping agents had TSR ratios greater than 0.8. All of the Georgia granite mixtures without liquid antistripping agent had TSR less than 0.8. These mixtures were designed to be volumetrically equivalent to the oolitic limestone mixtures. However, the coarse-graded granite mixtures had a higher TSR than the fine-graded granite mixtures. This is particularly noticeable for GA-C1, which had the highest TSR of the Georgia granite mixtures. These results are particularly interesting when compared to the volumetrically equivalent oolitic limestone results in Figure 3-1, where the coarse-graded limestone mixtures overall had lower TSR ratios than the fine-graded limestone mixtures. Each volumetrically equivalent granite mixture was expected to show lower TSR results than the comparable limestone mixture. For example, the WR-C1 mixture (TSR = 0.41) would have been expected to show higher TSR results than the equivalent GA-C1 mixture (TSR = 0.7). In summary, the granite SP-2 mixture had a TSR value above 0.8, the coarse-graded WR-C1 limestone mixture had low TSR values, and the coarse-graded Georgia granite GA-C1 mixture had a fairly high TSR value (0.7). These results were contradictory to FDOT experience with the aggregate types used. Oolitic limestone mixtures have a long history of excellent performance with respect to moisture resistance in the field, whereas the granite mixtures tested have consistently been shown to require antistripping agents to enhance the moisture resistance of these mixtures. This led to the conclusion that other effects were occurring that may not be captured by the tensile strength ratio.

Another interesting aspect of the AASHTO T-283 testing was the average saturation level for each mixture. Throughout the testing, a minimum saturation level of 55 percent was used. The goal was to place as much water into the specimen as AASHTO T-283 allowed. The saturation procedure called for a vacuum saturation for 15 minutes and then 15 minutes in a

water bath without vacuum. If the minimum saturation was not achieved, then another cycle was used until the minimum saturation was achieved. Table 3-3 gives the average saturation levels for the mixtures. There was a discrepancy between the conditioning for the fine- and coarse-graded mixtures. All the fine-graded mixtures achieved the minimum level with only one cycle of vacuum. However, the coarse-graded mixtures required at least two cycles, with some (WR-C2, SP-2, and NS-315) require as many as three cycles. The coarse-graded specimens were open enough to allow water to saturate the specimen, but the procedure for determining the saturation allowed water to drain from the specimen and thus causing the saturation levels to be below the minimum. The reason that more conditioning cycles increased the saturation likely has to do with the aggregate structure of the specimen. The voids between the coarse aggregates have a lower permeability than the entire specimen because of the effective asphalt content and the fine aggregates in the voids. Therefore, it would take more effort to saturate the specimen to a given saturation level.

After the indirect tensile strength was determined for each mixture, the specimen was split so that a visual observation could be performed. The first observation made on the limestone mixtures was that stripping of the binder from the aggregate was not present. However, as seen in Figure 3-5, the failure of the mixture is different between the conditioned and unconditioned specimens. As seen in the figure, the unconditioned specimen failed by breaking the aggregates in the center portion of the specimen. For the conditioned specimen, the failure plane was between the aggregates leading to the conclusion that the failure was caused by loss of cohesion in the mixture. This means that these mixtures may be susceptible to water damage due to pore pressures. The other limestone mixtures exhibited the same patterns. In contrast, all of the granite mixtures exhibited the classical stripping mechanism. As seen in

Unconditioned Conditioned

Figure 3-5. Unconditioned and conditioned limestone specimen (WR-C2).

Figure 3-6, the conditioned Nova Scotia granite specimen shows extreme stripping. Therefore, the loss of tensile strength can be attributed to the loss of aggregate-asphalt bond.

Unconditioned Conditioned

Figure 3-6. Unconditioned and conditioned granite specimen (NS315).

3.6 Evaluation of Potential Relationship between Mixture Permeability and Tensile Strength Ratio

One mixture parameter that could have an impact on the moisture sensitivity of a mixture is the permeability of the mixture. If a mixture is very permeable, the water penetrates the mixture very easily, thus presumably causing a greater risk of moisture damage. The permeability of the six limestone mixtures was known from previous work (Nukunya et al. 2001). Listed in Table 3-3 are the permeabilities of the mixtures tested. Figures 3-7, 3-8, and 3-9 show plots of TSR versus permeability for all mixtures tested. There appears to be no apparent relationship between permeability and TSR for the mixtures tested. Based on the previous discussion, it appears that the TSR may not always be a good indicator of mixture damage. In addition, it is also possible that permeability may not always directly reflect the moisture damage potential of mixtures. For example, some coarse-graded mixtures may tend to have larger and fewer interconnected voids that cause that mixture to have a higher permeability.

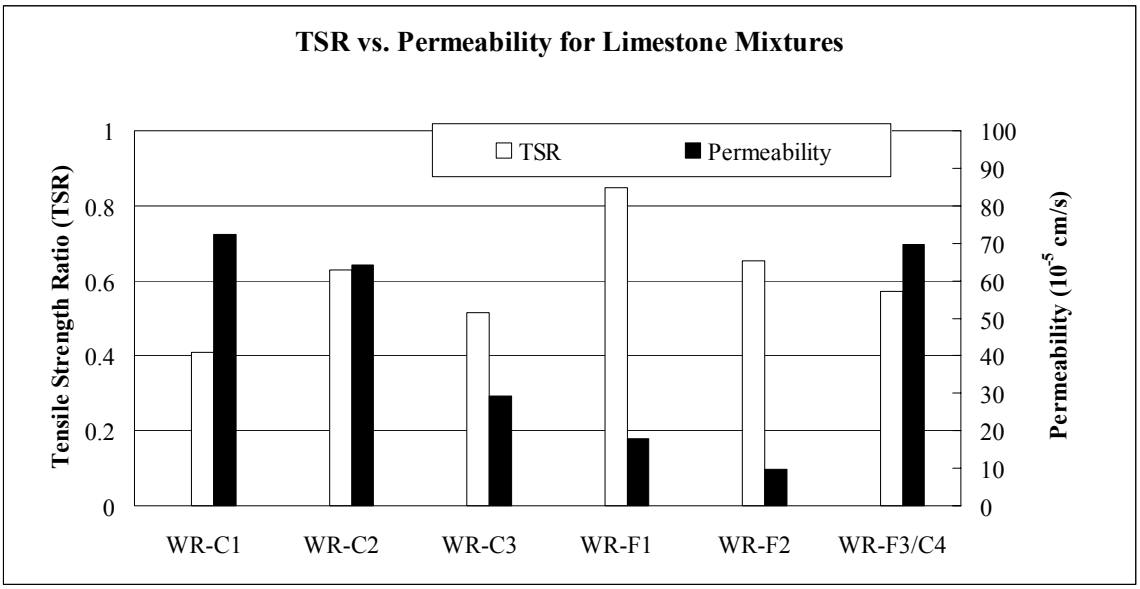

Figure 3-7. Tensile strength ratio and permeability (limestone mixtures).

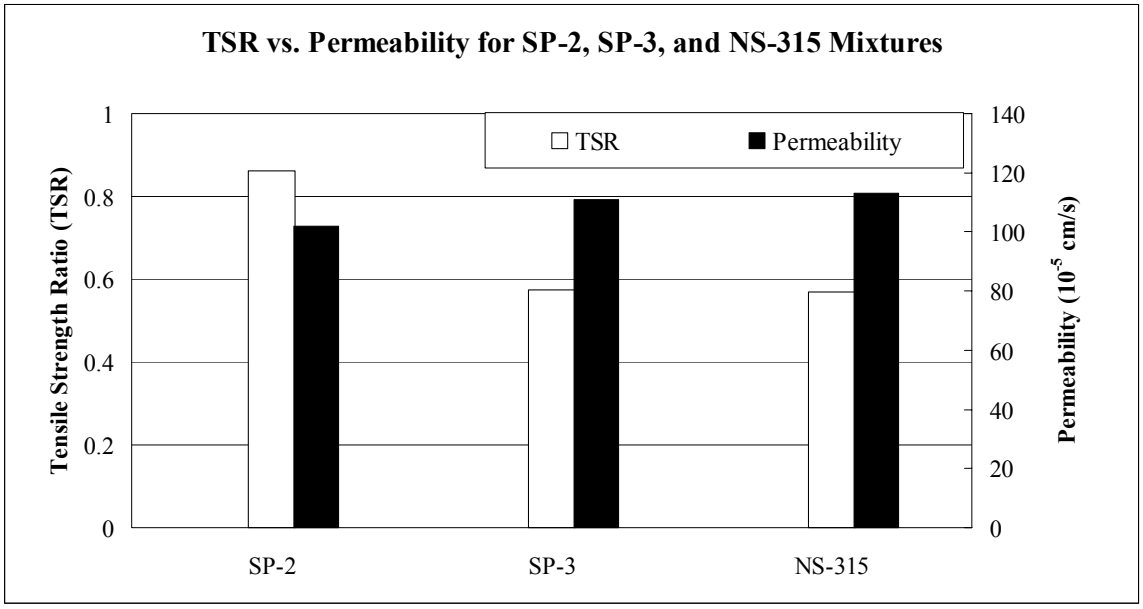

Figure 3-8. Tensile strength ratio and permeability (SP-2, SP-3, and NS-315 mixtures).

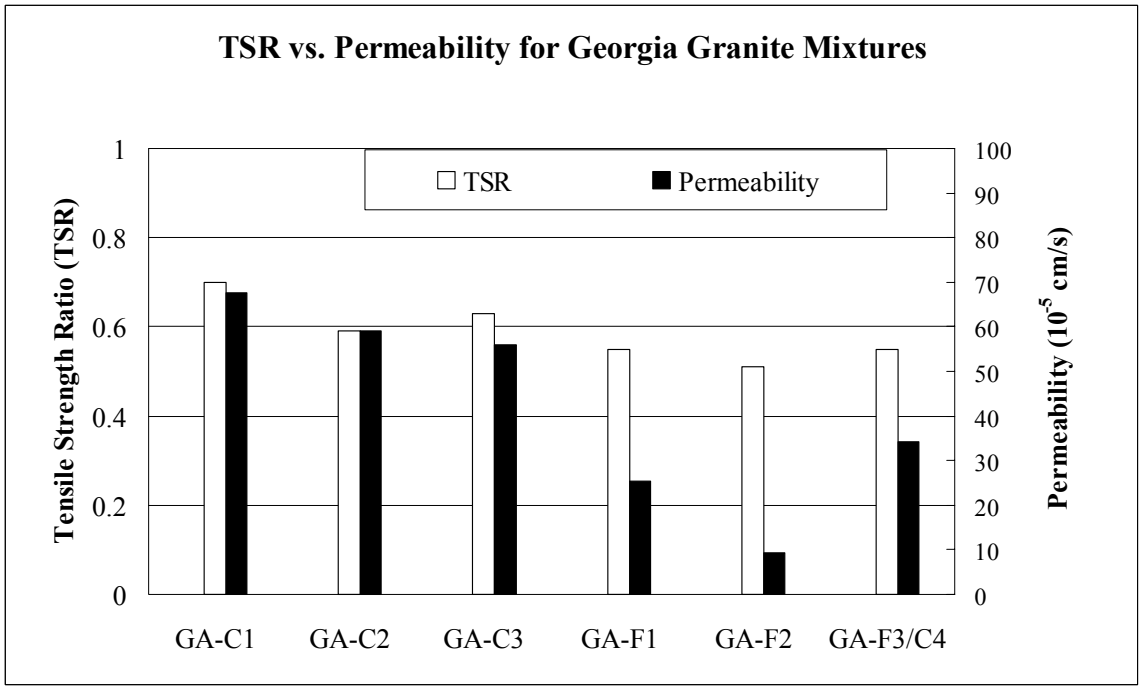

Figure 3-9. Tensile strength ratio and permeability for Georgia granite mixtures.

In the voids between the coarse aggregates in these mixtures, the mastic (asphalt, fine aggregates, and air voids) has a much lower permeability. To achieve a saturated state, and thus presumably maximum potential for moisture damage, the water must saturate the mastic. Highly permeable coarse-graded mixtures may tend to not hold on to water easily and thus not allowing the mastic to saturate. In comparison, lower permeability fine-graded mixtures may tend to have more numerous, but smaller air voids, thus exposing a greater volume of the mixture to moisture.

In summary, for the mixtures tested in this chapter, there does not appear to be a direct link between tensile strength ratio and permeability of mixtures. Therefore, in order to understand the cause and effect between moisture damage and mixture characteristics, it is necessary to explore the effects of mixture microstructure on moisture damage. Importantly, there also is a clear need to establish a fundamental mixture performance criterion for evaluating the moisture damage of mixtures, since current tensile strength ratio approaches do not seem to provide results that are consistent with field experience.

3.7 Summary and Conclusions

This chapter explored the use of the AASHTO T-283 mixture conditioning and testing approach to evaluate mixture potential for moisture damage. A total of 15 mixtures of varying aggregate types and gradations were tested. The failure mechanism associated with each conditioned mixture was studied, and a potential relationship between mixture permeability and tensile strength ratio was explored. The results showed a discrepancy between observed performance of oolitic limestone mixtures with a long history of excellent performance with respect to moisture resistance in the field, compared to the granite mixtures used, which have consistently been shown to require antistripping agents to enhance the moisture resistance of these mixtures. This led to the conclusion that other effects were occurring that may not be

captured by the tensile strength ratio. In addition, the results obtained indicate that the AASHTO T-283 requirement of a minimum saturation level for all mixtures may be questionable. High permeability coarse-graded mixtures had to be subjected to repeated rounds of saturation conditioning in order to meet the saturation requirements. This may have resulted in these coarse-graded mixtures having experienced further damage due to the saturation conditioning. It may be better and more reasonable to allow each mixture to find its own level of saturation after a single vacuum saturation cycle. This would more closely account for the natural resistance of mixtures in the field.

Finally, a possible relationship between tensile strength ratio and mixture permeability was explored. The findings indicated no apparent relationship between mixture permeability and tensile strength ratio, which may be due to both high variability in the TSR measurements and the effects of microstructure on the void continuity and void distribution of mixtures.

In summary, in order to understand the cause and effect between moisture damage and mixture characteristics, it is necessary to explore the effects of mixture microstructure on moisture damage. However, first there also is a clear need to establish a fundamental mixture performance criterion for evaluating the moisture damage of mixtures, since current tensile strength ratio approaches do not seem to provide results that are consistent with field experience.

3.8 References

Al-Swailmi, S., and Terrel, R.L., "Evaluation of Water Damage of Asphalt Concrete Mixtures Using the Environmental Conditioning System (ECS)," *Proceedings*, Association of Asphalt Paving Technologists (AAPT), Vol. 61, 1992.

Choubane, B., Page, G.C., and Musselman, J.A., "Investigation of Water Permeability of Coarse Graded Superpave Pavements," *Proceedings*, AAPT, Vol. 67, 1998.

Choubane, B., Page, G.C., and Musselman, J.A., "Effects of Different Water Saturation Levels on the Resistance of Compacted HMA Samples to Moisture Induced Damage," presented at the 80th Annual Transportation Research Board Meeting, Washington D.C., 2000.

Curtis, C.W., Stroup-Gardiner, M., Brannan, C.J., and Jones, D.R., "Adsorption of Asphalt on Aggregate to Evaluate Water Sensitivity," *Transportation Research Record #1362*, Transportation Research Board (TRB), National Research Council (NRC), Washington, D.C., 1992.

Lottman, R.P., "Laboratory Test Method for Predicting Moisture-Induced Damage to Asphalt Concrete," *Transportation Research Record #843*, TRB, NRC, Washington, D.C., 1982.

Nukunya, B., Roque, R., Tia, M., and Birgisson, B., "Evaluation of VMA and Other Volumetric Properties as Criteria for the Design and Acceptance of Superpave Mixtures," *Journal of the Association of Asphalt Paving Technologists*, Vol. 70, 2001.

Terrel, R.L., and Al-Swailmi, S., "Water Sensitivity of Asphalt Aggregate Mixes: Test Selection," *SHRP-A-403*, Strategic Highway Research Program (SHRP), NRC, Washington, DC, 1994.

Tunnicliff, D.G., and Root, R.E., "Use of Antistripping Additives in Asphaltic Concrete Mixtures," NCHRP Report 274, National Cooperative Highway Research Program (NCHRP), TRB, 1984.

CHAPTER 4
USE OF NONDESTRUCTIVE TESTING TECHNIQUES AS TOOLS FOR MONITORING CHANGES IN HMA MIXTURE INTEGRITY DUE TO EXPOSURE TO MOISTURE

4.1 Introduction

The problem of moisture damage in hot mix asphalt pavements occurs when water can infiltrate the pavement system and prematurely deteriorate the pavement. The presence of pore water in mixtures can cause premature failure of hot-mix asphalt pavements, primarily through loss of adhesion between the asphalt binder and the aggregates or the loss of cohesion in the asphalt binder (Parker and Gharaybeh 1987). Loss of adhesion can lead to stripping and raveling, and sometimes scouring in open graded mixtures. Loss of cohesion can lead to a weakened pavement that is susceptible to pore pressure damage and premature cracking (Kandal 1994; Kandhal and Rickards 2001). In a real pavement, the mechanisms causing pore pressure damage, cohesion damage, and adhesion damage are likely present and not easily separable. These same mechanisms are also active during laboratory conditioning, but not necessarily to the same degree as in the field. To understand how hot mix asphalt (HMA) mixtures react to different environmental conditions, the mixtures should be monitored throughout the laboratory conditioning process or the lifespan of the pavement in the field. At the present time, systems to monitor changes in mixture integrity have significant variability and are restricted to laboratory testing. Therefore, a new test and testing procedure that allows for the monitoring of laboratory-prepared and field cores with repeatable results should be developed so that the performance of the mixtures is better known.

The use of nondestructive testing techniques for the monitoring of moisture damage in mixtures has a lot of intuitive appeal. In addition to not requiring the destruction of the

specimens, these methods tend to be expedient in terms of the evaluation time, and therefore offer the promise of enhanced economic benefits in terms of savings of man-hours.

In this chapter, three distinct nondestructive approaches will be evaluated for use in the evaluation of moisture damage in mixtures. These testing methods are: 1) the ultrasonic pulse wave velocity test; 2) the resonant frequency test; and 3) the acoustic hammer test combined with higher order modal analysis.

Both the ultrasonic pulse wave velocity test and the resonant frequency test have been used successfully for other materials, such as plastics and Portland cement concrete (Davis et al. 1964), to detect flaws within the material or for monitoring changes within the material. Both tests have the ability to be quick and simple tests with the added bonus of being true non-destructive tests. After specimen setup, the testing time for the ultrasonic pulse wave velocity test is about 1 to 2 seconds, and of the order of 30-60 seconds, including analysis time, for the resonant frequency test and the acoustic hammer test. The tests require no on-specimen sensors.

In this paper, the ultrasonic pulse wave velocity test, the resonant frequency test, and the acoustic hammer test are evaluated as possible tools for monitoring changes in the integrity of mixtures due to moisture conditioning. The results presented show that the small strain modulus obtained with the ultrasonic pulse wave velocity test and the resonant frequency test appears to be sensitive to changes in mixture integrity due to moisture. However, the optimal use of these tests may be in the monitoring of changes in materials, rather than the establishment of definitive values that can be used in specifications. On the other hand, the acoustic hammer test with higher order modal analysis does seem to offer the promise to differentiate well between specimens that have been conditioned versus specimens that have not been moisture conditioned.

4.2 Objectives and Scope

The main objective with this study is to evaluate: 1) the ultrasonic pulse wave velocity test; 2) the resonant frequency test; and 3) the acoustic hammer test combined with higher order modal analysis for monitoring moisture and moisture damage effects in mixtures.

4.3 Materials and Methodology

4.3.1 Aggregate Solution

Two groups of aggregates were used. The first consisted of an oolitic limestone aggregate, and the second of crushed granite from Georgia and Nova Scotia. Both aggregate groups are used extensively in Florida and are considered to be excellent materials resulting in well-performing mixtures used by the Florida Department of Transportation.

4.3.2 Specimen Preparation

The oolitic limestone mix was made up of four components: coarse aggregate, fine aggregate, screenings, and mineral filler. They were blended together in different proportions to provide six HMA mixtures of coarse and fine gradations (Nukunya 2001; Nukunya et al. 2001). The first group of granite mixtures was made up of four components: coarse aggregate, fine aggregate, screenings, and mineral filler. They were blended together in different proportions to provide six 12.5-mm nominal maximum aggregate size mixtures of coarse and fine gradations. These mixtures are denoted as: GA-C1, GA-C2, GA-C3, GA-F1, GA-F2, and GA-F3, with the letters C and F denoting coarse-graded and fine-graded mixtures according to whether the gradation passes below or above the Superpave™ restricted zone. The limestone mixtures consisted of six previously designed limestone Superpave™ mixtures (WR-C1, WR-C2, WR-C3, WR-F1, WR-F2, and WR-F3). The rest of the granite mixtures consisted of three

mixtures commonly used by the FDOT. The first two mixtures consisted of Georgia granite, Florida limestone, and recycled asphalt pavement (RAP). One mixture was a coarse 12.5 mm nominal maximum aggregate size (entitled SP2) and the other was a coarse 19 mm nominal maximum aggregate size (entitled SP3). The third granite mixture, entitled NS315 is a coarse 19 mm nominal maximum aggregate size consisting of Nova Scotia granite. The purpose of selecting granite and limestone mixtures of varying gradation was to ensure that the mixtures tested were of different aggregate type, permeability, and other volumetric properties. The resulting gradations are shown in Table 4-1 (a) and (b). The mixtures ranged from what could be described as fine uniformly-graded and fine dense-graded to coarse uniformly-graded and coarse gap-graded.

All mixtures were designed according to the Superpave™ volumetric mix design method. The binder used for all limestone and granite mixtures was an AC-30 asphalt binder (corresponds to PG67-22 in Florida). The design asphalt contents for all the mixtures used in this study were determined such that each mixture had 4 percent air voids at N_{design} = 109 revolutions.

The following tests and analyses were performed:

- Mixtures were produced in the laboratory following the procedure outlined in AASHTO T-283. First, the aggregates and asphalt binder were heated to 150° C (300° F) for three hours prior to mixing. Once the mixing was completed, the mixture was allowed to cool to room temperature for two hours. After the cooling period, the loose mixture was long-term aged for 16 hours at 60° C (140° F). After the mixture was aged for 16 hours, it was reheated to 135° C (275° F) for two hours before compaction. The specimens were then compacted with a Superpave™ gyratory compactor to 7-8 percent air voids. A total of 18 samples of each mix were prepared.

Table 4-1. Gradations for Mixtures

(a) Percent Passing

Sieve Size	WR-C1	WR-C2	WR-C3	WR-F1	WR-F2	WR-C4/F3	SP-2	SP-3	NS315
25 (1)	100	100	100	100	100	100	100	100	100
19 (3/4)	100	100	100	100	100	100	98	100	97
12.5 (1/2)	97	91	98	96	91	95	89	98	83
9.5 (3/8)	90	74	89	85	78	85	84	89	66
4.75 (#4)	60	47	57	69	61	67	41	47	38
2.36 (#8)	33	30	36	53	44	37	31	25	23
1.18 (#16)	20	20	24	34	35	26	24	18	18
600 (#30)	15	14	18	23	24	20	17	15	14
300 (#50)	11	10	13	15	16	14	13	11	10
150 (#100)	7.6	6.7	9.2	9.6	9.1	8.6	9	7	6.5
75 (#200)	4.8	4.8	6.3	4.8	6.3	5.8	4	4	3.5

(b) Percent Material Passing Each Sieve Size

Sieve Size (mm)	GA-C1	GA-C2	GA-C3	GA-F1	GA-F2	GA-F3
19.0	100.0	100.0	100.0	100.0	100.0	100.0
12.5	97.4	90.9	97.3	94.7	90.5	94.6
9.5	89.0	72.9	89.5	84.0	77.4	85.1
4.75	55.5	45.9	55.4	66.4	60.3	65.1
2.36	29.6	28.1	33.9	49.2	43.2	34.8
1.18	19.2	18.9	23.0	32.7	34.0	26.0
0.60	13.3	13.2	16.0	21.0	23.0	18.1
0.30	9.3	9.2	11.2	12.9	15.3	12.5
0.15	5.4	5.6	6.8	5.9	8.7	7.7
0.075	3.5	3.9	4.7	3.3	5.4	5.8

- For each mixture, nine samples were then subjected to saturation according to the AASHTO T-283 procedure. Throughout the testing, a target saturation level of level of 65 to 80 percent was maintained. The saturation procedure called for a vacuum saturation for 15 minutes and then 15 minutes in a water bath without vacuum. If the minimum saturation was not achieved, then another cycle was used until the minimum saturation was achieved. The differences in saturation levels between the fine and coarse mixtures were noted.

- After the target saturation level was achieved, the specimens were placed in a 60° C (140° F) hot water bath for 24 hours. After the hot bath, the conditioned specimens were split up into groups of three. The first batch of conditioned mixtures was split to visually observe the effects of water conditioning on the mixes. The second batch was left to dry and cool down at room temperature. The effects of pore water and moisture damage with time were monitored with nondestructive pulse wave velocity and resonance frequency testing equipment over a period of 24 hours after conditioning.
- Before, the acoustic hammer testing, the mixtures were allowed to drain for 30 days, followed by 48 hours of conditioning in a constant humidity chamber. All mixtures were weighed before acoustic hammer testing to make sure that the mixtures did not contain excess moisture at time of testing.

Finally, three more samples for each mixture were prepared to conduct falling headwater permeability testing to evaluate the effects of void structure and access of water to the specimen. Test method and apparatus designation FM 5-565 was designed by FDOT (Choubane et al. 1998; Choubane et al. 2000). Table 4-2 lists the permeability for all mixtures tested.

Table 4-2. Mixture Permeability

Mixture	Permeability (10^{-5} cm/s)
WR-C1	72.4
WR-C2	64.2
WR-C3	29.4
WR-C4/F3	69.6
WR-F1	17.8
WR-F2	9.7
SP-2	102.0
SP-3	111.0
NS315	113.0
GA-C1	67.5
GA-C2	59.0
GA-C3	56.0
GA-F1	25.3
GA-F2	9.3
GA-F3	34.2

4.3.3 Mixture Volumetric Properties

Table 4-3 (a) and (b) summarizes the volumetric properties of the mixtures studied.

4.4 Part 1 – Ultrasonic Pulse Wave Velocity Test

Ultrasonic pulse waves are mechanical waves that move through material by displacing the particles of the material (Davis et al. 1964; Rojas et al. 1999) at a predominant frequency of 55 kHz. The ultrasonic wave is generated by piezoelectric crystals. These crystals typically consist of ceramics that expand rapidly when electric current is passed through the crystal. In order to produce the wave through the specimen, platens containing the crystals are placed firmly against the surface of the material. When the piezoelectric crystal expands, it pushes against the material producing a wave that moves through the material. In order to calculate the velocity of the wave, another crystal is attached to the specimen, usually on the opposite side, and when the waves strikes the receiving crystal, the crystal will act in reverse and produce an electric current. The electric signal is usually relayed to an oscilloscope, which will record the waveform.

Table 4-3. Mixture Properties

(a) Volumetric Properties of Granite and Limestone Mixtures

Properties	Mixture					
	GA-C1	GA-C2	GA-C3	GA-F1	GA-F2	GA-F3
Asphalt Content (%)	6.63	5.26	5.25	5.68	4.56	5.14
Specific Gravity of Asphalt	1.035	1.035	1.035	1.035	1.035	1.035
Bulk Specific Gravity	2.345	2.399	2.391	2.374	2.433	2.404
Theoretical Specific Gravity	2.442	2.500	2.492	2.473	2.532	2.505
Air Voids (%)	4.0	4.0	4.1	4.0	3.9	4.0
Voids in Mineral Aggregate (%)	18.5	15.4	15.7	16.6	13.6	15.1
Voids filled with Asphalt (%)	78.5	73.8	74.2	75.9	71.2	73.3
Effective Specific Gravity of Aggregate	2.710	2.719	2.709	2.706	2.725	2.720
Absorbed Asphalt (%)	0.3	0.4	0.3	0.3	0.5	0.5
Effective Asphalt (%)	6.3	4.9	5.0	5.4	4.1	4.7
Dust to Asphalt Ratio	0.6	0.8	0.9	0.6	1.2	1.2
Surface Area (m^2/kg)	3.3	3.5	4.2	4.1	5.3	4.9
Film Thickness theoretical, microns	19.9	14.3	12.1	13.4	7.7	9.9

Table 4-3. Mixture Properties–continued

(b) Other Properties

Specimen	Unit	WR-C1	WR-C2	WR-C3	WR-F1	WR-F2	WR-C4/F3	SP2	SP3	NS315
Maximum Specific Gravity	**Gmm**	2.3279	2.3466	2.3486	2.3378	2.3752	2.3466	2.470	2.496	2.455
Specific Gravity of Asphalt	**Gb**	1.035	1.035	1.035	1.035	1.035	1.035	1.035	1.035	1.035
Bulk Specific Gravity of Compacted Mix	**Gmb**	2.2349	2.2545	2.2535	2.2436	2.2814	2.2441	2.372	2.419	2.342
Asphalt Content	**Pb**	6.5	5.8	5.3	6.3	5.4	5.6	5.7	4.9	5.0
Bulk Specific Gravity of Aggregate	**Gsb**	2.469	2.465	2.474	2.488	2.489	2.469	2.606	2.692	2.608
Effective Specific Gravity of Aggregate	**Gse**	2.549	2.545	2.528	2.554	2.565	2.537	2.702	2.697	2.651
Asphalt Absorption	**Pba**	1.320	1.323	0.897	1.074	1.229	1.129	0.701	0.702	0.610
Effective Asphalt Content of Mixture	**Pbe**	5.266	4.554	4.451	5.293	4.238	5.534	5.03	4.18	4.420
Percent VMA in Compacted Mix	**VMA**	15.4	13.8	13.6	15.6	13.2	14.0	13.3	13.5	15.9
Percent Air Voids in Compacted Mix	**Va**	3.995	3.925	4.049	4.029	3.949	3.942	3.97	3.08	4.6
Percent VFA in Compacted Mix	**VFA**	74.058	71.559	70.226	74.170	70.082	71.884	70.3	77.2	71.1
Dust/Asphalt Ratio		0.74	0.83	1.18	0.761	1.16	1.04	0.614	0.816	0.7
Surface Area (m^2/kg)	**SA**	4.87	4.64	5.68	6.05	6.31	5.64	4.93	4.38	4.01
Theoretical Film Thickness (microns)	**FT**	11.2	10.1	8.0	9.0	6.9	8.1	9.1	10.0	9.1
Effective Film Thickness (microns)	**UFFT**	39.2	39.3	24.1	19.3	17.1	24.9	38.3	45.5	56.7

In order to determine the wave velocity, the total time that the wave travels from the transmitting crystal to the receiving crystal is determined from the waveform displayed on the oscilloscope.

Typically, two types of ultrasonic pulses are produced, namely compression (p-wave) and shear (s-wave) waves. In order to determine the elastic constants, the theory of elastodynamics is used. Even though asphalt concrete is a viscoelastic material, the theory of elasticity can be used since the displacements and corresponding strains are very small and the actual movements are very short in duration. For the sake of simplicity, the asphalt mixture can be assumed as a homogenous, isotropic solid. The resulting Young's and shear moduli are obtained from the wave velocities as follows:

$$E = \frac{\rho V_s^2 \left(3 V_p^2 - 4 V_s^2\right)}{V_p^2 - V_s^2} \tag{4.1}$$

$$G = \rho V_s^2 \tag{4.2}$$

where ρ = density, kg/m^3

V_p = compression wave velocity, m/s

V_s = shear wave velocity, m/s

E = modulus of elasticity, N/m^2 (Pa)

G = shear modulus, N/m^2 (Pa)

The test duration is very small. The ultrasonic pulse wave velocity instrumentation used in this study produces over 400 pulses per second. The resulting wave velocities are based on the average arrival times of these 400 pulses.

4.4.1 Relationship With Volumetrics and Density

Figure 4-1 (a) shows how the small strain Young's modulus changes with the density of the specimen. As expected, when the density increases, the small strain Young's modulus of

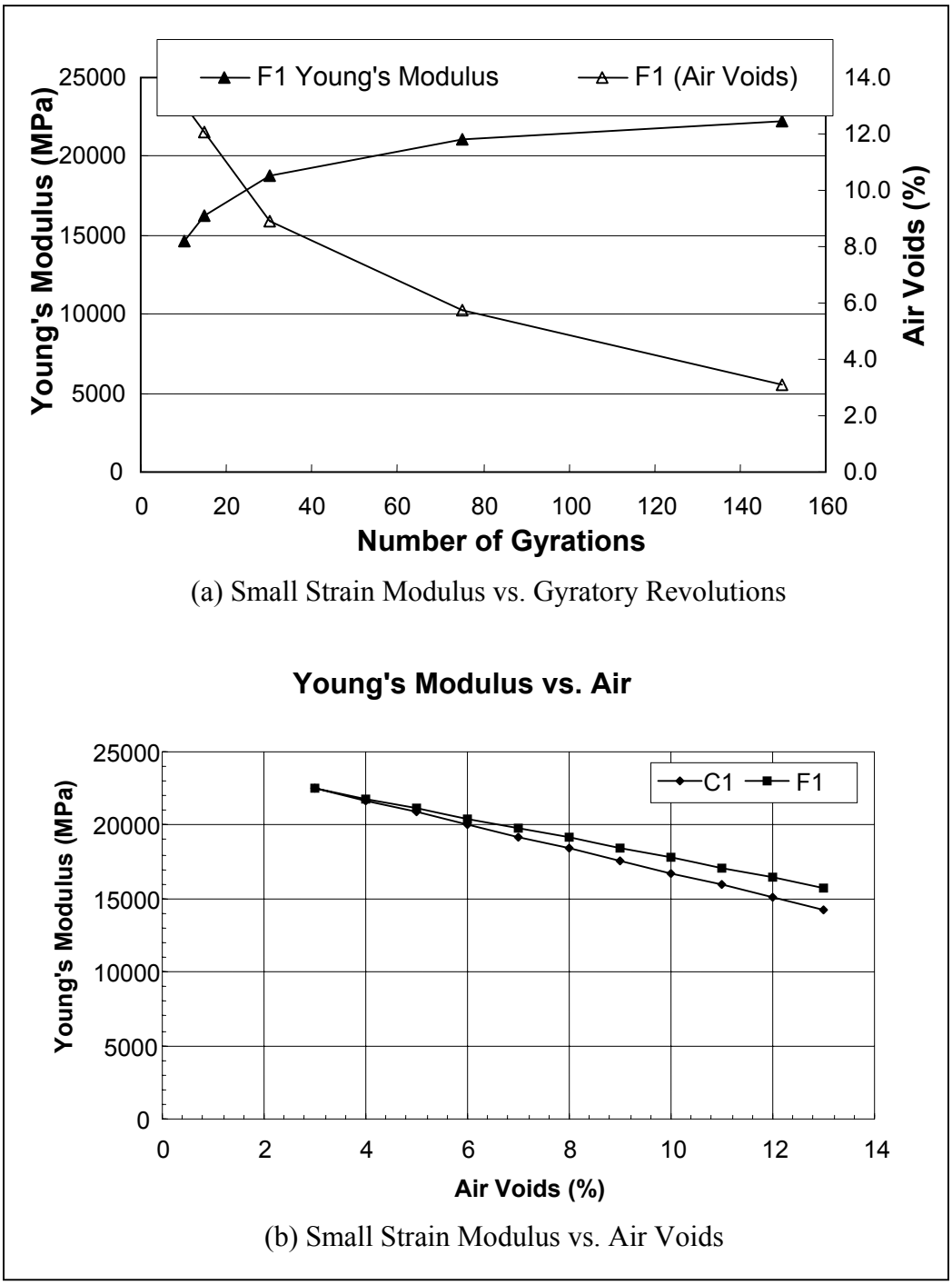

(a) Small Strain Modulus vs. Gyratory Revolutions

(b) Small Strain Modulus vs. Air Voids

Figure 4-1. Comparison of small strain modulus and air voids during gyratory compaction.

the specimen increases. Also the rate that the stiffness increases is similar to the compaction rate, with an initial rapid gain in stiffness, followed by a gradual reduction in the rate of stiffness

gain, as the specimen gets denser and the air voids decrease. Figure 4-1 (b) shows that the relationship between the air voids and the small strain Young's modulus is linear. In summary, the small strain modulus obtained with the pulse wave velocity equipment appears to follow expected trends in density and air voids.

4.4.2 Nondestructive Monitoring of Conditioning and Pore Water Effects in Mixtures

In this part of the paper, damage is induced in mixtures by moisture conditioning to evaluate:

1) the use of the ultrasonic pulse wave velocity test for monitoring changes in mixture integrity; and
2) the effects of conditioning and pore water effects on the aggregate structure.

First, the ultrasonic pulse wave velocity test was performed before conditioning, as well as periodically after conditioning to generate a time history of moisture effects in the mixtures. Second, the ultrasonic pulse wave velocity test was used to determine the influence of aggregate structure on pore water effects in mixtures. In particular, the length of time after conditioning that it takes the small strain modulus for a conditioned mixture to reach 95 percent of the value of the small strain Young's modulus before conditioning is shown to be affected by the fine sand size portion of the mixture. Finally, results are presented that show that the small strain modulus ratio of conditioned and unconditioned mixtures varies with the film thickness for the mixtures studied, implying the presence of damage due to conditioning.

4.4.3 Observed Failure Modes

In the following, the visual observations of the failure modes due to conditioning are observed for the limestone and granite mixtures. After conditioning, the conditioned and

unconditioned specimens were split so that a visual observation could be performed. The limestone and granite mixtures showed a significant difference in failure modes. Figure 4-2 (a) shows a comparison of the observed failure mechanisms between conditioned and unconditioned limestone specimens. The unconditioned limestone specimens failed by breaking the aggregates in the center portion of the specimen. However, a cohesive type of failure was observed for the

(a) Limestone Mixture C3

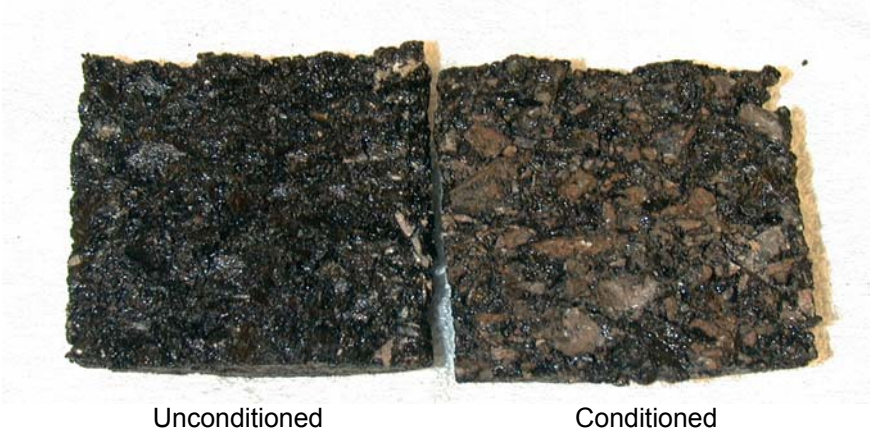

(b) Granite Mixture NS315

Figure 4-2. Comparison of unconditioned and conditioned specimens.

very dense-graded C3, the fine-graded F1 and F2 mixtures, and the gap-graded C4/F3 mixture, where the failure plane was between the aggregates, rather than through the aggregates. However, the coarse-graded C1 and C2 mixtures showed less evidence of changes in the cohesion of the mixtures.

In summary, the results for the limestone mixtures show that even though limestone mixtures may not show significant stripping, they may still be susceptible to water damage due to pore pressures and reduced cohesion. The results also imply that the aggregate structure may play a key role in the magnitude of changes in the cohesive properties of mixtures.

In contrast, based on visual observations, all the granite mixtures exhibited a classical adhesion failure mechanism, which resulted in stripping, as shown in Figure 4-2 (b). The 19.0-mm nominal aggregate size NS315 granite mixture showed the greatest amount of stripping, with the 12.5-mm SP2 mix showing the least amount of stripping.

4.4.4 Characterization of Pore Water Effects in Mixtures Using the Ultrasonic Pulse Wave Velocity Test

Figure 4-3 shows the time history of the normalized modulus over the first 24 hours after conditioning for the mixtures studied. For the limestone mixtures, the small strain modulus initially decreases between the one and two hour mark, until it reaches a low point at about 2 hours after conditioning and then starts to recover. The granite mixtures start recovering immediately after the water bath, with the lowest modulus ratio occurring at the first reading after the water bath (at 1 hour).

The difference in response between the high absorption limestone and less absorptive granite mixtures means that pore water effects are present and strongly influence the behavior of the mixtures immediately after the water bath. The decrease in small strain modulus ratio for the limestone mixtures immediately after the water bath, followed by recovery, implies the presence

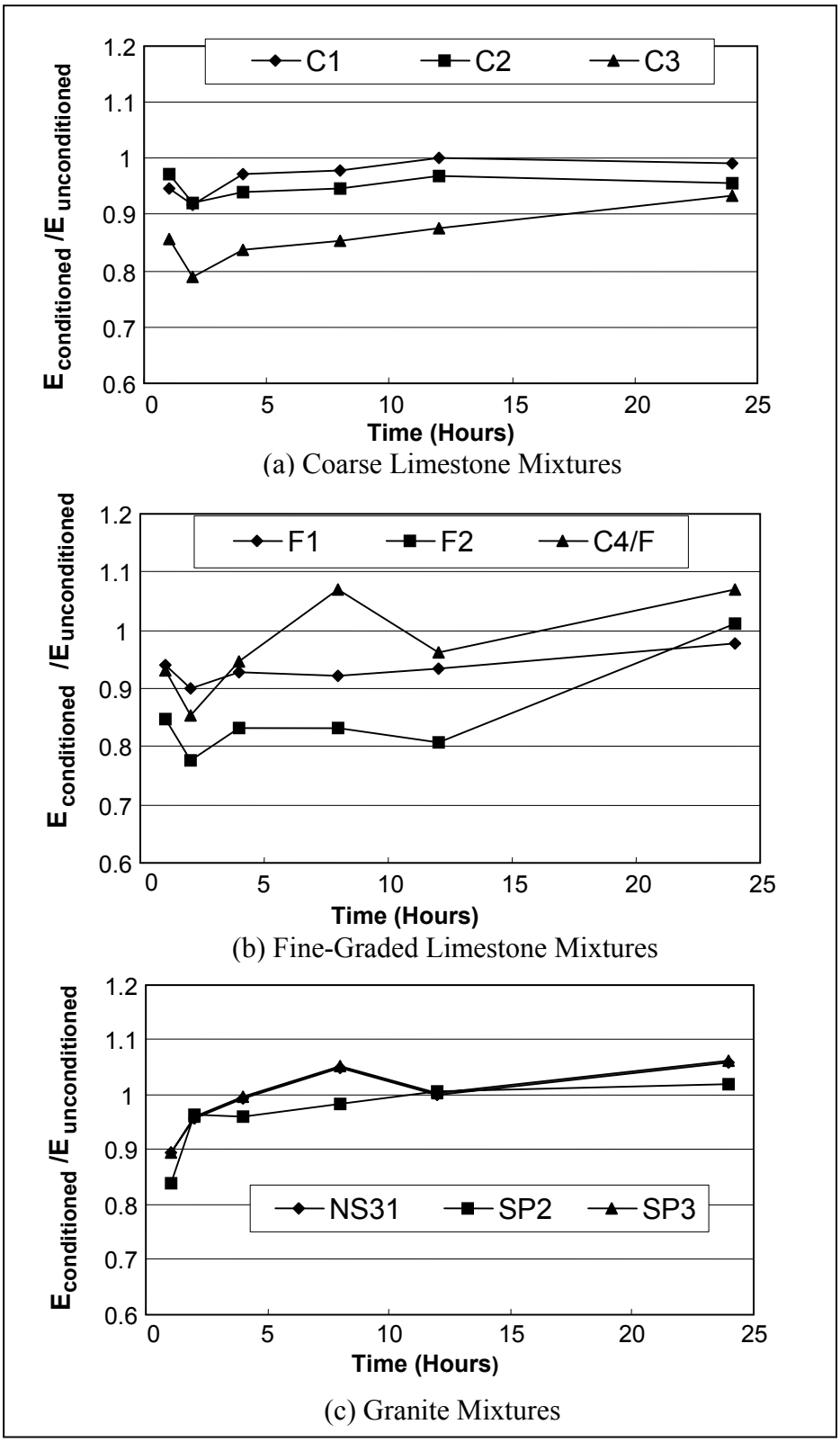

Figure 4-3. Plot of changes in small strain modulus ratio over 24 hours.

of pore water capillary effects that are counteracting the drainage of the mixtures. In contrast, the low absorption granite mixtures start the recovery immediately, implying that capillary effects may not be as significant.

The findings imply that both pore water effects and damage due to water may be present immediately after conditioning. Figure 4-4 shows a typical plot of how the small strain modulus changes with degree of saturation. The results clearly show that the time of testing after conditioning is very important for consistency of results.

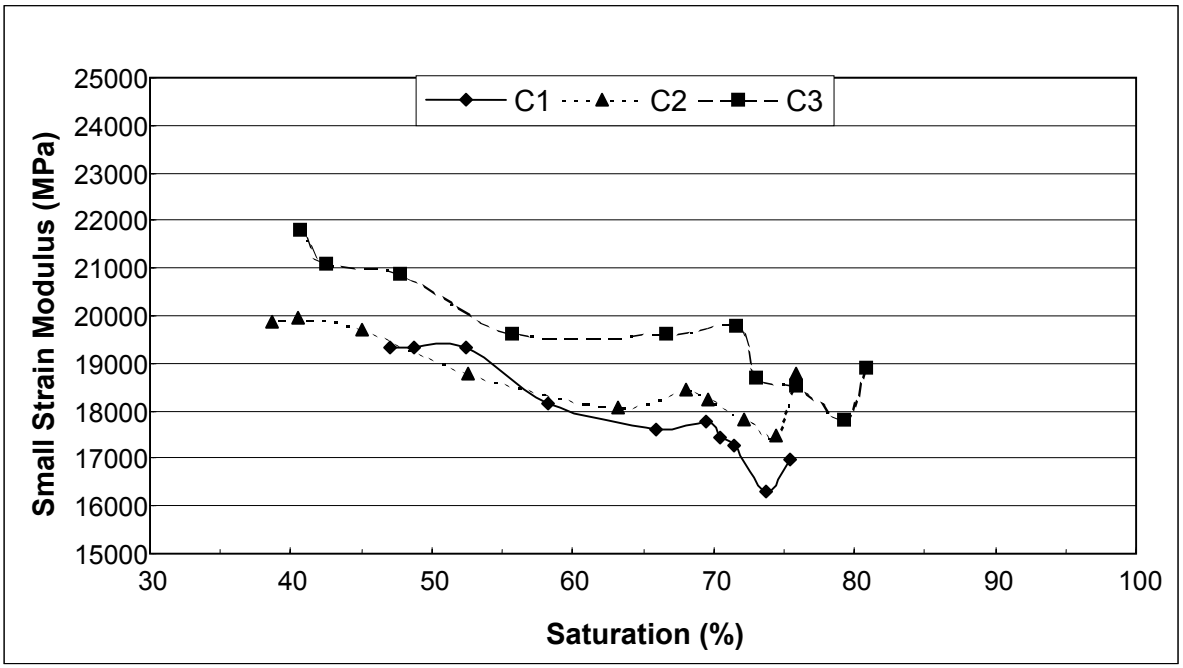

Figure 4-4. Variation in small strain modulus with degree of saturation for coarse-graded limestone mixtures.

4.4.5 Influence of Aggregate Structure on Pore Water Effects Using the Ultrasonic Pulse Wave Velocity Test

It is well known that the behavior of mixtures depends to a large extent on the presence of fines. Fine materials tend to attract and retain moisture far better than coarse materials due to their large surface area. Work by Nukunya et al. (2001) has shown that the aggregate structure of mixtures above and below the Superpave™ restricted zone is fundamentally different, as

shown in Figure 4-5. Mixtures above the restricted zone, which are commonly referred to as fine-graded mixtures, have more continuous grading such that the fine aggregates are an integral part of the stone matrix. Coarse mixtures (i.e., below the restricted zone), on the other hand, tend to have aggregate structures that are dominated by the coarse aggregate portion (i.e., stone-to-stone contact). Consequently, the coarse aggregate particles are coated by the mixture made up of asphalt and fine aggregates, and the fine aggregates within that matrix have access to all the asphalt within the mixture. The result is that despite a less permeable structure, water has better access to all the fine aggregates in fine-graded mixtures. In contrast, coarse-graded mixtures are effectively composed of two components: The first one is the interconnected coarse aggregate, which defines the overall permeability of the mixture. The second component is the low permeability fine mixture embedded in between the coarse aggregate particles. In the following the effects of aggregate structure will be evaluated on the conditioning and water damage of mixtures (see Table 4-2 for the permeability of the mixtures studied). As expected, the coarse-graded mixtures tend to have a higher permeability than the fine-graded mixtures.

Figure 4-5. Aggregate structure for coarse and fine mixtures (Nukunya et al. 2001).

Because of the differences in aggregate structure between fine- and coarse-graded mixtures, air voids in coarse-graded mixtures tend to be defined by the larger aggregate-to-aggregate contact structure in the mixture. Thus, a coarse-graded mixture is likely to have fewer and larger

air voids, whereas a fine-graded mixture with the same air void content tends to have more numerous, but smaller air voids that are distributed throughout the mastic. This means that the total surface area of the air voids in a coarse-graded mixture is generally lower than for a fine-graded mixture, resulting in less of the mastic being exposed to water.

A key aspect of the AASHTO T-283 conditioning protocol used, is the requirement for a minimum saturation level for the specimens. Throughout the testing, a minimum target saturation level of 70 percent was used (changes to AASHTO T-283 in 2003 require a saturation level of 70 to 80 percent). The saturation procedure called for a vacuum saturation for 15 minutes and then 15 minutes in a water bath without vacuum. If the minimum saturation was not achieved, then another cycle was used until the minimum saturation was achieved.

Due to the more continuous grading of the fine-graded mixtures, all of the fine mixtures achieved the minimum saturation level with only one cycle of vacuum. However, the higher permeability coarse-graded mixtures required at least two cycles, with some (C2, SP2, and NS315) requiring as many as three cycles, with the saturation level increasing with each cycle. The fine part embedded in between the coarse aggregate particles of these coarse-graded mixtures was not very accessible to moisture. Table 4-4 gives the final saturation levels for the mixtures. The

Table 4-4. Mixture Permeability, Saturation Levels, and Small Strain Modulus Recovery Time

Mixture	Permeability (10^{-5} cm/s)	Saturation (percent)	Time to Recover 95% of Unconditioned Small Strain Modulus (hours)
WR-C1	72.37	72.3	3.5
WR-C2	64.24	61.8	8
WR-C3	29.39	77.6	72
WR-C4/F3	69.63	75.8	4
WR-F1	17.81	84.2	16
WR-F2	9.68	80.1	21
SP-2	102	58.9	1.89
SP-3	111	74.2	1.88
NS315	113	60.9	1.84

three coarse-graded mixtures (C2, SP2, and NS315) that required three cycles of saturation never reached the target saturation level of 70 percent.

The results show that requiring a certain minimum level of saturation may potentially induce excessive damage on coarse-graded mixtures. In fact, the aggregate structure of coarse-graded mixtures may reduce the exposure to moisture by shielding the fine part of the mixture and maintaining high enough permeability for water to readily flow through the mixture. The influence of aggregate structure on pore water effects was evaluated by monitoring the time for the conditioned modulus to reach 95 percent of the unconditioned modulus. Table 4-4 shows the recovery times for the mixtures. The coarse-graded mixtures generally recovered to 95 percent of the original value in eight hours or less. Interestingly, the gap-graded mix C4/F3 recovered to the 95 percent benchmark in 4 hours, which is a relatively fast rate of recovery. In contrast, the fine-graded mixtures (F1 and F2) took between 16 and 21 hours to reach 95 percent recovery. The very dense-graded C3 mix showed a slow recovery, and did not recover to 95 percent of the initial value within the first 24 hours. The results imply that once moisture has entered the low permeability fine portion of such a very dense-graded mix, it may be as difficult to drain the mixture, as it was to saturate it in the first place. Finally, the low absorption granite mixes all recovered to the 95 percent benchmark before the two hour reading, meaning that pore water effects were not as significant for the low absorption granite mixtures as for the high absorption limestone mixtures.

From soil mechanics, it is known that the fine sand size portion of the gradation has a strong influence on the drainage of soils (Cedergren 1974). Hence, the portion of the gradations passing the no. 100 sieve was obtained, and a new parameter entitled the F/A ratio was defined. The F/A ratio consists of the portion of the gradation passing the no. 100 sieve divided by the asphalt content of the mixture. Figure 4-6 (a) shows how the recovery time increases as the F/A

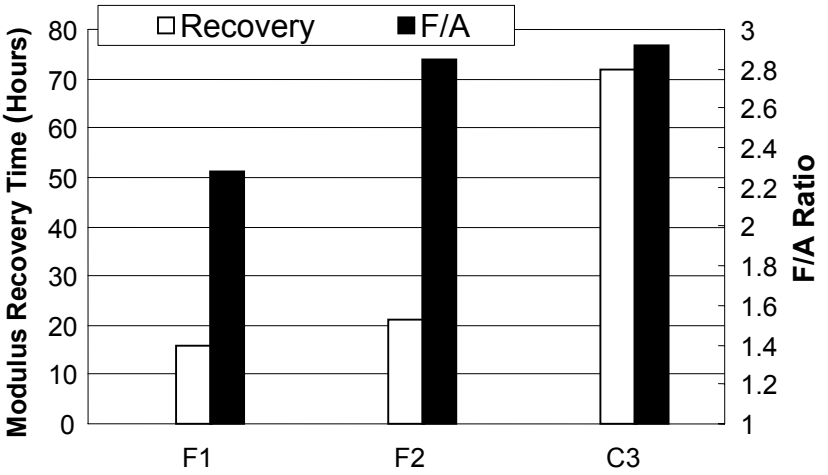

(a) Fine-Graded (F1 and F2) and Very Dense Graded (C3) Mixtures

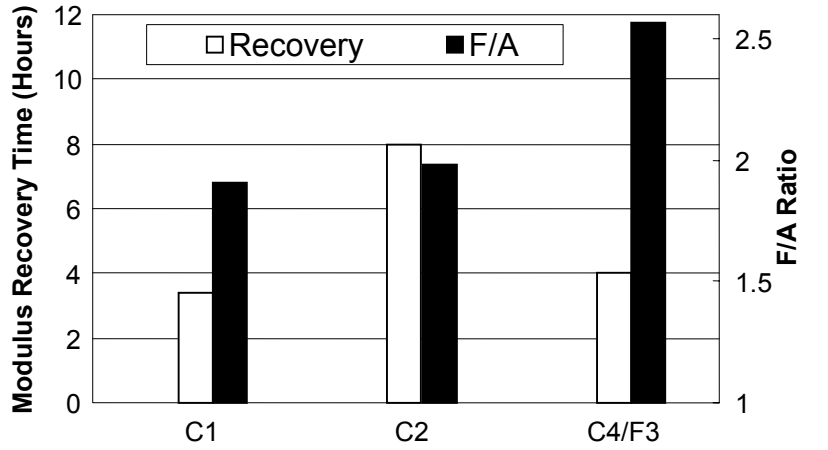

(b) Coarse-Graded (C1 and C2) and Gap-Graded (C4/F3) Mixtures

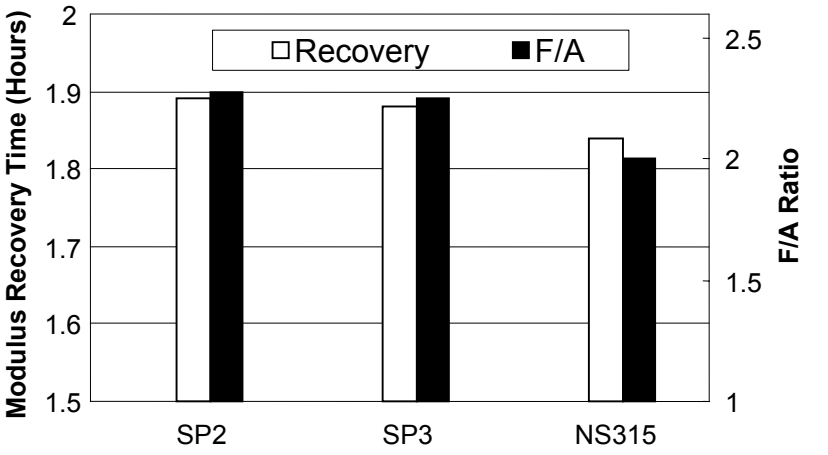

(c) Coarse-Graded Granite Mixtures

Figure 4-6. Plot of small strain modulus recovery time and F/A Ratio.

ratio increases for the fine-graded mixtures, as well as for the very dense-graded C3 mixture. Figure 4-6 (b) shows the recovery time versus F/A ratio for the coarse-graded mixtures, and the gap graded C4/F3 mixture. As the F/A ratio increases, the recovery time also increases, except for the gap-graded C4/F3 mix, where other gradation effects may have complicated the response. Figure 4-6 (c) shows the recovery time versus F/A ratio for the coarse-graded granite mixtures. All the granite mixtures recovered very quickly (< 2 hours). Again, the same trend holds – as the F/A ratio decreases, the recovery time also decreases.

Finally, it should be noted that somewhat similar trends as those shown in Figure 4-6 could be obtained from the dust/asphalt content ratio, but without the clear delineation between mixtures. Hence, not only the dust plays a role in water damage, but also a portion of the fine sand in the mix.

The results from this part of the study show that the absorption characteristics of the aggregates and the fine sand part (passing the no. 100 sieve) of the aggregate gradation control the length of time that moisture is present in mixtures. Hence, fine-graded mixtures and very dense coarse-graded mixtures may be more moisture susceptible than coarse-graded mixtures.

4.4.6 Effect of Film Thickness on the Small Strain Modulus Ratio

Since water conditioning of mixtures is a surface phenomenon, the binder is damaged from the surface inward. A mixture with a low film thickness is expected to damage more than a mixture with a thicker film, irrespective of surface area. The appropriate film thickness calculation is affected by the aggregate structure of the mix. As discussed previously, coarse-graded mixtures are effectively composed of two components: the first one is the interconnected coarse aggregate, and the second component is the fine mixture embedded in between the coarse

aggregate particles. The coarse aggregate particles are coated by the mixture made up of asphalt and fine aggregates, and the fine aggregates within that matrix have access to all the asphalt within the mixture. This results in film thicknesses that are much greater than those calculated using conventional calculation procedures that assume that the asphalt is uniformly distributed over all aggregate particles. To account for the different nature of the aggregate structure in coarse-graded mixtures, a modified film thickness calculation, entitled the "effective film thickness," was developed by Nukunya et al. (2001).

Figure 4-7 (a) and (b) show how the small strain modulus ratio due to conditioning varies with the film thickness for the limestone mixtures studied. For the purposes of consistency, the conditioned modulus ratio was taken at the low-points from Figure 4-3 (a), 4-3 (b), and 4-3 (c). For coarse-graded mixtures, the results (Figure 4-7 (a)) clearly show that as the effective film thickness decreases, the modulus ratio also decreases, indicating more damage in mixtures with lower film thicknesses. Similarly, Figure 4-7 (b) shows that for fine-graded mixtures, the theoretical film thickness has a strong influence on the amount of damage measured. The granite mixtures also show the same trend, as shown in Figure 4-7 (c), with the exception of the NS315 mixture, which may be due to other aggregate or mineral effects, since the aggregate used was of different origin than the SP2 and SP3 mixes.

The results from this part of the study show that the effects of aggregate structure on moisture damage need to be evaluated with the appropriate volumetric film thickness description. The effective film thickness calculation seemed to best reflect the changes in coarse-graded mixtures due to conditioning, whereas the theoretical film thickness appeared to work well for the fine-graded mixtures.

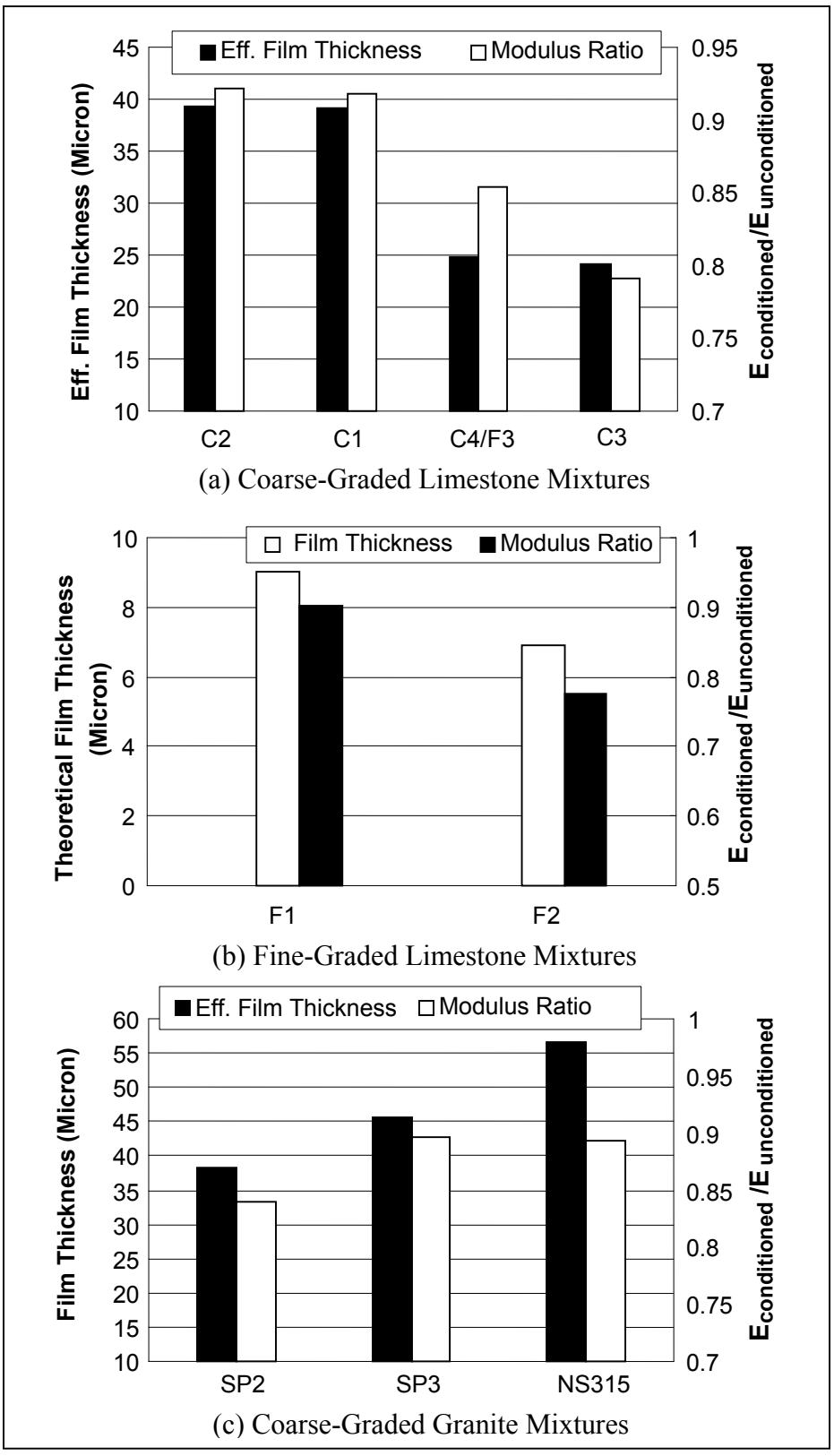

Figure 4-7. Plot of small strain modulus ratio versus effective film thickness.

4.5 Part 2 – Resonance Frequency Test

4.5.1 Background

The resonance frequency method was developed in the late 1930s, when it was discovered that the resonant frequency of a material can be matched with a harmonic tone produced by materials when tapped with a hammer (Malhorta and Carino 1991). Since then, the method has evolved and incorporated the use of electrical equipment for measurement.

An important property of any elastic material is its natural frequency of vibration. A material's natural frequency of vibration can be related to its density and dynamic modulus of elasticity. Durability studies of concrete and other materials have been performed indirectly using resonant frequency as an indicator of strength and static modulus of elasticity. These relationships for resonant frequency were originally derived for homogenous and elastic materials. However, the method also applies to concrete specimens if the specimens are large in relation to their constituent materials (Malhorta and Carino 1991).

The study of physics has determined resonant frequencies for many shapes, including slender rods, cylinders, cubes, prisms and various other regular three-dimensional objects. Young's dynamic modulus of elasticity of a specimen can be calculated from the fundamental frequency of vibration of a specimen according to Equation 4.3 (Malhorta and Carino 1991):

$$E = \frac{4\pi^2 L^4 N^2 d}{m^4 k^2} \tag{4.3}$$

where E = Young's dynamic modulus of elasticity

d = density of the material

L = length of the specimen

N = fundamental flexural frequency

k = the radius of gyration about the bending axis

m = a constant (4.73)

4.5.2 Testing Protocol

ASTM has created a standard test that covers measurement of the fundamental transverse, longitudinal and torsional resonant frequencies of concrete specimens for the purpose of calculating dynamic Young's modulus of elasticity (ASTM C-215-97 2001). This test method calculates the resonant frequencies using two types of procedures, the forced resonance method or the impact resonance method. The forced resonance method is more commonly used than the impact resonance method due to the ease of testing and interpretation of results. The forced vibration method uses a vibration generator to induce vibration in the test specimen while the vibration pickup transducer is coupled to the specimen. The driving frequency is varied until the pickup signal reaches a peak voltage. The specimen's maximum response to the induced vibration occurs at the resonant frequency. Figure 4-8 illustrates the typical setup of a resonant frequency device. The vibration generator is coupled to the right side of the specimen while the pickup is coupled to the left.

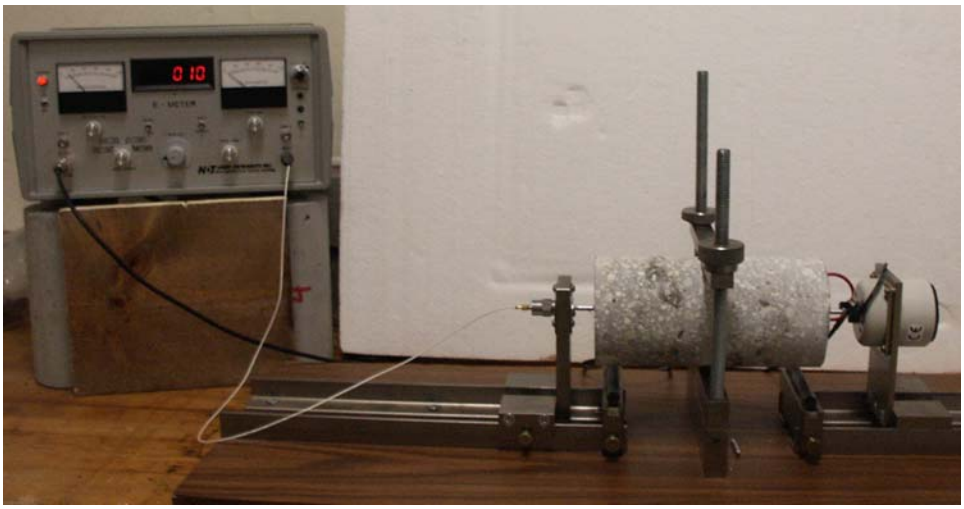

Figure 4-8. Typical forced resonant frequency setup.

The impact resonance method is similar to the impact-echo and impulse response methods. The impact resonance method employs a small impactor to induce a stress wave into the specimen. However, the forced resonant frequency method uses a lightweight accelerometer to measure the output signal. The signal is then processed to isolate the fundamental frequency of vibration.

The standard test method is limited to the testing of laboratory specimens (i.e., cylinders or prisms), and at present there is no standardized method applying the use of resonant frequency to larger specimens or to specimens of irregular shape.

4.5.3 Test Monitoring Results

Table 4-5 lists the small strain modulus and percent saturation versus days after end of conditioning for the six granite mixtures tested (i.e., GA-C1, GA-C2, GA-C3, GA-F1, GA-F2, GA-F3). Figures 4-9 through 4-14 show plots of changes in percent saturation and small strain modulus from resonant frequency for six days after conditioning. The saturation and modulus values at time zero denote the unconditioned modulus in dry state and the initial saturation level obtained through the vacuum saturation procedure before the 24-hr hot water bath conditioning.

Table 4-5. Small Strain Modulus Versus Percent Saturation from Resonant Frequency Test Over 6 Days

Days after Conditioning	Mixture											
	GA-C1		GA-C2		GA-C3		GA-F1		GA-F2		GA-F3	
	Ed (MPa)	Saturation (%)	Ed (MPa)	Saturation (%)	Ed (MPa)	Saturation (%)	Ed (MPa)	Saturation (%)	Ed (MPa)	Saturation (%)	Ed (MPa)	Saturation (%)
0 (Uncond.)	**456**	**63.6**	**421**	**61.9**	**433**	**61.2**	**376**	**72.9**	**467**	**66.6**	**444**	**67.7**
1	316	57.2	**345**	38.2	**441**	46.3	**287**	52.1	**375**	53.2	**392**	48.6
2	226	49.9	**238**	33.0	**327**	40.2	**168**	46.7	**297**	47.0	**346**	43.5
3	234	47.2	**362**	29.4	**235**	35.7	**252**	42.5	**369**	32.2	**299**	40.7
4	388	43.0	**358**	26.5	**435**	31.8	**351**	39.2	**429**	29.3	**422**	26.6
5	384	40.2	**347**	24.1	**398**	28.6	**357**	37.3	**321**	28.1	**354**	24.9
6	375	36.6	**340**	22.7	**378**	25.3	**362**	34.9	**284**	24.8	**298**	23.0

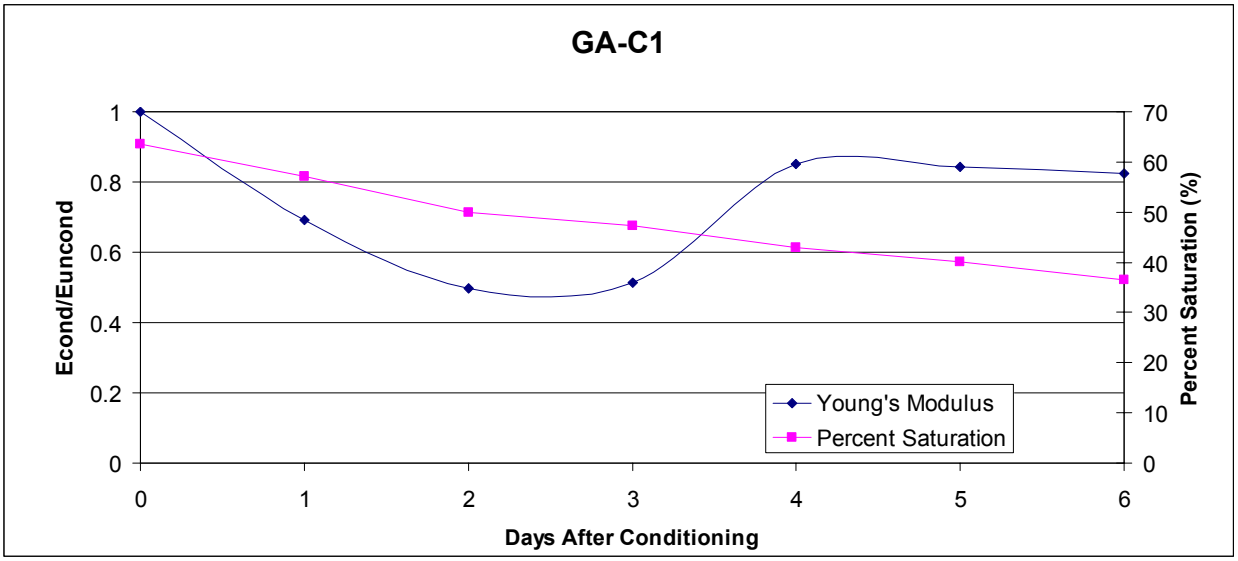

Figure 4-9. Plot of changes in small strain modulus versus percent saturation from resonant frequency test over 6 days for Mixture GA-C1.

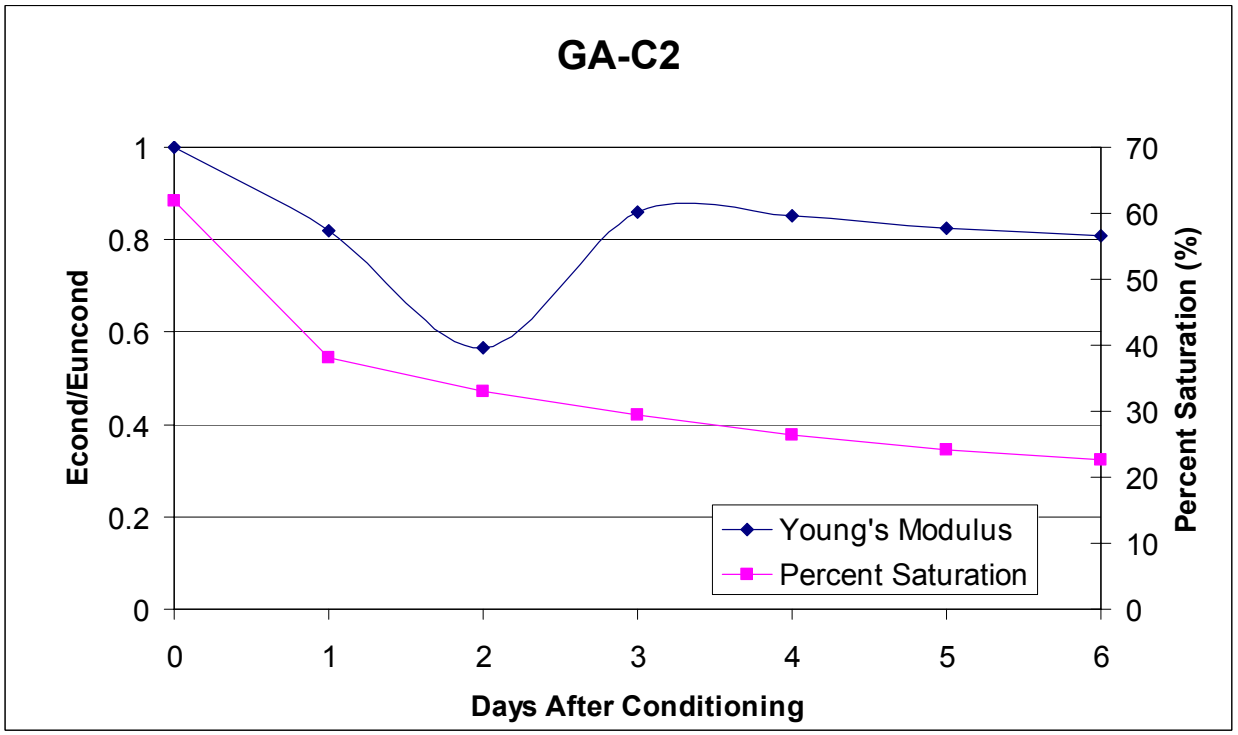

Figure 4-10. Plot of changes in small strain modulus versus percent saturation from resonant frequency test over 6 days for Mixture GA-C2.

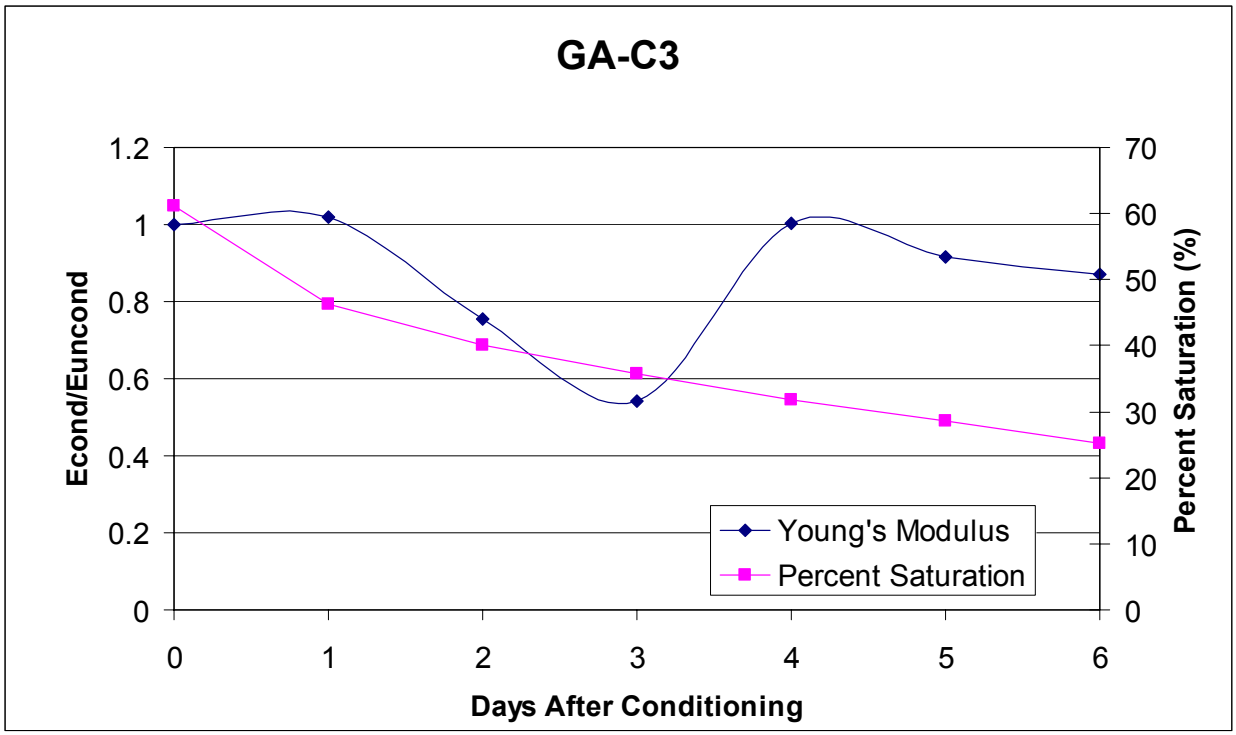

Figure 4-11. Plot of changes in small strain modulus versus percent saturation from resonant frequency test over 6 days for Mixture GA-C3.

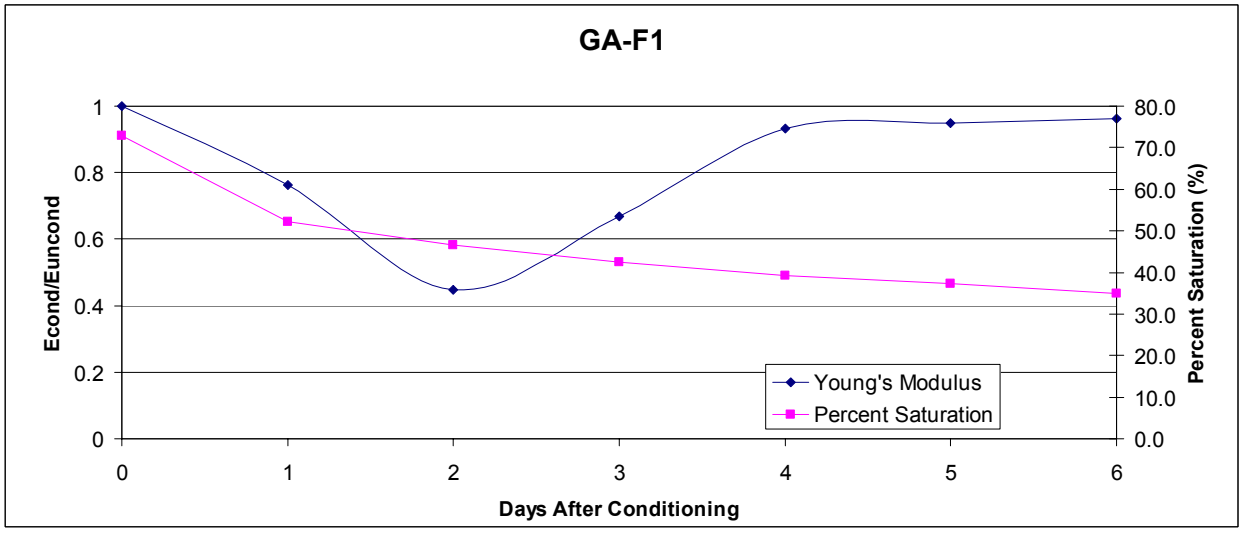

Figure 4-12. Plot of changes in small strain modulus versus percent saturation from resonant frequency test over 6 days for Mixture GA-F1.

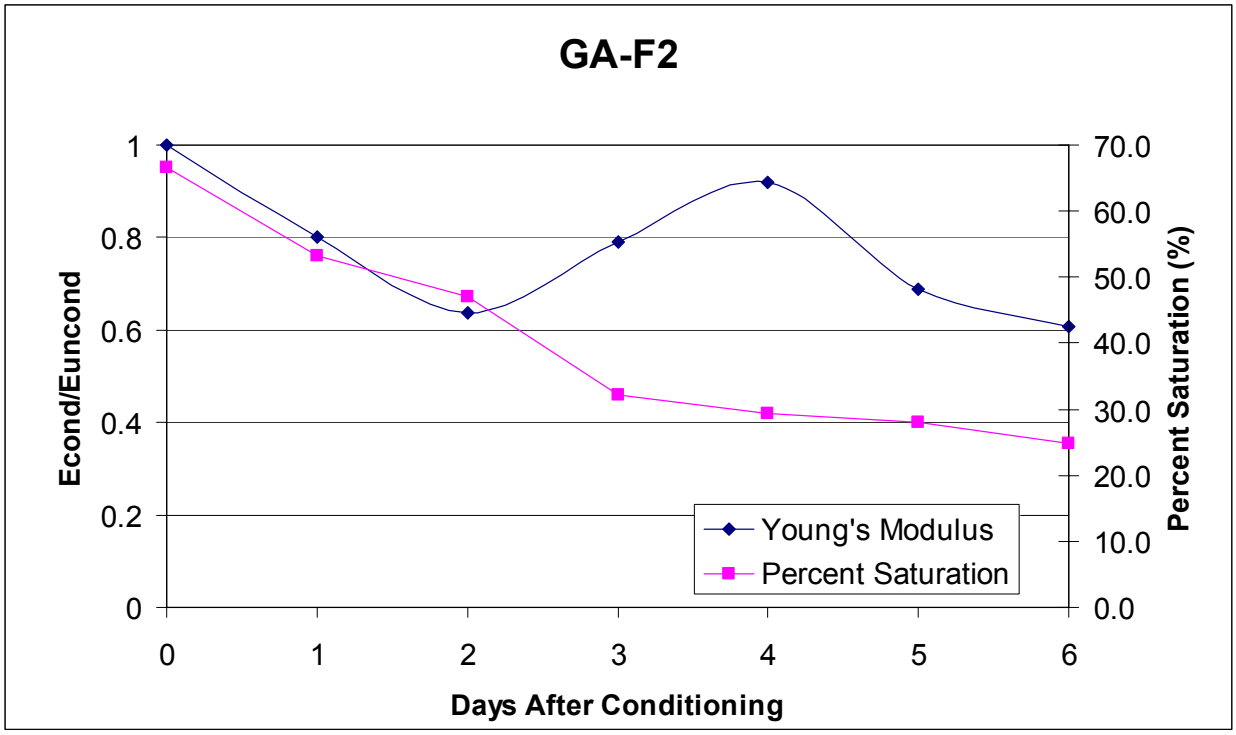

Figure 4-13. Plot of changes in small strain modulus versus percent saturation from resonant frequency test over 6 days for Mixture GA-F2.

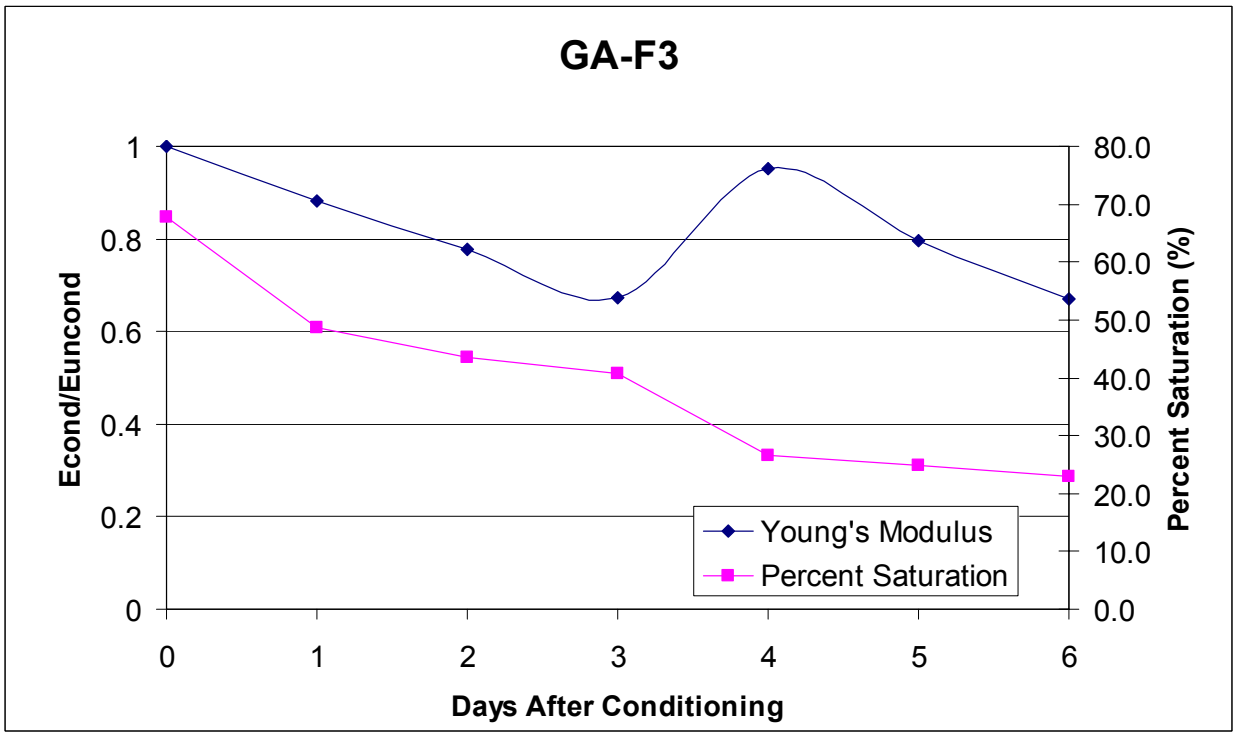

Figure 4-14. Plot of changes in small strain modulus versus percent saturation from resonant frequency test over 6 days for Mixture GA-F3.

The results for all of the mixtures follow a similar pattern: Immediately after conditioning, the small strain modulus decreases followed by an increase in modulus between days 3 and 4, which again is followed by either the stabilization of the modulus or a subsequent further decrease in the modulus. Interestingly, at day six, the mixture still contained significant volume of water. The saturation levels for the mixtures at day 6 ranged from a low of 22.7 percent for the GA-C2 mixture to a high of 36.6 percent for the GA-C1 mixture. Similarly, at day six the ratio of the conditioned to unconditioned modulus for the mixtures ranged from a high of 0.96 for mixture GA-F1 to a low of 0.61 for GA-F2. Unfortunately, these results follow a similar pattern to the ultrasonic pulse wave velocity test results presented previously, in that they indicate that the resonant frequency test may be better suitable for monitoring changes in mixtures over time, in lieu of attempting to use these methods for establishing absolute values of modulus or even modulus ratios that can be used for specifications. For example, the GA-F1 mixture was visually observed to have stripping that was similar in magnitude to those of GA-F2 and GA-F3, but yet after 6 days of draining the small strain modulus had only decreased by 4 percent for GA-F1.

4.6 Part 3 – Acoustic Hammer Test with Modal Analysis

4.6.1 Background

This part of the study seeks to improve upon the current method of determining moisture damage by investigating a more reliable, non-destructive means of damage. There is a clear need for a test which can be consistently accurate at detection and measurement of damage within an HMA sample regardless of the the strength of the material after conditioning. After damage is induced using vacuum saturation and a 24-hour hot water bath a modal hammer test is performed. Tests are performed on several damaged and undamaged samples (pills). The test accounts for changes in strength and ductility of the mixture as reflected in the damping and

stiffness of the system. These characteristics of the system affect the frequencies and mode shapes measured. Any changes in a system in the form of cracks, or loosening of the binder will affect the physical properties of the system and result in some change in the measured modal properties (Farrar and Doebling 1997). The test depends on the measured properties of undamaged samples as a baseline for indication of damage. The objective of this part of the research is to evaluate the use of the new test for detecting the effects of moisture damage on the transfer function of mixtures.

4.7 Methodology

4.7.1 Aggregate Selection and Conditioning

The mixture chosen for this experiment was GA-F1, which is a fine-grained granite mixture, with a known history of exhibiting stripping from exposure to moisture. Fifteen specimens of the GA-F1 mixture were prepared according to the AASHTO T-283 procedure, discussed previously. The percent air voids for these specimens is shown in Table 4-6. Eight samples were left undamaged and were not moisture conditioned after compaction to serve as a base line for comparison while four samples were vacuum saturated and conditioned in a hot water bath for 24 hours and the last three samples were conditioned in a hot water bath for 24 hours without vacuum saturation.

Table 4-6. Percent Voids Within Prepared Samples, Measured Before Further Conditioning

Undamaged Sample Identification	% Air voids	Damaged Sample Identification	% Air voids
GAF1-1	7.96	GAF1-9	7.79
GAF1-2	7.73	GAF1-10	7.63
GAF1-3	7.38	GAF1-11	7.58
GAF1-4	7.6	GAF1-12	7.60
GAF1-5	7.6	GAF1-13	7.8
GAF1-6	7.5	GAF1-14	7.4
GAF1-7	7.79	GAF1-15	7.7
GAF1-8	7.63		

4.7.2 Testing and Data Acquisition

As shown in Figure 4-15, the modal hammer test was performed on a suspended sample to isolate the material from its environment thus allowing free vibration during testing. The samples are suspended from two end plates of 1/16 in. thick aluminum sheet metal. An aluminum end plate (thickness = 1/16 in.) is attached to the test pill (length = 6 in.) with epoxy. The plate is the same diameter as the pill (3.875 in.) and allows for a more even distribution of the applied force. The sample is suspended from a rigid support using fishing line. In the center of one end plate is a piezoelectric accelerometer (PCB Piezotronics Model #353B15), which will detect vibrations within the sample. The modal hammer (PCB Model #086C03) with a brass tip is used to apply an impulse force in the center of the opposite end plate. The sensor signals are conditioned using a PCB signal conditioner (PCB Model #482A16) and are measured using a Siglab spectrum analyzer (Siglab Model #50-21). Siglab software is then used to convert the sensor's voltage input into frequency and time response data. The frequency response function measurements are averaged five times to reduce error. Within the experiment the coherence

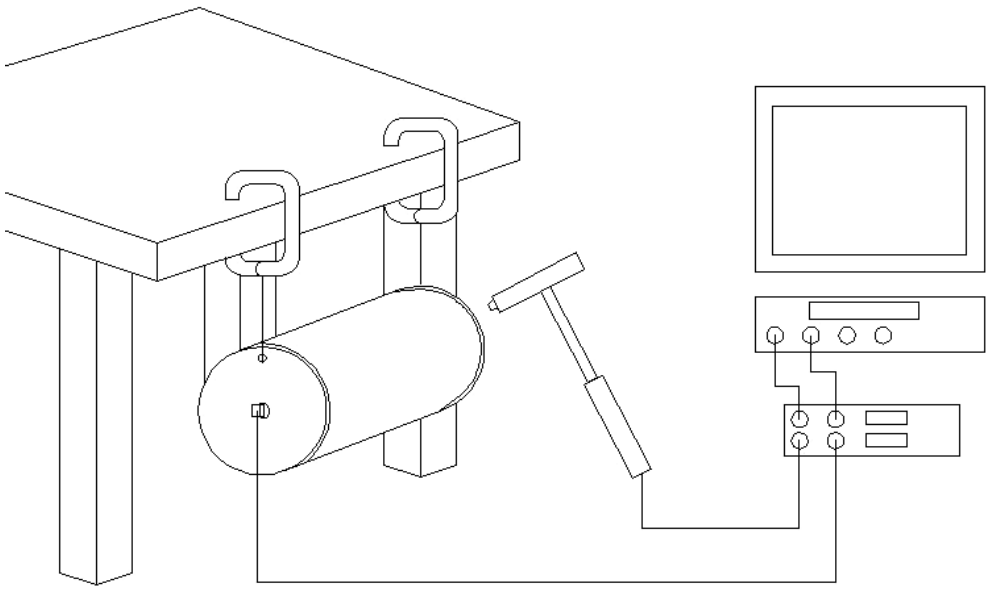

Figure 4-15. Schematic of experiment setup.

between the force input and the accelerometer measurement was performed. All samples, damaged and undamaged, are so tested and results are compared graphically.

4.8 Results

4.8.1 Vacuum Saturated Conditioning

The results of the vacuum saturated data set show the damaged samples have on average an increased peak magnitude from those of the undamaged samples as well as a frequency shift to the left in both magnitude and phase. For all the measurements made, the coherence remained above 0.98 up until 12,393 Hz, except at three frequencies (5,530, 9,234, and 11,136 Hz). For these three frequencies the amplitude of the autospectrum of the force input was reduced and caused a drop in the coherence to a value of 0.94. Figures 4-16 and 4-17 show the averaged frequency response functions for the four vacuum saturated samples as compared to the average

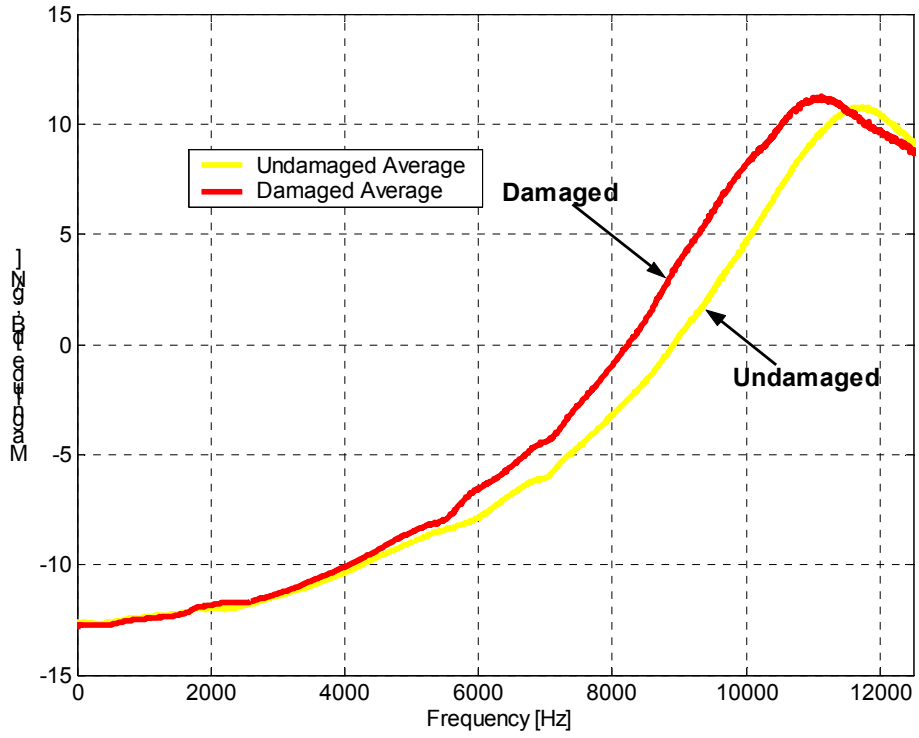

Figure 4-16. Magnitude of acceleration with respect to force comparison of averaged results for the four vacuum saturated samples and eight undamaged samples.

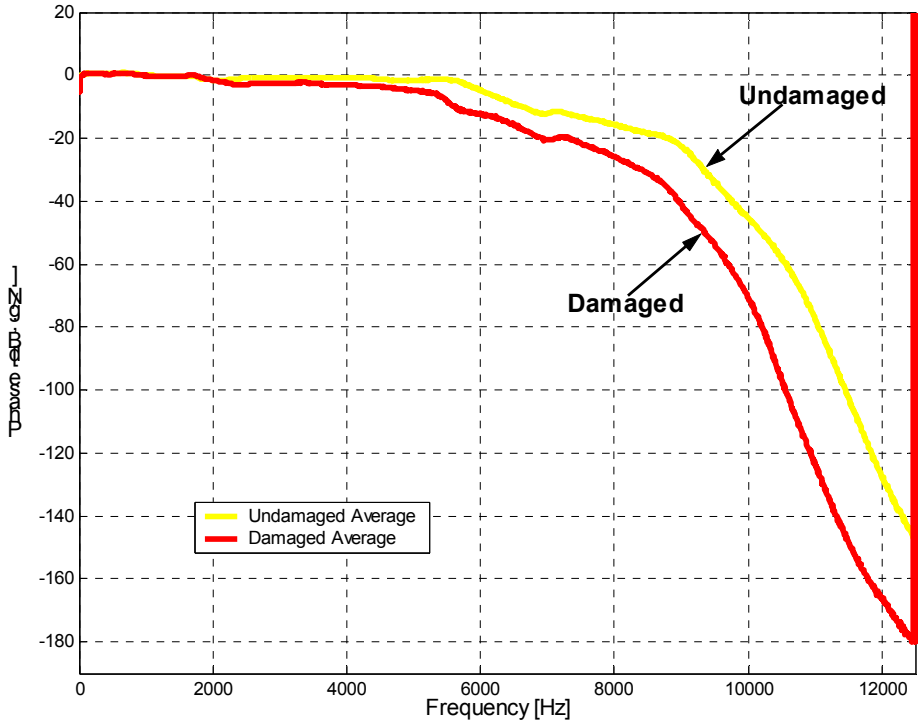

Figure 4-17. Phase of acceleration with respect to force comparison of averaged results for the four vacuum saturated samples and eight undamaged samples.

of the eight undamaged pills. The increase in peak magnitude is not consistent for all damaged samples as can be seen by comparison of each pill in Figure 4-18. This same figure does however illustrate that the frequency shift seen in the averaged result occurs in each individual test case. The average peak magnitude frequency shift is 554 Hz.

The averaged resulting phase of acceleration with respect to force for the vacuum saturated data set is displayed in Figure 4-17 for comparison. Once again, a frequency shift occurs between undamaged and damaged response for all pills tested. There is a range of resulting responses within the undamaged samples, as seen in the individual results in Figure 4-18. This may be due to varying percent voids or slight variations in granite used. However, the phase transition of conditioned pills consistently occur at a lower frequency. The average

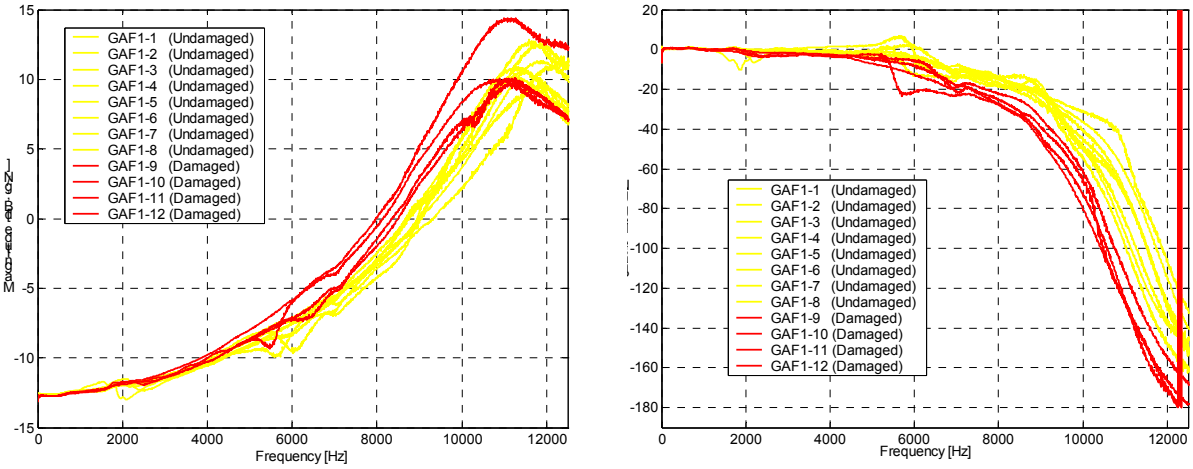

Figure 4-18. Magnitude and phase of acceleration with respect to force of the damaged pills conditioned with vacuum saturation, GAF1-9 through 12, as compared to the undamaged pills.

frequency shift between damaged and undamaged results measured at –90° phase angle is 875 Hz, a larger margin than that of the peak magnitudes.

4.8.2 Non-saturated Conditioning

The non-vacuum saturated samples have less water reaching the core of the sample and therefore less severe stripping should occur. However, the results of the non-vacuum saturated data set are similar or more pronounced than those of the vacuum saturated group. Figure 4-19 shows a graph of the magnitude of the acceleration with respect to force. The results show that the damaged samples have on average an increased peak magnitude with a frequency shift of 844 Hz from the undamaged average (290 Hz greater margin than the vacuum saturated set). Once again, the increase in peak magnitude is not as consistent as frequency shift for all damaged cases as can be seen by comparison of each test sample in Figure 4-20.

The averaged resulting phase of acceleration with respect to force for the non-vacuum saturated data set is displayed in Figure 4-21. The frequency shift that occurs between undamaged and damaged response is on average 1,076 Hz when measured at –90° phase angle

(201 Hz greater margin than the vacuum saturated phase). The phase of acceleration again has a greater margin between damaged and undamaged than that of the peak magnitude within this test group.

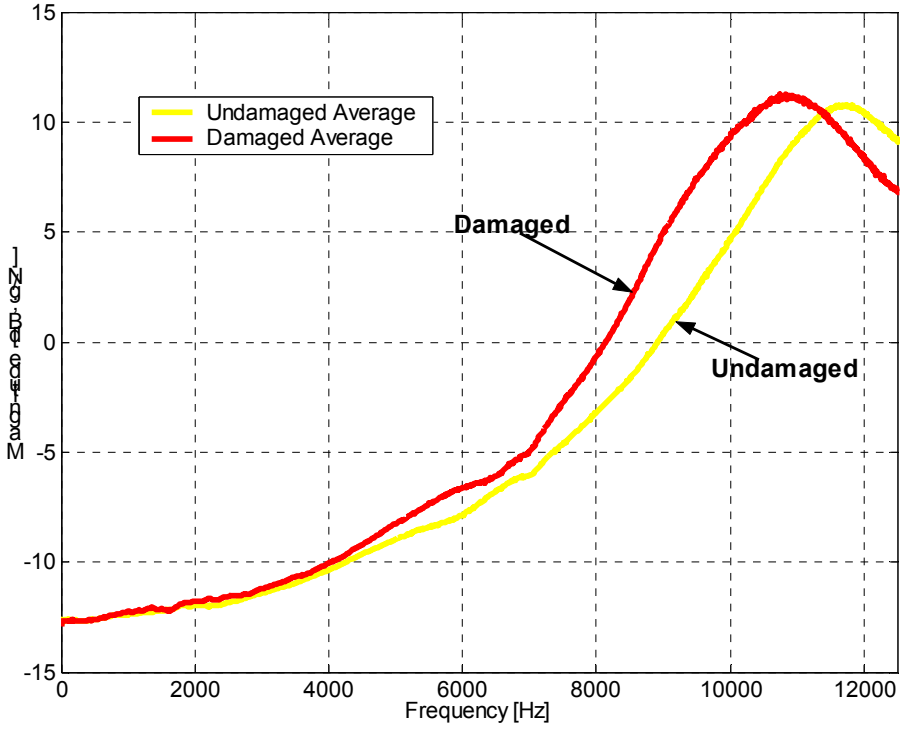

Figure 4-19. Magnitude of acceleration with respect to force comparison of averaged results for the three non-vacuum saturated samples and eight undamaged samples.

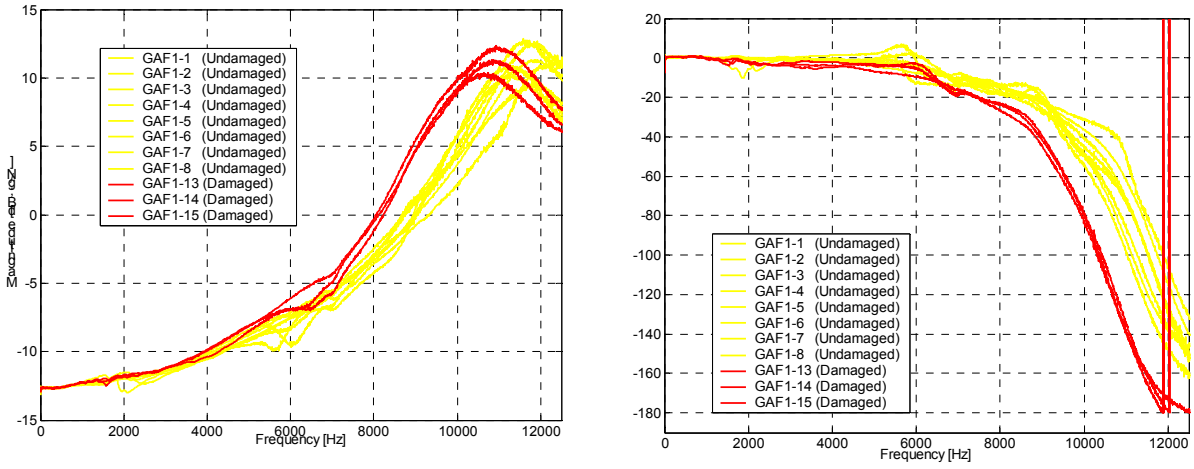

Figure 4-20. Magnitude and phase of acceleration with respect to force of the damaged pills conditioned without vacuum saturation, GAF1-13 through 15, as compared to the undamaged pills.

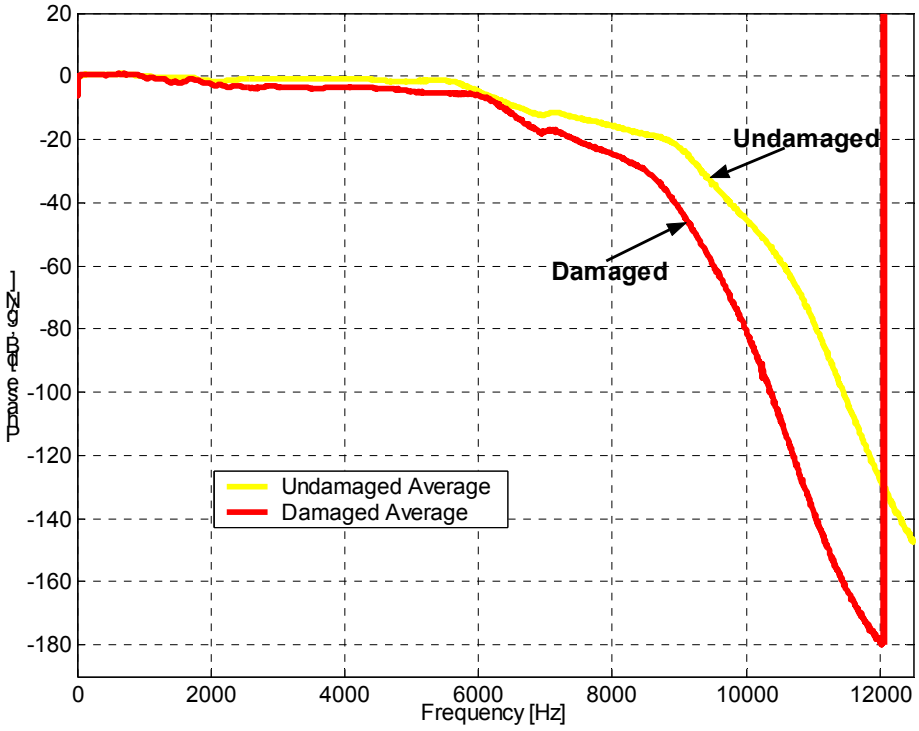

Figure 4-21. Phase of acceleration with respect to force comparison of averaged results for the three non-vacuum saturated samples and eight undamaged samples

4.9 Summary and Conclusions

Summary and conclusions based on the findings of this research are presented as follows:

- The small strain modulus obtained with the ultrasonic pulse wave velocity test appears to follow expected trends in density and air voids.
- The ultrasonic pulse wave velocity test appears to be sensitive to changes in mixture integrity due to moisture conditioning.
- The ultrasonic pulse wave velocity test appears to be sensitive to pore water effects after moisture conditioning.
- Pore water effects and moisture damage are both present in mixtures after conditioning.
- The mixtures tested exhibited a characteristic time-dependent change in mixture properties after conditioning:

  - Absorptive limestone mixtures showed a decrease in modulus ratio immediately after conditioning, followed by a gradual recovery.
  - Low absorption granite mixtures started recovery immediately after conditioning.
- The variation in mixture properties immediately after conditioning shows that the time of testing after conditioning is very important for consistency of results.
- The absorption characteristics of the aggregates and the portion of the gradation passing the no. 100 sieve affects the length of time that moisture is present in mixtures. Hence, mixtures with high F/A ratios, such as fine-graded mixtures and very dense coarse-graded mixtures may be more moisture susceptible than coarse-graded mixtures due to the longer recovery times of these mixtures.
- The effects of aggregate structure on moisture damage need to be evaluated with the appropriate volumetric film thickness description. The effective film thickness calculation, developed at the University of Florida (Nukunya 2001) accounts for the different nature of the aggregate structure of coarse-graded mixtures and seems to best reflect the changes in coarse-graded mixtures due to conditioning, whereas the theoretical film thickness appeared to work well for the fine-graded mixtures.
- The requirement of a target saturation level in conditioning protocols may induce excessive damage on coarse-graded mixtures.

In this paper, moisture conditioning was used to induce changes in the mixtures studied. The ultrasonic pulse wave velocity test was used to monitor the resulting changes in the mixtures. The ultrasonic pulse wave velocity test is a very quick test, with a testing time of about 1-2 seconds after setup that results in repeatable measurements of the small strain modulus of mixtures. The test requires no on-specimen sensors. The specimen is mounted into a simple

isolation frame and the test is performed immediately. The resulting small strain modulus appears to be sensitive to changes in mixture integrity due to damage, and therefore may be a possible tool for the characterization of damage in asphalt mixtures. More work remains to be performed to define relationships between the values obtained and other mixtures properties. However, the current results indicate that the ultrasonic pulse wave velocity test may be used as an indicator of damage in specimens, as well as a monitoring device for detecting changes in the integrity of mixtures.

The results from the resonant frequency method also show that the method appears to work well in monitoring changes over time in mixtures. However, the results also indicate that the resonant frequency test may not be suitable for measuring absolute values of modulus that can be used in a specification framework. These findings should be tempered by the fact all specimens contained moisture throughout the testing period, introducing other effects into the measurements, such as gradation and void structure-dependent suction within the specimen. The presence of moisture and likely suction will likely lead to higher variability in test results, as compared to dry specimens. Unfortunately, the results also showed that it takes a long time for moisture to evacuate a sample that has been saturated previously. Hence, there is a clear need for a consistent conditioning of all mixtures to consistent moisture and humidity conditions, before testing.

The use of a modal hammer test to detect the presence of moisture damage within a hot-mix asphalt sample is effective for fine-grained granite mixtures. Based on the results it is shown that a comparison of the peak magnitudes of acceleration with respect to force of a moisture conditioned specimen to that of a known undamaged sample is not sufficient for identifying the presence of moisture damage. A frequency shift from the undamaged case,

however, is consistently present within damaged samples in both magnitude and phase and may be used for identifying which pills have been conditioned. The results also show the test does not indicate the severity of the damage within a specimen as the less saturated samples produced a greater frequency shift as compared to the undamaged set. Further testing is recommended to determine the test's reliability when using any of the various types of mixtures available as well as its ability to detect loss of cohesion of the binder.

4.10 References

ASTM, *Standard Test for the Fundamental Transverse, Longitudinal and Torsional Resonant Frequencies of Concrete Specimens*, American Society for Testing and Materials, West Conshohocken, Pennsylvania, 2001, pp. C215-97.

Cedergren, H.R., *Drainage of Highways and Airfield Pavements*, Wiley Interscience Publication, New York, 1974.

Choubane, B., Page, G.C., and Musselman, J.A., "Investigation of Water Permeability of Coarse Graded Superpave Pavements," *Journal of the Association of Asphalt Paving Technologists*, Vol. 67, 1998.

Choubane, B., Page, G.C., and Musselman, J.A., "Effects of Different Water Saturation Levels on the Resistance of Compacted HMA Samples to Moisture Induced Damage," presented at the 80th Annual Transportation Research Board Meeting, Washington D.C., 2000.

Davis, H.E., Troxell, G.E., and Wiskocil, C.T., *The Testing and Inspection of Engineering Materials*, McGraw-Hill Book Company, New York, 1964.

Farrar, C.R., and Doebling, S.W., "An Overview of Modal-Based Damage Identification Methods," *Proceedings*, DAMAS Conference, Sheffield, UK, June 1997.

Kandhal, P.S., "Field and Laboratory Investigation of Stripping in Asphalt Pavement: State of the Art Report." *Transportation Research Record No. 1454*, TRB, NRC, Washington, D.C., 1994.

Kandhal, P. S., and Rickards, I. S., "Premature Failure of Asphalt Overlays from Stripping: Case Histories," *Journal of the Association of Asphalt Paving Technologists*, 2001.

Malhotra, V. M., and Carino, N. J., *CRC Handbook on Nondestructive Testing of Concrete*, CRC Press, Boca Raton, 1991.

Nukunya, B., "Evaluation of Aggregate Type and Gradation and Other Volumetric Properties as Criteria for the Design and Acceptance of Durable Superpave Mixtures," Ph.D. Dissertation, University of Florida, Gainesville, FL, 2001.

Nukunya, B., Roque, R., Tia, M., and Birgisson, B., "Evaluation of VMA and Other Volumetric Properties as Criteria for the Design and Acceptance of Superpave Mixtures," *Journal of the Association of Asphalt Paving Technologists*, Vol. 70, 2001.

Parker, Jr., F., and Gharaybeh, F.A., "Evaluation of Indirect Tensile Tests for Assessing Stripping of Alabama Asphalt Concrete Mixtures," *Transportation Research Record No. 115*, TRB, NRC, Washington, D.C., 1987.

Rojas, J., Nazarian, S., Tandon, V., and Yaun, D., "Quality Management of Asphalt-Concrete Layers Using Wave Propagation Techniques," *Journal of the Association of Asphalt Paving Technologists*, Vol. 68, 1999.

CHAPTER 5
EVALUATION OF PORE PRESSURES IN MIXTURES DURING MIXTURE PERFORMANCE TESTING IN COMPRESSION

Based on the results in Chapters 3 and 4, it appears that there may be a number of physical effects that influence moisture damage of mixtures and the characterization of moisture damage in mixtures. In particular, it appears that once moisture enters specimens it takes a long time to drain out again. There is also a large national study sponsored by the National Cooperative Highway Research Program (NCHRP) currently underway that is evaluating complex modulus test under triaxial compression loading for as a potential candidate for evaluating the moisture damage in mixtures. This NCHRP project is entitled "NCHRP Project 9-34: Improved Conditioning Procedure for Predicting the Moisture Susceptibility of HMA Pavements." It is therefore of significant interest to determine the effect of moisture and saturation on the loading response of mixtures.

In this chapter, the following topics will be presented: 1) pore pressure response of saturated mixtures undergoing static triaxial testing; 2) pore pressure response of saturated and partially saturated mixtures undergoing complex modulus testing; and 3) finite element modeling of pore pressure response of mixtures under idealized loading conditions. First, the materials and mixtures tested will be discussed, followed by a discussion of the saturation procedures used in the laboratory testing part, and the presentation of the test results. Finally, the finite element modeling results are presented.

5.1 Objectives

The objectives with this study are to evaluate the effects of pore pressure on mixture performance response under static and cyclic loading conditions. A secondary object is to model

the effects of pore pressures under controlled loading and dilation conditions to evaluate whether the mixtures tested follow effective stress principles in a similar manner as soil and rock.

5.2 Scope

In the following, first the materials and methods used will be presented, followed by a discussion of static testing results, complex dynamic modulus testing results, and finite element modeling results.

5.3 Materials Used and Preparation

5.3.1 Aggregates, Gradations, and Binder Used

The aggregate used in this part of the study consisted of crushed granite from Georgia, which has been used extensively in Florida and are considered to be excellent materials resulting in well-performing mixtures. The resulting granite mixtures were made up of four components: coarse aggregate, fine aggregate, screenings, and mineral filler. They were blended together in different proportions to provide two 12.5-mm nominal maximum aggregate size mixtures of coarse and fine gradations, respectively. These mixtures are denoted as: GA-C1 and GA-F1, with the letters C and F denoting coarse-graded and fine-graded mixtures according to whether the gradation passes below or above the Superpave™ restricted zone. The purpose of selecting two mixtures of varying gradation was to ensure that the mixtures tested were of different permeability, and other volumetric properties. The resulting gradations are shown in Table 5-1. Design asphalt contents for the two mixtures were determined such that each mixture had 4 percent air voids at N_{design} = 109 gyrations. Finally, PG 67-22 (AC-30) asphalt was used for all limestone and granite mixtures in this study. Table 5-2 shows the volumetric properties for the mixtures used.

Table 5-1. Gradations for Granite Mixtures

Sieve Size (mm)	Percent Material Passing each Sieve Size	
	GA-C1	GA-F1
19.0	100.0	100.0
12.5	97.4	94.7
9.5	89.0	84.0
4.75	55.5	66.4
2.36	29.6	49.2
1.18	19.2	32.7
0.60	13.3	21.0
0.30	9.3	12.9
0.15	5.4	5.9
0.075	3.5	3.3

Table 5-2. Volumetric Properties of Granite and Limestone Mixtures

Properties	Mixture	
	GA-C1	GA-F1
Asphalt Content (%)	6.63	5.68
Specific Gravity of Asphalt	1.035	1.035
Bulk Specific Gravity	2.345	2.374
Theoretical Max. Specific Gravity	2.442	2.473
Air Voids (%)	4.0	4.0
Voids in Mineral Aggregate (%)	18.5	16.6
Voids filled with Asphalt (%)	78.5	75.9
Effective Specific Gravity of Aggregate	2.710	2.706
Absorbed Asphalt (%)	0.3	0.3
Effective Asphalt (%)	6.3	5.4
Dust to Asphalt Ratio	0.6	0.6
Surface Area (m^2/kg)	3.3	4.1
Film Thickness theoretical, microns	19.9	13.4

5.3.2 Mixture Preparation and Specimen Saturation Procedure

The following procedures for specimen preparation were used:

- All mixtures were designed according to the Superpave volumetric mix design method.
- Mixtures were produced in the laboratory following the procedure outlined in AASHTO T-283. First, the aggregates and asphalt binder were heated to 150° C (300° F) for three

hours prior to mixing. Once the mixing was completed, the mixture was allowed to cool to room temperature for two hours. After the cooling period, the loose mixture was long-term aged for 16 hours at 60° C (140° F). After the mixture was aged for 16 hours, it was reheated to 135° C (275° F) for two hours before compaction. The specimens were then compacted on the IPC Servopac Superpave™ gyratory compactor to 7 ± 0.5 percent air voids.

- Dynamic Modulus Testing and Static Triaxial Testing: Since the NCHRP 1-37A Draft Test Method DM-1 - Standard Test Method for Dynamic Modulus of Asphalt Concrete Mixtures (NCHRP 2004; Witczak et al. 2002*)* had not been developed at the onset of the testing program, the older ASTM D 3497 (ASTM 1997) testing procedure for dynamic modulus testing was followed, with major modifications, summarized by Witczak et al. (2000; 2002). Most of the key features of the NCHRP 1-37A Draft Test Method DM-1 were followed, with the exception of:
  - frequencies and temperatures of testing, and
  - specimen preparation, as discussed below.

  The testing frequencies (16 Hz, 4 Hz, and 1 Hz) were recommended in ASTM D 3497 (ASTM 1997). In addition, testing was performed at 10-Hz frequency to obtain a better distribution of testing frequencies. In order to obtain a measure of the temperature dependency of the dynamic modulus for the mixtures tested, the test temperatures were selected at 10° C, 25° C, and 40° C. The specimen preparation for all tests performed included the following steps:
  - Compaction in a Superpave™ gyratory compactor mold with an inner diameter of 102-mm (4.0 in) to a compacted specimen height of 170-mm to 180-mm;

– Trim (saw) ends of specimens to obtain 102-mm diameter samples that are 150-mm tall.

For each test combination, three samples of each mix were prepared. The dynamic modulus values obtained for each mixture are the average results from three test specimens. Four one-specimen vertical LVDT's were used to measure the vertical deformation of the specimen during each test.

The sample preparation and the measurement of specimen deformation in the static triaxial test followed that of the complex dynamic modulus test. Further details about the static triaxial testing are provided later in this chapter.

For each mixture and testing condition, three samples were subjected to vacuum saturation, in which the specimens were placed in a vacuum saturation vessel. A vacuum of 25 in-Hg was applied to the vessel for 15 minutes. After 15 minutes, the vacuum was removed from the vessel and the specimens are allowed to set in the vessel for another 15 minutes. This allowed the water to infiltrate the deeper voids in the specimen that was previously filled with air. The sample was considered saturated after this process was completed, however, a smaller vacuum of 5 psi was applied a second time for five minutes to remove all air in the chamber and lines, just prior to testing.

Once the saturation procedure was completed, the specimen was wrapped in latex membrane and the specimen was placed on the pedestal inside the chamber. The chamber wall and lid were fitted exactly to insure their seal. The chamber was filled with room temperature water. The water in the cell was heated by to the prescribed temperature (10° C, 25° C, or 40° C) using the environmental conditioning system described in Chapter 10. Once the specimen was determined to be at the prescribed temperature, a temperature controlled heating pad was

wrapped around the chamber wall. An insulation blanket was then placed around the heating pad. At that point, the tubes of the hydraulic setup were purged of air by pushing water through them using the volume changer. The chamber was connected to the hydraulic volume changer. Water was then pushed into the bottom of the chamber with the upper part of the chamber connected to the annulus tubes with their vent open. This allowed the chamber to be forced out. Next, the vent at the top of the chamber was switched to the connection leading to the vacuum control panel. The pressure was decreased by 10.2 in-Hg (5.0 psi) in order to remove any remaining air in the system and sample. This decrease in pressure was maintained for 15 minutes. The valve to the vacuum tube was closed and water was allowed to recede back into the chamber to replace the air that had just been removed. The sample was allowed to sit for another 15 minutes before this final air removal process was completed. At this point, a saturated sample had been enclosed in an airtight environmental chamber completely filled with water at normal pressure. To verify the saturation process, the volume of water delivered into the specimen was compared to the volume exiting it. The volume of water entering the specimen was calculated by recording the linear displacement of the volume changer and converting that displacement into a volume. The corresponding volume of water exiting the specimen was read directly in the burette on the distribution panel.

The final phase of saturation used a backpressure technique. With both the influent and the effluent valves open, pressure was increased until the confining pressure and pore pressure readings at both ends of the specimen were approximately 60 psi and 55 psi, respectively. The confining and pore pressures were incrementally increased such that a maximum effective stress of 5 psi was maintained. The backpressure was applied for 30 minutes prior to the determination of the B-value. The B-value measures the pore water pressure per increment of confining stress and is thus used to determine saturation. This relation is expressed as:

$$B = \frac{\Delta u}{\Delta \sigma} \qquad \text{(Eq. 5.1)}$$

where Δu = change in pore water pressure

$\Delta \sigma$ = change in confining stress

This relation suggests two fundamental assumptions:

1. The specimen contains enough connected voids to transfer pore water pressure is through the skeleton.
2. The specimen's skeleton is elastic such that the induced confining pressure is transferred to the water-filled voids and not carried exclusively by the skeleton.

In research done to assess the potential factors affecting HMA permeability, coarse graded asphalt mixtures were shown to contain larger individual air voids and thus an increased potential for interconnected voids (Cooley et al. 2001). This supported the premise that a specimen could be successfully saturated by the conduction of water through it from end to end.

During development of the backpressure saturation protocol, a trend was observed in the resulting B-value as the effective stress was increased. As the effective stress was increased, the B-value would increase, stabilize, and then decrease sharply. This trend is believed to be a function of the geometry of the specimen's circumferential surface as well as the relative stiffness of the skeleton. Conceptual illustrations of this trend are shown in Figures 5-1 and 5-2, as the effective stress is increased, the corresponding B-value goes through three distinct phases. At the start of Phase 1, the effective stress is approximately 3 psi; the membrane is in contact with the high points on the circumferential surface of the specimen and suspended over the surface indentations cushioned on water. As the effective stress is increased, the membrane is forced into the indentations, in the process absorbing some of the stress in its deformation; this results in an increasing B-value. At the start of Phase 2, the membrane is stretched into the

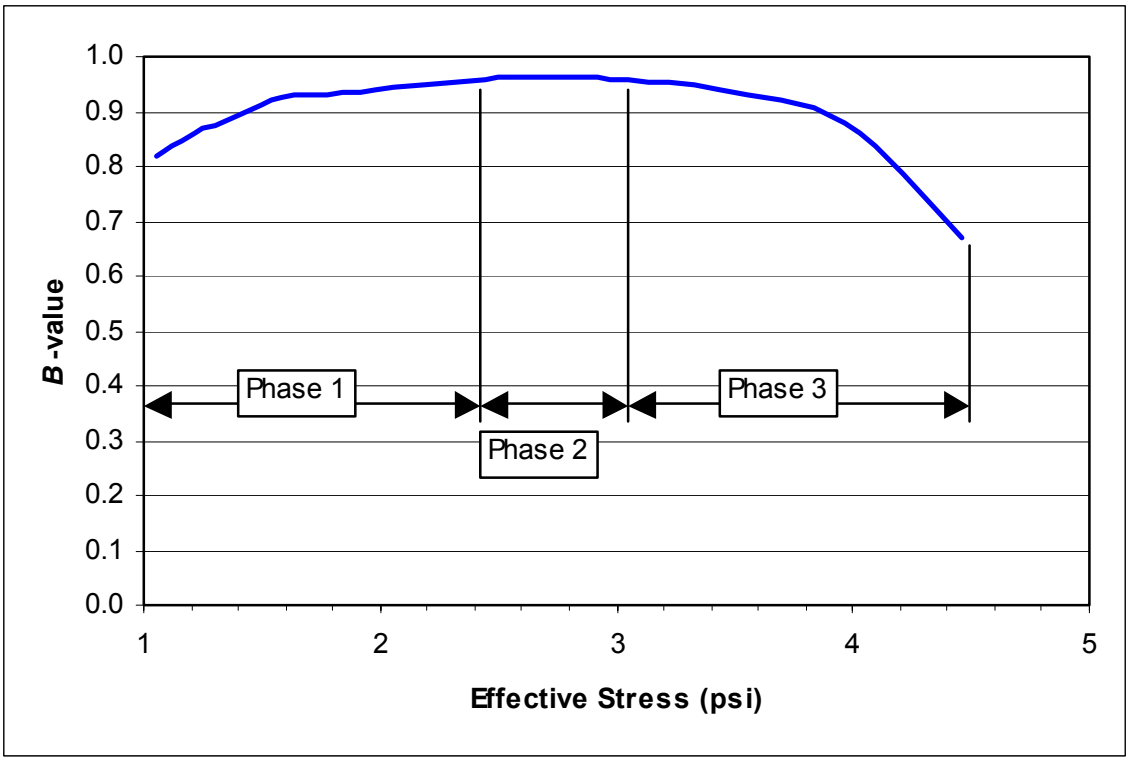

Figure 5-1. Calculated B-value with increasing confining stress.

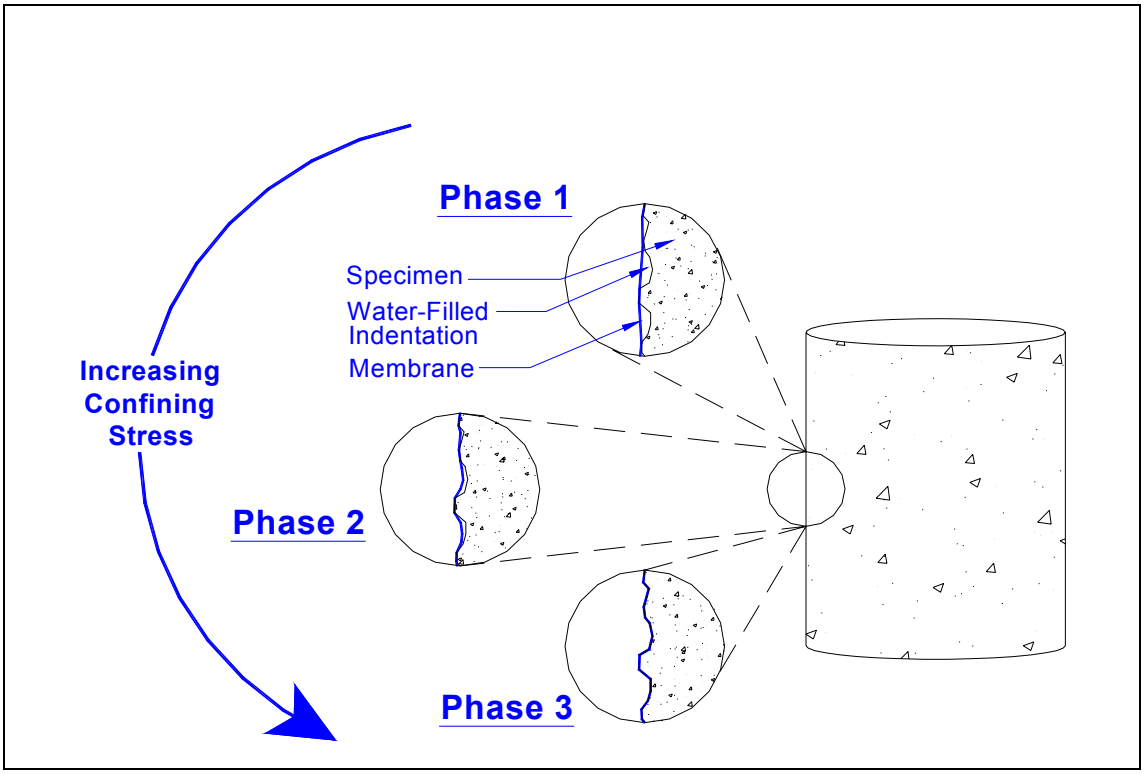

Figure 5-2. Membrane position with increasing confining pressure.

indentations and compression of the water within the specimen has occurred. As the effective stress is further increased, the membrane is forced further into the voids of the specimen until a limit is reached. Within this phase, the optimal B-value is reached. The thickness (0.012 in.) of the membrane prevents it from further penetration into the voids of the specimen with an increase in confining pressure. At this point, Phase 3 begins wherein the increasing confining pressure yields a correspondingly small increase in pore pressure. This relationship results in a decreasing B-value.

With the process understood, the approach to a B-value was achieved by increasing the confining pressure in small increments to reveal the optimal B-value range. With typical initial effective stress conditions employed for each specimen, and similar surface geometry, the optimum B-value was achieved within approximately the same quantity of confining stress increase.

Figures 5-3 and 5-4 show typical B-value responses for mixtures GA-F1 and GA-C1 at testing temperature of 40° C. The GA-F1 mixture was determined to be saturated at the third B-value trial. The GA-C1 mixture was determined to be saturated after the forth B-value trial. Finally, Figure 5-5 shows a comparison of B-values between GA-C1 and GA-F1 at 40° C. Even though these two mixtures were fully saturated, the B-value for GA-F1 is always smaller than for GA-C1. This difference in B-values is likely due to different skeletal stiffnesses of the two mixtures, with mixture GA-F1 being stiffer than GA-C1.

Finally, once a stable B-value reading was obtained, the testing was initiated. For testing of saturated specimens, the valves at the top of the bottom of the specimen were kept closed throughout testing. For drained testing, the valves at the top and the bottom of the specimen were kept open and in contact with the water source throughout testing.

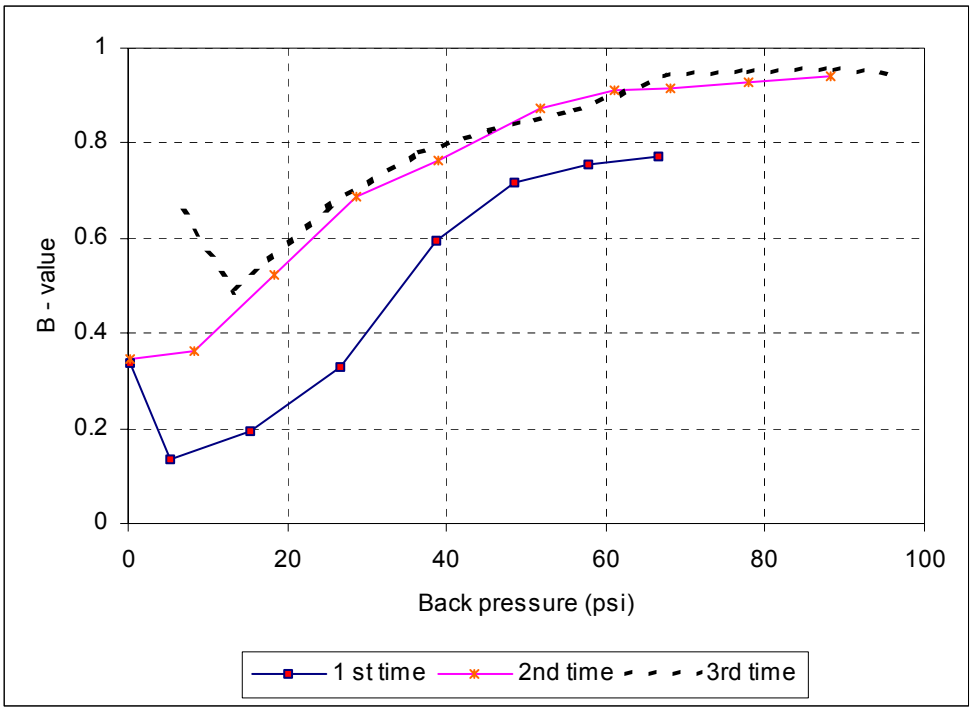

Figure 5-3. Determination of B-value during backpressure saturation for mixture GA-F1 and test temperature of 40° C.

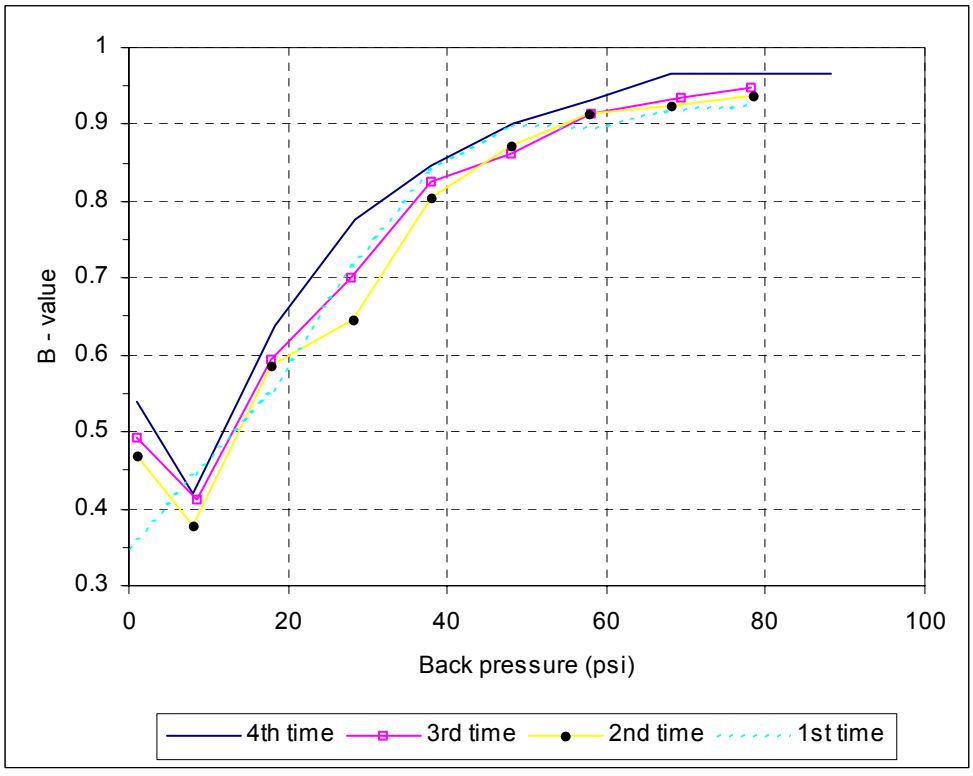

Figure 5-4. Determination of B-value during backpressure saturation for mixture GA-C1 and test temperature of 40° C.

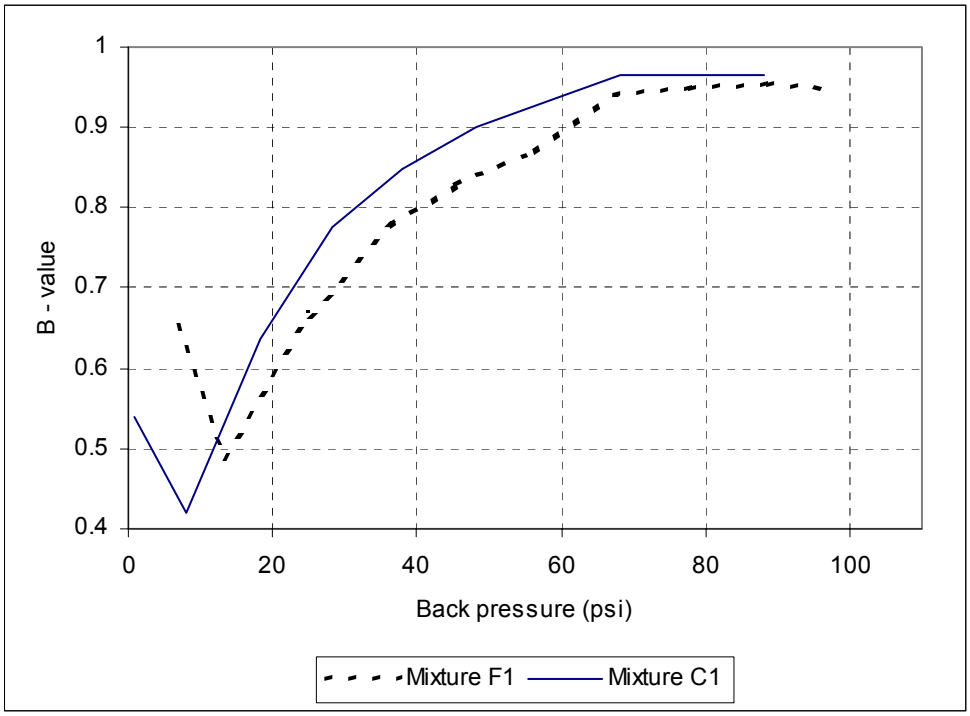

Figure 5-5. Comparison of typical final B-value response for mixtures GA-C1 and GA-F1 at a test temperature of 40° C.

5.4 Static Triaxial Compression Testing

The Consolidated Undrained (CU) test is performed with the influent and effluent lines to the specimen closed. With a confining stress applied to the specimen, the deviator stress is increased until shear failure occurs. Since drainage is not allowed during the test, pore water pressure will increase, if the specimen is contracting during shear and decrease if the specimen is dilating. For example, in dense specimens such as clay, the pore water pressure will increase with strain to a limit and then decrease and become negative (Lambe 1969). The decrease is owed to the specimen dilating resulting in an increase of specimen volume.

The CU test is initiated by closing the valve to the confining water, thus locking in a prescribed confining stress. The axial load is subsequently applied at constant rate. During the test, a data acquisition system recorded: axial displacement, axial load, top, bottom, and

confining pressure at one-second intervals. Axial displacement continued until either a perceived decrease in stress carrying capacity occurred or a maximum 0.75 inches displacement of the piston occurred. The maximum displacement is a function of the cell and a displacement past this limit would expose the piston seals beyond the confines of the piston sleeve allowing confining pressure to be lost.

The specimen was loaded by prescribing a constant displacement rate of 0.0025 in/s for the axial piston. Figure 5-6 (a) shows typical stress-strain results for GA-F1 at a testing temperature of 25° C. Figure 5-6 (b) shows the corresponding change in pore pressure versus axial strain.

The observed pore pressure response in Figure 5-6 (b) is very similar to that of a dense sand or heavily over consolidated clay. The pore pressure increased with the load in the first part. The pore pressure started to decrease when the strain of the sample reached about 0.45 percent, and the pore pressure changed from positive to negative. At a very dense state, the mixture tends to dilate with increased shear stresses. When the mixture dilated, the volume of the mixture increases as well. Since the CU test is performed under undrained conditions, this volume increase reduces the value of the pore water pressure.

Figure 5-7 (a) and (b) depict typical stress-strain and pore pressure responses during shearing for mixture GA-F1 at a test temperature of 40° C. The development of the pore water pressure was similar to that observed at a testing temperature of 25° C (Figure 5-6 (b)). The pore pressure peaked at an axial strain of 0.3 percent, followed by a reduction due to dilation.

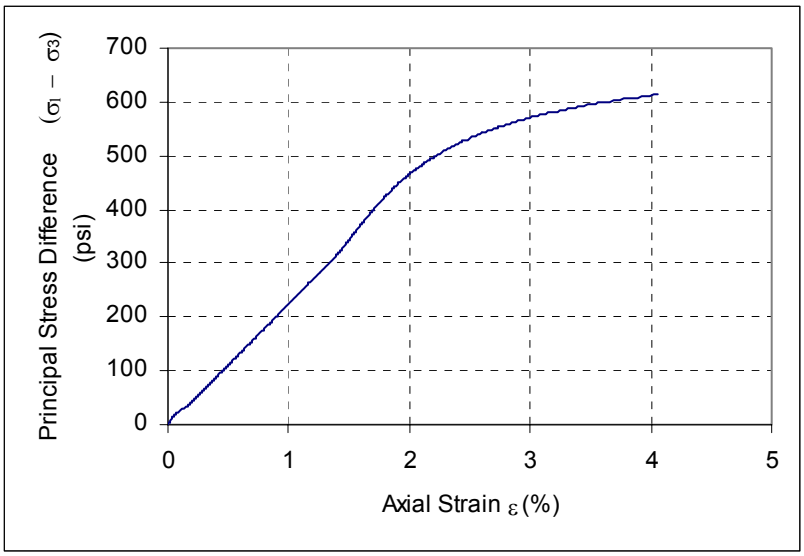

(a) Stress-strain relationship

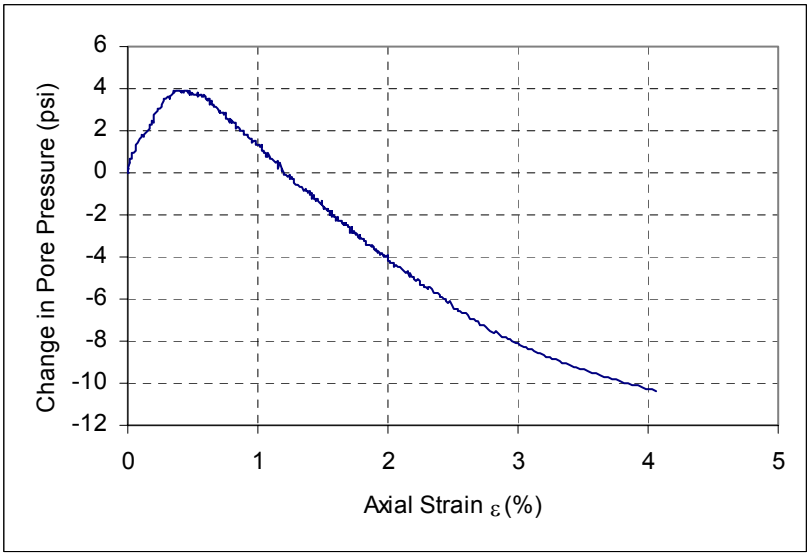

(b) Pore pressure versus axial strain relationship

Figure 5-6. Typical results for mixture GA-F1 at a test temperature of 25° C.

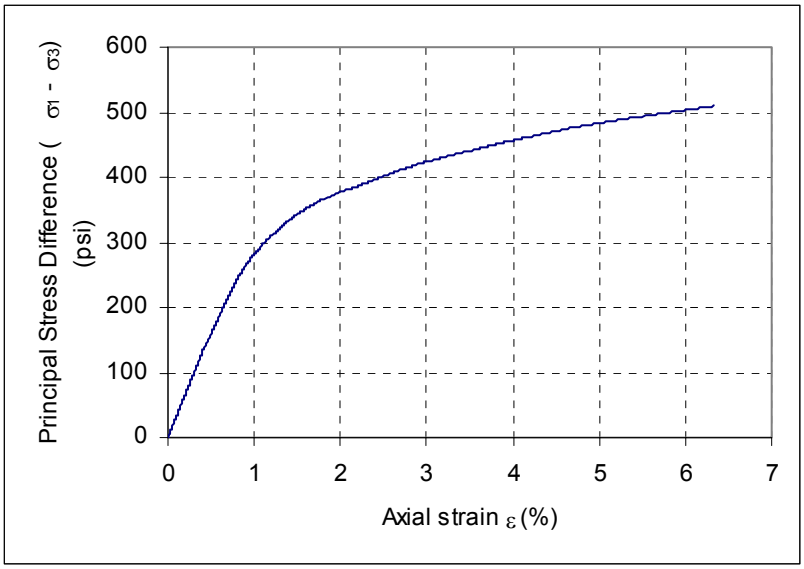

(a) Stress-strain relationship

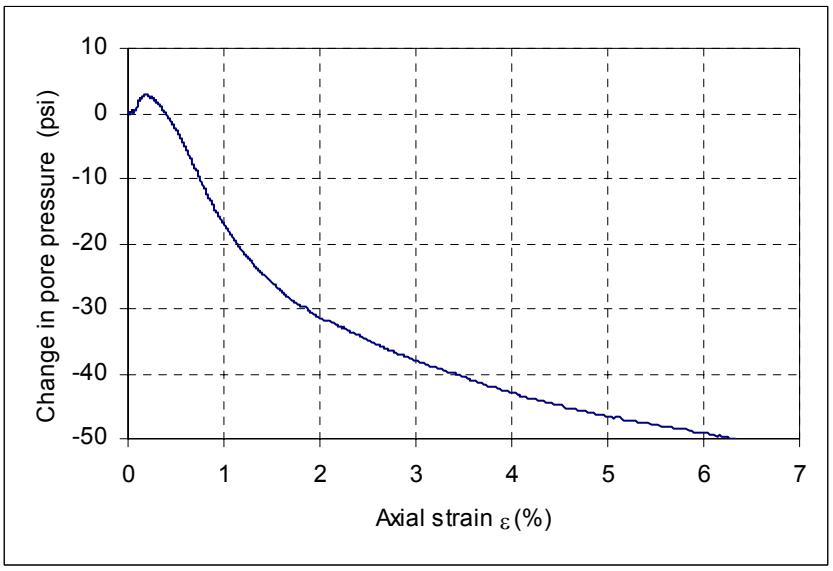

(b) Pore pressure versus axial strain relationship

Figure 5-7. Typical results for mixture GA-F1 at a test temperature of 40° C.

Figures 5-8 (a) and (b) depict typical stress-strain and pore pressure responses during shearing for mixture GA-C1 at a test temperature of 25° C. The test was stopped at a failure strain of 3.7%. The load at 3.7% strain is 546 psi. The pore pressure peaked at an axial strain of 0.24 percent, followed by a reduction due to dilation.

Figure 5-9 (a) and (b) depict typical stress-strain and pore pressure responses for mixture GA-C1 at a test temperature of 40° C. Even though the mixture was not loaded to failure, the trend in the pore pressure follows the previous test results for mixtures GA-C1 and GA-F1. Again, the pore pressure peaked at an axial strain of 0.17 percent, followed by a reduction due to dilation.

Figure 5-10 shows a comparison between the change in pore pressure versus testing temperature for mixture GA-F1. Because asphalt becomes softer at higher temperatures, the failure stress at 40° C is smaller than at 25° C. As expected, at the higher test temperature of 40° C, the pore water pressure peaks at a lower strain value, and develops higher negative pore pressures at failure than the mixture tested at 25° C.

Finally, Figure 5-11 shows a comparison of induced pore pressures during shear for mixtures GA-C1 and GA-F1 at a test temperature of 25° C degrees. The coarser-graded GA-C1 mixture resulted in larger negative pore pressure at failure, compared to the finer-graded GA-F1 mixture. This may be due to the coarse aggregate-to-aggregate contact structure in mixture GA-C1 forcing the mixture to dilate more to develop a failure plane than the finer graded GA-F1.

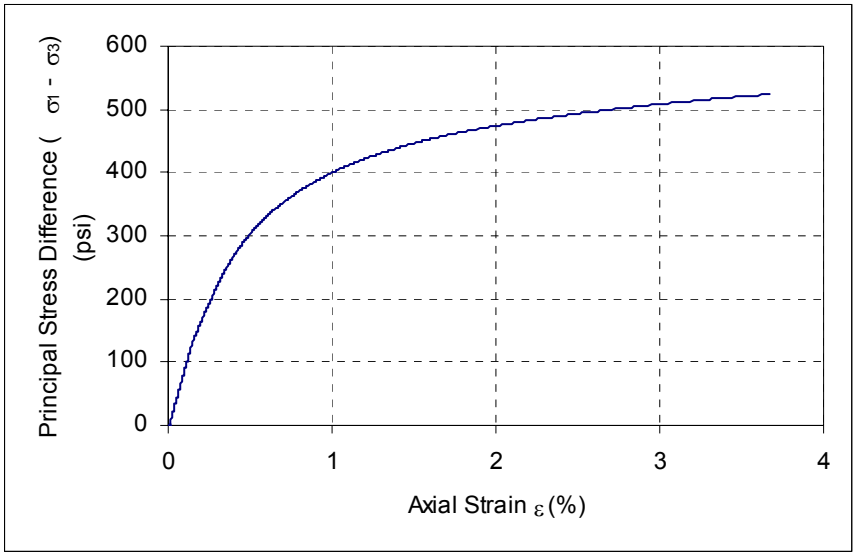

(a) Stress-strain relationship

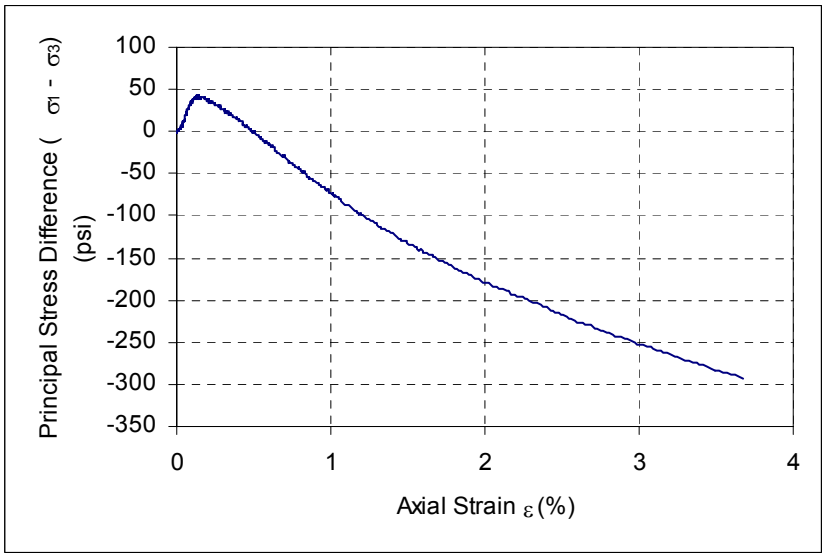

(b) Pore pressure versus axial strain relationship

Figure 5-8. Typical results for mixture GA-C1 at a test temperature of 25° C.

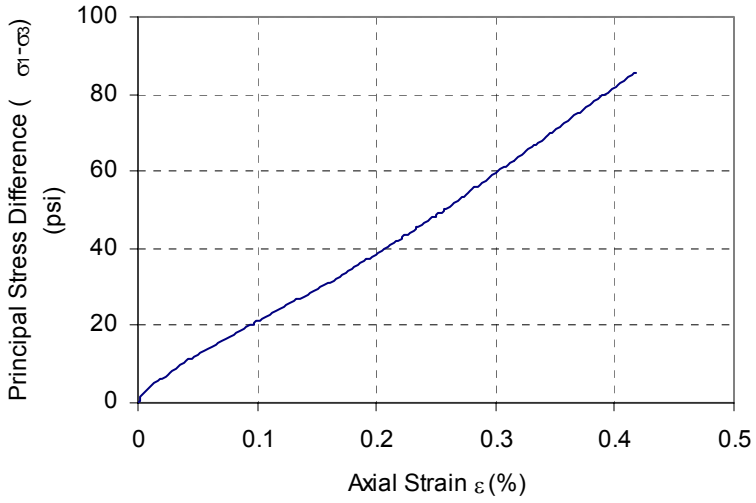

(a) Stress-strain relationship

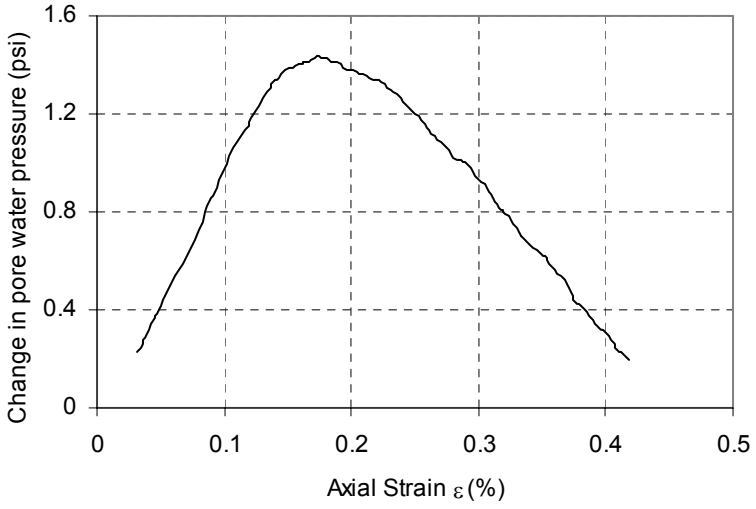

(b) Pore pressure versus axial strain relationship

Figure 5-9. Typical results for mixture GA-C1 at a test temperature of 40° C.

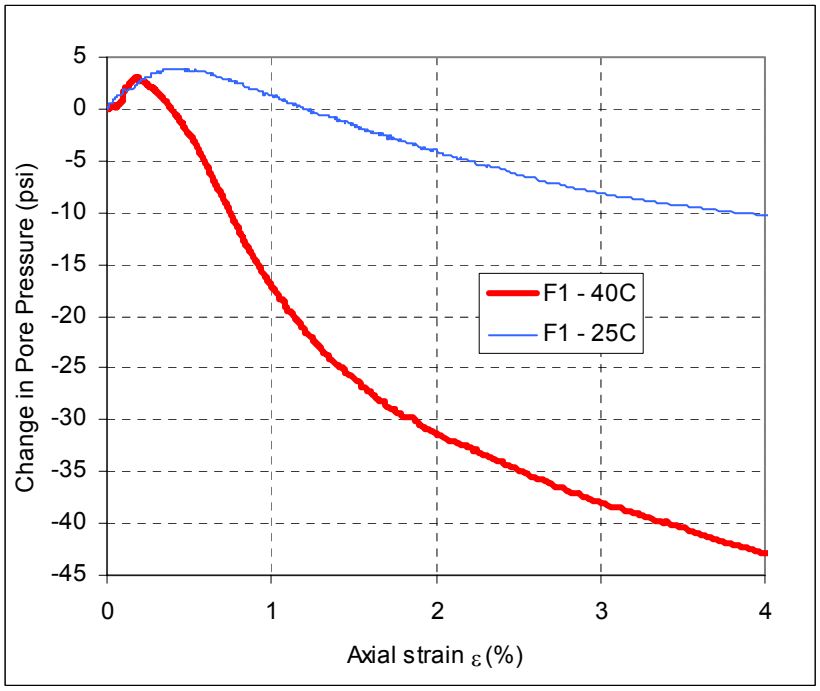

Figure 5-10. Comparison between mobilized pore pressure versus testing temperature for mixture GA-F1 (Test temperatures are 25° C and 40° C).

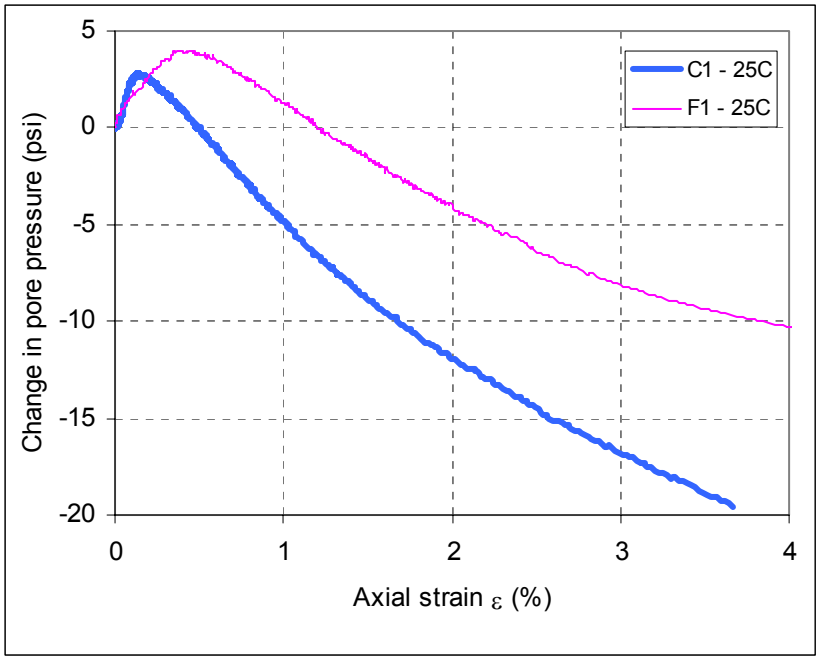

Figure 5-11. Comparison of induced pore pressures for mixtures GA-C1 and GA-F1 at test temperature of 25° C.

5.5 Static Triaxial Test with Fixed End Platens

In order to investigate the pore pressure response of mixtures when the material is not allowed to dilate, the following testing conditions were evaluated using the GA-C1 mixture: 1) the mixture was brought to a uniform isotropic state of stress of 60 psi, at which point the top and bottom platens were fixed and kept from moving during the rest of the test, followed by 2) the application of the loading stress to the specimen from the sides of the specimen, as shown in Figure 5-12. In order to enhance the pore pressure response further, the testing temperature was taken as 40° C and the mixture was kept fully saturated and undrained throughout testing. Figure 5-13 shows the resulting pore pressure response due to the applied horizontal stress during the testing. The results clearly show that virtually all of the additional stress is now carried by the pore fluid and thus resulting in pore pressures that are equal to the applied horizontal stress. Again, these results clearly illustrate that pore pressures can play a dominant role in the behavior of mixtures.

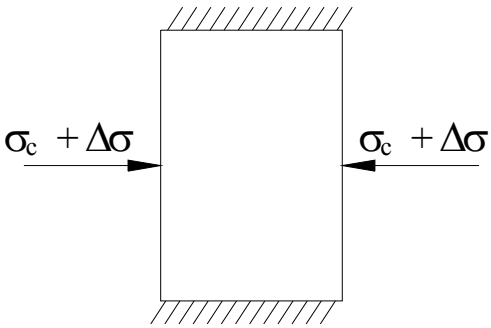

Figure 5-12. Boundary conditions for a triaxial test in which the dilation during loading is restricted.

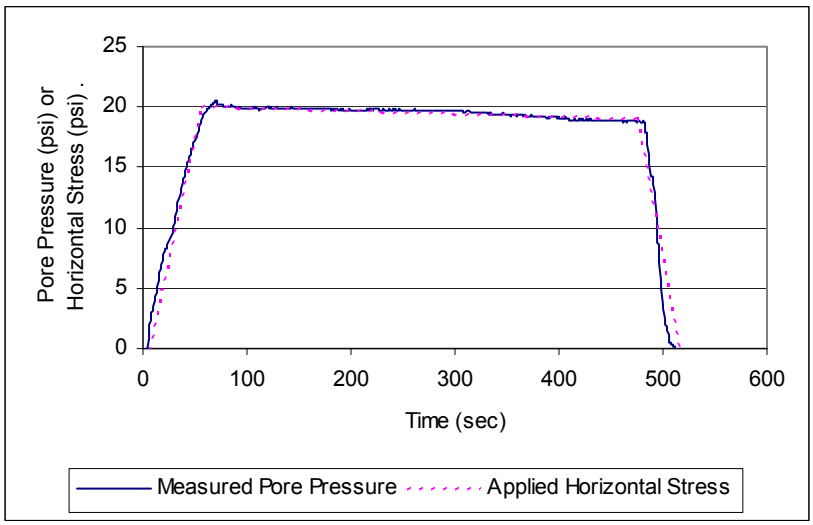

Figure 5-13. Measured pore pressure response due to applied horizontal stress for mixture GA-C1 at testing temperature of 40° C.

5.6 Complex Modulus Testing

The complex dynamic modulus testing was performed at test temperatures of 10° C and 40° C, at the following saturation conditions: 1) initially saturated and undrained conditions; 2) initially saturated and drained; and 3) dry. Table 5-3 lists the mixtures, temperatures, and saturation conditions evaluated. For the undrained and drained conditions, an effective stress of approximately 1 psi was introduced to the specimen. For the lower temperature the confining stress was approximately 10 psi and at the higher temperature approximately 2 psi confining stress was placed onto the specimen. The effective stress was chosen to be substantial enough to indicate a pore pressure response to cyclic loading but low enough in order to limit the magnitude of axial load needed to induce strain in the specimen. Testing in the drained condition followed those done in the undrained condition, with the dry specimen testing performed prior to saturation. Prior to drained testing, the valves leading to the top and bottom of the specimen was opened and the pore pressure allowed to dissipate over a period of 5 minutes. Complex dynamic modulus testing was then conducted.

Table 5-3. Mixtures, Temperatures, and Saturation Conditions for Complex Modulus Testing

Mixture	Dry		Undrained		Drained	
GA-F1	10° C	40° C	10° C	40° C	10° C	40° C
GA-C1	10° C	40° C	10° C	40° C	10° C	40° C

Figure 5-14 shows typical measured pore pressure response from complex dynamic modulus testing. The vertical cyclic stress is applied at the rate of 1 Hz at a testing temperature of 10° C. The results show that the pore pressure increased with the increase of the applied load even though the magnitude is about 10 times smaller. Interestingly, there is also a time lag between the pore pressure and the applied vertical cyclic stress.

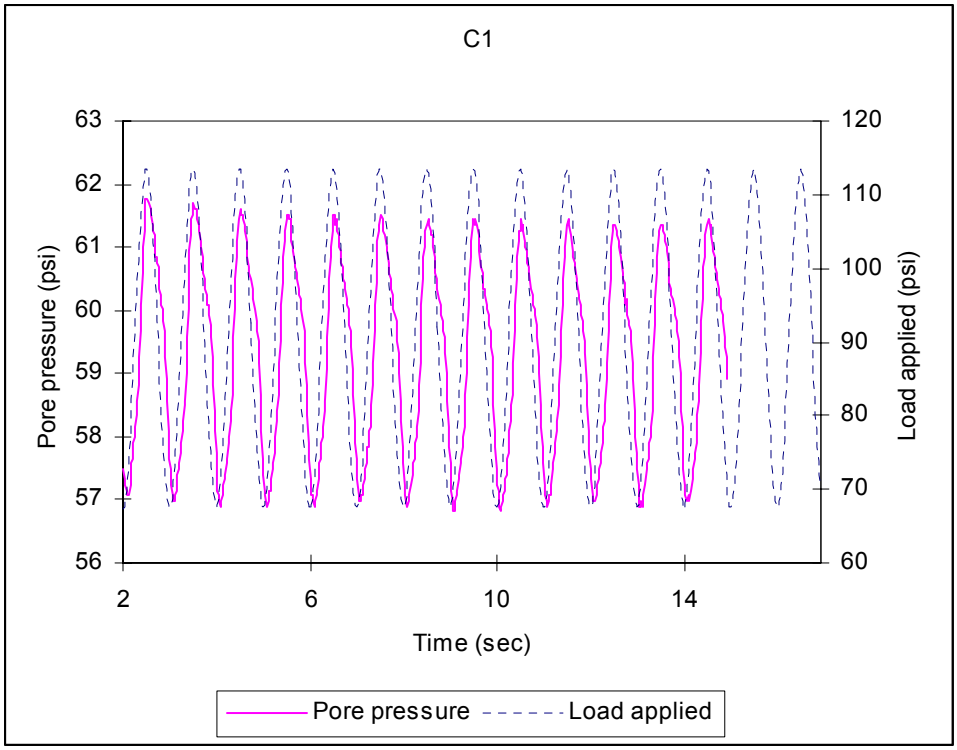

Figure 5-14. Typical pore pressure response during complex dynamic modulus testing of mixture GA-C1 (Test frequency is 1 Hz and temperature is 10° C).

The complex dynamic modulus results are shown from Figure 5-15 to Figure 5-18. As expected, the complex dynamic modulus appears to be increasing with frequency. For mixture GA-C1 (Figures 5-15 and 5-16), there is a considerable increase in complex modulus value when the condition of the sample changed from dry mode to saturated mode. However, there is little difference between the undrained and the drained testing conditions. These trends are even clearer when the mixture is tested at 40° C. The increase in stiffness under undrained conditions over dry conditions is expected due to the high bulk stiffness of water. Importantly, these results clearly show that mixtures exhibit a pore pressure response that can affect the stiffness response in flexible pavements. The results also show that even though a coarse-graded mixture like the GA-C1 mixture is allowed to drain for a few minutes before testing, it essentially remains saturated and responds like a saturated mixture. In addition, the loading per cycle is too fast for any significant drainage to take place during loading of drained specimens.

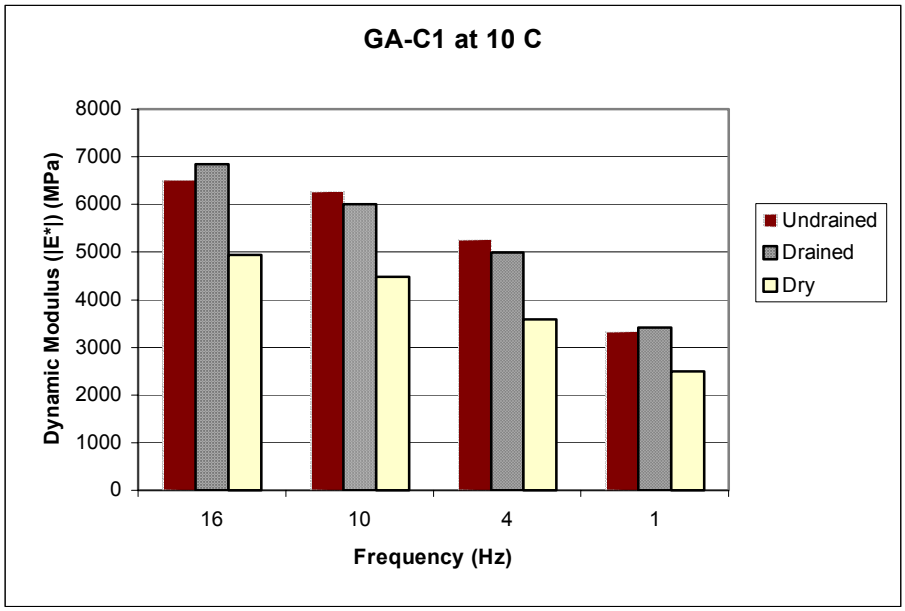

Figure 5-15. Complex dynamic modulus versus frequency for mixture GA-C1 under undrained, drained, and dry test conditions and test temperature of 10° C.

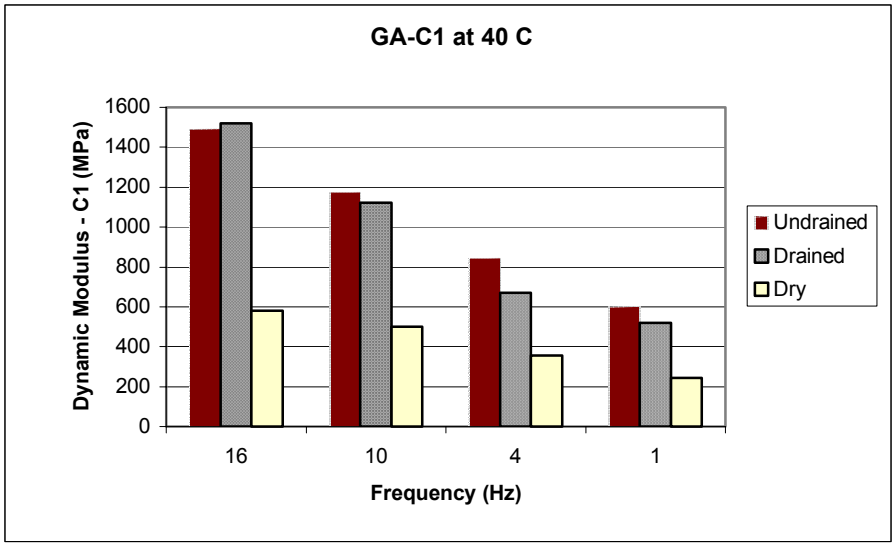

Figure 5-16. Complex dynamic modulus versus frequency for mixture GA-C1 under undrained, drained, and dry test conditions and test temperature of 40° C.

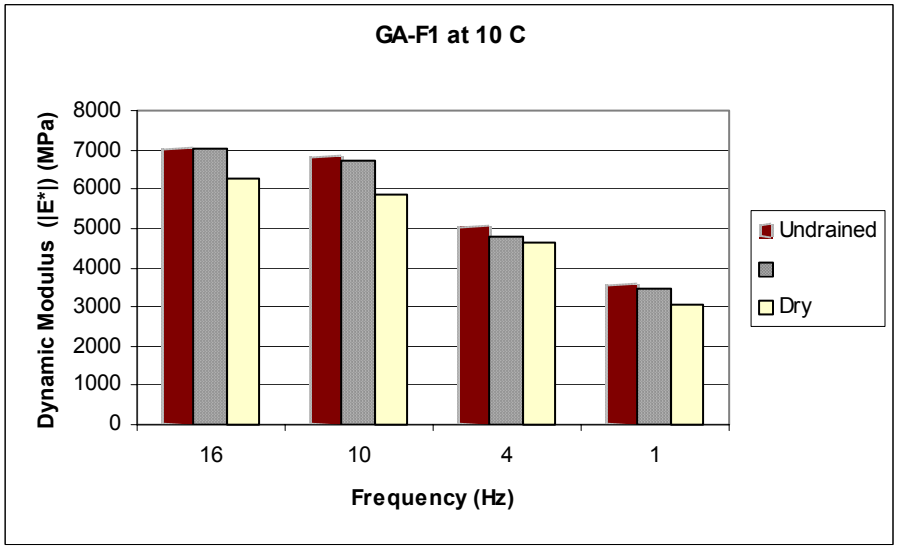

Figure 5-17. Complex dynamic modulus versus frequency for mixture GA-F1 under undrained, drained, and dry test conditions and test temperature of 10° C.

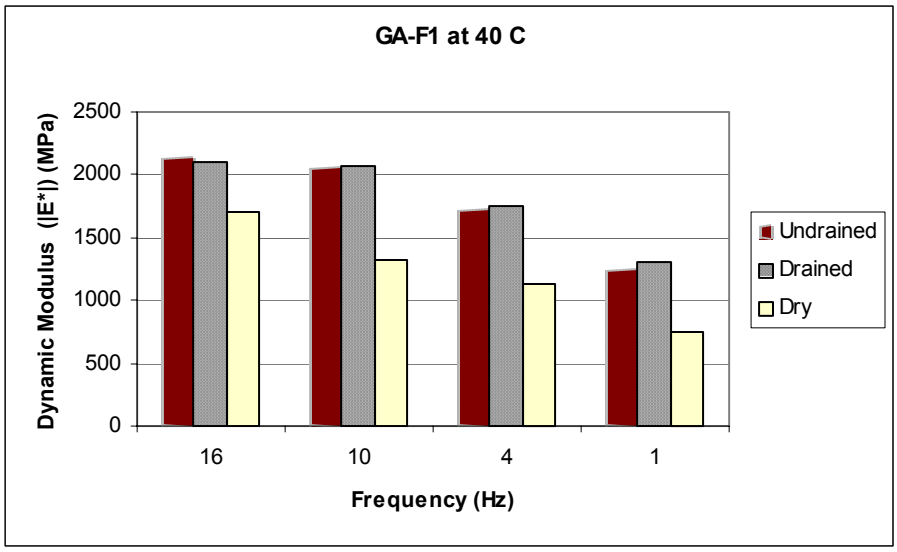

Figure 5-18. Complex dynamic modulus versus frequency for mixture GA-F1 under undrained, drained, and dry test conditions and test temperature of 10° C.

In the complex dynamic modulus results for mixture GA-F1 (Figures 5-17 and 5-18), again, the complex modulus does not change significantly from drained to undrained conditions at testing temperature of 10° C, whereas the undrained modulus is slightly higher than for the dry conditions. This difference between undrained and dry modulus values increases with temperature.

In summary, it can be concluded that the mixtures tested exhibit pore pressure response that is significant enough to affect and in some cases overwhelm the complex dynamic modulus response in a dry state of these mixtures. Importantly, since pore pressures are a function of the void structure of mixtures, these pore pressure effects are highly likely to change from one mixture to another, based on the gradation and the mixture volumetric properties.

5.7 Finite Element Modeling of Pore Pressure Response in Mixtures During Loading

In order to develop and understanding the behavior of pore pressure in a saturated undrained asphalt mixtures, a finite element model of GA-C1 using the loading case presented in Figure 5-12 was constructed. The test conditions consisted of triaxial loading conditions, with the end platens fixed, and horizontal stress applied at testing temperature of 40° C. The finite element modeling was performed using the program PlasFEM, which was developed at the University of Florida (Pinto 1997). PlasFEM is capable of modeling in one, two or three dimensions both the solid phase and fluid phase under both static and dynamic loading (Pinto 1997). The test conditions shown in Figure 5-12 were modeled using linear elastic material with pore pressures (i.e., poroelastic material). The element type used in the modeling consisted of a nine-node axisymmetric element, shown in Figure 5-19. The nodes have four degrees of freedom corresponding to fluid and solid displacements in the X and Y directions. Only the four corner nodes of each element have the 5^{th} additional pore pressure degrees of freedom (i.e., nodes 1, 2, 3, 4).

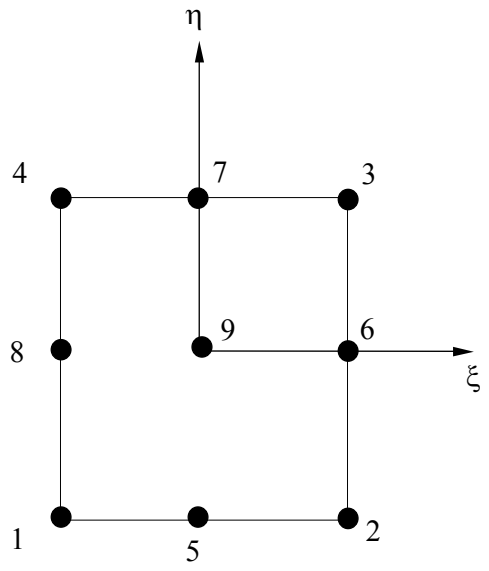

Figure 5-19. A diagram of a nine-node axisymmetric element.

The material properties used as input properties for the model were obtained from prior laboratory test results performed on the GA-C1 mixture at 40° C. The permeability was obtained from falling head testing of the mixture performed with the FDOT permeameter. The Young's modulus was obtained from prior complex dynamic modulus test results at a testing frequency of 0.33 Hz.

Table 5-4 lists the material properties used in the finite element model.

Table 5-4. Material Properties Used for the PlasFEM Finite Element Model

Young' Modulus	Poisson's Ratio	Initial Porosity	Mass Density		Bulk Modulus of the Fluid	Permeability
			Solids	Fluid		
1.0E6 kN/m^2	0.4	0.07	2.0 Mg/m^3	1.0 Mg/m^3	1.0E11 kN/m^2	2.664E-6 m/s

Figure 5-20 shows a comparison between measured and FEM predicted pore pressures for the problem studied. The predicted pore pressures closely match the measured pore pressures from the laboratory testing. The results of finite element modeling of experimentally observed pore pressures show a close match between the modeled and the measured pore pressures. Since the finite element model used is based on effective stress principles, this means that the mixtures tested also behave according to effective stress principles, meaning that pore pressures will directly affect the strength and stiffness of mixtures in the same way that they do for soils and rock. Importantly, this close correspondence between measured and predicted results also indicates that the pore pressure effect may play a significant role in the behavior of mixtures under saturated loading conditions, such as those found in a typical flexible pavement after a rain event.

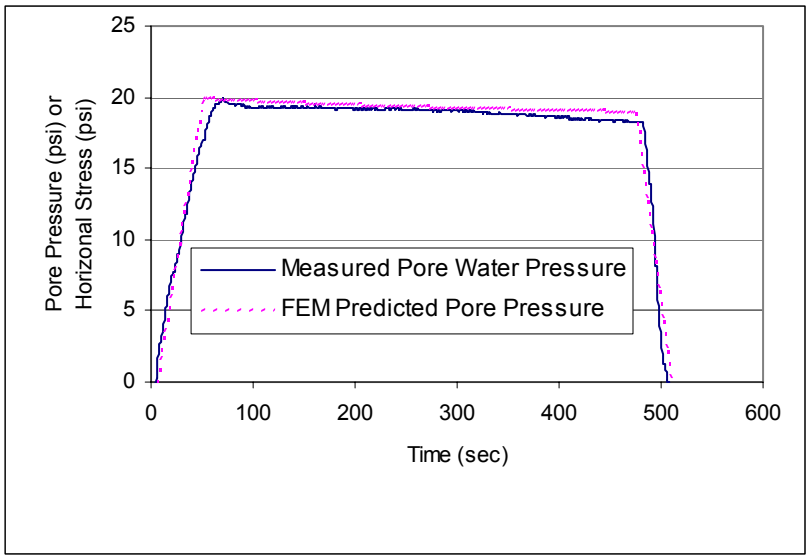

Figure 5-20. Comparison of measured and predicted pore pressure response for mixture GA-C1 at testing temperature of 40° C.

5.8 Summary and Conclusions

In this chapter, the pore pressure response of mixtures under static and cyclic triaxial loading conditions was studied. In particular, the following topics were studied: 1) pore pressure response of saturated mixtures undergoing static triaxial testing; 2) pore pressure response of saturated and partially saturated mixtures undergoing complex modulus testing; and 3) finite element modeling of pore pressure response of mixtures under idealized loading conditions.

The results presented clearly show that the mixtures tested exhibit a significant pore pressure response, which may greatly affect the response of saturated and partially saturated mixtures over dry mixtures. The results of finite element modeling of experimentally observed pore pressures show a close match between the modeled and the measured pore pressures. Since the finite element model used is based on effective stress principles, this means that the mixtures tested also behave according to effective stress principles, meaning that pore pressures will directly affect the strength and stiffness of mixtures in the same way that they do for soils and

rock. Importantly, this close correspondence between measured and predicted results also indicates that the pore pressure effect may play a significant role in the behavior of mixtures under saturated loading conditions, such as those found in a typical flexible pavement after a rain event.

For the complex dynamic modulus test, a pore pressure response that is significant enough is exhibited to affect and in some cases overwhelm the complex dynamic modulus response in a dry state of these mixtures. Importantly, since pore pressures are a function of the void structure of mixtures, these pore pressure effects are highly likely to change from one mixture to another, based on the gradation and the mixture volumetric properties.

In conclusion, the presence of moisture in mixtures will greatly affect the strength and modulus of mixtures. Therefore, it may be important to account for pore pressures in mixtures during moisture conditioning. Also of key importance is ensuring that all mixtures are brought to a constant dry condition under constant humidity conditions before any type of performance testing to evaluate moisture damage in mixtures.

5.9 References

ASTM (American Society for Testing and Materials). *Annual Book of ASTM Standard*s: *D 3497: Vol. 4.20*, ASTM, Philadelphia, 1997.

Cooley, L.A., Brown, E., and Maghsoodloo, S., "Development of Critical Field Permeability and Pavement Density Values for Coarse-Graded Superpave Pavements," *NCAT Report No. 01-03*, 2001.

Lambe, T.W., and Whitman, R.V., *Soil Mechanics*, John Wiley & Sons, Inc., New York, 1969.

NCHRP (National Cooperative Highway Research Program), *1-37A-2002 Design Guide* (Draft), NCHRP, Transportation Research Board, Washington, D.C., 2004.

Pinto, Paulo. Coupled Finite Element Formulations for Dynamic Soil-Structure Interaction. Ph.D. Dissertation, University of Florida, Gainesville, 1998.

Witczak, M.W., Bonaquist, R., Von Quintus, H., and Kaloush, K., "Specimen geometry and aggregate size effects in uniaxial compression and constant height shear tests," *Proceedings*, Association of Asphalt Paving Technologists (AAPT), Vol. 69, pp. 733-793, 2000.

Witczak, M.W., Pellinen, T.K., and El-Basyouny, M.M., "Pursuit of the simple performance test for asphalt concrete fracture/cracking," *Journal of the Association of Asphalt Paving Technologists*, Vol. 71, pp. 767-778, 2002.

CHAPTER 6
EVALUATION OF WATER DAMAGE USING HOT MIX ASPHALT FRACTURE MECHANICS

6.1 Background

Moisture damage in hot-mix asphalt (HMA) mixtures occurs when water can infiltrate the pavement system. Pore water in mixtures can cause premature failure of hot-mix asphalt pavements, primarily through loss of adhesion between the asphalt binder and the aggregates or the loss of cohesion in the asphalt binder (Parker and Gharaybeh 1987). Loss of adhesion can lead to stripping and raveling. Loss of cohesion can lead to a weakened pavement that is susceptible to pore pressure damage and premature cracking (Kandhal 1994; Kandhal and Rickards 2001). In a real pavement, the mechanisms causing pore pressure damage, cohesion damage, and adhesion damage are likely present and not easily separable. These same mechanisms are also active during laboratory conditioning, but not necessarily to the same degree as in the field. Based on the results obtained in Chapters 4 and 5, it is clear that mixtures illustrate pore pressure effects that may greatly affect performance-testing results, including both strength and stiffness. In addition, there is a strong need to identify a theoretical framework for the analysis of moisture damage in mixtures that is not susceptible to the added variability associated with pore pressure effects during testing. In order to identify and isolate damage effects in mixtures, it is always desirable to test the mixture under tensile loading conditions. During tension, damaged sections within the mixture are strain further, and microcracks are opened up, hence enhancing the ability to identify these effects in mixtures.

The laboratory testing procedures currently available for testing HMA moisture susceptibility were primarily developed to determine the degree of resistance to moisture damage by a particular combination of asphalt and aggregate, compare mixes composed of different types and quantities of aggregate, or to evaluate the effectiveness of antistripping agents (Lottman 1982;

Tunnicliff and Root 1984; Curtis et al. 1992; Al-Swailmi and Terrel 1992; Terrel and Al-Swailmi 1994). These moisture susceptibility tests all evaluate the effects of water damage in the laboratory by measuring the relative change of a single parameter before and after conditioning (i.e., Tensile Strength Ratio, Resilient Modulus Ratio). These parameters do not distinguish between the different mechanisms present in a conditioned mixture, including the identification of the effects of pore water versus actual moisture damage.

Depending on materials, loading, and environment, it may be that one or all of the mechanisms of water damage are present and dominant in an actual pavement. However, for a proper evaluation of any given mixture and testing procedure, it is necessary to isolate and quantify the effects of each of the predominant mechanisms contributing to moisture damage. In fact, the lack of delineation between pore water effects and actual moisture damage may lead to erroneous conclusions. Water damage effects in HMA pavements may be bracketed by two extreme conditions: 1) the rapid application of cyclic pore pressures under saturated conditions that correspond to critical field conditions, and 2) the longer term continuous low level exposure to water without pore pressures. This chapter focuses on the second category, namely the characterization of damage caused by a longer-term exposure of mixtures to water without the presence of pore pressures.

Based on the results obtained from the monitoring of small strain modulus with saturation level using the ultrasonic pulse wave velocity test in Chapter 4, Superpave IDT creep, resilient modulus, and strength tests were performed on conditioned and unconditioned mixtures without the complicating effects of the presence of pore water. Finally, a limited number of Hamburg Loaded Wheel Tests were performed to provide a comparison to the Superpave IDT test results. The results illustrate the effects of moisture damage on the fracture properties of mixtures and

the influence of aggregate type and gradation characteristics on moisture damage susceptibility. Water damage in mixtures is complicated by aggregate structure and aggregate type, meaning that each mixture property is affected differently and to different degrees by water damage from one mixture to another. The evaluation of water damage needs to account for these different effects in a consistent, unified manner. Based on the results in this paper, the use of a single parameter to evaluate moisture damage must be questioned. Rather, a single unified framework that accounts for changes in key mixture properties is needed to effectively evaluate the effects of water damage in mixtures. One such framework is the HMA fracture mechanics framework, developed at the University of Florida (Zhang et al. 2001; Roque et al. 2002).

The HMA fracture mechanics framework is used to integrate the varying effects of water damage on key mixture properties into a single number (ratio of the number of cycles to failure after and before conditioning) that reflects the change in the cracking performance of the mixture due to water conditioning. The results show that HMA fracture mechanics provides a rational framework for the evaluation of moisture damage in mixtures that accounts for changes in multiple parameters, not just a single parameter. Importantly, the approach presented can be used to evaluate the effects of water damage, independent of the conditioning procedure. Using a consistent framework for evaluating the detrimental effects of water damage, the effects of various different conditioning procedures can also be evaluated more thoroughly.

6.2 Objectives

This chapter focuses on the evaluation of moisture and moisture damage effects on mixtures with different aggregate characteristics and gradations. Using a number of mixtures of different void structure and aggregate characteristics, the objectives of this research were to:

- Determine the effects of water damage on the cracking parameters of mixtures, without the complicating effects of pore pressures during testing.
- Evaluate the use of the HMA fracture mechanics framework developed at the University of Florida to quantify the effects of moisture damage in mixtures.
- Compare results obtained from the Hamburg Loaded Wheel Test to those obtained from the Superpave IDT and the HMA fracture mechanics framework.
- Evaluate the effects of aggregate structure and aggregate type on water damage.
- Make appropriate recommendations regarding the testing of water damage in mixtures, including environment and time of testing, and relevant mixture properties.

6.3 Scope

The chapter addresses the effects of aggregate gradation and aggregate type on the water damage of mixtures. The use of the HMA fracture mechanics framework developed at the University of Florida (Zhang et al. 2001; Roque et al. 2002) is evaluated for quantifying the effects of water damage in mixtures.

The research approach essentially involved evaluating the effects of changes in mixture gradations, pore structure, and aggregate type on:

- Moisture damage effects without pore water effects in terms of:
  - Tensile Strength
  - Resilient Modulus
- Moisture damage effects using the HMA fracture mechanics framework developed at the University of Florida using:
  - Creep Compliance and m-value from Superpave IDT creep test.

- Fracture energy limit, dissipated creep strain energy limit, and number of cycles to failure under tensile fracture conditions.
- Compare results to those obtained with an established torture test like the Hamburg Loaded Wheel Tester.

6.4 Materials and Methodology

6.4.1 Aggregate Selection

Two groups of aggregates were used. The first consisted of an oolitic limestone aggregate that has in the past not shown significant stripping potential, and the second consisted of crushed granite from Georgia and Nova Scotia that have shown potential for stripping. Both aggregate groups are used extensively in Florida and are considered to be excellent materials resulting in well-performing mixtures.

6.4.2 Specimen Preparation and Testing

Laboratory Investigation. The oolitic limestone mix was made up of four components: coarse aggregate, fine aggregate, screenings, and mineral filler. They were blended together in different proportions to provide six HMA mixtures of coarse and fine gradations (Nukunya 2001; Nukunya et al. 2001). Two previously designed Superpave mixtures prepared by the Florida Department of Transportation (FDOT), one coarse-graded (C1) and one fine-graded (F1), were used as the basis for the research. Two more gradations were then produced by changing the coarse portions (larger than no. 8 sieve size) of the gradations to produce job mix formulas with substandard void structure and permeability. The purpose of this was to test the effects of gradation, permeability, and other volumetric properties on the durability related water damage of HMA. Secondly, the fine portion of the gradation curve was changed to produce more gradations of variable void structure

and permeability. In all, six oolitic limestone mixtures were produced: C1, C2, and C3, for the coarse gradations and F1, F2, and C4/F3 for the fine gradations. The C4/F3 mixture was derived from the fine mixture (F1), but had to be adjusted to fall below the restricted zone to achieve a higher permeability. Thus, it is really a coarse graded mixture, so it was given a dual classification. The resulting gradations are shown in Table 6-1 (a), with C1 and F1 being the two FDOT gradations. The mixtures ranged from what could be described as fine uniformly-graded and fine dense-graded to coarse uniformly-graded and coarse gap-graded. In addition, six Georgia granite mixtures were designed to be volumetrically equivalent to the oolitic limestone mixtures. The Georgia granite mixtures are designated as: GA-C1, GA-C2, GA-C3, GA-F1, GA-F2, GA-C4/F3. The gradations for the Georgia granite mixtures are listed in Table 6-1 (b).

Table 6-1. Gradations for Mixtures

(a) Limestone Mixtures

	Percent Passing					
Sieve Size	C1	C2	C3	F1	F2	C4/F3
19 mm (3/4)	100	100	100	100	100	100
12.5 mm (1/2)	97	91	98	96	91	95
9.5 mm (3/8)	90	74	89	85	78	85
4.75 mm (#4)	60	47	57	69	61	67
2.36 mm (#8)	33	30	36	53	44	37
1.18 mm (#16)	20	20	24	34	35	26
600 μm (#30)	15	14	18	23	24	20
300 μm (#50)	11	10	13	15	16	14
150 μm (#100)	7.6	6.7	9.2	9.6	9.1	8.6
75 μm (#200)	4.8	4.8	6.3	4.8	6.3	5.8

(b) Georgia Granite Mixtures

	Percent Passing					
Sieve Size (mm)	GA-C1	GA-C2	GA-C3	GA-F1	GA-F2	GA-C4/F3
19.0	100.0	100.0	100.0	100.0	100.0	100.0
12.5	97.4	90.9	97.3	94.7	90.5	94.6
9.5	89.0	72.9	89.5	84.0	77.4	85.1
4.75	55.5	45.9	55.4	66.4	60.3	65.1
2.36	29.6	28.1	33.9	49.2	43.2	34.8
1.18	19.2	18.9	23.0	32.7	34.0	26.0
0.60	13.3	13.2	16.0	21.0	23.0	18.1
0.30	9.3	9.2	11.2	12.9	15.3	12.5
0.15	5.4	5.6	6.8	5.9	8.7	7.7
0.075	3.5	3.9	4.7	3.3	5.4	5.8

The other granite mixtures consisted of three mixtures commonly used by the FDOT. The first two mixtures consisted of Georgia granite, Florida limestone, and recycled asphalt pavement (RAP). One mixture was a coarse 12.5-mm nominal maximum aggregate size (SP2) and the other was a coarse 19-mm nominal maximum aggregate size (SP3). The third granite mixture (NS315) is a coarse 19-mm nominal maximum aggregate size mixture consisting of Nova Scotia granite. The gradations for these other granite mixtures, are shown in Table 6-2.

Design asphalt contents for all the limestone and granite mixtures were determined such that each mixture had 4 percent air voids at N_{design} = 109 revolutions. Finally, PG 67-22 (AC-30) asphalt was used for all limestone and granite mixtures in this study.

The following tests and analyses were performed:

- Mixtures were designed according to the Superpave volumetric mix design method. Initial mixtures included existing FDOT limestone and granite mixtures with either 12.5-mm or 19.0-mm nominal maximum aggregate size. Other 12.5-mm limestone mixtures were designed to have gradations of variable void structure and permeability.

Table 6-2. Gradations for Granite Mixtures

Sieve Size	SP-2	SP-3	NS315
25 mm (1)	100	100	100
19 mm (3/4)	98	100	97
12.5 mm (1/2)	89	98	83
9.5 mm (3/8)	84	89	66
4.75 mm (#4)	41	47	38
2.36 mm (#8)	31	25	23
1.18 mm (#16)	24	18	18
600 μm (#30)	17	15	14
300 μm (#50)	13	11	10
150 μm (#100)	9	7	6.5
75 μm (#200)	4	4	3.5

- Mixtures were produced in the laboratory following the procedure outlined in AASHTO T-283. First, the aggregates and asphalt binder were heated to 150 °C (300 °F) for three hours prior to mixing. Once the mixing was completed, the mixture was allowed to cool

to room temperature for two hours. After the cooling period, the loose mixture was long-term aged for 16 hours at 60 °C (140 °F). After the mixture was aged for 16 hours, it was reheated to 135 °C (275 °F) for two hours before compaction. The specimens were then compacted on the IPC Servopac Superpave gyratory compactor to 7-8 percent air voids. A total of 14 samples of each mix were prepared.

- For each mixture, nine samples were subjected to saturation according to the AASHTO T-283 procedure. Throughout the testing, a target saturation level of 65 and 80 percent was maintained. (Changes to AASHTO T-283 in 2003 require a saturation level of 70-80 percent). The saturation procedure called for a vacuum saturation for 15 minutes and then 15 minutes in a water bath without vacuum. If the minimum saturation was not achieved, then another cycle was used until the minimum saturation was achieved.
- The conditioned mixtures were allowed to drain for three days. Then, conditioned and unconditioned specimens were cut, by a wet saw, into 2-inch thick specimens. The specimens were placed in a dehumidifier chamber for 24 hours. This ensured that the surface of the specimen was dry. Superpave IDT was used to perform Resilient Modulus (M_R), Creep Compliance, and Strength tests (NCAT 1996; Roque et al. 1997; Sedwick 1998) from which the following properties were determined: tensile strength, resilient modulus, fracture energy limit (FE), dissipated creep strain energy limit (DCSE), creep compliance, and m-value. The FE and DCSE values and the modulus can be accurately determined using the Superpave Indirect Tensile Test following the procedures developed by Roque and Buttlar, and Buttlar and Roque (Roque and Buttlar 1992; Buttlar and Roque 1994). Using these mixture properties and the HMA fracture mechanics framework developed at the University of Florida, the reduction in the number of cycles to failure

was calculated. Failure was defined as the number of cycles needed to grow a one-inch (25.4-mm) long crack under repeated loading conditions in the Superpave IDT test. This phase of the research focused on the evaluation of the effects of water damage on the actual mixture, as compared to the combined effects of water and damage.

- Two specimens of each Georgia granite mixture (GA-C1, GA-C2, GA-C3, GA-F1, GA-F2, GA-C4/F3), as well as WR-C1 and WR-F1, were prepared according to the AASHTO T-283 procedure, and tested in the Hamburg Loaded Wheel Tester. The testing temperature in the Hamburg Loaded Wheel Test was set at 80° C. The testing was continued until either rut of 12.5 mm depth was measured, or the number of loading cycles reached 20,000.
- Finally, three more specimens of each mixture each were prepared to conduct falling head water permeability testing to evaluate the effects of void structure and access of water to the specimen. Test method and apparatus designation FM 5-565 was designed by FDOT (Choubane et al. 1998; Choubane et al. 2000). The test method covers the laboratory determination of the water conductivity of a compacted asphalt mixture. The method gives a comparison of water permeability between asphalt samples tested in the same manner. The method can be used to test both laboratory compacted cylindrical samples and field core samples.

6.4.3 Mixture Volumetric Properties

Table 6-3 (a) and (b) summarizes the volumetric properties of the mixtures studied. It should be noted that the effective film thickness (EFT) was developed by Nukunya et al. (2001) to account for the nature of the coarse aggregate-to-aggregate contact structure in coarse-graded mixtures.

Table 6-3. Volumetric Properties of Mixtures

(a) Limestone and Granite Mixtures Excluding the Georgia Granite Mixtures

Specimen		C1	C2	C3	F1	F2	C4/F3	SP2	SP3	NS315
Maximum Specific Gravity	Gmm	2.3279	2.3466	2.3486	2.3378	2.3752	2.3466	2.470	2.496	2.455
Specific Gravity of Asphalt	Gb	1.035	1.035	1.035	1.035	1.035	1.035	1.035	1.035	1.035
Bulk Specific Gravity of Compacted Mix	Gmb	2.2349	2.2545	2.2535	2.2436	2.2814	2.2441	2.372	2.419	2.342
Asphalt Content	Pb	6.5	5.8	5.3	6.3	5.4	5.6	5.7	4.9	5.0
Bulk Specific Gravity of Aggregate	Gsb	2.469	2.465	2.474	2.488	2.489	2.469	2.606	2.692	2.608
Effective Specific Gravity of Aggregate	Gse	2.549	2.545	2.528	2.554	2.565	2.537	2.702	2.697	2.651
Asphalt Absorption	Pba	1.320	1.323	0.897	1.074	1.229	1.129	0.701	0.702	0.610
Effective Asphalt Content of Mixture	Pbe	5.266	4.554	4.451	5.293	4.238	5.534	5.03	4.18	4.420
Percent VMA in Compacted Mix	VMA	15.4	13.8	13.6	15.6	13.2	14.0	13.3	13.5	15.9
Percent Air Voids in Compacted Mix	Va	3.995	3.925	4.049	4.029	3.949	3.942	3.97	3.08	4.6
Percent VFA in Compacted Mix	VFA	74.058	71.559	70.226	74.170	70.082	71.884	70.3	77.2	71.1
Dust/Asphalt Ratio		0.74	0.83	1.18	0.761	1.16	1.04	0.614	0.816	0.7
Surface Area (m^2/kg)	SA	4.87	4.64	5.68	6.05	6.31	5.64	4.93	4.38	4.01
Theoretical Film Thickness (microns)	FT	11.2	10.1	8.0	9.0	6.9	8.1	9.1	10.0	9.1
Effective Film Thickness (microns)	EFT	39.2	39.3	24.1	19.3	17.1	24.9	38.3	45.5	56.7

Table 6-3. Volumetric Properties of Mixtures–continued

(b) Granite and Limestone Mixtures

Properties	Mixtures					
	GA-C1	GA-C2	GA-C3	GA-F1	GA-F2	GA-C4/F3
Asphalt Content (%)	6.63	5.26	5.25	5.68	4.56	5.14
Specific Gravity of Asphalt	1.035	1.035	1.035	1.035	1.035	1.035
Bulk Specific Gravity	2.345	2.399	2.391	2.374	2.433	2.404
Theoretical Specific Gravity	2.442	2.500	2.492	2.473	2.532	2.505
Air Voids (%)	4.0	4.0	4.1	4.0	3.9	4.0
Voids in Mineral Aggregate (%)	18.5	15.4	15.7	16.6	13.6	15.1
Voids filled with Asphalt (%)	78.5	73.8	74.2	75.9	71.2	73.3
Effective Specific Gravity of Aggregate	2.710	2.719	2.709	2.706	2.725	2.720
Absorbed Asphalt (%)	0.3	0.4	0.3	0.3	0.5	0.5
Effective Asphalt (%)	6.3	4.9	5.0	5.4	4.1	4.7
Dust to Asphalt Ratio	0.6	0.8	0.9	0.6	1.2	1.2
Surface Area (m^2/kg)	3.3	3.5	4.2	4.1	5.3	4.9
Film Thickness theoretical, microns	19.9	14.3	12.1	13.4	7.7	9.9

6.5 Use of the HMA Fracture Mechanics for Evaluating Water Damage in Hot Mix Asphalt Mixtures

Previous work by Zhang et al. (2001) has shown that the fracture properties of mixtures can be described within a viscoelastic fracture mechanics-based framework, entitled "HMA Fracture Mechanics," developed at the University of Florida. The implication with the work presented by Zhang et al. (2001) is that it may not be sufficient to monitor changes in a single parameter such as strength or stiffness to evaluate the effects of micro- and macro-damage in mixtures. Rather, changes in stiffness and strength are typically accommodated by changes in the viscoelastic properties of mixtures, as well as strength and stiffness.

In the following the effects of moisture conditioning in mixtures will be evaluated using HMA fracture mechanics. The basic components of the HMA fracture mechanics framework will be reviewed briefly, followed by the application of HMA fracture mechanics for evaluating the water damage in HMA mixtures.

6.5.1 Threshold Concept

The concept of the existence of a fundamental crack growth threshold is central to the HMA fracture mechanics framework presented by Zhang et al. (2001). The concept is based on the observation that micro-damage (i.e., damage not associated with crack initiation or crack growth) appears to be fully healable, while macro-damage (i.e., damage associated with crack initiation or growth) does not appear to be healable. This indicates that a damage threshold exists below which damage is fully healable. Therefore, the threshold defines the development of macro-cracks, at any time during either crack initiation or propagation, at any point in the mixture. As shown in Figure 6-1, if loading and healing conditions are such that the induced energy does not exceed the mixture threshold, then the mixture may never crack, regardless of the number of loads applied.

As discussed by Roque et al. (2002), fracture (crack initiation or crack growth) can develop in asphalt mixtures in two distinct ways, defined by two distinct thresholds (Figure 6-2). First (case 1), continuous repeated loading using stresses significantly below the tensile strength would lead to cracking if the rate of damage accumulation exceeds the rate of healing during the loading period. The energy threshold associated with this case is lower than the threshold required to fracture the mixture with a single load application. Second (case 2), fracture would occur if any single load applied during the loading cycle exceeds the threshold required to fracture the mixture with a single load application. Finally, case 3 shows that fracture would not occur during a single load application unless the upper threshold is exceeded, even when the lower threshold is exceeded.

It has been determined that the dissipated creep strain energy (DCSE) limit and the fracture energy limit (FE) of asphalt mixtures suitably define the lower and upper threshold values

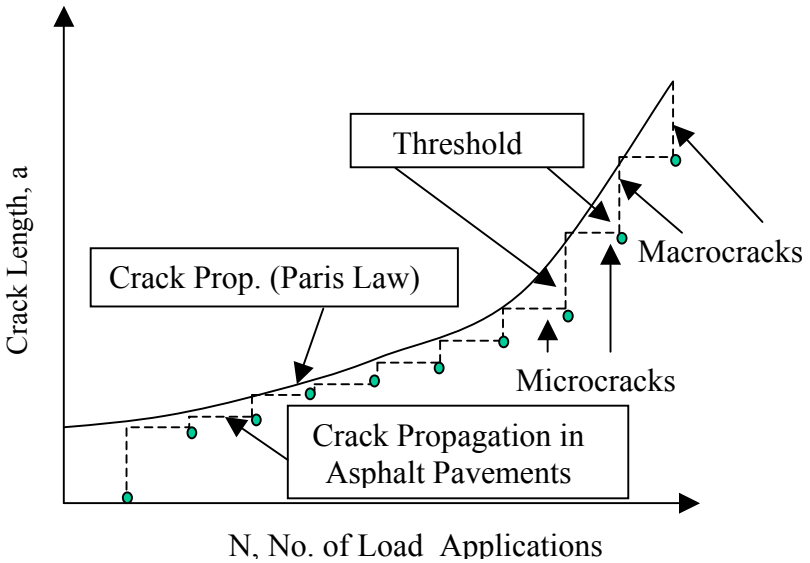

Figure 6-1. Illustration of crack propagation in asphalt mixtures.

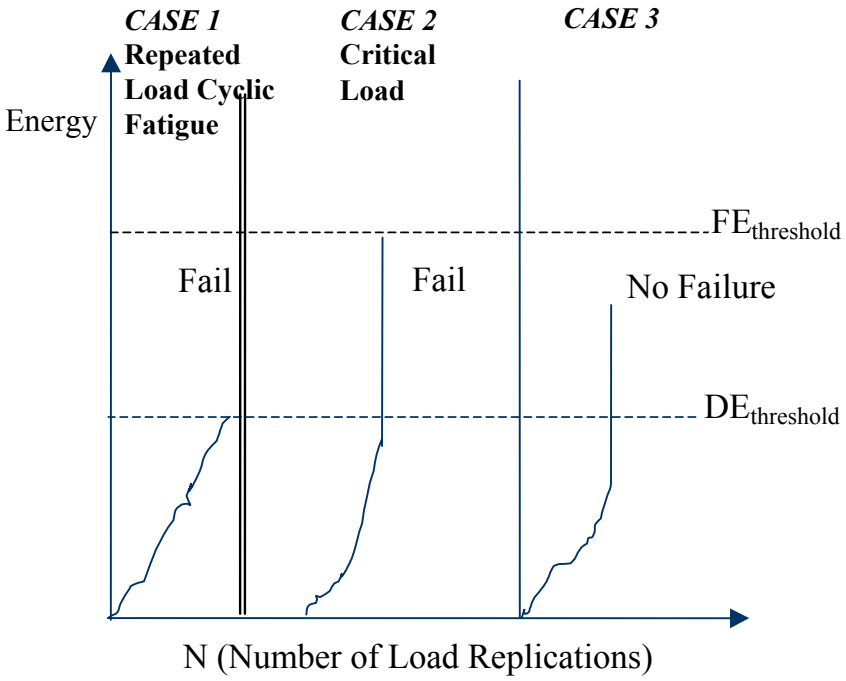

Figure 6-2. Illustration of potential loading condition (continuous loading).

for cases 1 and 2, respectively. These parameters can be easily determined from the stress-strain response of a tensile strength test, as shown in Figure 6-3, and discussed by Roque et al. (2002). It is necessary to know the elastic modulus of the mixture to determine the elastic energy at fracture. Thus, the FE limit and the DCSE limit account indirectly for the effects of strength, stiffness, strain to failure, as well as the viscoelastic response of mixtures.

6.5.2 Key HMA Fracture Mechanics Mixture Parameters

Based on the HMA fracture mechanics framework, there are four key parameters that govern the cracking performance of asphalt mixtures:

- FE limit: fracture energy at the initiation of fracture
- DCSE limit: dissipated creep strain energy to failure
- m-value: parameter governing the creep strain rate
- h: healing rate parameter.

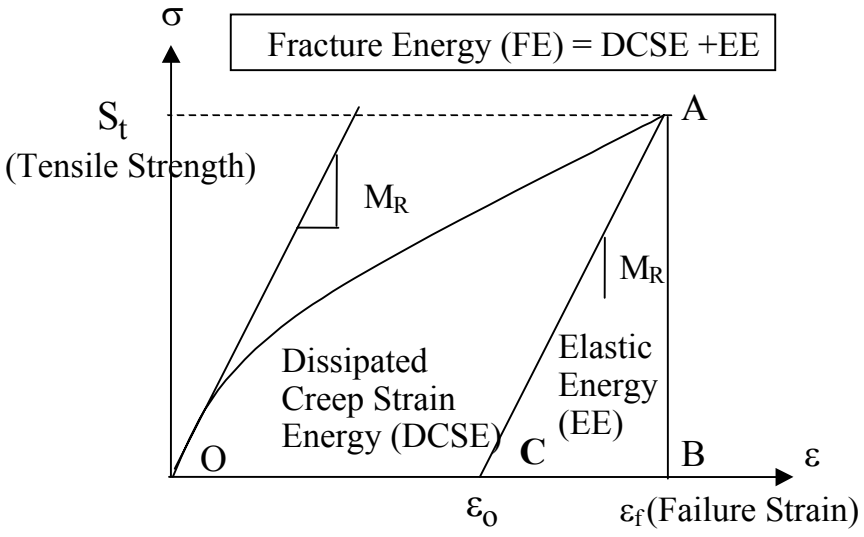

Figure 6-3. Determination of dissipated creep strain energy.

In addition, mixture stiffness, as described by modulus, will affect stress distribution in the pavement system. Figure 6-4 shows the effects of m-value on the rate of damage accumulation. The higher the m-value, the faster is the rate of accumulation of DCSE per cycle, and thus the faster the DCSE limit is reached. Similarly, the healing rate parameter, h, inversely affects the rate of DCSE per cycle. These parameters can be used not only to predict damage and crack growth in mixtures subjected to generalized loading conditions, but they are also suitable for use in the evaluation of changes in mixture performance due to water damage. For example, it is clear that cracking performance deteriorates as the DCSE limit decreases. Similarly, a lower m-value will result in a lower rate of damage accumulation. However, a lower m-value does not necessarily assure improved cracking performance, since mixtures with lower m-values may also have lower DCSE limits and lower rates of healing.

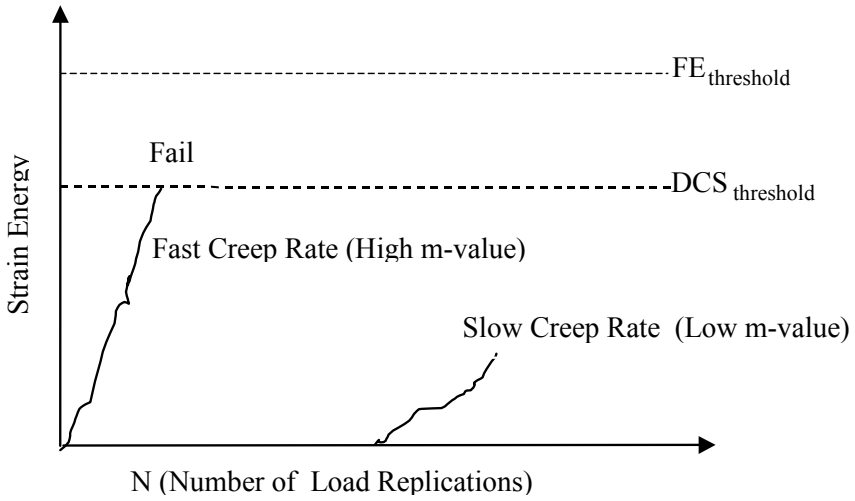

Figure 6-4. Effects of rate of creep and m-value on rate of damage.

6.5.3 HMA Fracture Mechanics Crack Growth Law

The HMA crack growth law developed by Zhang et al. (2001) makes use of fracture mechanics theory along with the threshold concept and limits presented above. The basic elements of the law are illustrated in Figure 6-5, which shows a generalized stress distribution in the vicinity of a crack subjected to uniform tension. The specific stress distribution for a given loading condition will depend on several factors, including crack geometry and the failure limits of the specific mixture. The HMA fracture mechanics framework defined the area in front of

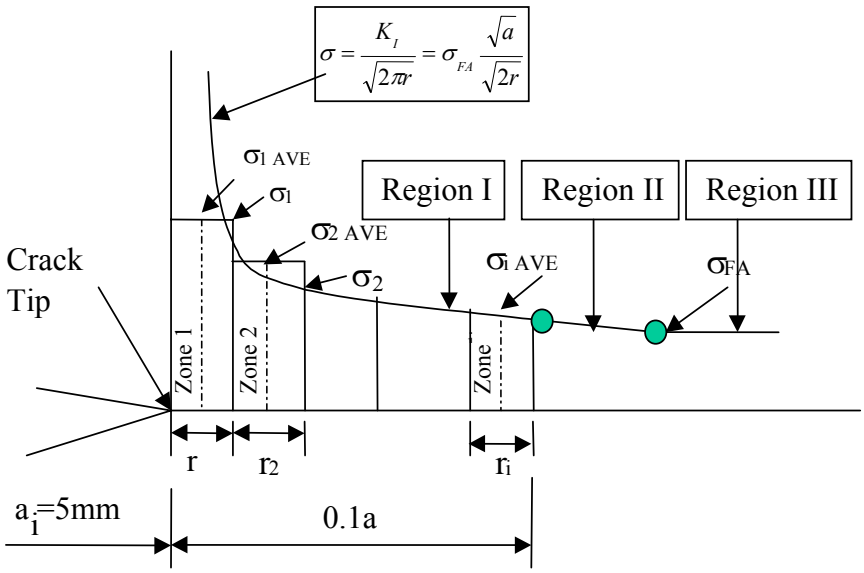

Figure 6-5. Stress distribution near the crack tip.

crack tip where stress reaches a maximum limit as a "process zone." The crack will propagate by the length of the process zone when strain energy representing damage in that zone exceeds the appropriate energy threshold. The details of the development of the crack growth law are discussed by Zhang et al. (2001).

Once a crack initiates, the length of the zone of maximum stress is predicted using fracture mechanics (Zhang et al. 2001; Dowling 1993). The HMA fracture model describes discontinuous crack growth by increasing the crack length in increments equal to the length of each crack zone, shown in Figure 6-5 (Zhang et al. 2001). The crack will advance if the accumulated dissipated creep strain energy limit in the zone exceeds the dissipated creep strain energy limit of the mixture. The details of the development of the crack growth law presented are discussed by Zhang et al. (2001).

6.5.4 Simplified HMA Fracture Mechanics Crack Growth Law Calculations Using a Spreadsheet

To evaluate the effects of water damage in mixtures using the HMA fracture mechanics framework, the number of cycles to grow a one-inch (25.4-mm) long crack under cyclic loading conditions in the Superpave IDT test is calculated for unconditioned and conditioned mixtures. The reduction in the number of cycles to failure due to conditioning is a measure of the reduction in the fracture resistance of the mixture due to water damage. To perform these calculations, a cyclic load has to be assumed. In this paper, the load is assumed to be haversine, with a 0.1 second loading period and a 0.9 second rest period. The magnitude of the load is taken as 1320 lbs, which corresponds to a uniform tensile stress in the center of the IDT specimen of 140 psi under uncracked conditions. This load was found to be high enough to minimize any complicating effects of healing during testing (Zhang et al. 2001). Subsequently, the ratio of the number of cycles to failure for conditioned and unconditioned specimens is calculated to evaluate the effects of water damage on mixtures. The fracture energy limit (FE) and the dissipated creep strain energy limit (DCSE) are obtained from a Superpave IDT strength test, as discussed previously. The tensile creep properties, including the m-value are obtained from a 100 second Superpave IDT creep test.

In order to calculate the number of cycles to grow a one-inch long crack, it is necessary to calculate the creep strain energy per cycle and the accumulated creep strain energy. The accumulated creep strain energy can be easily calculated using creep compliance parameters and the characteristics of the applied load, as discussed by Zhang et al. (2001) for any tensile loading condition. In the following, the focus will be on the calculation of the accumulated creep strain energy obtained from the Superpave IDT creep test.

For a haversine load applied in 0.1 seconds, the dissipated creep strain energy per cycle is determined as:

$$\text{DCSE/cycle} = \int_0^{0.1} \sigma_{AVE} \sin(10\pi t)\ \dot{\varepsilon}_P\ \sin(10\pi t)\, dt \tag{6.1}$$

where σ_{AVE} = average stress in the zone of interest and $\dot{\varepsilon}_P$ = creep strain rate. The creep strain rate can be estimated as the maximum creep strain rate from 100-second Superpave IDT creep tests. Based on the relationship between strain and creep compliance:

$$\varepsilon(t) = \sigma AVE\ D(t) \tag{6.2}$$

where D(t) = creep compliance, which can be represented using the following power function:

$$D(t) = D_0 + D_1\, t^m \tag{6.3}$$

where D_0, D_1, and m are parameters obtained from creep tests. Thus, the rate of creep strain is:

$$\dot{\varepsilon}_P = \sigma_{AVE} \frac{dD(t)}{dt} = \sigma_{AVE}\, D_1\, m\, t^{\,m-1} \tag{6.4}$$

and the maximum rate of creep strain is:

$$\dot{\varepsilon}_{P\,max}(100) = \sigma_{AVE}\, D_1\, m\, (100)^{\,m-1} \tag{6.5}$$

By substitution, one can obtain the dissipated creep strain energy per cycle as follows:

$$\text{DCSE/cycle} = \frac{1}{20}\,\sigma_{AVE}^{2}\,D_1\,m\,(100)^{m-1} \qquad (6.6)$$

Since the DCSE/cycle is now known, the number of cycles to reach the DCSE limit can be determined. Once the DCSE limit is reached, the crack is allowed to grow through the part of the process zone (e.g., zone 1 in Figure 6-5) nearest to the crack tip, and the average tensile stress is updated, and the process is repeated until the 1-inch crack length is reached. This procedure has been implemented into a simple spreadsheet program, where the only required input parameters are:

- M_r and stress-strain curve from a Superpave IDT strength test to calculate the FE and DCSE limits,
- Creep compliance from a Superpave IDT creep test for determining the m-value and D_1 to calculate the DCSE/cycle.

The resulting output from the spreadsheet consists of the number of cycles to failure (i.e., to grow a one-inch (25.4-mm) long crack), for conditioned and unconditioned mixtures. This crack length was selected based on crack propagation studies performed using the Superpave IDT test (Zhang et al. 2001). Details regarding the determination of the stress distributions and average stresses within each zone may be found in the paper by Zhang et al. (2001), and Roque et al. (2002).

6.6 Evaluation of Water Damage Using HMA Fracture Mechanics

In the following, the effects of water damage are isolated and evaluated without the complicating presence of significant pore water effects. First, changes due to moisture conditioning

in individual mixture properties are presented. These mixture properties include the indirect tensile strength, resilient modulus, creep compliance, m-value, fracture energy limit (FE), and dissipated creep strain energy limit (DCSE). For conditioned specimens, all of these properties were obtained from the Indirect Tension (IDT) strength test at 10 °C, at three days after the completion of the T-283 conditioning, as discussed previously. Second, the simplified HMA fracture mechanics-based crack growth law, presented previously, is used to calculate the number of cycles to failure (i.e., number of cycles to grow a one-inch (25.4-mm) long crack) in the center part of the Superpave IDT test for both conditioned and unconditioned specimens.

6.6.1 Tensile Strength and Resilient Modulus Results

In the presence of damage, tensile strength and the resilient modulus should decrease. Figure 6-6 for limestone mixtures and Figure 6-7 for granite mixtures show the effects of water damage on the indirect tensile strength. The very dense-graded C3 mix, and the gap-graded C4/F3 mix show the greatest change in tensile strength with conditioning. Similarly, all the granite mixes show a decrease in tensile strength due to conditioning, which is likely due to the irreversible adhesion damage (stripping) observed previously.

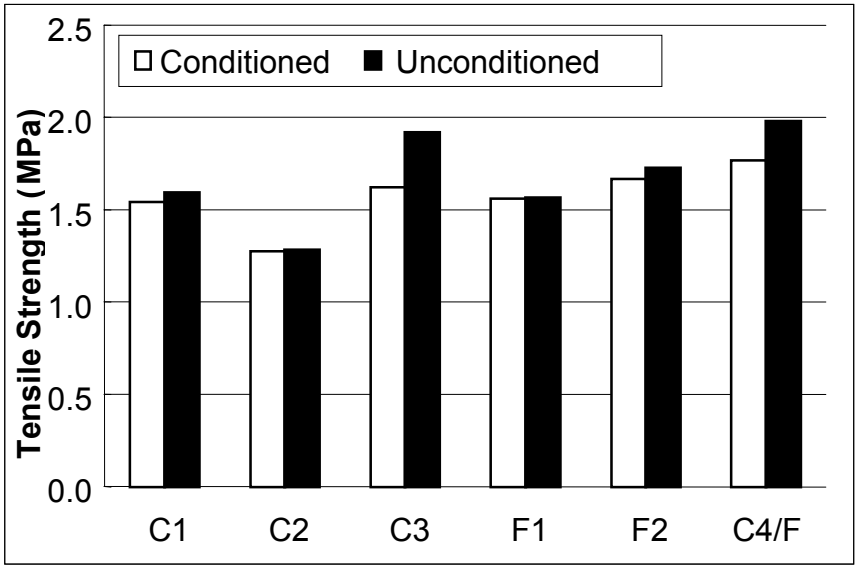

Figure 6-6. A plot of tensile strength for conditioned and unconditioned limestone mixtures.

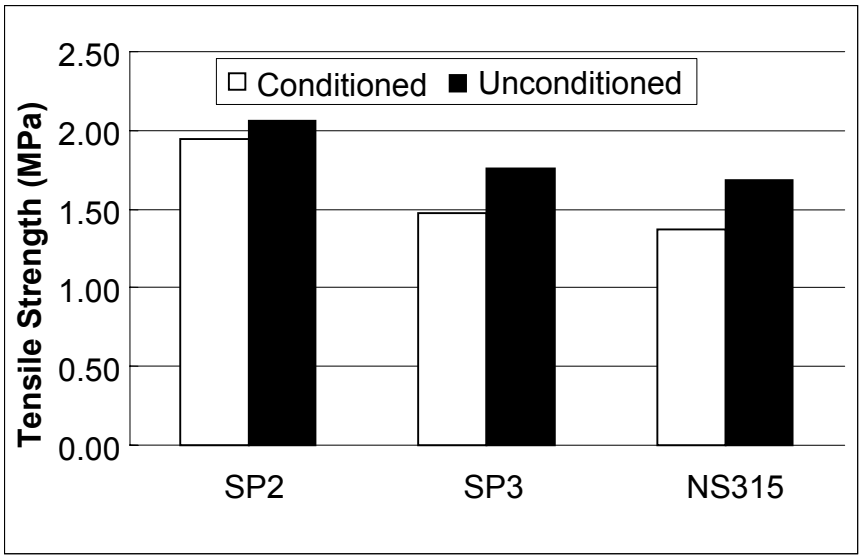

Figure 6-7. A plot of tensile strength for conditioned and unconditioned granite mixtures.

Figures 6-8 and 6-9 show a comparison of the resilient modulus for the mixtures studied. The resilient modulus decreases between the unconditioned and conditioned specimens for all mixtures, implying the presence of damage in all the mixtures. However, differences in response between mixtures of different gradations are hard to decipher from the resilient modulus test data.

6.6.2 Creep Compliance and m-Value Results

Figures 6-10 and 6-11 show the creep compliance for the mixtures. The creep compliance increased for the fine-graded limestone mixtures (F1 and F2), the gap-graded C4/F3 mixture, and the very dense-graded C3 mix, implying a change in the cohesive properties of the mix. Similarly, the granite mixtures all showed an increase in creep compliance, with the heavily stripped NS315 mixture showing the greatest increase in creep compliance.

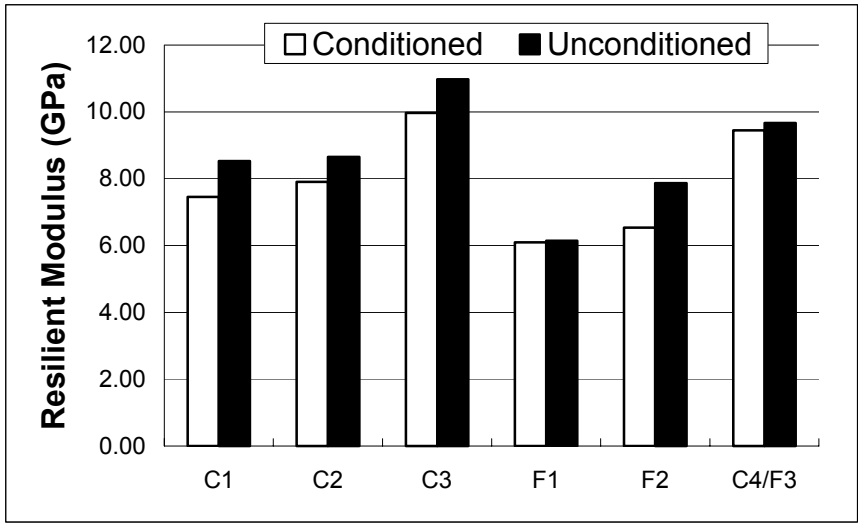

Figure 6-8. A plot of resilient modulus for limestone mixtures.

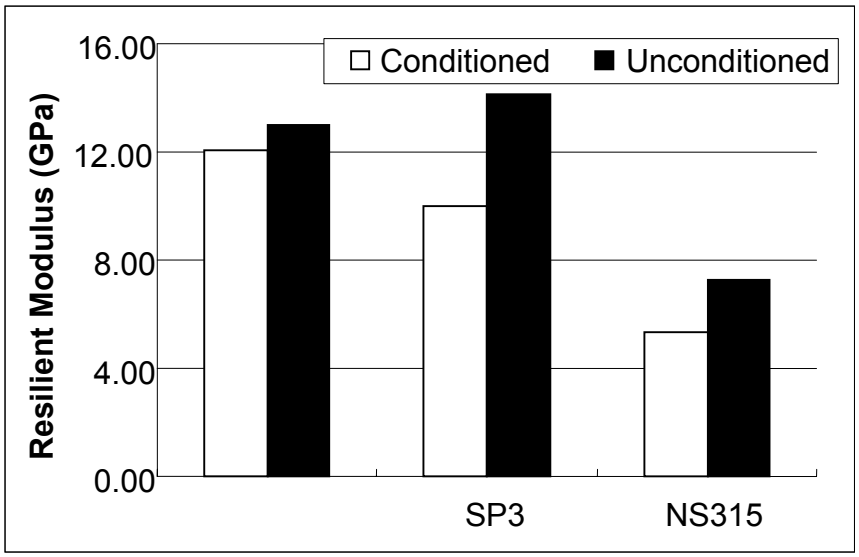

Figure 6-9. A plot of resilient modulus for granite mixtures.

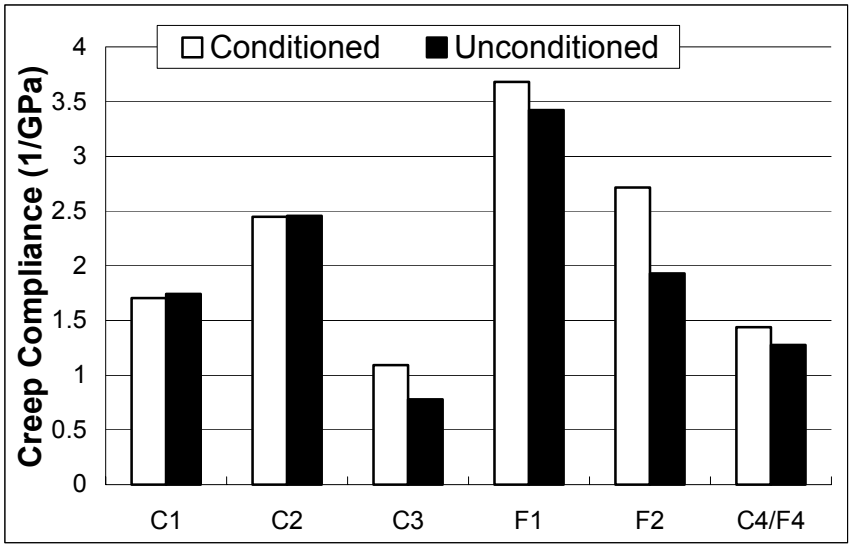

Figure 6-10. A plot of creep compliance for limestone mixtures.

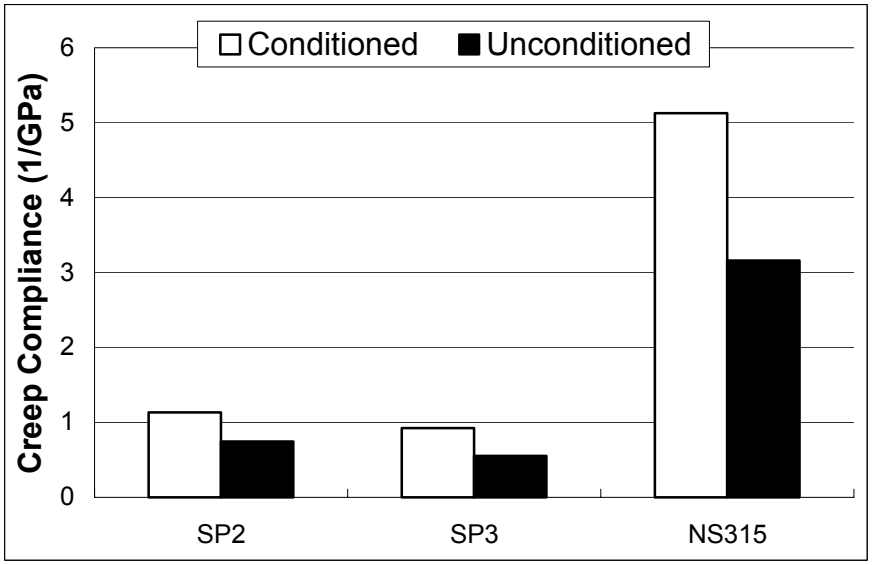

Figure 6-11. A plot of creep compliance for granite mixtures.

Figures 6-12 and 6-13 show the m-values for the mixtures. The fine-graded mixtures (F1 and F2), the gap-graded C4/F3 mix, and the very dense graded C3 mix show an increase in m-value due to moisture conditioning, whereas the coarse-graded mixtures, including the granite mixtures, show a decrease in m-value.

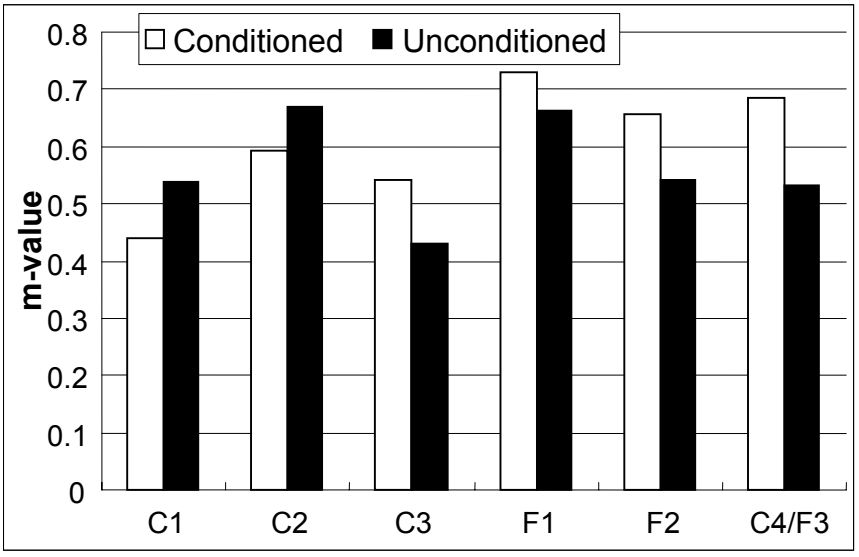

Figure 6-12. A plot of m-value for limestone mixtures.

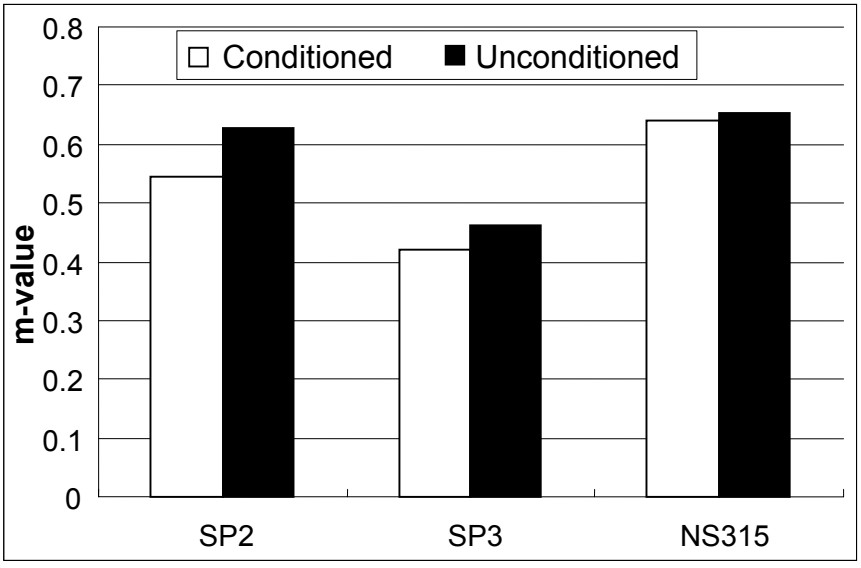

Figure 6-13. A plot of m-value for granite mixtures.

The limestone mixtures C4/F3, C3, F1, F2, most adversely affected by the increase in creep compliance and m-value, are the mixes with the lowest film thickness, resulting in a change in the cohesive properties of these mixtures.

6.6.3 Fracture Energy Limit and Dissipated Creep Strain Energy Limit Results

Figures 6-14 and 6-15 show the fracture energy (FE) limits for the mixtures. The conditioning process does not appear to have affected the fracture energy significantly except for three mixtures, the very dense graded C3, the gap-graded C4/F3 and NS315. The NS315 mixture exhibited large amount of stripping, which may have affected the fracture energy adversely. Similarly, Figure 6-16 and 6-17 show the dissipated creep strain energy (DCSE) limits for the mixtures. The trends are virtually the same as for the fracture energy limits, with the very dense-graded C3, the gap-graded C4/F3, and heavily stripped NS315 showing the largest changes in the DCSE limits.

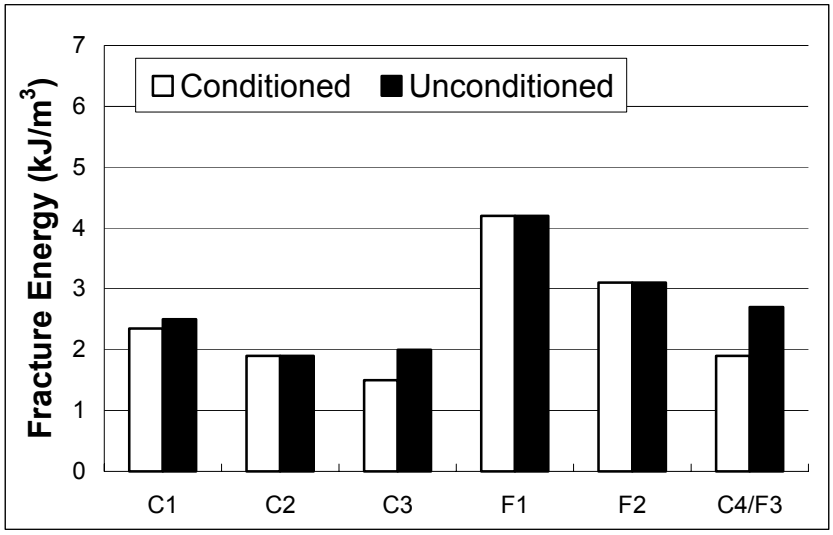

Figure 6-14. A plot of fracture energy for limestone mixtures.

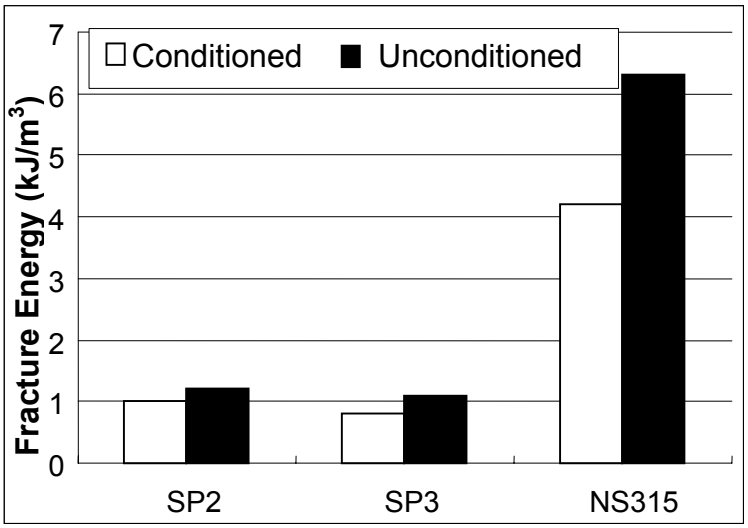

Figure 6-15. A plot of the fracture energy density for granite mixtures.

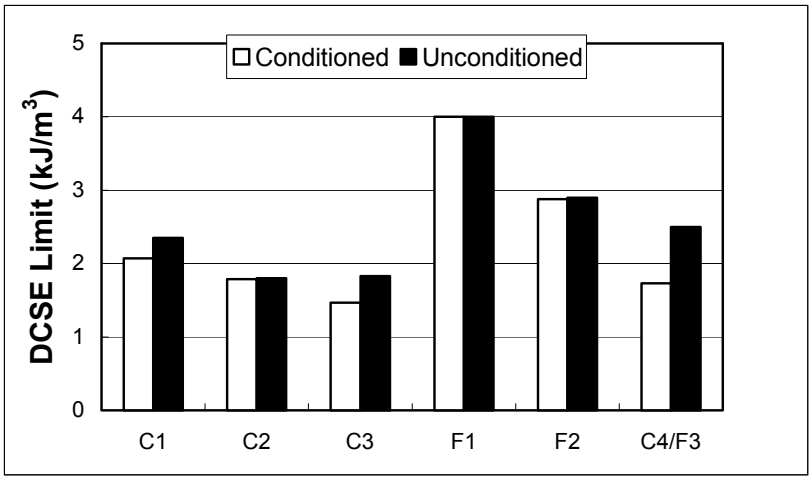

Figure 6-16. A plot of dissipated creep strain energy for limestone mixtures

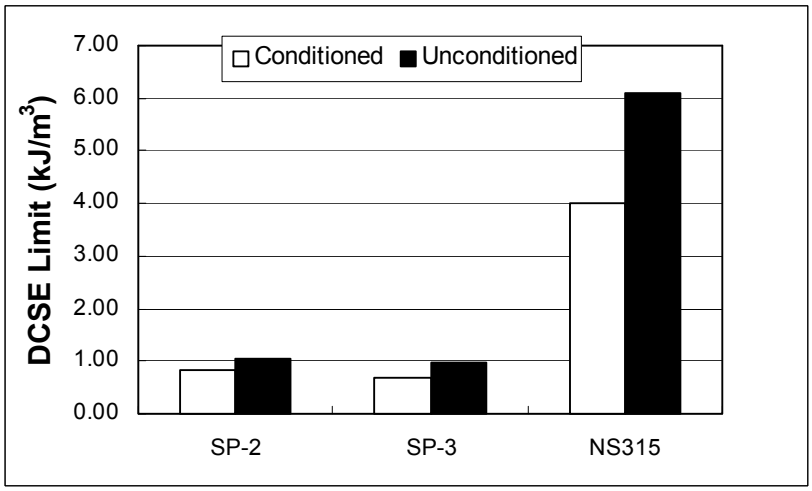

Figure 6-17. A plot of the dissipated creep strain energy density for granite mixtures.

6.6.4 HMA Fracture Mechanics Results

In contrast to focusing on changes in a single parameter due to water conditioning, the simplified HMA fracture mechanics framework for water damage accounts for the interaction of key mixture properties that are related to the cracking performance of mixtures.

Figure 6-18 shows the ratio of calculated number of cycles to failure for conditioned and unconditioned limestone mixtures, using the HMA fracture mechanics framework for water damage evaluations. The results show a significant drop in the number of cycles to failure for the following conditioned limestone mixtures: C4/F3, C3, F1, and F2. The gap graded C4/F3 mix, the very dense-graded C3, and the fine-graded F1, and F2 mixtures are the mixtures with the lowest film thickness (Table 6-3), and were observed to have cohesive moisture damage in the preliminary part of this study. These mixtures with the exception of the gap-graded C4/F3 mix, also had the longest small strain modulus recovery times after conditioning. In contrast, the high film thickness, short recovery time, coarse-graded mixtures (C1 and C2) tend to show virtually no change in the number of cycles to failure, implying negligible lasting moisture damage effects.

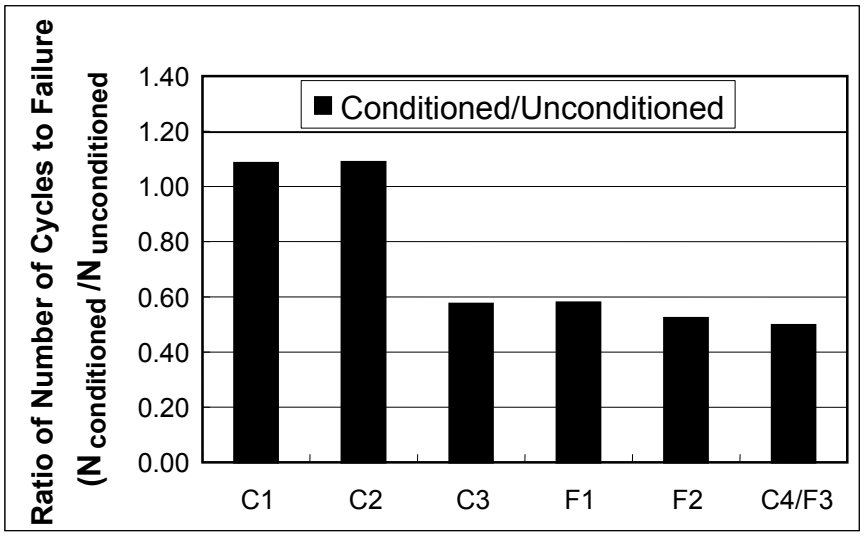

Figure 6-18. A plot of the number of cycles to failure ratio for conditioned and unconditioned limestone mixtures.

Figure 6-19 shows the ratio of the number of cycles to failure for the conditioned and un-conditioned granite mixtures. All granite mixtures showed a decrease in the number of cycles to failure. As expected, the most heavily stripped NS315 mixture shows the largest drop in the number of cycles to failure due to water conditioning.

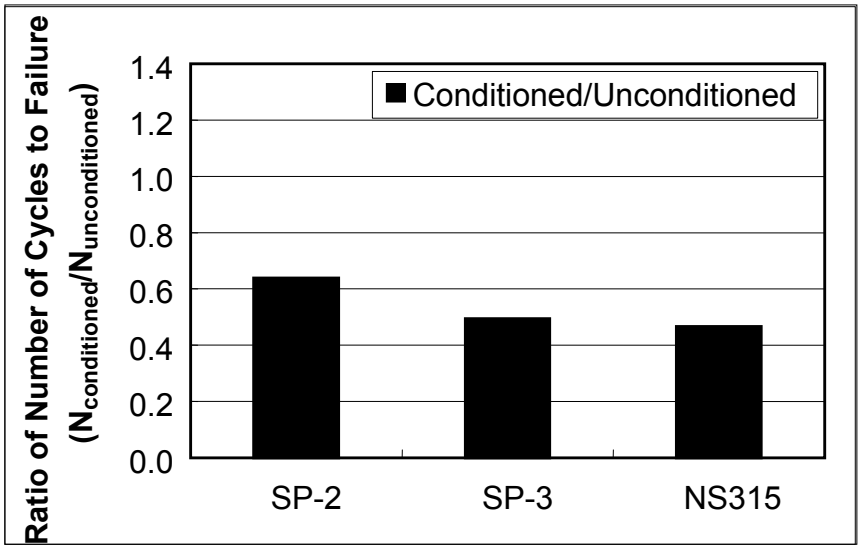

Figure 6-19. A plot of the number of cycles to failure ratio for conditioned and unconditioned granite mixtures.

6.6.5 Discussion of HMA Fracture Mechanics Results

The results from the Superpave IDT resilient modulus, creep, and strength testing show that the effects of water damage on mixtures include changes in multiple parameters, not just a single parameter. Importantly, the viscoelastic properties of mixtures appear are sensitive to water damage, including both cohesive and adhesive (stripping) water damage.

The simplified HMA fracture mechanics framework for water damage evaluation, presented in this paper, provides an approach for the evaluation of moisture damage in mixtures that accounts for changes in multiple parameters, not just a single parameter. Also, the HMA fracture mechanics framework provided results that corresponded well with observed laboratory failure

patterns in Chapter 4. Importantly, all of the mixture properties used can be obtained with 5 minutes of testing with the Superpave IDT test, after conditioning, and specimen preparation and test setup.

The results from using the integrated HMA fracture mechanics approach to evaluate water damage illustrated the effects of aggregate structure on water damage. The limestone mixtures C4/F3, C3, F1, F2, with the lowest film thickness (Table 6-3), are most susceptible to moisture damage, whereas the high film thickness coarse-graded mixtures (C1 and C2) tend to show less moisture damage effects. Similarly, the very dense graded C3 mix, and the F1, and F2 mixes had longer small strain modulus recovery times after conditioning, and therefore were exposed longer to moisture, with the exception of the gap-graded C4/F3 mixture, in which other gradation effects may have decreased the recovery time.

The results also imply that coarse-graded mixtures (e.g., C1 and C2) may be less susceptible to moisture damage than fine-or gap-graded mixtures. The air void structure in coarse-graded mixtures is primarily defined by the large aggregate-to-aggregate contact structure in the mixture, whereas for fine-graded mixtures, the air voids are distributed throughout the mastic. Thus, at the same air void levels, coarse-graded mixtures are likely to have fewer and larger air voids, whereas the fine-graded mixtures tend to have more numerous, but smaller air voids that are distributed throughout the mastic. This means that the total surface area of the air voids in a coarse-graded mixture is generally lower than for a fine-graded mixture, resulting in less of the mastic being exposed to water.

The use of the HMA fracture mechanics framework also showed that the effects of aggregate type dominated the response for the granite mixtures. Despite having a high film thickness (Table 6-3), the fast draining NS315 granite mixture showed a large drop in the number of cycles

to failure with water conditioning, implying that the response of mixtures that predominantly fail due to loss of adhesion and stripping is not controlled by gradation characteristics as much as by the aggregate type.

6.6.6 Comparison of Hamburg Loaded Wheel Tester Results to HMA Fracture Mechanics Results

Table 6-4 lists the results obtained from the Hamburg Loaded Wheel Test. Eight mixtures were tested: All Georgia granite mixtures: GA-C1, GA-C2, GA-C3, GA-F1, GA-F2, GA-C4/F3, and limestone mixtures C1 and C2. In addition, all of the Georgia granite mixtures were tested with and without the presence of a liquid antistripping agent. Table 6-5 (a) and (b) lists the corresponding results from the Superpave IDT test.

Table 6-4. Results from the Hamburg Loaded Wheel Test

Mixture	Number of Cycles to Strip, N_s	Number of Cycles to generate a 12.5 mm rut depth (N_s at 12.4 mm)
Without Liquid Antistripping Agent		
GA-C1	9143	10234
GA-C2	20000 (never reached)	20000 (never reached)
GA-C3	20000 (never reached)	16333
GA-F1	11500	14671
GA-F2	11800	18234
GA-C4/F3	11600	14701
With Liquid Antistripping Agent		
GA-C1	8485	7866
GA-C2	20000 (never reached)	20000 (never reached)
GA-C3	20000 (never reached)	20000 (never reached)
GA-F1	18544	20000 (never reached)
GA-F2	20000 (never reached)	20000 (never reached)
GA-C4/F3	20000 (never reached)	20000 (never reached)
Limestone Mixtures (Without Antistripping Agent)		
C1	18000	20000 (never reached)
F1	7100	20000 (never reached)

Table 6-5. Summary of Mixture Properties

(a) Mixtures Without an Antistripping Additive

Material	Resilient Modulus, M_R (GPa)	Tensile Strength, S_t (MPa)	Fracture Energy (kJ/m^3)	m-value	D_1 (1/psi)	DCSE (kJ/m^3)
GA-C1	5.1	1.44	6.00	0.62	1.74E-06	5.80
GA-C2	8.79	2.00	5.00	0.59	1.06E-06	4.77
GA-C3	9.99	1.99	3.80	0.57	8.70E-07	3.60
GA-F1	8.45	1.93	3.70	0.57	1.30E-06	3.48
GA-F2	10.2	2.52	3.60	0.48	1.58E-06	3.29
GA-F3	9.95	2.14	2.80	0.56	8.97E-07	2.57
WR-C1	8.53	1.59	2.50	0.54	9.51E-07	2.35

(b) Mixtures With an Antistripping Additive

Material	Resilient Modulus, M_R (GPa)	Tensile Strength, S_t (MPa)	Fracture Energy (kJ/m^3)	m-value	D_1 (1/psi)	DCSE (kJ/m^3)
GA-C1	5.335	1.54	8.20	0.57	2.41E-06	7.98
GA-C2	8.45	1.75	6.35	0.54	1.20E-06	6.17
GA-C3	12.75	2.06	4.75	0.53	9.66E-07	4.58
GA-F1	7.78	1.96	5.20	0.58	1.28E-06	4.95
GA-F2	11.26	2.14	4.20	0.50	9.32E-07	4.00
GA-F3	11.99	2.05	3.10	0.53	8.97E-07	2.92

There are primarily two numbers that are reported as results from the Hamburg Loaded Wheel Test. The first one is the number of cycles to strip, N_s, which is defined as the loading cycle where the rate of permanent displacement measured during the test markedly increases, as shown in Figure 6-20. Another number used by some agencies in the United States, including the Texas Department of Transportation, is the number of cycles to reach a 12.5 mm rut depth, herein denoted as N_s at 12.5 mm. Table 6-4 lists both results. It should be noted that the test was stopped after 20000 cycles. Hence, if the number of cycles to strip, N_s, or N_s at 12.5 mm, was not reached before 20000 cycles, the results are simply reported as 20000.

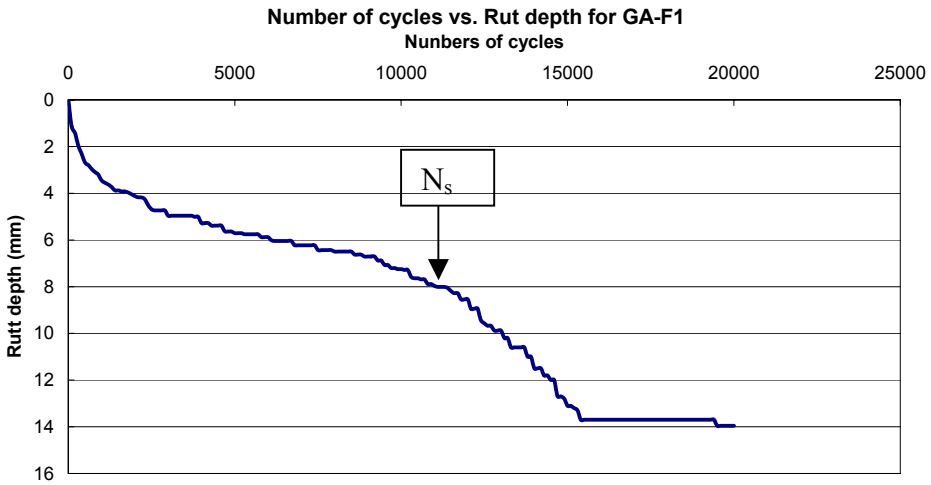

Figure 6-20. Typical results from the Hamburg Loaded Wheel Test showing the number of cycles versus rut depth. The point at which the rate of permanent deformation changes is denoted as the number of cycles to strip, N_s.

Figures 6-21 and 6-22 show a comparison between the number of cycles to strip, N_s, as determined with the Hamburg Loaded Wheel Test and the number of cycles to failure as determined from HMA fracture mechanics, for the Georgia granite mixtures tested. Similarly, Figure 6-23 show a comparison between the N_s at 12.5 mm and the number of cycles to failure as determined from HMA fracture mechanics. Figure 6-21 shows the results for mixtures without liquid antistripping additive and Figure 6-22 shows the results with mixtures containing a liquid antistripping additive. As shown in Table 6-4, most of the mixtures containing liquid antistripping additive, as well as the two limestone mixtures, never reached 12.5 mm rut depth, hence the test was stopped at 20,000 cycles. The results indicate that the both the HMA fracture mechanics framework and the Hamburg Loaded Wheel Test results follow similar trends. A mixture with a high number of cycles to strip generally seems to also show high number of cycles to failure, as determined with HMA Fracture mechanics. However, as shown in Table 6-4, the number of cycles to reach a 12.5 mm rut depth for mixture GA-C1 actually decreased from 10,234 cycles to 7,866 cycles with the addition of a liquid antistripping additive. This

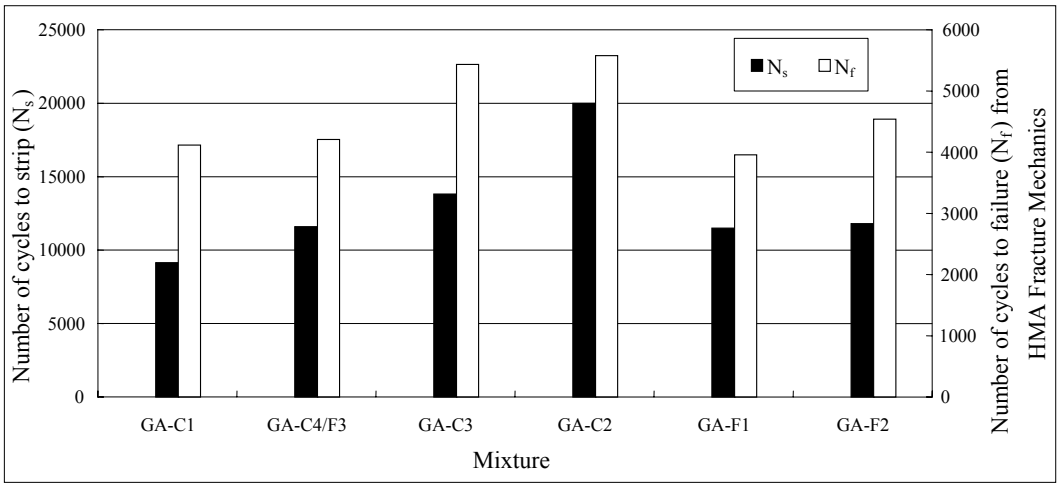

Figure 6-21. A comparison plot of number of cycles to strip from the Hamburg Loaded Wheel Test versus the number of cycles to failure from the HMA fracture mechanics framework for Georgia granite mixtures without liquid antistripping additive.

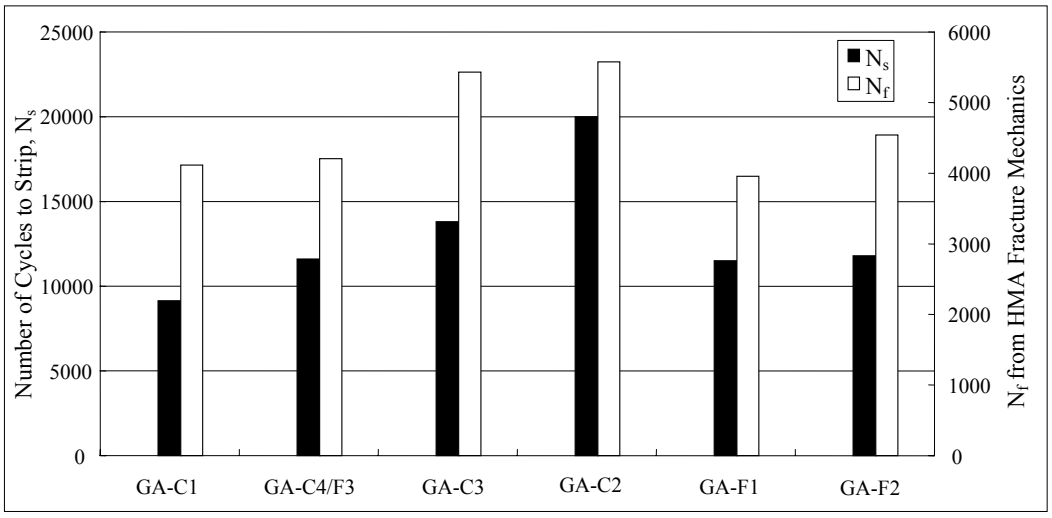

Figure 6-22. A comparison plot of number of cycles to strip from the Hamburg Loaded Wheel Test versus the number of cycles to failure from the HMA fracture mechanics framework for Georgia granite mixtures with liquid antistripping additive.

discrepancy in the Hamburg Loaded Wheel Test is cause for concern, and may be an indicator of the variability of the test. However, based on the overall correspondence between the results from the Hamburg Loaded Wheel Tester and the HMA fracture mechanics framework, it appears that in the absence of the more refined performance-based Superpave IDT testing results, the Hamburg Loaded Wheel Test may potentially serve as a torture test-based surrogate for determining the resistance of mixtures to moisture damage.

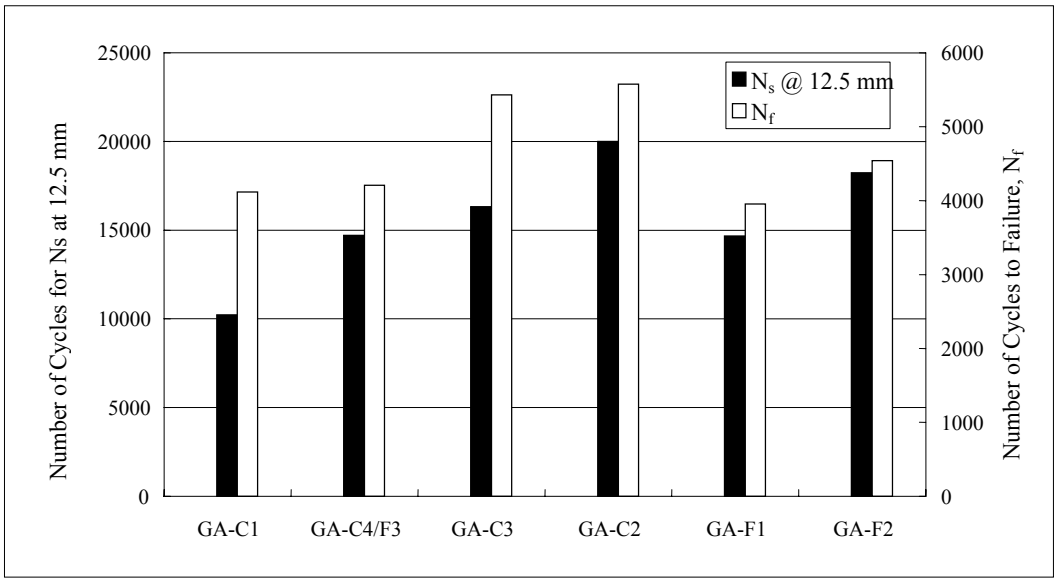

Figure 6-23. A comparison plot of number of cycles to cause a rut of 12.5 mm (N_s at 12.5 mm) from the Hamburg Loaded Wheel Test versus the number of cycles to failure from the HMA fracture mechanics framework for Georgia granite mixtures without liquid antistripping additive.

6.7 Summary and Conclusions

The summary and conclusions based on the findings of this research are presented as follows:

- The results from the Superpave IDT resilient modulus, creep, and strength testing show that the effects of water damage on mixtures include changes in multiple parameters, not just a single parameter. Importantly, the viscoelastic properties of mixtures appear are sensitive to water damage, including both cohesive and adhesive (stripping) water damage.
- The simplified HMA fracture mechanics framework for water damage evaluation, presented in this paper, provides a rational framework for the evaluation of moisture damage in mixtures that accounts for changes in multiple parameters, not just a single parameter.

- The results from the Hamburg Loaded Wheel Test part of this study clearly illustrate that both the HMA fracture mechanics framework and the Hamburg Loaded Wheel Test results follow similar trends. A mixture with a high number of cycles to strip generally seems to also show high number of cycles to failure, as determined with HMA Fracture mechanics. However, the Hamburg Loaded Wheel Test may be prone to higher testing variability as shown by the number of cycles to cause a 12.5 mm rut depth actually decreasing for GA-C1 when the liquid antistripping additive was added. However, in the absence of more detailed performance-based Superpave IDT testing results, the Hamburg Loaded Wheel Test may potentially serve as a torture test-based surrogate for determining the resistance of mixtures to moisture damage.

Water damage in mixtures is complicated by aggregate structure and aggregate type, meaning that each mixture and mixture property are affected to differently and to different degrees by water damage. The evaluation of water damage needs to account for these different effects in a consistent manner. The use of a single parameter to describe moisture damage must be questioned. The results presented indicate that if a sufficient amount of time between testing and conditioning is allowed in order to dissipate any pore water effects, successful and consistent characterization of moisture damage effects can be achieved, using the Superpave IDT and the HMA fracture mechanics framework.

The simplified HMA fracture mechanics framework presented in this Chapter integrates the varying effects of water damage on key mixture properties into a single number (ratio of the number of cycles to failure after and before conditioning) that reflects the change in the cracking performance of the mixture due to water conditioning. The HMA fracture mechanics framework uses mixture properties from the Superpave IDT creep, resilient modulus, and strength tests that

can be obtained with less than 5 minutes of testing after conditioning and test setup. Importantly, the approach presented can be used to evaluate the effects of water damage, independent of the conditioning procedure. Also, the specimen preparation protocols used for the Superpave IDT test require that mixtures be dried to a constant humidity, thus eliminating the effects of pore pressures on performance parameters that were observed in Chapter 5. Using a consistent framework for evaluating the detrimental effects of water damage, the effects of various different conditioning procedures can also be evaluated more thoroughly.

6.8 References

Al-Swailmi, S., and Terrel, R.L., "Evaluation of Water Damage of Asphalt Concrete Mixtures Using the Environmental Conditioning System (ECS)," *Proceedings*, Association of Asphalt Paving Technologists (AAPT), Vol. 61, 1992.

Buttlar, W.G., and Roque, R., "Development and Evaluation of the Strategic Highway Research Program Measurement and Analysis System for Indirect Tensile Testing at Low Temperatures," *Transportation Research Record 1454*, Transportation Research Board (TRB), National Research Council (NRC), Washington, D.C., pp. 163-171, 1994.

Choubane, B., Page, G.C., and Musselman, J.A., "Investigation of Water Permeability of Coarse Graded Superpave Pavements," *Proceedings*, AAPT, Vol. 67, 1998.

Choubane, B., Page, G.C., and Musselman, J.A., "Effects of Different Water Saturation Levels on the Resistance of Compacted HMA Samples to Moisture Induced Damage," presented at the 80th Annual Transportation Research Board Meeting, Washington D.C., 2000.

Dowling, N.E., *Mechanical Behavior of Materials*, Prentice Hall, Englewood Cliffs, NJ, 773 pp., 1993.

Curtis, C.W., Stroup-Gardiner, M., Brannan, C.J., and Jones, D.R., "Adsorption of Asphalt on Aggregate to Evaluate Water Sensitivity," *Transportation Research Record No. 1362*, TRB, NRC, Washington, D.C., 1992.

Kandhal, P.S., "Field and Laboratory Investigation of Stripping in Asphalt Pavement: State of the Art Report," *Transportation Research Record No. 1454*, TRB, NRC, Washington, D.C., 1994.

Kandhal, P.S., and Rickards, I.S., "Premature Failure of Asphalt Overlays from Stripping: Case Histories," presented at *Proceedings*, AAPT, 2001.

Lottman, R.P., "Laboratory Test Method for predicting Moisture-Induced Damage to Asphalt Concrete," *Transportation Research Record No. 843*, TRB, NRC, Washington, D.C., 1982.

Masad, E., Jandhyala, V.K., Dasgupta, N., and Somedavan, N., "Characterization of Air Void Distribution in Asphalt Mixtures Using X-Ray CT," *ASCE Journal of Materials in Civil Engineering*, 2002 (To Appear).

National Center for Asphalt Technology (NCAT), *Hot Mix Asphalt Materials, Mixture Design and Construction*, Auburn University, Alabama, 1996.

Nukunya, B., "Evaluation of Aggregate Type and Gradation and Other Volumetric Properties as Criteria for the Design and Acceptance of Durable Superpave Mixtures," Ph.D. Dissertation, University of Florida, Gainesville, FL, 2001.

Nukunya, B., Roque, R., Tia, M., and Birgisson, B., "Evaluation of VMA and Other Volumetric Properties as Criteria for the Design and Acceptance of Superpave Mixtures," *Journal of the Association of Asphalt Paving Technologists*, Vol. 70, 2001.

Parker, Jr., F., and Gharaybeh, F.A., "Evaluation of Indirect Tensile Tests for Assessing Stripping of Alabama Asphalt Concrete Mixtures," *Transportation Research Record No. 115*, TRB, NRC, Washington, D.C., 1987.

Rojas, J., Nazarian, S., Tandon, V., and Yaun, D., "Quality Management of Asphalt-Concrete Layers Using Wave Propagation Techniques," *Journal of the Association of Asphalt Paving Technologists*, Vol. 68, 1999.

Roque, R., and Buttlar, W.G., "The Development of a Measurement and Analysis System to Accurately Determine Asphalt Concrete Properties Using the Indirect Tensile Mode," *Journal of the Association of Asphalt Paving Technologists*, Vol. 61, pp. 304-332, 1992.

Roque, R., Buttlar, W.G., Ruth, B.E., Tia, M., Dickison, S.W., and Reid, B., "Evaluation of SHRP Indirect Tension Tester to Mitigate Cracking in Asphalt Pavements and Overlays," Final Report of the Florida Department of Transportation, University of Florida, Gainesville, FL, August 1997.

Roque, R., Birgisson, B., Sangpetgnam, B., and Zhang, Z., "Hot Mix Asphalt Fracture Mechanics: A Fundamental Crack Growth Law for Asphalt Mixtures," *Journal of the Association of Asphalt Paving Technologists* (Symposium), Vol. 71, 2002.

Sedwick, S.C., "Effect of Asphalt Mixture Properties and Characteristics on Surface Initiated Longitudinal Wheel Path Cracking," Master's Thesis, University of Florida, Gainesville, FL, 1998.

Terrel, R.L., and Al-Swailmi, S., "Water Sensitivity of Asphalt Aggregate Mixes: Test Selection," *SHRP-A-403*, Strategic Highway Research Program (SHRP), NRC, Washington, D.C., 1994.

Tunnicliff, D.G., and Root, R.E., "Use of Antistripping Additives in Asphaltic Concrete Mixtures," *NCHRP Report 274*, National Cooperative Highway Research Program (NCHRP), TRB, 1984.

Zhang, Z., Roque, R., Birgisson, B., and Sangpetngam, B., "Identification and Verification of a Suitable Crack Growth Law," *Proceedings,* AAPT, Vol. 70, 2001.

CHAPTER 7
A PERFORMANCE-BASED FRACTURE CRITERION FOR THE EVALUATION OF MOISTURE SUSCEPTIBILITY IN HOT MIX ASPHALT

7.1 Introduction

Chapter 6 presented an evaluation of the Superpave IDT fracture parameters for characterizing moisture damage in mixtures. The results clearly showed that the testing of mixture properties in tension provides a degree of sensitivity that allows for not only the evaluation of the effect of moisture damage, but also allows for distinction of moisture damage among mixtures of same aggregate type but with different gradations. The laboratory testing procedures currently available for testing Hot Mix Asphalt (HMA) moisture susceptibility were primarily developed to determine the degree of resistance to moisture damage by a particular combination of asphalt and aggregate, compare mixes composed of different types and quantities of aggregate, or to evaluate the effectiveness of anti-stripping agents (Lottman 1982; Tunnicliff and Root 1984; Curtis et al. 1992; Al-Swailmi and Terrel 1992; Terrel and Al-Swailmi 1994). These moisture susceptibility tests all evaluate the effects of moisture damage in the laboratory by measuring the relative change of a single parameter before and after conditioning (i.e., Tensile Strength Ratio, Resilient Modulus Ratio). Birgisson, Roque, and Page (2003) showed that the use of a single parameter to evaluate moisture damage must be questioned. Rather than a single parameter, a unified framework that accounts for changes in key mixture properties is needed to effectively evaluate the effects of moisture damage in mixtures. One such framework is the HMA fracture mechanics framework, developed at the University of Florida (Zhang et al. 2001; Roque et al. 2002). The results presented in Chapter 6 showed that moisture damage has an impact on the fracture resistance of mixtures that is accurately captured by the fundamental parameters of the HMA fracture mechanics model. Consequently, this allows mixture designers a way to rationally evaluate the effects of damage on mixture performance, thus forming the basis for

mixture specification criteria for the effects of moisture damage on mixtures. The parameter used in the HMA Fracture Mechanics model is the N_f parameter, which defines the number of cycles required to grow a one-inch long crack in a Superpave IDT test specimen. Unfortunately, this criterion is neither easily transparent nor understood. Therefore, is still a need to develop a true performance-based criterion that can be used both to consistently evaluate the level or magnitude of moisture damage in mixtures, as well as evaluate the overall fracture resistance of the mixture.

This chapter evaluates the use of a new performance-based fracture criterion, the Energy Ratio (ER) for quantifying the effects of moisture damage on the fracture resistance of mixtures. The Energy Ratio is used to determine the effects of moisture damage on changes in the fracture resistance of six granite mixtures that were prepared with and without the use of an antistripping additive. The granite aggregate used is a known stripping aggregate. In addition, for comparison purposes, one limestone mixture with a known high resistance to stripping was also used. The limestone mixture used has been widely used by the Florida Department of Transportation. The results of this study show that the ER is capable of detecting a range of moisture damage in mixtures, and it is also shown to detect the presence of antistripping agents in mixtures. Based on the results presented, the ER may form the basis of a promising combined performance-based specification criterion for evaluating the effects of moisture damage in mixtures as well as the overall resistance to fracture. The ER also provides a framework for focusing in a systematic way on key mixture properties and factors that affect the moisture sensitivity for a given mixture.

7.2 Objectives

Using a number of mixtures with aggregates of known moisture damage susceptibility, the primary objective of this research was to evaluate the use of a new fracture mechanics-based

criterion, the ER, for quantifying the effects of moisture damage on the fracture resistance of mixtures. A secondary objective is to evaluate the effectiveness of the ER is detecting the presence of antistripping additives in mixtures. Finally, if warranted from findings, appropriate recommendations will be made regarding the determination of moisture damage in mixtures, including the effects of relevant mixture properties.

7.3 Scope

This chapter deals with the use of the Superpave Indirect Tension Test (IDT) fracture parameters as described by e.g., Zhang et al. (2001), along with a new fracture performance-based criterion, the ER, for the evaluation of moisture damage on mixtures containing aggregates of known stripping performance. Below, a brief overview of HMA fracture mechanics and the ER will be presented, followed by a description of the materials and methodologies used. Finally, comparisons will be made between ER for mixtures that are both moisture conditioned as well as unconditioned. The key Superpave IDT fracture parameters monitored include creep properties, resilient modulus, tensile strength, fracture energy limit, and dissipated creep strain energy limit.

7.4 Hot-Mix Asphalt Fracture Mechanics

Birgisson, Roque, and Page (2003) showed that moisture damage strongly affects the fracture resistance of mixtures. This means that HMA fracture mechanics can also be used to quantify the effects of moisture damage on mixtures.

The central feature of the hot mix asphalt fracture mechanics framework developed by the University of Florida is the threshold concept. Cracks in hot mix asphalt have been observed to grow in a discontinuous (stepwise) manner (Jacobs et al. 1996; Kim et al. 1997; Roque et al. 1999; Zhang et al. 2001). Traditional linear elastic fracture mechanics assume that a continuous

crack growth curve can be fitted to the crack growth data, which is inconsistent with the observations of a discontinuous crack growth. Zhang et al. (Zhang et al. 2001) discovered that a damage threshold exists, which defines the development of stepwise macro-cracks at any point in the mixture. Damage below the threshold is considered micro-damage (i.e., damage not associated with crack initiation or crack growth) and appears to be fully healable after a resting period, while macro-damage (i.e., damage associated with crack initiation or growth) occurs when the threshold is exceeded, and does not appear to be healable.

Zhang et al. (2001; 2001) showed that the dissipated creep strain energy (DCSE) limit and the fracture energy limit (FE) of asphalt mixtures suitably define the lower and upper thresholds, respectively. These energy limits can be easily determined from the stress-strain response of a tensile strength test and resilient modulus test using the Superpave Indirect Tensile Test following the procedures developed by Roque and Buttlar (Roque and Buttlar 1992; Buttlar and Roque 1994).

The rate of damage growth under the energy threshold is governed by the creep properties of the mixture. The creep compliance of mixtures can be represented using the following power function:

$$D(t) = D_0 + D_1 t^m \tag{7.1}$$

where: D(t) is creep compliance, D_0, D_1, and m are parameters obtained from creep tests. Hence, the rate of microdamage is assumed to be controlled by the m-value and D_1.

In summary, based on the concepts and HMA fracture model, the following key parameters appear to govern the cracking performance of asphalt mixtures:

- DCSE limit: dissipated creep strain energy to failure;
- m-value: parameter governing the creep strain rate; and

- D_1 parameter: parameter governing the creep strain rate.

In addition, the tensile stress in the pavement controls where and how fast a crack initiates and grows for a given pavement configuration. Figure 7-1 shows a conceptual illustration of the HMA fracture mechanics framework, namely the energy thresholds (FE and DCSE) and the effects of rate of creep and m-value on rate of damage. The higher the m-value, the faster is the rate of accumulation of DCSE per cycle, and thus the faster the DCSE limit is reached.

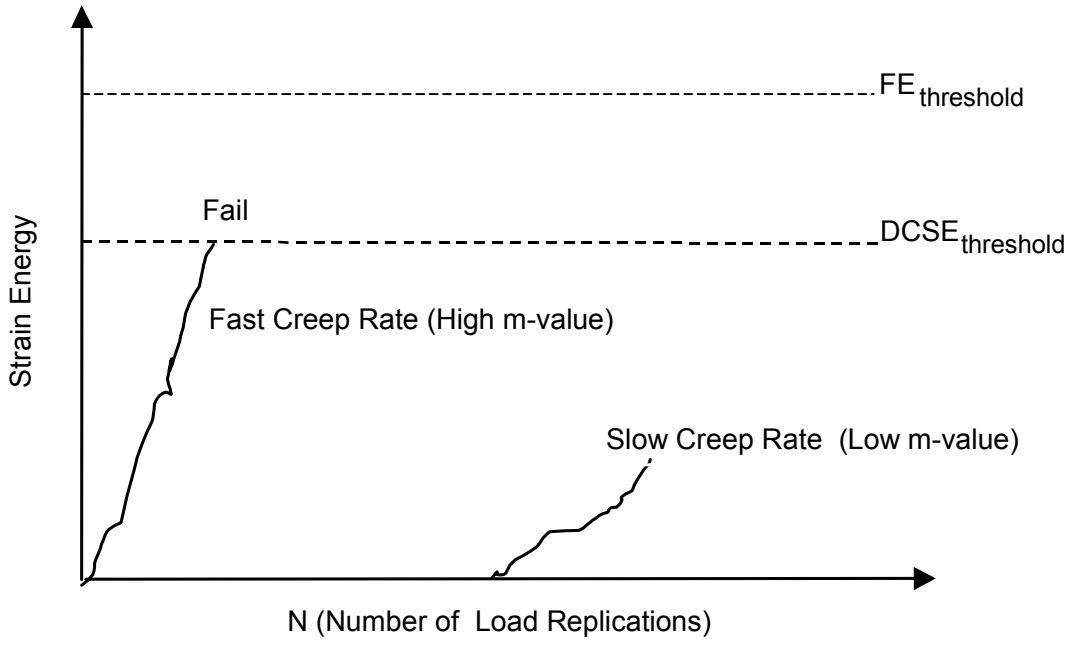

Figure 7-1. Hot mix asphalt fracture mechanics: Energy thresholds and the effects of rate of creep and m-value on rate of damage.

Based on detailed forensic investigations of 36 field pavement sections of known cracking performance in Florida, a HMA fracture mechanics-based performance specification criterion, termed the "Energy Ratio" (ER), was developed by Jailiardo (2003). This parameter is a measure of the fracture resistance of mixtures, and is expressed by:

$$ER = \frac{DCSE_f}{DCSE_{min}} = \frac{a \times DCSE_f}{m^{2.98} \times D_1} \quad (7.2)$$

where:

$DCSE_f$ = Dissipated Creep Strain Energy (in KJ/m^3),

$DCSE_{min}$ = Minimum Dissipated Creep Strain Energy for adequate cracking performance (in KJ/m^3),

D_1 and m are creep parameters in 1/psi, and

$$a = 0.0299\sigma^{-3.1}(6.36 - S_t) + 2.46 \times 10^{-8}$$

in which σ = tensile stress of asphalt layer (in psi), and

S_t = tensile strength (in MPa).

Based on the observed pavement performance from these 36 field sections, Jailiardo (2003) was able to determine a minimum DCSE for adequate cracking performance for the mixtures used. Jailiardo (2003) also recommended a minimum required ER (ER_{min}) for various traffic levels. For 3 million ESAL, the recommended ER_{min} is 1.1, for 10 million ESAL, ER_{min} is 1.3, and for 30 million ESAL, ER_{min} is 1.7. Hence, ER forms the basis for a performance-based fracture criterion for flexible pavements.

Since it is known that the fracture resistance of mixtures is strongly affected by moisture damage (Birgisson, Roque, and Page, 2003), in the following ER will be evaluated as a mechanics-based criterion for evaluating the moisture sensitivity of mixtures. To allow for consistent comparisons of the mixtures studied, the tensile stress of the asphalt layer was taken to be a constant 120 psi, which is consistent with calculated values for typical Florida pavements, which tend to have stiff bases and thinner layers of asphalt.

7.5 Materials and Methodology

7.5.1 Aggregates, Gradations, and Binder Used

Two groups of aggregates were used. The first consisted of crushed granite from Georgia that has shown potential for stripping. The second consisted of an oolitic limestone aggregate

that has in the past not shown significant stripping potential. Both aggregate groups are used extensively in Florida and are considered to be excellent materials resulting in well-performing mixtures.

The granite mixtures were made up of four components: coarse aggregate, fine aggregate, screenings, and mineral filler. They were blended together in different proportions to provide six 12.5-mm nominal maximum aggregate size mixtures of coarse and fine gradations. These mixtures are denoted as: GA-C1, GA-C2, GA-C3, GA-F1, GA-F2, GA-F3, with the letters C and F denoting coarse-graded and fine-graded mixtures according to whether the gradation passes below or above the Superpave restricted zone. One previously designed coarse-graded Superpave mixture (WR-C1) prepared by the Florida Department of Transportation (FDOT) was also used as the basis for the research. The purpose of selecting granite mixtures of varying gradation was to ensure that the mixtures tested were of different permeability, and other volumetric properties, but with of the same aggregate type, while using the limestone mixture (WR-C1) for comparison purposes, since it is known to be highly resistant to stripping. The resulting gradations are shown in Table 7-1. The mixtures ranged from what could be described as fine uniformly-graded and fine dense-graded to coarse uniformly-graded and coarse gap-graded.

Table 7-1. Gradations for Granite and Limestone Mixtures

Sieve Size (mm)	Percent Material Passing each Sieve Size						
	GA-C1	GA-C2	GA-C3	GA-F1	GA-F2	GA-F3	WR-C1
19.0	100.0	100.0	100.0	100.0	100.0	100.0	100.0
12.5	97.4	90.9	97.3	94.7	90.5	94.6	97.0
9.5	89.0	72.9	89.5	84.0	77.4	85.1	90.0
4.75	55.5	45.9	55.4	66.4	60.3	65.1	60.0
2.36	29.6	28.1	33.9	49.2	43.2	34.8	33.0
1.18	19.2	18.9	23.0	32.7	34.0	26.0	20.0
0.60	13.3	13.2	16.0	21.0	23.0	18.1	15.0
0.30	9.3	9.2	11.2	12.9	15.3	12.5	11.0
0.15	5.4	5.6	6.8	5.9	8.7	7.7	7.6
0.075	3.5	3.9	4.7	3.3	5.4	5.8	4.8

Design asphalt contents for all the mixtures were determined such that each mixture had 4 percent air voids at N_{design} = 109 gyrations. Finally, PG 67-22 (AC-30) asphalt was used for all limestone and granite mixtures in this study. Additionally, consistent with FDOT practice, all the granite mixtures were also prepared with PG 67-22 asphalt containing 0.5 percent liquid antistripping agent by weight of total asphalt, commonly used in Florida. Table 7-2 shows the volumetric properties for the mixtures used.

Table 7-2. Volumetric Properties of Granite and Limestone Mixtures

Properties	Mixture						
	GA-C1	GA-C2	GA-C3	GA-F1	GA-F2	GA-F3	WR-C1
Asphalt Content (%)	6.63	5.26	5.25	5.68	4.56	5.14	6.50
Specific Gravity of Asphalt	1.035	1.035	1.035	1.035	1.035	1.035	1.035
Bulk Specific Gravity	2.345	2.399	2.391	2.374	2.433	2.404	2.235
Theoretical Specific Gravity	2.442	2.500	2.492	2.473	2.532	2.505	2.328
Air Voids (%)	4.0	4.0	4.1	4.0	3.9	4.0	4.0
Voids in Mineral Aggregate (%)	18.5	15.4	15.7	16.6	13.6	15.1	15.4
Voids filled with Asphalt (%)	78.5	73.8	74.2	75.9	71.2	73.3	74.16
Effective Specific Gravity of Aggregate	2.710	2.719	2.709	2.706	2.725	2.720	2.549
Absorbed Asphalt (%)	0.3	0.4	0.3	0.3	0.5	0.5	1.3
Effective Asphalt (%)	6.3	4.9	5.0	5.4	4.1	4.7	5.3
Dust to Asphalt Ratio	0.6	0.8	0.9	0.6	1.2	1.2	0.7
Surface Area (m^2/kg)	3.3	3.5	4.2	4.1	5.3	4.9	4.9
Film Thickness theoretical, microns	19.9	14.3	12.1	13.4	7.7	9.9	11.2

7.5.2 Mixture Preparation and Moisture Conditioning

All mixtures were produced in the laboratory following the procedure outlined in AASHTO T-283. First, the aggregates and asphalt binder were heated to 150 °C (300 °F) for three hours prior to mixing. Once the mixing was completed, the mixture was allowed to cool to room temperature for two hours. After the cooling period, the loose mixture was long-term conditioned for 16 hours at 60° C (140° F). After the mixture was conditioned for 16 hours, it was reheated to 135° C (275° F) for two hours before compaction. The specimens were then compacted on the IPC Servopac Superpave gyratory compactor to 7± 0.5 percent air voids. Six samples of each mix were prepared.

For each mixture, three samples were then subjected to saturation according to the AASHTO T-283 procedure. Throughout the testing, a target saturation level of 65 and 80 percent was maintained (changes to AASHTO T-283 in 2003 require a saturation level of 70-80 percent). After the target saturation level was achieved, the specimens were placed in a 60° C (140° F) water bath for 24 hours.

Once the moisture conditioning was completed, the conditioned mixtures were allowed to drain for 36 hours. Then, conditioned and unconditioned specimens were cut, by a wet saw, into 50-mm (2-inch) thick specimens. The specimens were placed in a dehumidifier chamber for 48 hours to dry them of any remaining moisture and bring them to a constant humidity level. The Superpave IDT test was used to perform Resilient Modulus (M_R), Creep Compliance, and Strength tests (NCAT 1996; Roque et al. 1997; Sedwick 1998) from which the following properties were determined: tensile strength, resilient modulus, fracture energy limit (FE), dissipated creep strain energy limit (DCSE), and creep properties. Using these mixture properties and the fracture mechanics-based Energy Ratio fracture performance specification criterion developed at the University of Florida, the effects of moisture damage on the fracture resistance of the mixtures were calculated. All Superpave IDT tests were performed at a constant testing temperature of 10° C (50° F).

7.6 Evaluation of Moisture Damage Using the Energy Ratio

In the following, the effects of moisture damage on the fracture resistance of mixtures are evaluated. Tables 7-3 and 7-4 show a summary of the mixture fracture properties obtained from the Superpave IDT fracture properties testing for mixtures with and without antistripping agents, respectively. It should be noted that all granite mixtures tested without the antistripping agent showed visible stripping of the asphalt film from the aggregates, whereas the limestone mixture

(WR-C1) and the granite mixtures with the antistripping additive did not show visible signs of stripping.

Table 7-3. Summary of Mixture Properties for Mixtures Without an Antistripping Additive

Material	Resilient Modulus, M_R (GPa)	Tensile Strength, S_t (MPa)	Fracture Energy (kJ/m^3)	m-value	D_1 (1/psi)	DCSE (kJ/m^3)	Energy Ratio, ER
Conditioned							
GA-C1	4.08	1.12	2.90	0.66	1.54E-06	2.75	0.50
GA-C2	8.35	1.84	2.80	0.65	1.03E-06	2.60	0.67
GA-C3	9.07	1.77	2.10	0.63	9.10E-07	1.93	0.62
GA-F1	7.05	1.59	2.80	0.63	1.52E-06	2.62	0.53
GA-F2	10.1	1.96	2.30	0.56	1.24E-06	2.11	0.70
GA-F3	8.14	1.75	2.10	0.62	1.44E-06	1.91	0.42
WR-C1	7	1.33	2.20	0.44	1.50E-06	2.07	1.25
Unconditioned							
GA-C1	5.1	1.44	6.00	0.62	1.74E-06	5.80	1.07
GA-C2	8.79	2.00	5.00	0.59	1.06E-06	4.77	1.57
GA-C3	9.99	1.99	3.80	0.57	8.70E-07	3.60	1.55
GA-F1	8.45	1.93	3.70	0.57	1.30E-06	3.48	1.06
GA-F2	10.2	2.52	3.60	0.48	1.58E-06	3.29	1.22
GA-F3	9.95	2.14	2.80	0.56	8.97E-07	2.57	1.16
WR-C1	8.53	1.59	2.50	0.54	9.51E-07	2.35	1.18

Table 7-4. Summary of Properties for Mixtures With Antistripping Additive

Material	Resilient Modulus, M_R (GPa)	Tensile Strength, S_t (MPa)	Fracture Energy (kJ/m^3)	m-value	D_1 (1/psi)	DCSE (kJ/m^3)	Energy Ratio, ER
Conditioned							
GA-C1	4.78	1.32	4.05	0.60	2.02E-06	3.87	0.697
GA-C2	8.42	1.72	3.60	0.61	9.63E-07	3.42	1.153
GA-C3	9.00	1.81	2.40	0.60	7.40E-07	2.22	1.008
GA-F1	7.46	1.69	3.80	0.66	1.20E-06	3.61	0.776
GA-F2	10.94	1.81	2.90	0.62	5.68E-07	2.75	1.513
GA-F3	9.28	1.75	2.40	0.62	1.14E-06	2.23	0.605
Unconditioned							
GA-C1	5.335	1.54	8.20	0.57	2.41E-06	7.98	1.350
GA-C2	8.45	1.75	6.35	0.54	1.20E-06	6.17	2.454
GA-C3	12.75	2.06	4.75	0.53	9.66E-07	4.58	2.290
GA-F1	7.78	1.96	5.20	0.58	1.28E-06	4.95	1.405
GA-F2	11.26	2.14	4.20	0.50	9.32E-07	4.00	2.435
GA-F3	11.99	2.05	3.10	0.53	8.97E-07	2.92	1.531

In the following, first the results for mixtures without the presence of antistripping agents will be discussed, followed by a discussion of results for mixtures with an antistripping agent.

7.6.1 Results for Mixtures Without Antistripping Additive

Table 7-3 shows how the FE and DCSE limits decreased and the m-value increased with moisture conditioning for each of granite mixtures tested. The results clearly show that both the

strain energy limits (FE, DCSE) and the creep properties of mixtures are affected by moisture damage, implying that a consistent framework is needed to determine the changes in mixtures due to moisture damage.

Figure 7-2 shows a comparison of the ER for conditioned and unconditioned mixtures without an antistripping additive. For the unconditioned granite mixtures, the ER ranged from 1.06 for GA-F1 to 1.57 for the very coarse-graded GA-C2. For the conditioned granite mixtures, the ER ranged from 0.42 for the gap-graded GA-F3 mixture to 0.7 for the fine-graded GA-F2, showing a significant drop in the fracture resistance as measured by ER as a result of moisture damage. As expected, the oolitic limestone mixture (WR-C1) did not show a drop in the ER due to water conditioning, implying that it was not significantly affected by moisture conditioning.

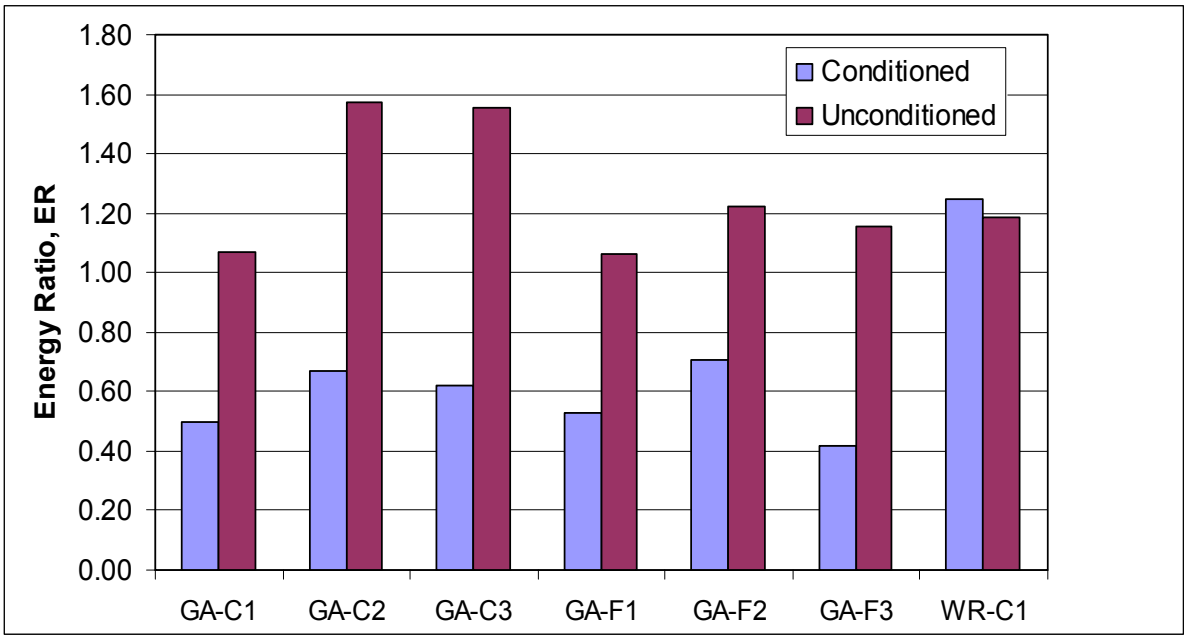

Figure 7-2. Comparison of energy ratio for moisture conditioned and unconditioned mixtures.

7.6.2 Results for Mixtures With a Liquid Antistripping Additive

Figure 7-3 shows a comparison of the fracture energy limits for unconditioned granite mixtures with and without the liquid antistripping agent. The fracture energy limit increased for

all the granite mixtures containing the liquid antistripping additive, implying as expected that the bond between the asphalt film and the aggregate was improved. Similarly, Figure 7-4 shows a comparison of the ER for unconditioned mixtures with and without the antistripping additive. Again, the results show that the antistripping additive improves the ER of the mixtures, thus also improving the resistance to cracking.

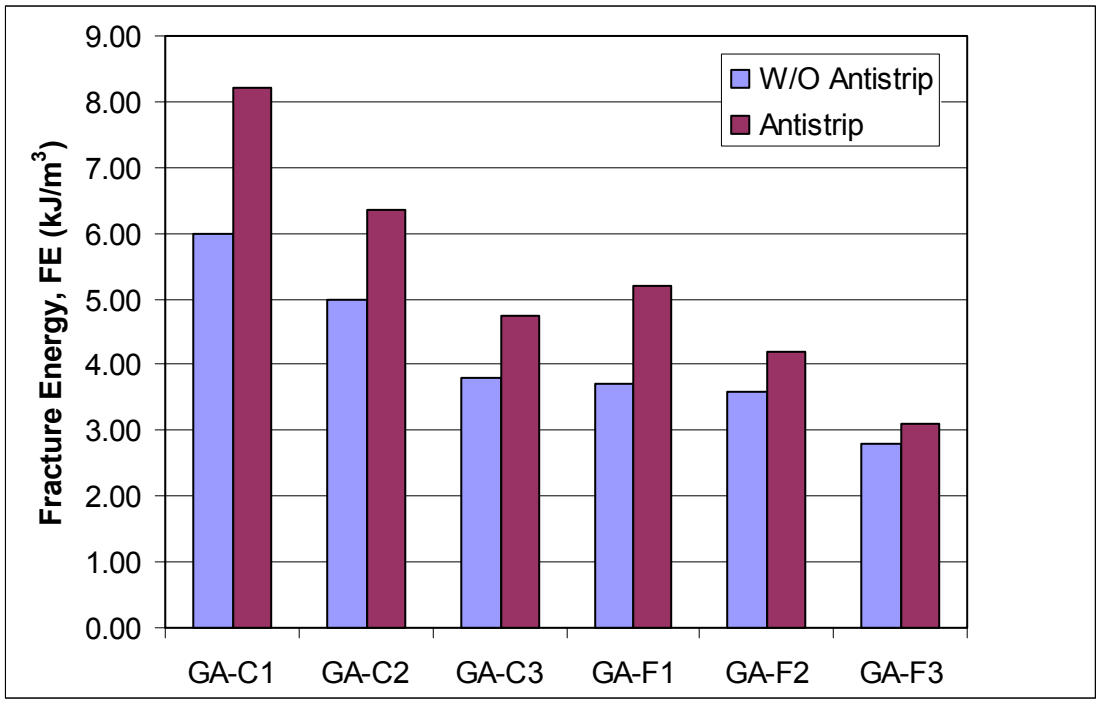

Figure 7-3. Comparison of fracture energy for unconditioned mixtures with and without antistripping agents.

Figure 7-5 shows that the ER decreased with moisture conditioning for all the mixtures tested, meaning that the moisture conditioning decreased the fracture resistance of the mixtures despite the presence of an antistripping additive. However, Figure 7-6 shows that mixtures containing the antistripping additive have a higher ER after moisture conditioning compared to mixtures without the antistripping additive. Finally, Figure 7-7 shows a comparison between ratios of ER for moisture conditioned mixtures with and without antistripping agents. Again, the

results show that the mixtures with the antistripping additive had a smaller decrease in ER than mixtures without the antistripping additive.

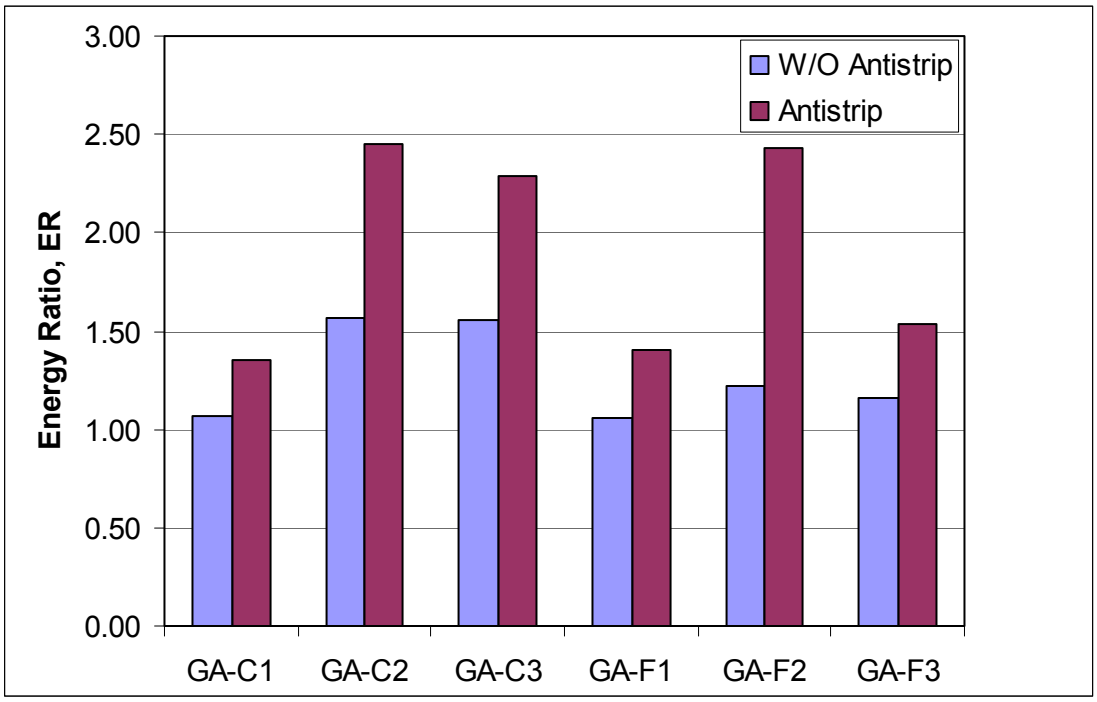

Figure 7-4. Comparison of energy ratio for unconditioned mixtures with and without antistripping agents.

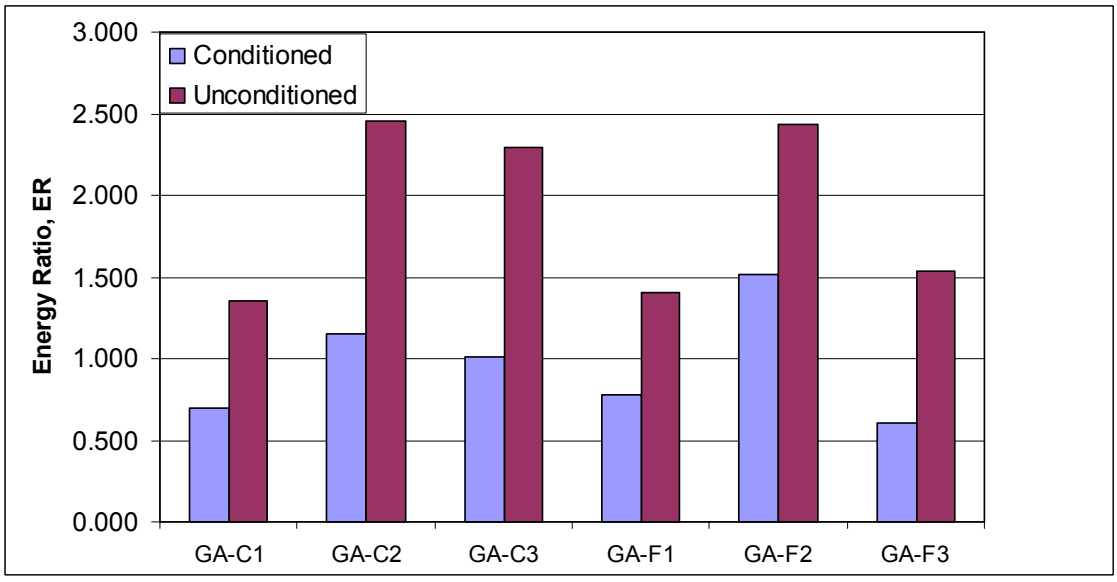

Figure 7-5. Comparison of energy ratio for moisture conditioned and unconditioned mixtures with an antistripping additive.

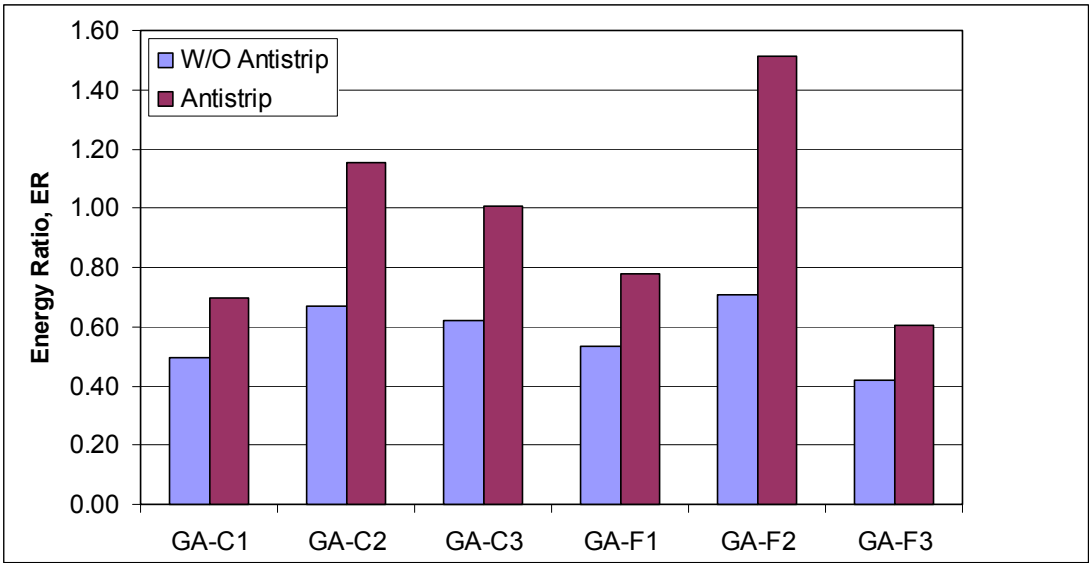

Figure 7-6. Comparison of energy ratio for conditioned mixtures with and without antistripping agents.

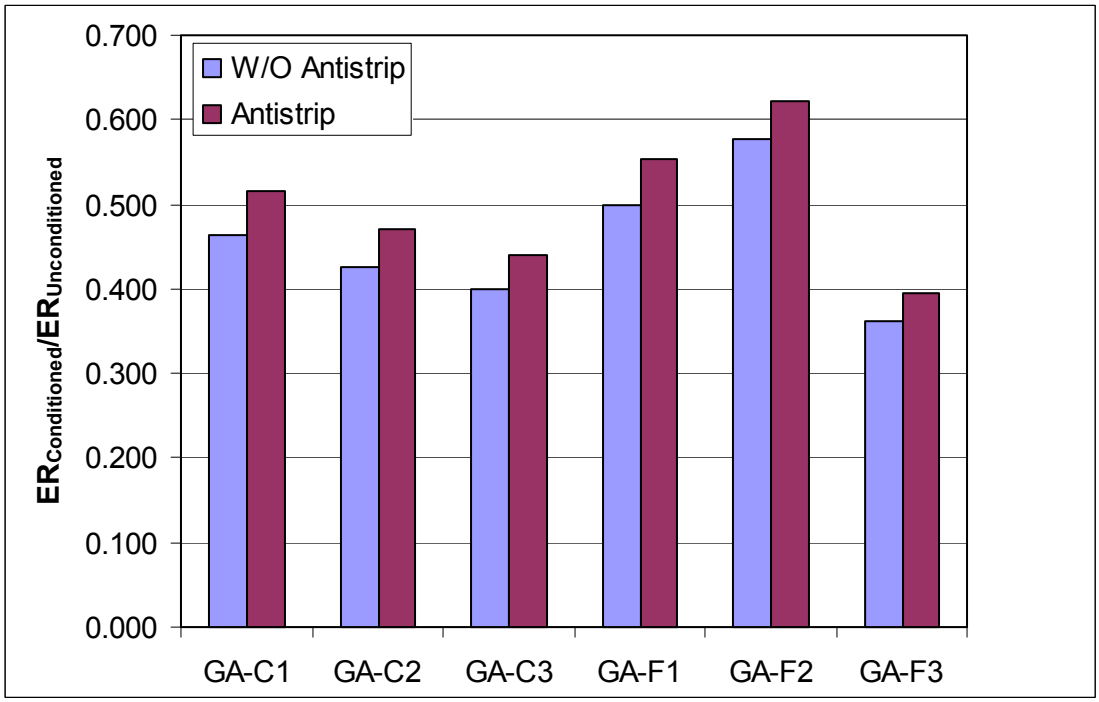

Figure 7-7. Comparison of ratios of energy ratios for moisture conditioned mixtures with and without antistripping agents.

In summary, the ER is capable of detecting changes in the fracture resistance of mixtures due to moisture conditioning. Also, importantly, the ER is capable of detecting changes in the fracture properties of mixtures due to the presence of an antistripping additive.

7.7 Summary and Conclusions

The HMA fracture mechanics framework developed at the University of Florida has been shown previously (Birgisson et al. 2003) to provide a rational framework for the evaluation of the effects of moisture damage on the fracture resistance of mixtures. Consequently, this allows mixture designers a way to rationally evaluate the effects of damage on mixture performance, thus forming the basis for mixture specification criteria for the effects of moisture damage on mixtures. This chapter evaluated the use of a new HMA fracture mechanics-based parameter, the ER for quantifying the effects of moisture damage on the fracture resistance of mixtures. In summary, the effects of moisture conditioning on the ER were as follows:

- ER decreased for granite mixtures containing aggregates that were known strippers; and
- ER stayed relatively unchanged for a limestone mixture that was known to resist moisture damage.

In addition, the effects of an antistripping additive on ER were as follows:

- For unconditioned mixtures, ER increased with the addition of an antistripping additive, as compared to mixtures without an antistripping additive;
- For conditioned mixtures, ER was also higher for mixtures containing an antistripping additive, as compared to mixtures without an additive; and
- For mixtures containing an antistripping additive, the ratio of ER before and after conditioning was also higher than for mixtures without an additive.

The results imply that the addition of an antistripping additive resulted in an improved bond between the asphalt film and the aggregates, thus reducing the overall effects of moisture conditioning, but not eliminating moisture damage completely. Importantly, the ER is capable of detecting changes in the fracture properties of mixtures due to the presence of an antistripping additive.

Based on the results presented, the ER may form the basis of a promising performance-based fracture criterion for evaluating both the effects of moisture damage and the inherent fracture resistance of mixtures. The ER also provides a framework for focusing in a systematic way on key mixture properties and factors that affect the moisture sensitivity for a given mixture. The mixture properties required can all be obtained from Superpave IDT creep, resilient modulus, and strength tests, which can be obtained with less than 5 minutes of testing after conditioning and test setup.

Finally, the ER can be used to evaluate the effects of moisture damage, independent of the conditioning procedure. Using a consistent framework for evaluating the detrimental effects of moisture damage, the effects of various different conditioning procedures can also be evaluated more thoroughly.

7.8 References

Al-Swailmi, S., and Terrel, R.L., "Evaluation of Water Damage of Asphalt Concrete Mixtures Using the Environmental Conditioning System (ECS)," *Proceedings*, Association of Asphalt Paving Technologists (AAPT), Vol. 61, 1992.

Birgisson, B., Roque, R., and Page, G., "Evaluation of Water Damage Using Hot Mix Asphalt Fracture Mechanics," *Journal of the Association of Asphalt Paving Technologists*, Vol. 73, 2003.

Buttlar, W.G., and Roque, R., "Development and Evaluation of the Strategic Highway Research Program Measurement and Analysis System for Indirect Tensile Testing at Low Temperatures," *Transportation Research Record No. 1454*, Transportation Research Board (TRB), National Research Council (NRC), Washington, D.C., pp. 163-171, 1994.

Curtis, C.W., Stroup-Gardiner, M., Brannan, C.J., and Jones, D.R., "Adsorption of Asphalt on Aggregate to Evaluate Water Sensitivity," *Transportation Research Record No.1362*, TRB, NRC, Washington, D.C., 1992.

Jacobs, M.M.J., Hopman, P.C., and Molenaar, A.A.A., "Application of Fracture Mechanics Principles to Analyze Cracking in Asphalt Concrete," *Journal of the Association of Asphalt Paving Technologists*, Vol. 65, pp. 1-39, 1996.

Jailiardo, A., "Development of Specification Criteria to Mitigate Top-Down Cracking," Master's Thesis, University of Florida, Gainesville, FL, 2003.

Kim, Y.R., Lee, H-J., and Little, D.N., "Fatigue Characterization of Asphalt Concrete Using Viscoelasticity and Continuum Damage Theory," *Journal of the Association of Asphalt Paving Technologists*, Vol. 66, pp. 520-569, 1997.

Lottman, R.P., "Laboratory Test Method for Predicting Moisture-Induced Damage to Asphalt Concrete," *Transportation Research Record No. 843*, TRB, NRC, Washington, D.C., 1982.

NCAT, *Hot Mix Asphalt Materials, Mixture Design and Construction*, National Center for Asphalt Technology (NCAT), Auburn University, Alabama, 1996.

Roque, R., and Buttlar, W.G., "The Development of a Measurement and Analysis System to Accurately Determine Asphalt Concrete Properties Using the Indirect Tensile Mode," *Journal of the Association of Asphalt Paving Technologists*, Vol. 61, pp. 304-332, 1992.

Roque, R., Buttlar, W.G., Ruth, B.E., Tia, M., Dickison, S.W., and Reid, B., "Evaluation of SHRP Indirect Tension Tester to Mitigate Cracking in Asphalt Pavements and Overlays," Final Report of the Florida Department of Transportation, University of Florida, Gainesville, FL, August 1997.

Roque, R., Zhang, Z., and Sankar, B., "Determination of Crack Growth Rate Parameters of Asphalt Mixtures Using the Superpave Indirect Tension Test (IDT)," *Journal of the Association of Asphalt Paving Technologists*, Vol. 68, pp. 404-433, 1999.

Roque, R., Birgisson, B., Sangpetgnam, B., and Zhang, Z., "Hot Mix Asphalt Fracture Mechanics: A Fundamental Crack Growth Law for Asphalt Mixtures," *Journal of the Association of Asphalt Paving Technologists* (Symposium), Vol. 71, pp. 816-827, 2002.

Sedwick, S.C., "Effect of Asphalt Mixture Properties and Characteristics on Surface Initiated Longitudinal Wheel Path Cracking," Master's Thesis, University of Florida, Gainesville, FL, 1998.

Terrel, R.L., and Al-Swailmi, S., "Water Sensitivity of Asphalt Aggregate Mixes: Test Selection," *SHRP-A-403*, Strategic Highway Research Program (SHRP), NRC, Washington, D.C., 1994.

Tunnicliff, D.G., and Root, R.E., "Use of Antistripping Additives in Asphaltic Concrete Mixtures," *NCHRP Report 274*, National Cooperative Highway Research Program (NCHRP), TRB, 1984.

Zhang, Z., Roque, R., and Birgisson, B., "Evaluation of Laboratory Measured Crack Growth Rate for Asphalt Mixtures," *Transportation Research Record No. 1767*, TRB, NRC, Washington, D.C., pp. 67-75, 2001.

Zhang, Z., Roque, R., Birgisson, B., and Sangpetngam, B., "Identification and Verification of a Suitable Crack Growth Law (with Discussion)," *Journal of the Association of Asphalt Paving Technologists*, Vol. 70, pp. 206-241, 2001.

CHAPTER 8
FUNDAMENTAL CONSIDERATIONS I – HOT MIX ASPHALT MOISTURE DAMAGE AS A FUNCTION OF AIR VOID SIZE DISTRIBUTION AND BOND ENERGY

8.1 Background

The results presented in Chapter 6 indicated that it may not be sufficient to monitor changes in a single mechanical property such as stiffness or strength to evaluate the complex interactions that are involved in moisture damage. In Chapter 7 the use of a parameter referred to as the "energy ratio" (ER) was proposed to assess the mix resistance to moisture damage taking into account different key mixture properties including the dissipated creep strain energy, compliance, and tensile strength. This parameter was supported by the principles of fracture mechanics and forensic research of 36 field pavement sections of known cracking performance (Roque et al. 2004). The use of the ER was preceded in Chapter 6 by the use of the number of cycles to grow a one-inch long crack under cyclic loading in the Superpave IDT test. The number of cycles is calculated from measurements of the creep strain energy per cycle and the creep strain energy limit. Other researchers have developed constitutive relationships that use the pseudo strain definition were also developed to separate the energy dissipated in HMA facture from the energy dissipated in viscous flow. These constitutive relationships were developed based on experimental measurements of asphalt mastics and mixtures under small strain (or stress) loading that does not cause damage, and higher strain levels that induce damage (Lytton 2004). Recently, experimental and analysis methods have been developed to assess the cohesive and adhesive bond energies under dry and wet conditions (Cheng et al. 2002; Lytton 2004). These studies related bond energies to the mix fracture and healing behavior which govern HMA resistance to moisture damage.

In summary, the potential effects of pore pressures on mixture performance have been identified in Chapters 3, 4, and 5, and a theoretical analysis and testing framework has been identified for consistent testing and quantification of moisture damage in mixtures. However, the moisture conditioning of mixtures still needs to be evaluated. Water damage effects in HMA pavements may be bracketed by two extreme conditions: 1) the rapid application of cyclic pore pressures under saturated conditions that correspond to critical field conditions, and 2) the longer term continuous low level exposure to water without pore pressures. Based on the findings in the previous chapters, there is a clear need to better understand the fundamentals related to pore pressure effects in pavements. In particular, in order to understand better the most important mechanism of moisture damage in pavements, there are still questions remaining on the following issues: 1) the relationship between mixture air void distribution, binder and aggregate type effect as measured by bond energy, and moisture damage, and 2) quantification of likely ranges of pore pressures in field mixtures.

It has also been long recognized that water permeability is an important factor influencing moisture damage. Consequently, a number of studies have focused on measuring permeability (Maupin 2001; Cooley and Brown 2000). The underlying assumption in some of these studies is that a proportional relationship exists between HMA permeability and moisture damage. Therefore, recommendations were put forward on limiting the maximum permeability, which is expressed as a function of percent air voids (Cooley and Brown 2000). Al-Omari et al. (2002) presented experimental measurements demonstrating the complexity of the air void distribution which makes it difficult to accurately predict permeability from average percent air voids only. As such, there is a pressing need to understand permeability and moisture damage based on air void size distribution. This can be achieved through nondestructive X-ray

Computed Tomography measurements of air voids and analysis of their characteristics (Tashman et al. 2002; Al-Omari et al. 2002).

This chapter integrates X-ray CT measurements, probabilistic analysis of air void size distribution, measurements of the material mechanical properties within a fracture mechanics framework, and analysis of the cohesive and adhesive bond energies to better understand the mechanisms involved in moisture damage. The ultimate goal is to gain a better insight into the fundamental mechanisms and material properties that are associated with moisture damage induced by pore pressures.

8.2 Objectives and Scope

The main objective of this chapter is to identify some of the fundamental mixture properties that affect moisture damage in mixtures. In particular, this chapter determines the influence of air void size, air void distribution, and bond energy on moisture damage. The effect of the resulting air void distributions on water flow in hot mix asphalt pavements is also evaluated. These objectives are achieved through:

1. Measurements and analysis of moisture damage of asphalt mixes prepared using two different aggregate types and varying gradations. The analysis was conducted using parameters derived based on the principles of fracture mechanics, presented previously in Chapters 6 and 7.
2. Probabilistic analysis of air voids distribution with the assistance of X-ray Computed Tomography measurements and image analysis techniques.
3. Investigating the relationship between permeability and air void size distribution.

4. Identifying the effects of air void size and adhesive and cohesive bond energies on moisture damage as measured and characterized with the HMA fracture mechanics approach in Chapters 6 and 7.
5. Evaluating the effect of air void distributions on water flow in hot mix asphalt pavements through finite element modeling of flow patterns based on air void distributions from cores obtained from the field.

However, first an overview of the digital x-ray tomographic imaging techniques used in this study will be presented.

8.3 Overview of Digital X-Ray Tomographic Imaging Techniques Used to Characterize the Void Structure of Mixtures

In the following, a description of the use of X-Ray Computed (CT) image analysis in evaluating the internal structure of asphalt concrete will be provided. The internal structure includes air void distribution, aggregate orientation, aggregate contact, and aggregate segregation. X-ray Computed Tomography imaging is a complete non-destructive technique to obtain digital information on 3D geometry and properties of an opaque solid object (Denison et al. 1997). The main components of X-ray Computed Tomography (CT) are shown in Figure 8-1, where the x-ray is shown passing through a slice of the specimen. The intensity of the x-ray is measured before it enters the specimen and after it passes through it. After obtaining x-ray images for a horizontal slice of the specimen, the specimen is shifted vertically by a fixed amount and the procedure is continued. Differences in intensity of the x-ray images represent density variations within the specimen. Therefore, X-ray CT of the specimen results in images that display the density at every point in two-dimensional slices (Masad et al. 2001).

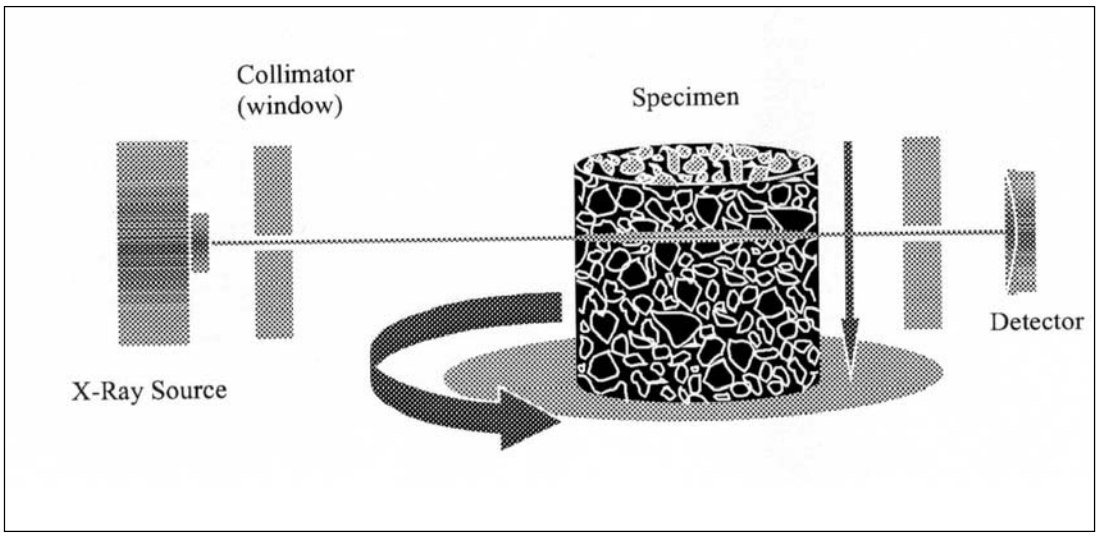

Figure 8-1. Components of X-ray Computed Tomography system (Masad 2001)

Figure 8-2 shows a typical X-Ray CT image of a horizontal cut of an asphalt concrete specimen with a diameter of 150 mm. The image is shown in a grayscale (256 levels of intensity) with dimensions of 512 × 512 pixels, which means each pixel in the image represent a point with a size of 0.195 mm in a horizontal section. The dark colors represent the air voids and the bright colors represent the aggregates.

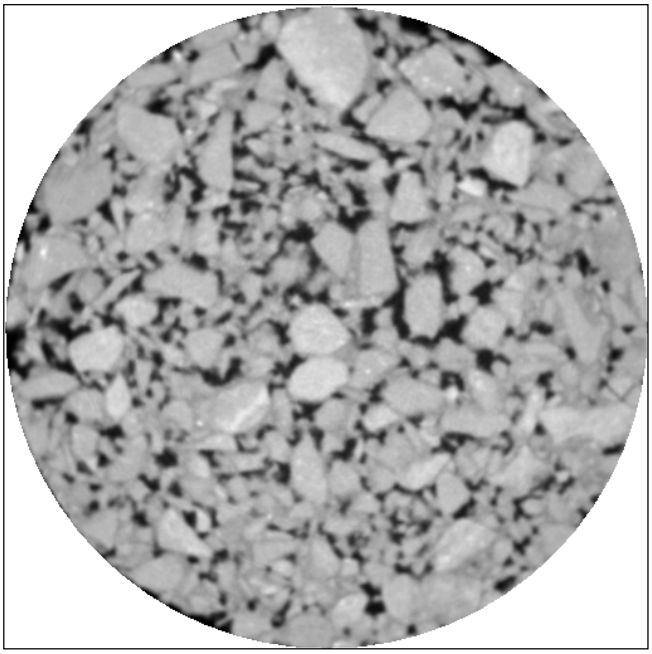

Figure 8-2. Horizontal X-Ray CT image of asphalt concrete specimen.

8.3.1 Determination of Aggregate Orientation

The orientation of an aggregate can be measured by the angle between its longest axis and a horizontal line on the scanned image, as shown in Figure 8-3. The longest axis is defined as the greatest distance between two pixels of an aggregate boundary contour. Using the orientation of individual aggregates, statistical parameters can be calculated to quantify the directional distribution of aggregates.

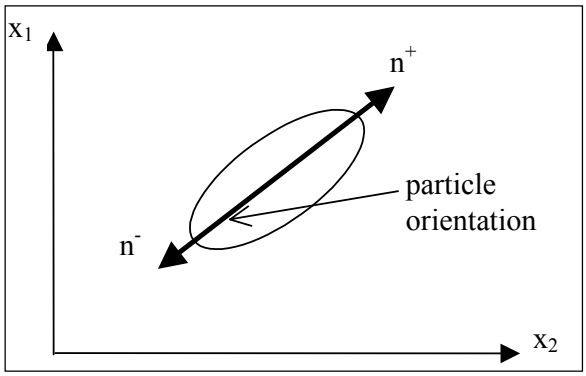

Figure 8-3. Particle orientation.

These parameters include the vector magnitude Δ and the average angle of inclination from the horizontal line θ were defined by Curray (1956) as:

1. $$\Delta = \frac{100}{N}\sqrt{\left(\sum \sin 2\theta_k\right)^2 + \left(\sum \cos 2\theta_k\right)^2} \quad (8.1)$$

2. $$\theta = \frac{\sum |\theta_k|}{N} \quad (8.2)$$

where θ_k = the angle from the major axis to the horizontal line of individual aggregate.

Δ = the vector magnitude, varies from 0% to 100%. Complete random distribution of aggregate orientation will give the value of % percent. Value of 100 percent means all the aggregates have the same direction.

The method to obtain the aggregate orientation was described by Masad et al. (1999; 2001; 2002). First samples are cut into vertical sections, as shown in Figure 8-4. The images of these vertical sections are captured by a digital camera connected to a computer, as shown in Figure 8-5. Using image analysis software ImageTools (1997), the aggregate orientation in two dimensions can be calculated.

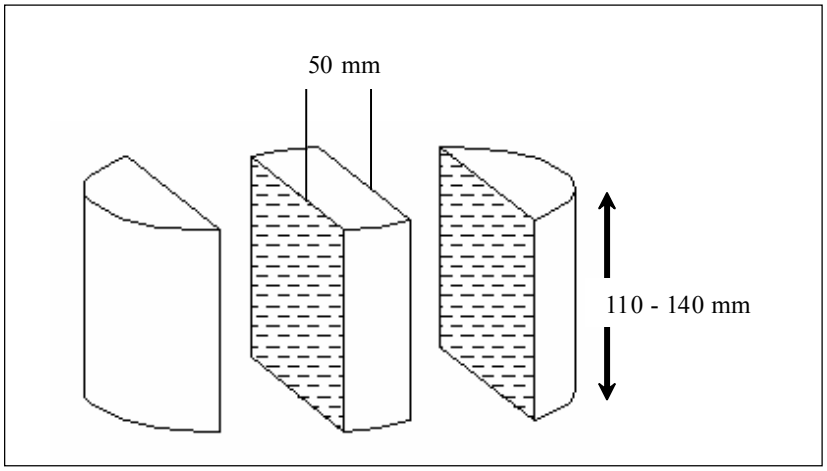

Figure 8-4. Vertical cuts of the specimen.

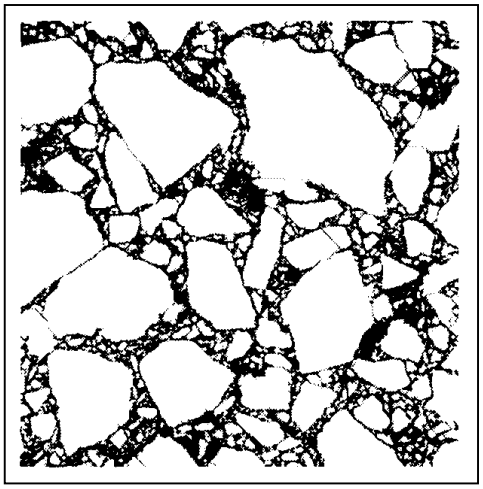

Figure 8-5. Image captured by digital camera, Masad et al. (2001).

To describe the three-dimensional distribution of aggregate orientation, the following tensor can be used:

3. $$M_{ij} = \begin{bmatrix} (1+\Delta)/(3+\Delta) & 0 & 0 \\ 0 & (1+\Delta)/(3+\Delta) & 0 \\ 0 & 0 & (1-\Delta)/(3+\Delta) \end{bmatrix} \quad (8.3)$$

The tensor is based on the following two key assumptions, proven applicable to HMA specimens by Masad et al. (2001):

- The specimen aggregates have an axial symmetry with a symmetry axis parallel to the vertical direction.
- The major and minor axes of the aggregate distribution correspond to horizontal and vertical directions.

The aggregate orientation methodology has been used successfully by Masad et al. (1999; 2002) to evaluate the development of the internal structure of AC mixes during laboratory compaction by the Superpave Gyratory Compactor and in the field.

8.3.2 Aggregate Segregation

Aggregate segregation has been recognized as a leading cause for poor performance of the HMA. Masad et al. (2002) proposed a method to evaluate segregation of HMA specimens. The image captured from the specimen was divided in two parts, the inner part, and the outer part, as shown in Figure 8-6. The average diameter of each part was calculated, followed by the calculation of the segregation as:

4. $$S_L = \left(\frac{\text{Average diameter of aggregates in the outer region}}{\text{Average diameter of aggregates in the inner region}} - 1 \right) \times 100\% \quad (8.4)$$

S_L indicated the lateral segregation. There is no segregation if $S_L = 0\%$.

This segregation characterization approach was used by Masad et al. (2001) to evaluate the effect of field and Superpave Gyratory Compaction on HMA specimens.

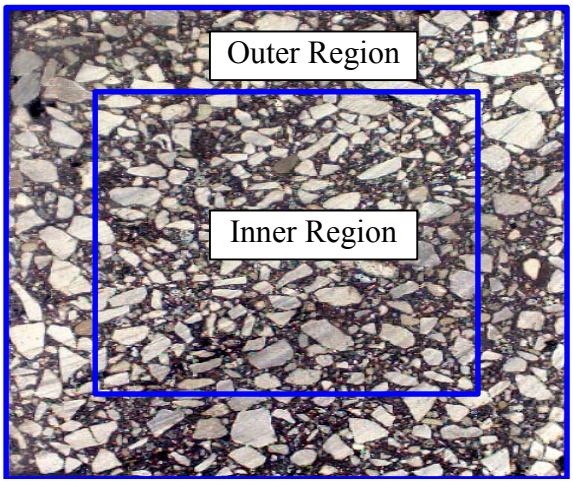

Figure 8-6. Inner and outer regions for segregation analysis, Masad (2001).

8.3.3 Surface Area Parameter

Another useful micromechanics-based parameter is the surface area parameter. The surface area parameter is defined as the ratio of total surface area of the void-solid phase interface, to the total volume of porous material. The specific surface area of aggregates is a comprehensive measurement of size, shape and roughness (Wang and Lai 1998). It also represents the gradation: fine aggregates have a larger specific surface area. In asphalt mixtures, the specific surface area of aggregates can be directly related to the asphalt binder thickness and therefore related to the rutting and fatigue performance of asphalt concrete.

In this research, the surface area parameter was estimated using X-Ray CT image analysis method as described by Al-Omari et al. (2002). It is calculated for each slice of the horizontal cut of the sample and assembled for the whole mix.

8.3.4 Air Void Distribution

Air void distribution controls the permeability and affects the aging characteristics of asphalt mixes. Tashman (2001) has conducted a study to characterize the air void distribution in Superpave gyratory specimens and field cores using an X-ray Computed Tomography system.

Masad et al. (1999) has described the procedure for quantifying air void distribution. In the image, the air voids are shown on dark color (e.g., Figure 8-2). A threshold gray intensity is selected. A gray intensity lower than the threshold intensity is considered to be an air void. Using the threshold value, the original image is transformed to a binary image of black (air voids) and white (solid). The image analysis software (UTHCSA image tool) was used to capture the size of all existing air voids on each image. The ratio of air voids area over the total area of each image gives the air voids for each slice. The stack of these slice values will result in the air void distribution.

8.3.5 Aggregate Contacts

Masad (2002) and Tashman (2001) have described the use of Image Pro Plus (1999) to determine aggregate contacts in mixtures. The main stress transfer mechanism among the particles is assumed to be through the stiffness of the mastic. The contact domain has the same thickness as the image resolution. The contact domains were captured by first converting the gray image to a binary image (Figure 8-7a). Then the aggregates in contact are separated using the "Watershed filter" (Figure 8-7 b). The image is then inverted in color and a "Thinning filter" is applied (Figure 8-7c). This image is combined with the original binary image using an "AND" logic operator. With this operator, two images (shown in Figures 8-7a and 8-7c) are compared, and the pixels that have the same black color (mastic) are allowed to remain (Figure 8-7d). The resultant image consists of segments of lines representing the region of aggregate contacts.

Work by Masad et al. (2001) has shown that aggregate orientation results in a better correlation to the mixture stiffness anisotropy than the number and size of aggregate contacts, although the aggregate contact characteristics have been considered traditionally as a key criterion for determining asphalt concrete anisotropy.

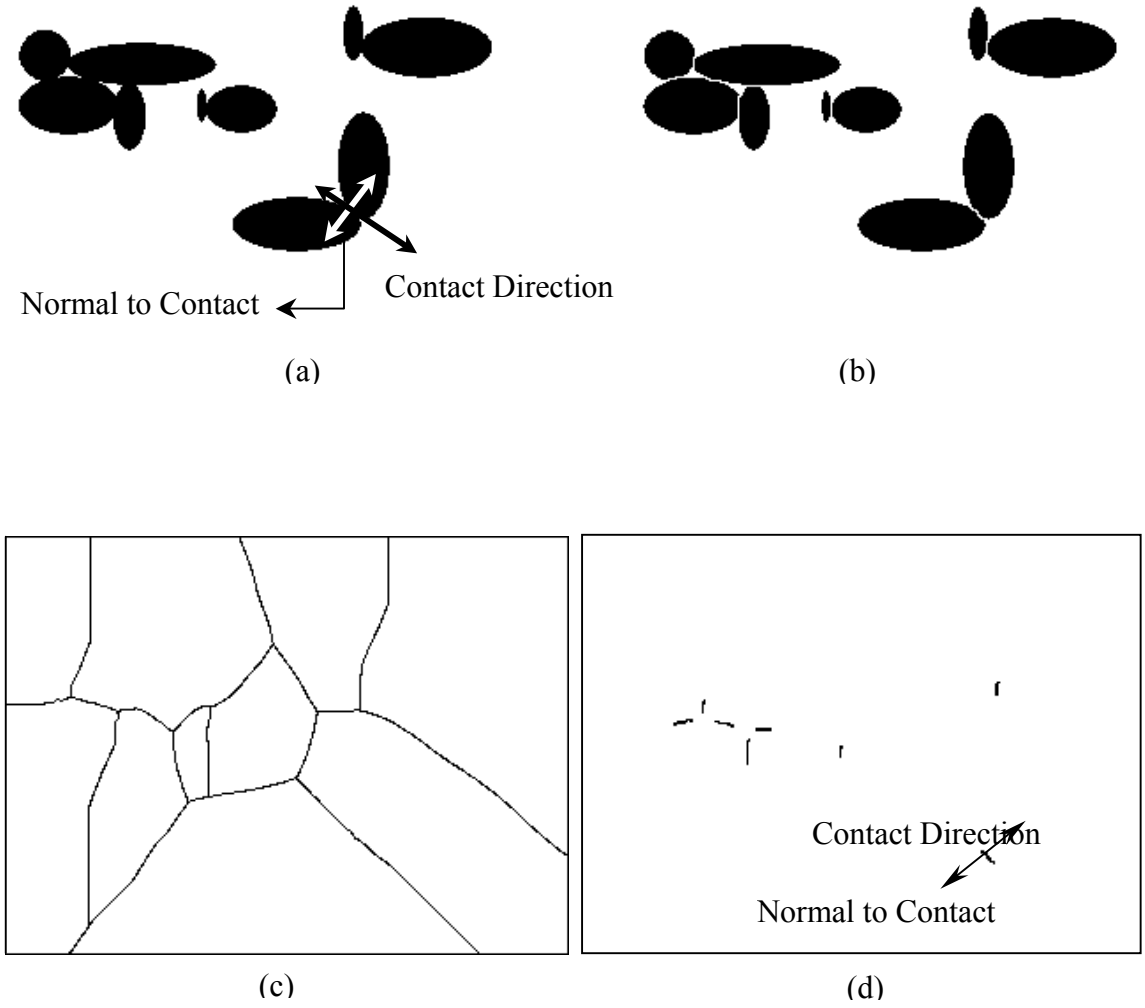

Figure 8-7. Illustration of the method for measuring aggregate contacts.

8.4 Asphalt Mixtures and Experimental Measurements

The specimens used in this part of the study were prepared using two types of aggregates: Georgia granite (GA) and Florida limestone (WR). These two aggregates are commonly used throughout Florida. Experience has shown that the limestone does not have significant potential for stripping whereas the granite does.

Both types of mixtures were prepared with coarse aggregate, fine aggregate, screenings, and mineral filler that were blended together in different proportions to make six different HMA

mixtures as shown in Table 8-1. All mixtures were designed to meet the Superpave volumetric requirements with a design number of gyrations (N_{des}) equal to 109 gyrations. The volumetrics of all mixes are reported in Table 8-2. The asphalt used to prepare these mixtures was PG 67-22 (AC-30). The C designation in Table 8-1 indicates coarse gradation passing below the restricted zone, while the F designation refers to fine gradation passing above the restricted zone. The dual designation of F3/C4 is used to indicate that this gradation was modified from a fine mix that is typically used in Florida to fall under the restricted zone with the purpose of achieving a higher permeability. The corresponding nomenclature of the limestone and granite specimens coincides with approximately the same gradation. All specimens were prepared to 7% target percent air voids. The purpose of varying the gradation was to obtain mixtures with different air void size distribution and permeability values but with the same aggregate type, in order to test the influence of these factors on moisture damage.

Permeability of the mixtures was measured using the falling head method according to the Florida DOT procedure (Choubane et al. 1998; 2000). The resistance to moisture damage was quantified using the HMA fracture mechanics-based framework discussed in Chapter 6. The HMA fracture mechanics framework is based on the existence of a fundamental fracture threshold. A strain energy based threshold delineates between healable micro-damage and non-healable macro-damage. Micro-damage is not related to crack initiation or crack growth and is totally healable after a resting period. On the other hand, macro-damage is associated with crack growth and the damage provoked is irreversible. It was found that the dissipated creep strain energy (DCSE) and the fracture energy (FE), define the threshold value for cyclic and continuously increasing loading conditions, respectively.

Table 8-1. Limestone and Granite Mixture Gradations

Sieve Size	Limestone: Percent Passing					
	WR-C1	WR-C2	WR-C3	WR-F1	WR-F2	WR-F3/C4
19 mm (3/4)	100.0	100.0	100.0	100.0	100.0	100.0
12.5 mm (1/2)	97.0	91.0	98.0	96.0	91.0	95.0
9.5 mm (3/8)	90.0	74.0	89.0	85.0	78.0	85.0
4.75 mm (#4)	60.0	47.0	57.0	69.0	61.0	67.0
2.36 mm (#8)	33.0	30.0	36.0	53.0	44.0	37.0
1.18 mm (#16)	20.0	20.0	24.0	34.0	35.0	26.0
600 μm (#30)	15.0	14.0	18.0	23.0	24.0	20.0
300 μm (#50)	11.0	10.0	13.0	15.0	16.0	14.0
150 μm (#100)	7.6	6.7	9.2	9.6	9.1	8.6
75 μm (#200)	4.8	4.8	6.3	4.8	6.3	5.8
Sieve Size	Granite: Percent Passing					
	GA-C1	GA-C2	GA-C3	GA-F1	GA-F2	GA-F3/C4
19 mm (3/4)	100.0	100.0	100.0	100.0	100.0	100.0
12.5 mm (1/2)	97.4	90.9	97.3	94.7	90.5	94.6
9.5 mm (3/8)	89.0	72.9	89.5	84.0	77.4	85.1
4.75 mm (#4)	55.5	45.9	55.4	66.4	60.3	65.1
2.36 mm (#8)	29.6	28.1	33.9	49.2	43.2	34.8
1.18 mm (#16)	19.2	18.9	23.0	32.7	34.0	26.0
600 μm (#30)	13.3	13.2	16.0	21.0	23.0	18.1
300 μm (#50)	9.3	9.2	11.2	12.9	15.3	12.5
150 μm (#100)	5.4	5.6	6.8	5.9	8.7	7.7
75 μm (#200)	3.5	3.9	4.7	3.3	5.4	5.8

Table 8-2. Volumetrics for Limestone and Granite Mixtures

Volumetric Property	Limestone						Granite					
	WR-C1	WR-C2	WR-C3	WR- F1	WR-F2	WR-F3/C4	GA-C1	GA-C2	GA-C3	GA-F1	GA-F2	GA-F3/C4
Max. Specific Gravity (G_{mm})	2.328	2.347	2.349	2.338	2.375	2.347	2.442	2.500	2.492	2.473	2.532	2.505
Binder Specific Gravity (G_b)	1.035	1.035	1.035	1.035	1.035	1.035	1.035	1.035	1.035	1.035	1.035	1.035
Bulk Specific Gravity (G_{mb})	2.235	2.255	2.254	2.244	2.281	2.254	2.442	2.399	2.391	2.473	2.433	2.404
Percent Binder (P_b)	6.5	5.8	5.3	6.3	5.4	5.6	6.63	5.26	5.25	5.68	4.56	5.14
Aggregate Specific Gravity G_{sb})	2.469	2.465	2.474	2.488	2.489	2.468	2.687	2.687	2.686	2.686	2.687	2.687
Aggregate Effective Specific Gravity (G_{se})	2.549	2.545	2.528	2.554	2.565	2.537	2.710	2.719	2.709	2.706	2.725	2.720
Absorbed Percent Binder P_{ba}	1.1	1.3	0.9	1.1	1.2	1.1	0.37	0.43	0.31	0.28	0.53	0.46
Effective Percent Binder P_{be}	5.3	4.6	4.5	5.3	4.2	4.5	6.32	4.85	4.96	5.42	4.06	4.70
Voids in Mineral Aggregates VMA (%)	15.4	13.8	13.6	15.6	13.2	14.0	18.5	15.4	15.7	16.6	13.6	15.1
Design Percent Air Voids Va (%)	4.0	3.9	4.0	4.0	3.9	3.9	4.0	4.0	4.1	4.0	3.9	4.0
Voids Filled with Asphalt VFA (%)	74.0	71.6	70.2	74.2	70.1	71.8	78.5	73.8	74.2	75.9	71.2	73.3
Dust to Asphalt Ratio D/A	1.0	0.8	1.2	0.8	1.4	1.0	0.6	0.8	0.9	0.6	1.2	1.2

These limits can be determined from a tensile strength test and resilient modulus test using the Superpave Indirect Tensile test (Roque et al. 2002). The DCSE corresponds to the area under the tensile strength/strain curve that is not recoverable and can be calculated as the total area under the curve (i.e., fracture energy), minus the area that corresponds to the elastic energy. The elastic energy is equal to the area under this curve limited by a line with slope equal to the resilient modulus, and a vertical line that crosses the x-axis at the strain at failure. Hence, in order to know what the elastic energy at fracture is, it is vital to determine in advance the resilient modulus of the mix.

In Chapter 6, it was shown through the determination of the Superpave Indirect Tension Test fracture parameters (i.e., creep, resilient modulus, and tensile strength, tests) on conditioned and unconditioned mixtures that the effects of moisture damage on the multiple parameters associated with the fracture resistance of mixtures could be summarized into one single number. This number corresponded to the number of cycles to failure N_f, required to grow a 1- inch crack length. This number is calculated based on the crack growth law model developed by the same authors.

In order to simplify the evaluation of moisture damage, The Energy Ratio (ER) was proposed in Chapter 7, as a parameter to assess the mix resistance to moisture damage taking into account different key mixture properties that get affected. This ratio was developed based on forensic research of 36 field pavement sections of known cracking performance and is a function of the same parameters that are considered in the calculation of N_f. The ER is defined as:

5. $$ER = \frac{DCSE_f}{DCSE_{min}} = \frac{a \cdot DCSE_f}{m^{2.98} \cdot D_1} \quad (8.5)$$

where $DCSE_f$ is the dissipated creep strain energy to fracture, $DCSE_{min}$ is the minimum dissipated creep strain energy for adequate cracking performance, D_1 and m are parameters obtained from creep test, and a is a function of the tensile strength S_t, and the average tensile stress of asphalt layer σ_{avg} (psi), ($a = 0.0299\ \sigma_{avg}^{3.1}\ (6.36\text{-}S_t) + 2.46 \times 10^{-8}$). An average tensile stress of 120 psi was used.

The ER and N_f parameters were used in this study to assess moisture damage by calculating the ratio between the conditioned (C) and the unconditioned (U) values of these parameters. The Superpave IDT was used to test unconditioned and conditioned samples in order to determine these two parameters. The specimens were moisture conditioned similar to that required by AASHTO T-283 achieving a target saturation of 65 to 80 percent by allowing vacuum saturation during 15 minutes (changes in AASHTO T-283 in 2003 require a saturation level of 70-80 percent. Next, the specimen was placed in water bath without vacuum for an additional 15 minutes. If the minimum saturation was not achieved, another cycle was done until the target was attained. Finally, the specimen was placed in a water bath at 60° C for 24 hours and was allowed to drain for 24 hours, after which the specimens were cut into approximately 50-mm thick Superpave IDT specimens; then each cut specimen was placed in a dehumidifying chamber for 48 hours.

As can be seen in Figure 8-8, the granite specimens had smaller ER ratio, and hence, were more susceptible to moisture damage due to conditioning than the limestone specimens. These results were consistent with the moisture damage calculated using the N_f ratio (Figure 8-9), but the difference between the two mixes was more pronounced in the ER ratio than in the N_f ratio.

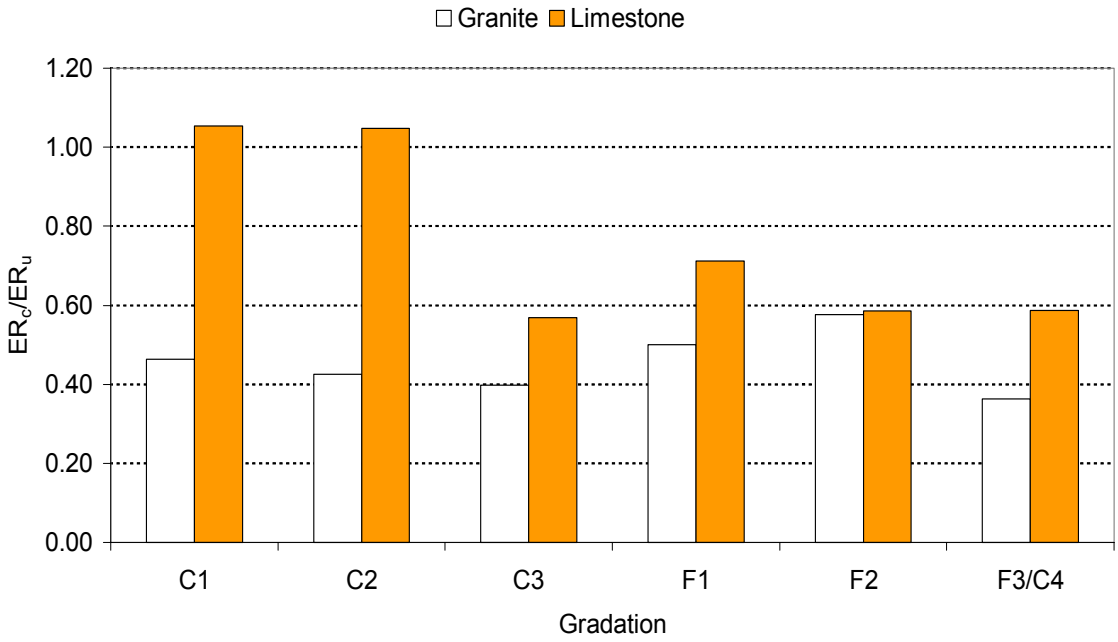

Figure 8-8. Comparison between granite and limestone using the ER ratio.

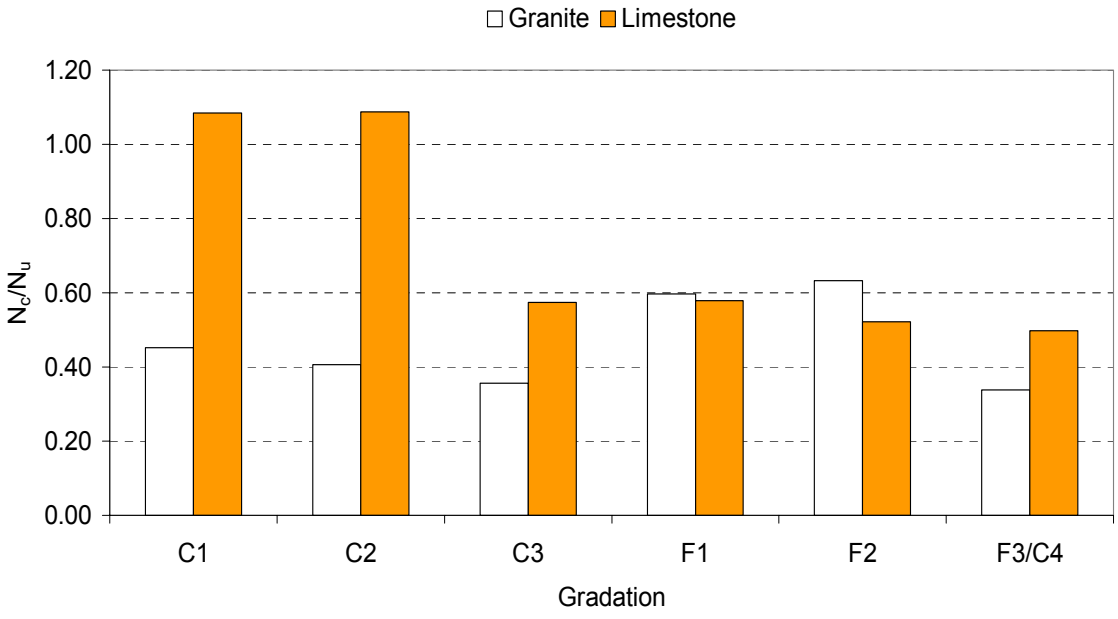

Figure 8-9. Comparison between granite and limestone using the N ratio.

8.4.1 Initial Micromechanical Analysis of Granite Mixtures Tested

Using digital images from X-ray Computed Tomographic imaging of the granite mixtures studied, an initial analysis of the relationship between micromechanical parameters and level of moisture damage was conducted. This methodology consists of studying the interior of opaque solid objects in a non-destructive fashion. Two-dimensional images or most commonly known, "slices," can be obtained through this process. Each slice reveals the interior of the object on a plane, and if stacked together, the slices can build up a three dimensional object. These slices are 1 mm in thickness with an overlap of 0.2 mm in between slices.

Specimens were scanned with a resolution of 0.195 mm/pixel. Images are captured in a grey scale that consists of 256 levels; each level corresponds to a density within the specimen. Therefore, in order to analyze the images, they have to be transformed into a binary format such that the voids can be isolated from the mastic and aggregates. By doing so, air voids appear in black, and all other phases appear in white. This procedure is done by setting a threshold value of grey intensity such that every pixel with an intensity value above the threshold is turned to black and every pixel with an intensity value below the threshold is turned to white. This threshold was determined in this study by finding an intensity value such that the total percent air voids calculated from the 3-D image analysis, matched the value obtained using the AASHTO T166 method.

After obtaining the binary images, air void size distribution was determined using a macro that was written in IPBasic, which is a built in language of ImagePro Plus (1999). The purpose of this macro was to load the whole set of images and quantify the diameter of each air void in these images. This data was used to determine the air void size distribution for each of the specimens.

Figures 8-10 and 8-11 show the ratio of conditioned to unconditioned ER for the granite mixtures tested versus the average total number of air voids. Interestingly, the number of air voids is inversely proportional to the water damage susceptibility. This means that the larger the number of air voids, the more the water damage affects the specimens.

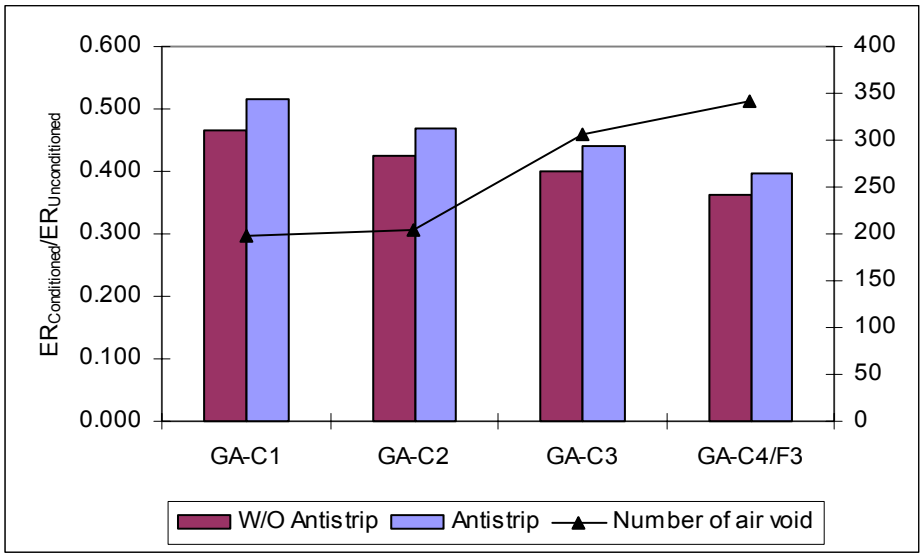

Figure 8-10. Correlation between the number of air void and energy ratio for coarse-graded granite mixtures.

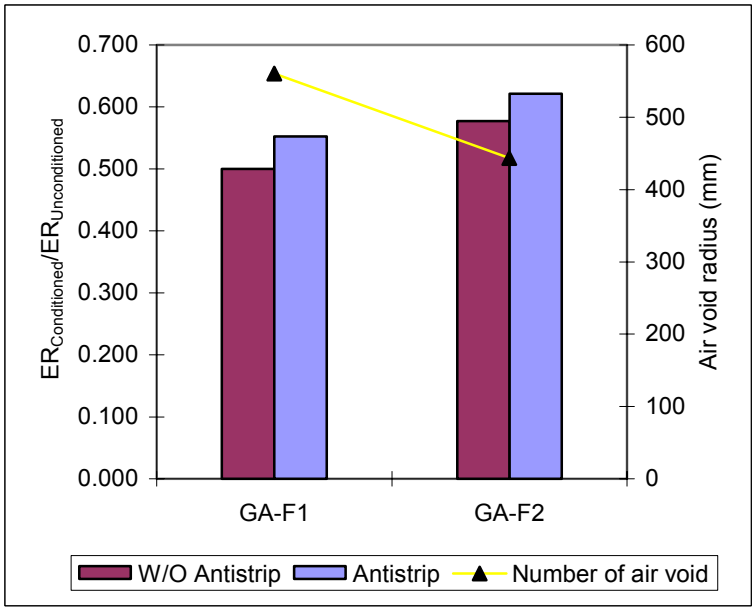

Figure 8-11. Correlation between the number of air void and Energy Ratio for fine-graded granite mixtures.

Similarly, the average air void radius versus the ER are plotted in Figures 8-12 and 8-13. The decrease in the average air void radius leads to the increase in water damage.

This again makes sense, since all of the mixtures had the same target percent air voids of 7 ±0.5 percent, implying that the decrease in the air void radius should lead to an increase in the number of air voids as shown earlier.

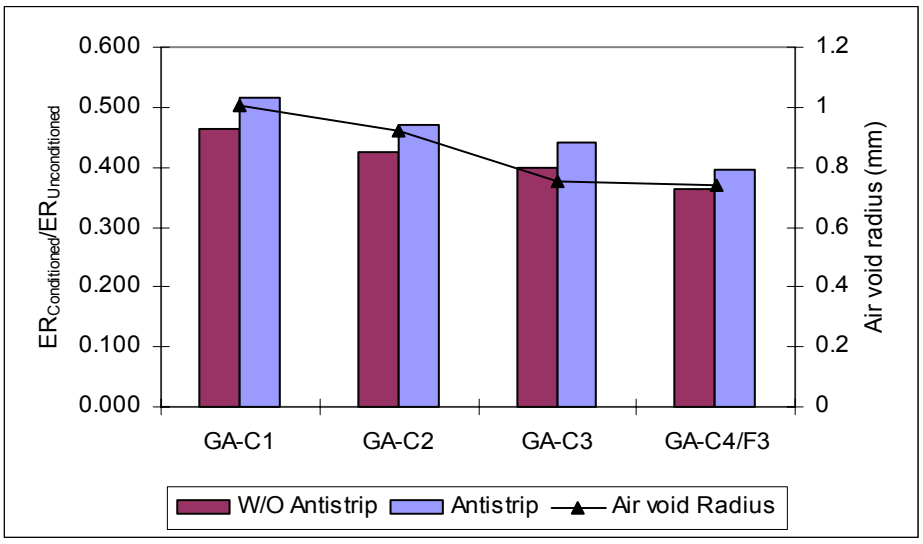

Figure 8-12. Correlation between the air void radius and energy ratio for coarse-graded granite mixtures

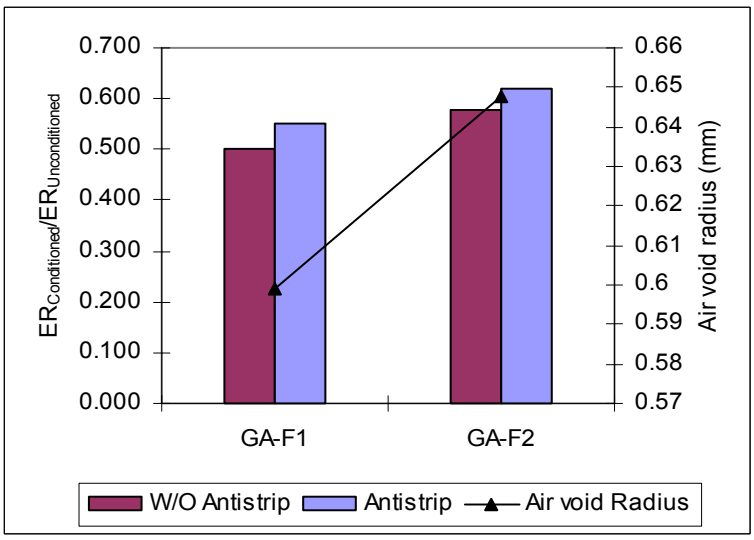

Figure 8-13. Correlation between the air void radius and energy ratio for fine-graded granite mixtures.

Figures 8-14 and 8-15 show the ratio of the conditioned versus unconditioned ER plotted against the surface area parameter. Interestingly, even though the fine mixtures in Figure 8-15 show an inverse relationship between the ER ratio and the surface area parameter, the coarse-graded mixtures in Figure 8-14 do not show a clear relationship.

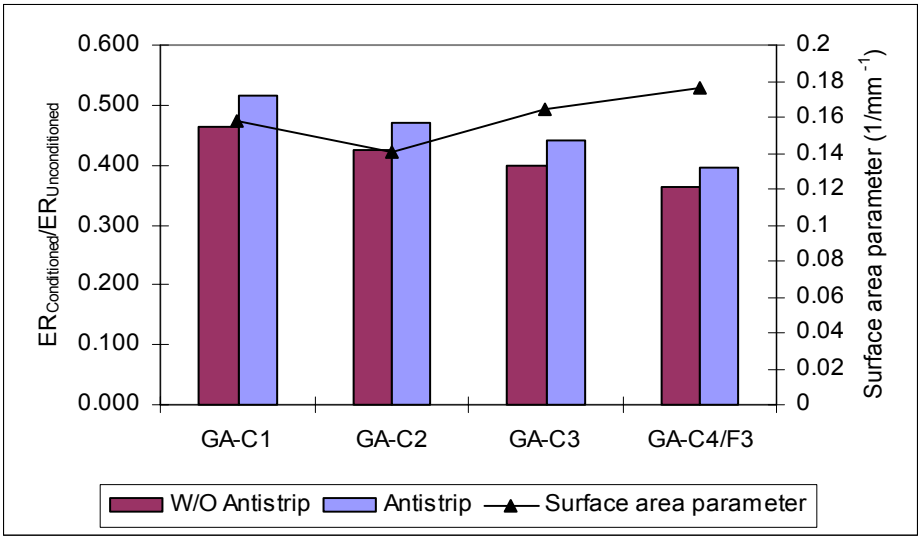

Figure 8-14. Correlation between the surface area parameter and energy ratio for coarse-graded granite mixtures.

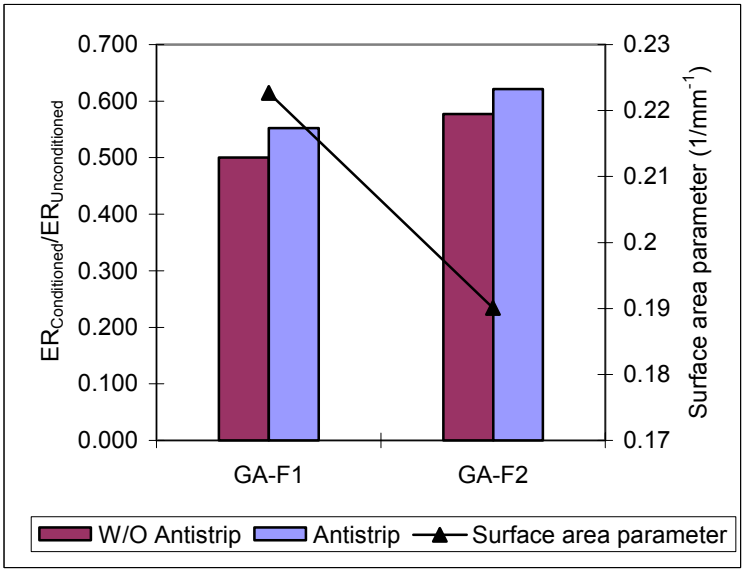

Figure 8-15. Correlation between the air void radius and energy ratio for fine-graded granite mixtures.

Finally, Figures 8-16 and 8-17 show the ratio of the conditioned versus unconditioned ER plotted against the percent air voids for the granite mixtures studied. Again, there is no discernable relationship between percent air voids and moisture damage. This may be in part due to the fact that all of the mixtures did have the same target air voids of 7 ± 0.5 percent, effectively leading to a normalization of the results with respect to percent air voids.

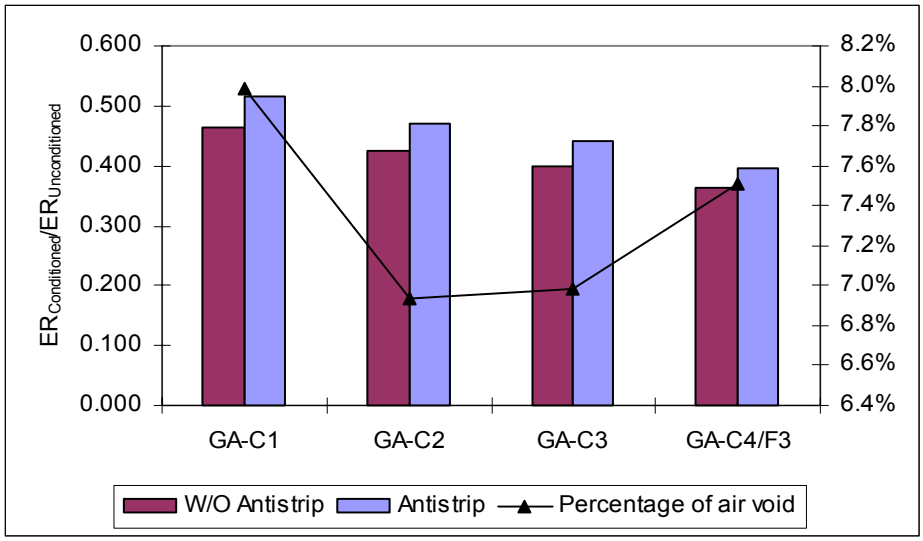

Figure 8-16. Correlation between the percentage of air void and energy ratio for coarse-graded granite mixtures.

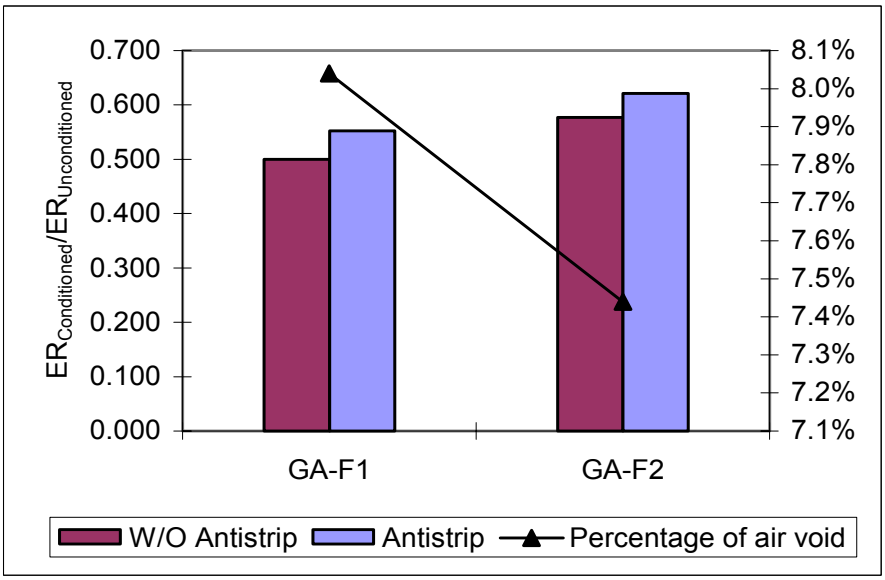

Figure 8-17. Correlation between the percentage of air void and energy ratio for fine-graded granite mixtures.

In order to gain a more definitive insight into the potential relationship between mixture damage as quantified the ER and micromechanical parameters, a statistical evaluation of the distribution of voids in the mixtures studied was performed and presented below.

8.5 Probabilistic Characterization of Air Void Distribution

Using the results from the X-Ray CT imaging technique, a probabilistic analysis of the air voids distribution in the limestone and granite mixtures was performed. The statistical quartiles of air void sizes were calculated as shown in Table 8-3. It can be seen that there were different air void sizes within the same mix type due to the different aggregates gradations. It is interesting to note that although the limestone and granite mixes had corresponding gradations, the granite mixes had in general larger air voids. The differences in the quartiles of each pair of corresponding gradations of the granite and limestone specimens (Granite air void Size – Limestone Air Void Size) are shown in Figure 8-18. The positive difference indicates larger air voids in the granite mixes. The difference between the granite and limestone mixes was more evident for the coarse gradations. This can be observed in the three dimensional visualizations of air voids and corresponding distributions for WR-C1 and GA-C1 specimens in Figure 8-19. It is evident that that limestone mixes had more and smaller air voids than the granite mixes.

The air void distribution was quantified by using the first and second moments about the origin of the air void size distribution as follows:

6. $$E(x) = \int_{x_{min}}^{x_{max}} x_i f(x_i) dx \tag{8.6}$$

7. $$E(x^2) = \int_{x_{min}}^{x_{max}} x_i^2 f(x_i) dx \tag{8.7}$$

Table 8-3. Quartiles of Air Void Size Distribution

Specimen	Diameter (mm)		
	1st Quartile	2nd Quartile	3rd Quartile
GA-C1	0.804	1.283	2.048
GA-C2	0.673	1.094	1.778
GA-C3	0.581	0.918	1.450
GA-F1	0.456	0.706	1.091
GA-F2	0.421	0.665	1.051
GA-F3/C4	0.531	0.850	1.359
WR-C1	0.602	0.957	1.522
WR-C2	0.554	0.890	1.429
WR-C3	0.488	0.780	1.246
WR-F1	0.425	0.655	1.009
WR-F2	0.387	0.609	0.958
WR-F3/C4	0.473	0.756	1.207

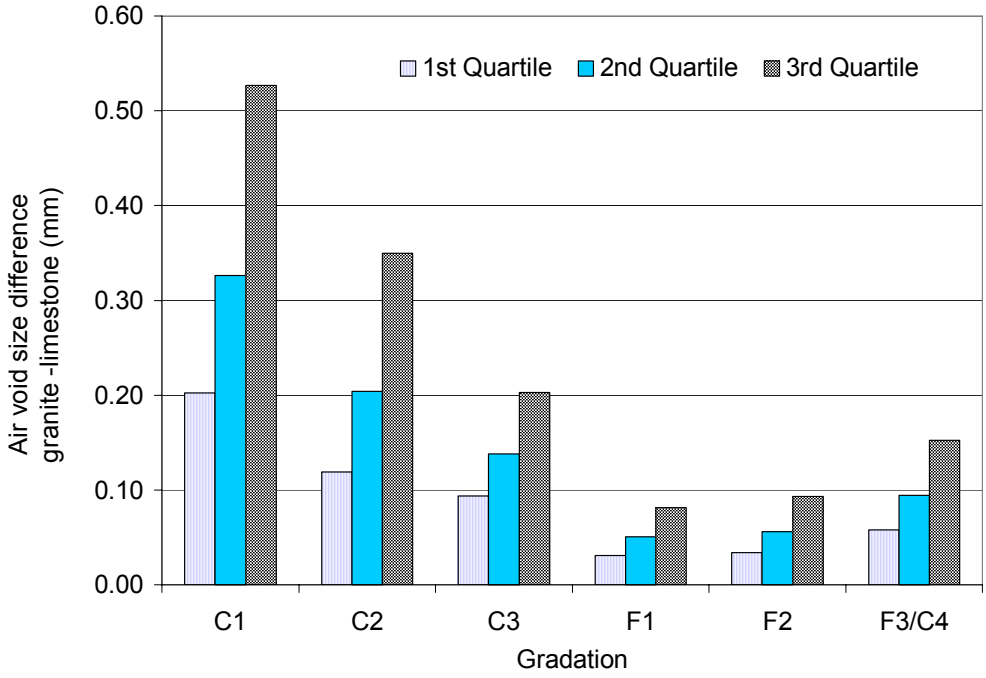

Figure 8-18. Quartile air void size difference between granite and limestone.

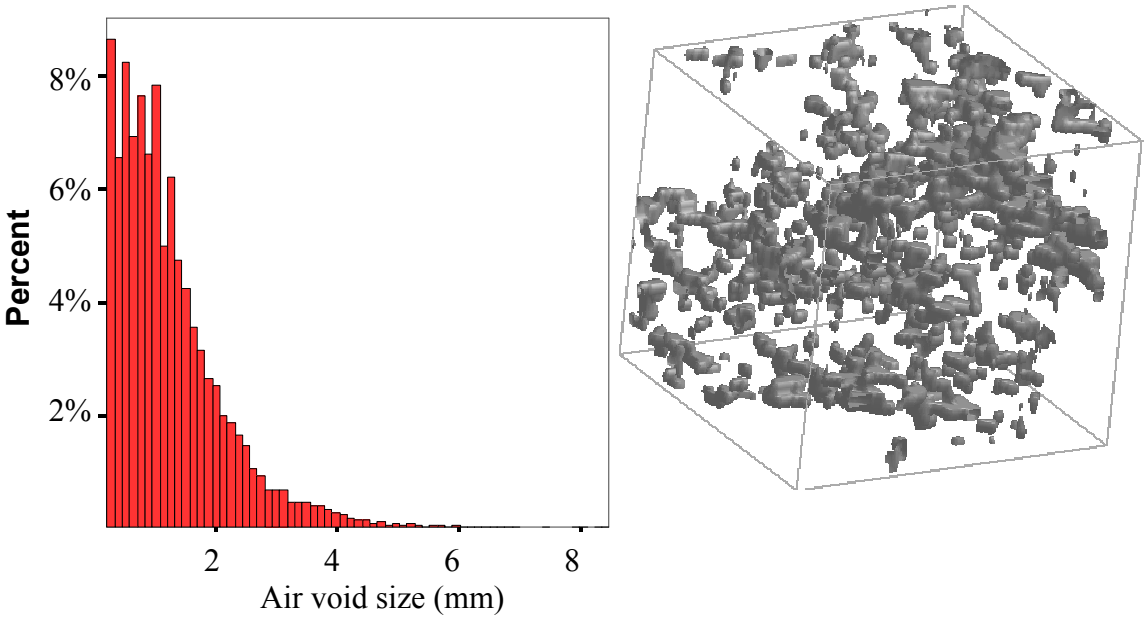

(a)

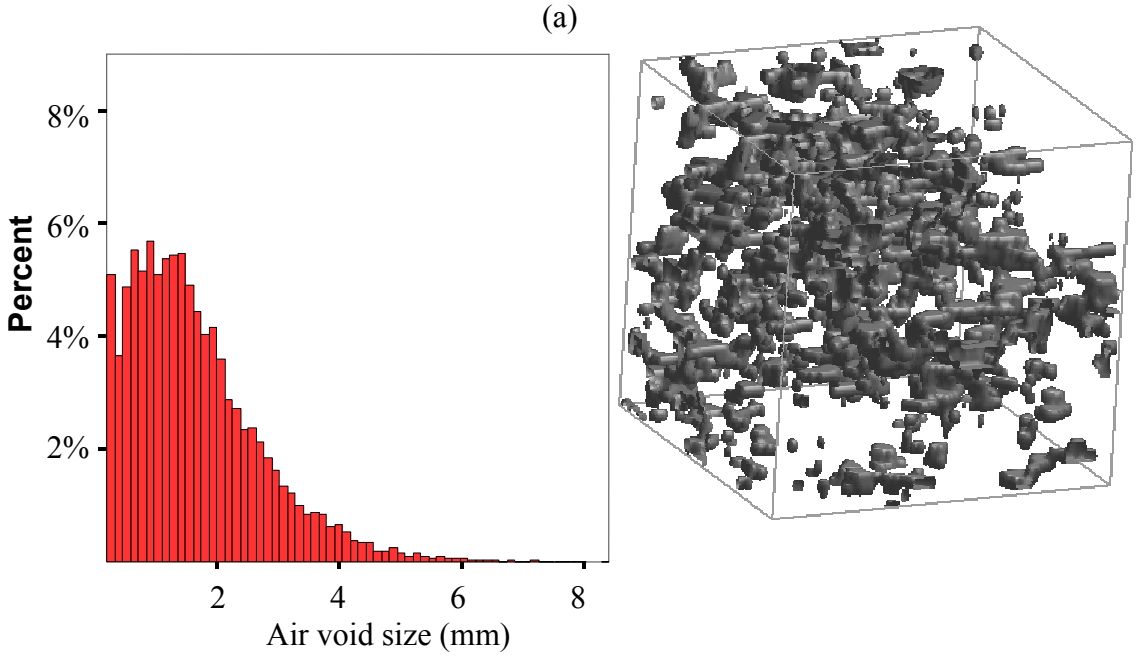

(b)

Figure 8-19. Distributions and three-dimensional visualization of air voids: (a) WR-C1; (b) GA-C1.

Where x_{min} and x_{max} are the minimum and maximum air void diameters, respectively, x_i is a random variable that represents the diameter of an air void, and $f(x_i)$ is the probability density function of air voids. The first moment ($E(x)$) is the expected value or mean of air void diameter, and the second moment ($E(x^2)$) is the expected value of the diameter squared.

The probability density function of air void size distribution was determined in order calculate the statistical parameters in Equations 8.6 and 8.7. The Pearson correlation coefficient was used to establish the degree of linearity between the cumulative probability of the data and the expected cumulative probability of a test distribution. The closer this coefficient is to one, the better the correlation between the two cumulative probabilities. Overall, the Lognormal distribution had the best fit with the air void distribution (Castelblanco 2004). The significance of the two statistical parameters in Equations 8.6 and 8.7 in terms of permeability and moisture damage is discussed in the following sections.

8.6 Permeability

Permeability is a very important property that affects moisture damage. Therefore, it is necessary to understand the relationship between air void size distribution and permeability. The variable diameter capillary model developed by Garcia-Bengochea (1978) for soils was used to find the relationship between permeability and air void distribution. This model was applied based on the assumption that the probability that air voids on two adjacent slices (consecutive images) are connected is completely correlated. This assumption is motivated by the very small distance (i.e., 0.8 mm) between adjacent slices. Also, this assumption is concurrent with the extreme case described by Huang and Holtz (1986). According to the model, the permeability is expressed as:

8. $$k = C_s n \int_{x_{min}}^{x_{max}} x_i^2 f(x_i) dx \qquad (8.8)$$

Where k is permeability, C_s is shape factor, n is percent air voids or porosity, and $f(x_i)$ is the probability density function of the distribution.

Garcia-Bengochea (1978) defined the pore size parameter (PSP) as the product of the percent air voids and the expected value of the air void diameter square. Therefore, the permeability can be expressed as:

$$k = C_s \ PSP, \ PSP = nE(x^2) \tag{8.9}$$

It was found that the relationship between k and PSP can be better described using the form in Equation 8.10 instead of that in Equation 8.9 (Garcia-Bengochea 1978):

$$\text{Log } k = m\log PSPS + b \tag{8.10}$$

Equation 8.10 represents a straight line with Log k as the dependent variable, and regression parameters m, and b, obtained from the fitted curve. Equation 8.10 can also be written as:

$$k = 10^b (PSP)^m \tag{8.11}$$

Equation 8.11 is equivalent to Equation 8.9 when $C_s = 10^b$ and m=1. The shape factor C_s, is included in order to account for the effect of the fluid properties, as well as to the shape of the voids. The integral in Equation 8.8 was calculated by setting up a macro written in Maple (2004), with the integral limits and the log normal probability density function parameters were obtained from the statistical analysis of air void sizes using Minitab (2002). The relationship between k and PSP is shown in Figure 8-20. The correlation coefficients from the regression analysis are fairly good.

8.7 Moisture Damage

In this section, the relationship between moisture damage, air void distribution, and material surface properties is investigated further.

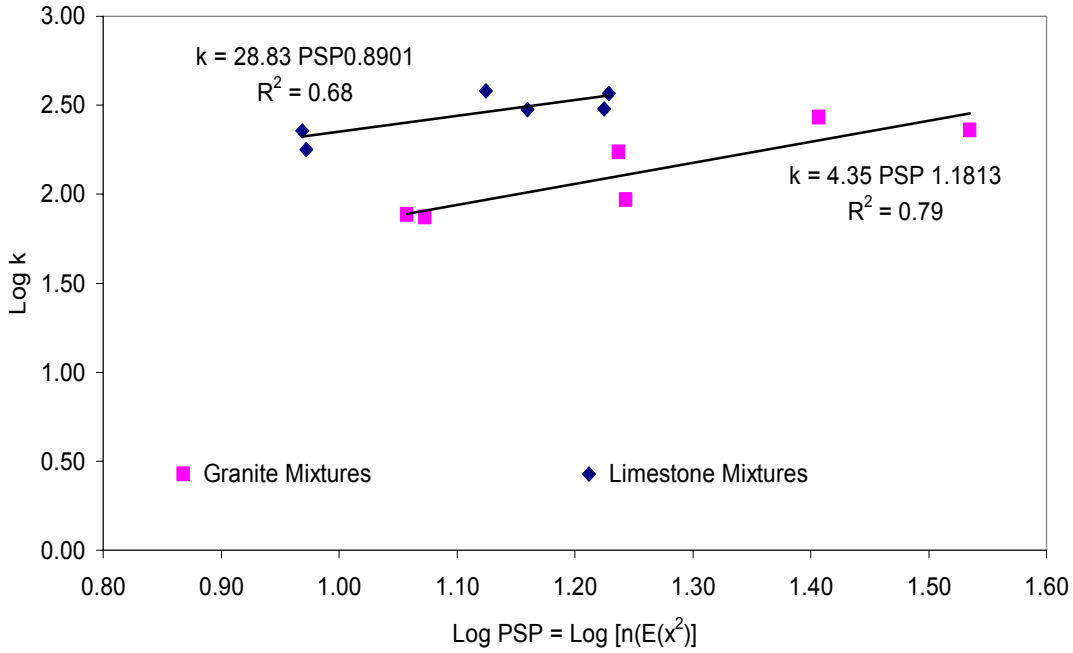

Figure 8-20. Permeability versus PSP using lognormal distribution (k is measured in 10^{-5}cm/sec).

8.7.1 Air Void Size

The relationships between the expected value of air void diameter (Equation 8.6) and ER and N ratios are shown in Figures 8-21 and 8-22. A polynomial regression trend line was used to fit the data as it gave the best correlation coefficient. For the granite mix, the N_f and ER ratios decreased with an increase in air void size until they reached a minimum value; after which these ratios started to increase again with an increase in air void size. The same trend, but not as clear, was also found for the limestone mixes.

From the patterns in Figures 8-21 and 8-22, it can be inferred that there is an average diameter size or a "pessimum size" at which moisture damage is maximum. A possible interpretation of this behavior is that small air void sizes reduce the infiltration of water to the mix, while large air voids make it easier for the water to drain out of the mix. Hence, good resistance to moisture damage is obtained at these two levels of air void sizes. However, there is

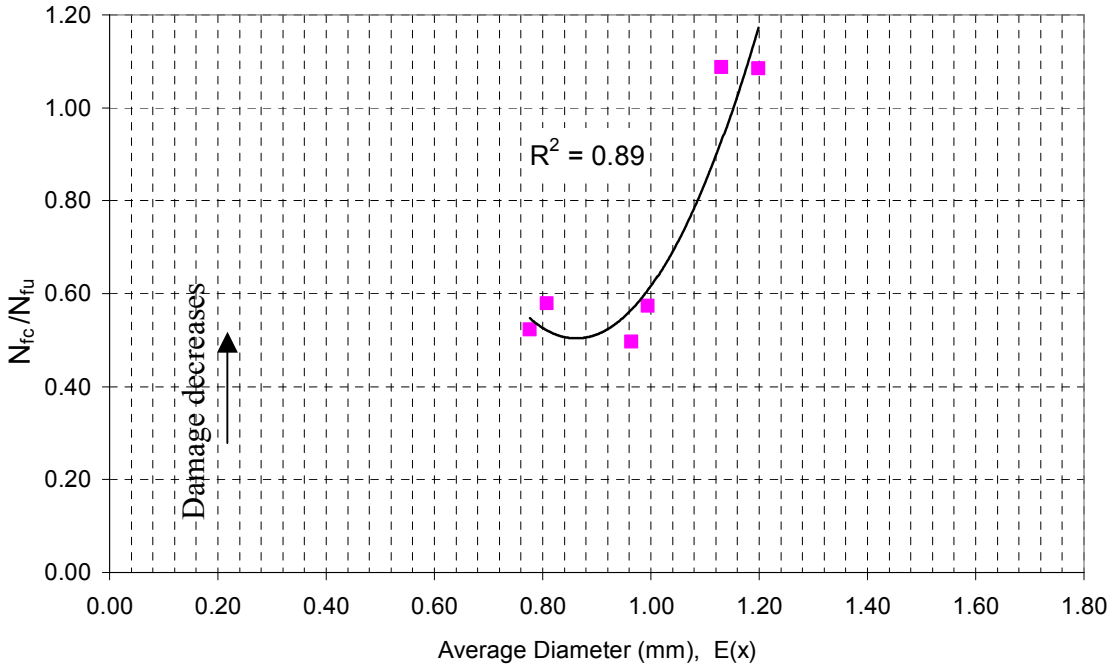

(a)

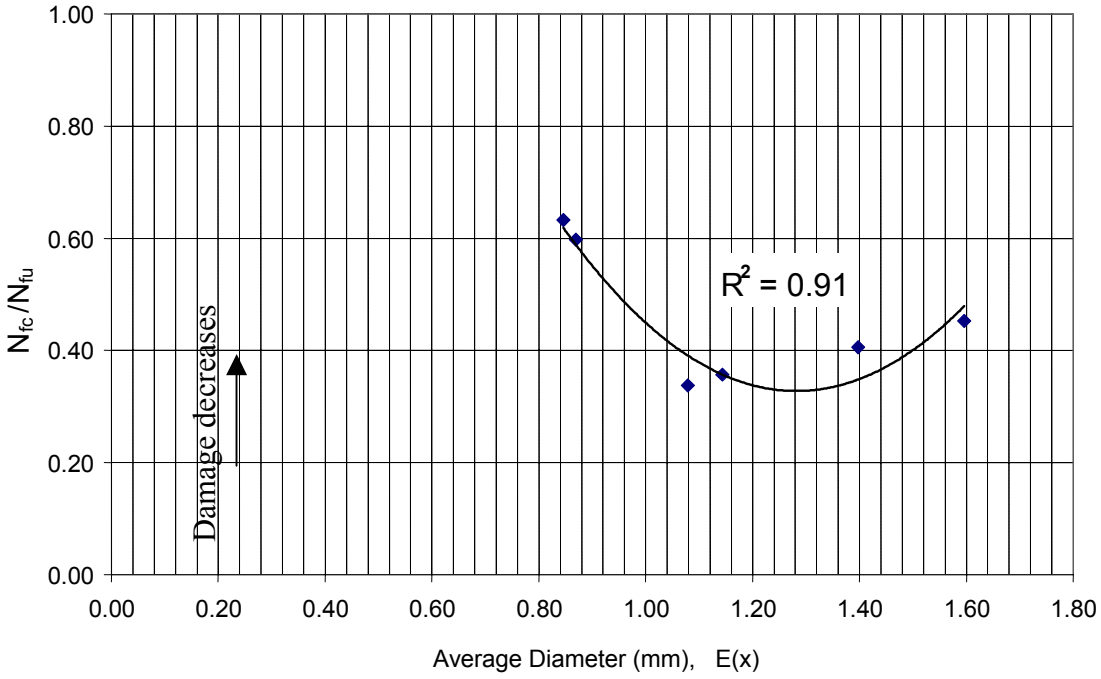

(b)

Figure 8-21. ER ratio as a function of average air void diameter: (a) limestone and (b) granite.

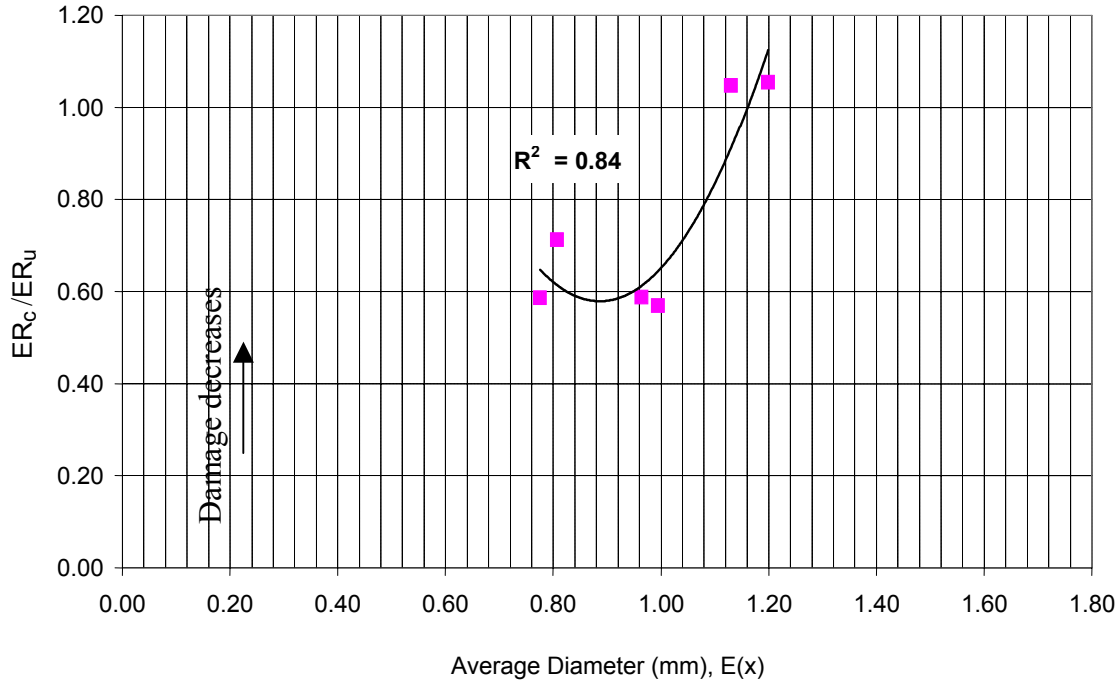

(a)

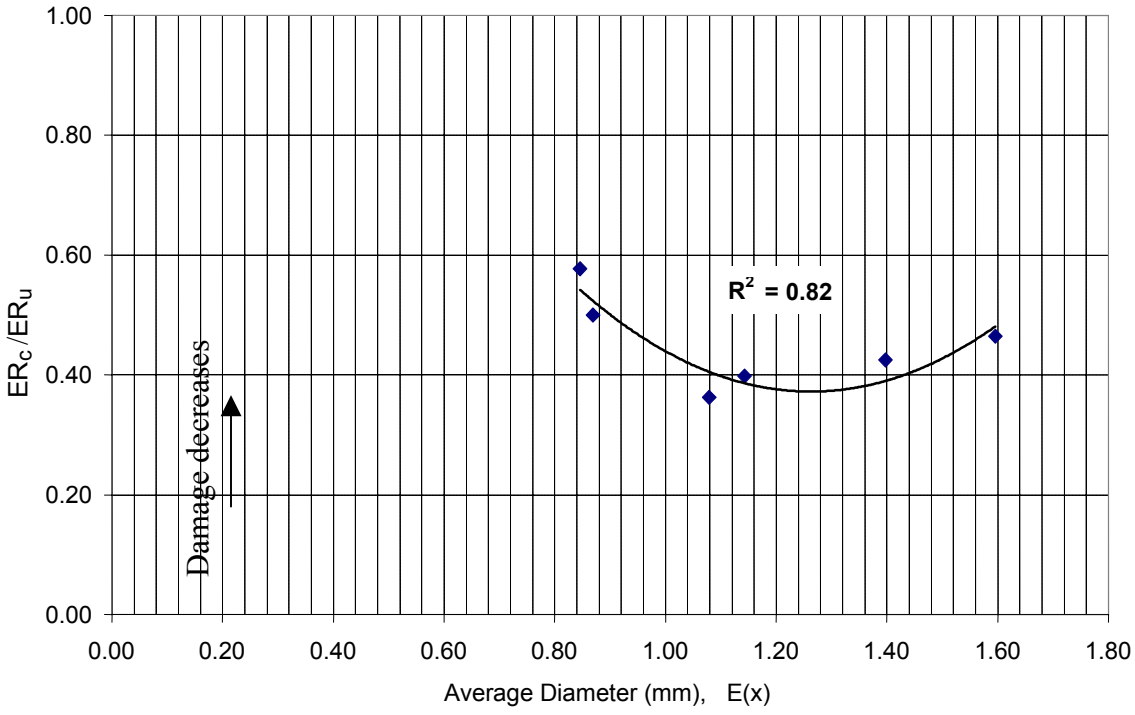

(b)

Figure 8-22. N_f ratio as a function of average air void diameter: (a) limestone and (b) granite.

a “pessimum” air void where water gets into the mix and it is difficult to drain it out leading to more moisture damage. This “pessimum” air void size depends on the type of the mix as shown in Figures 8-21 and 8-22. It was in the range between 1.2 and 1.4 mm for the granite mix; whereas it was in the range between 0.8 to 1.0 mm for the limestone mix.

A comparison between the air void size and permeability in Figure 8-20 and between permeability and moisture damage in Figure 8-23 emphasizes that moisture damage is not proportional to permeability. The greatest moisture damage (smallest N and ER ratios) occurred at intermediate permeability values which corresponded to the “pessimum” air void sizes. The concept of “pessimum” air void size and corresponding permeability values can be used to design mixes with better resistance to moisture damage.

A similar idea to the “pessimum” air void size was presented by Terrel et al. (1993), but for the total percent air voids. These authors found that there are three ranges of air void content that affect a mixture resistance to moisture damage differently. These ranges correspond to a low (impermeable), (intermediate), and high (free drainage) air void contents. The intermediate range of percent air voids was referred to as “pessimum” since specimens in this range experienced more moisture damage than specimens with percent air voids that belonged to the ranges of low and high percent air voids.

8.7.2 Surface Energy

The chemical composition of aggregates and binder play a major role in assessing their resistance to moisture damage. Therefore, air void distribution can be used to study moisture damage in specimens made from the same aggregate and binder, but it is not sufficient to analyze the difference in moisture damage between the granite and limestone mixes.

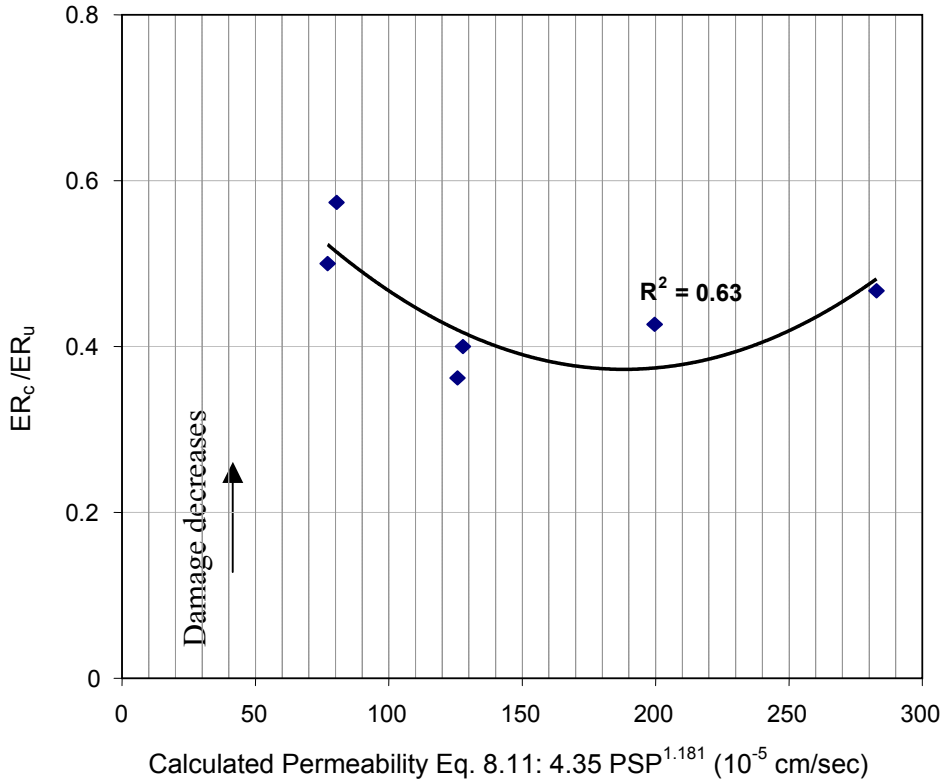

(a)

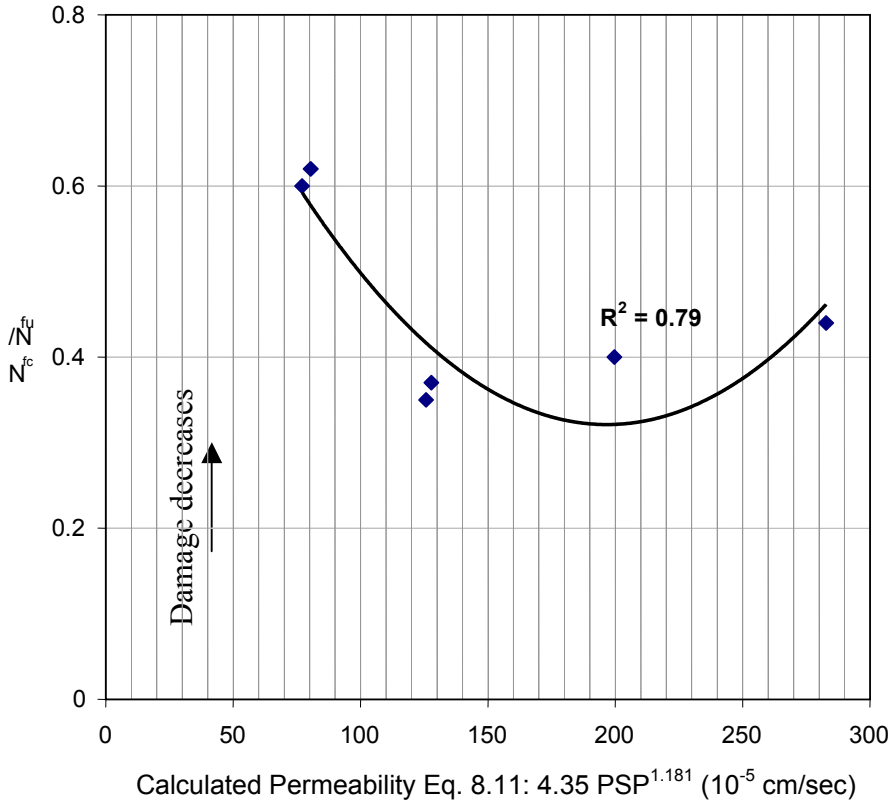

(b)

Figure 8-23. ER and N ratios as a function of calculated permeability for granite mixes.

The resistance of asphalt mixes to cohesive and adhesive damage due to moisture has been recently evaluated using the theory of surface energy. This theory allows calculating the cohesive and adhesive bonds in the mix and the resistance to fracture and healing under dry and wet conditions (Lytton 2004). An adhesive fracture is characterized by loss of attraction between the molecules at the interface between the asphalt and the aggregate. On the other hand, a cohesive fracture presents cracks within the asphalt itself. The total bond energy that governs the fracture of the material can be expressed as:

12. $$\Delta G = \Delta G^{LW} + \Delta G^{AB} \quad (8.12)$$

Where ΔG is the total bond energy, ΔG^{LW} is the Lifshitz-van der Waals apolar component of the bond energy, and ΔG^{AB} is the acid-base polar component of the surface free energy.

The bond energy components in Equation 8-12 are calculated as a function of the surface energies of the mix constituents. Schapery's fundamental law of fracture explains this surface energy as a balance between the strain energy that is released when a crack propagates and the energy that is necessary to surmount the viscous resistance of the material where the energy is released (Cheng et al. 2002).

The surface free energies of the aggregates and binder were measured such that a better understanding of moisture damage due to the presence of water could be attained. The Wilhelmy plate method and the Universal Sorption Device (USD) method were used to measure the surface free energy components of the asphalt and the aggregates, respectively, under fracture (dewetting) and healing (wetting) processes. Further details on these procedures are described in Lytton (2004). The adhesive and cohesive bond strengths were calculated from these surface energy measurements (Cheng et al. 2002; Lytton 2004). The resistance to fracture increases as the total dewetting or facture bond energy increases. The healing potential is enhanced with an

increase in the acid base component of the wetting bond energy. On the other hand, the Lifshitz-van der Waals component of the wetting bond energy affects healing negatively (Cheng et al. 2002).

As can be seen in Table 8-4, water increases the asphalt ability to heal (an increase in the acid base component) and reduces its resistance to fracture (a decrease in the total fracture bond energy). As explained by Cheng et al. (2002), this phenomenon occurs because the hydrogen atoms that the water has have good interaction or affinity with those of the AB component of the asphalt; hence, water makes the hydrogen bonds stronger, and enhances the healing capability. This reinforces the fact that, it is beneficial to have a greater AB component and a low LW component. However, the bonding of these hydrogen atoms, takes time and therefore it is associated with the long term healing of the asphalt (Cheng et al. 2002).

Limestone has better resistance to fracture than granite under dry conditions as indicated by the higher total fracture energy. Also, it can be inferred from the bond strength energies that the limestone has better resistance to fracture when water is present because its energy components are less negative compared to the granite. On the other hand, when water is in the interface, the limestone has a better capability to heal since its acid-base component is less negative,

Table 8-4. Cohesive and Adhesive Bond Energies under Dry and Wet Conditions (ergs/cm^2)

Component	Condition	Fracture	Healing	
		ΔG_b	ΔG_h^{LW}	ΔG_h^{AB}
Binder	Dry	90.5	43.36	1.80
	Wet	37.49	0.00	58.63
Granite + Binder	Dry	152.6	72.8	29.0
	Wet	–72.0	–0.08	–89.58
Limestone + Binder	Dry	168.4	87.6	26.1
	Wet	–60.7	–0.12	–82.05

thus there is less detachment of the asphalt from the aggregate. These results explain the better resistance of the limestone mixes to moisture damage compared with the granite mixes, although both mixes were deigned using similar gradations and volumetrics.

8.7.3 Simulation of Fluid Flow in Asphalt Pavements

X-ray CT was used to analyze the vertical distribution of air voids in field cores (Masad et al. 2005). Examples of some of the results are shown in Figure 8-24. As can be seen there are vertical gradients in the percent air voids in almost all cores but to different extents. It is expected that these gradients would affect the water flow patterns in asphalt mixes. In order to investigate this effect, the cores from two projects that had comparable average percent air voids

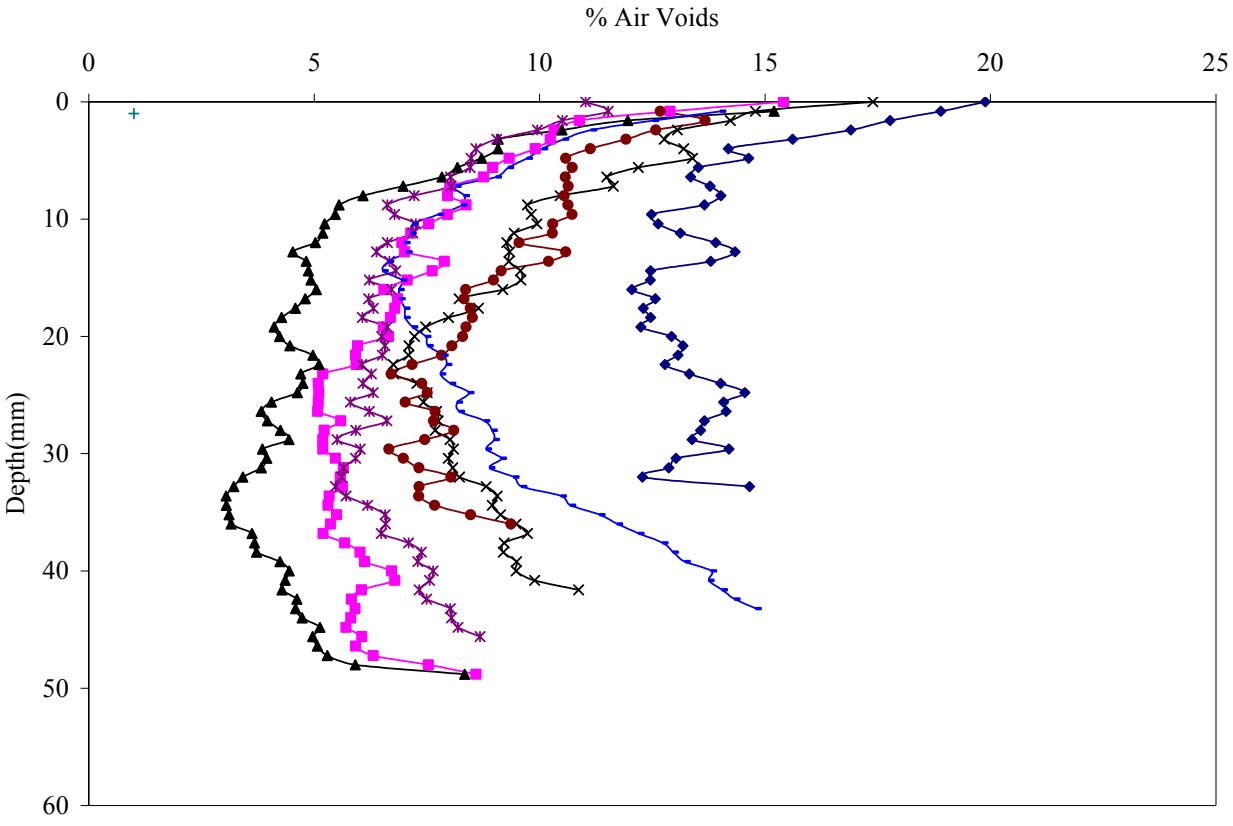

Figure 24. Examples of vertical distribution of percent air voids in field cores.

but different gradients were selected (Masad et al. 2005). The two projects had the largest and smallest difference in permeability between the top to the bottom hot mix asphalt layer. Project A had the largest change in permeability with depth, whereas project B had the smallest change with depth.

The cores were divided into sublayers of 10.4 mm thickness (13 X-ray CT slices). The cores varied in their thickness between 52 mm to 60 mm. Therefore, each core consisted of at least 4 sublayers. The percent air voids of the X-ray CT slices were averaged for each sublayer of the cores. Then, the percent air voids was determined for the corresponding sublayers of the cores that belong to the same project. It is noted that only the top four layers were included here in order to be able to compare the results of the two projects.

The flow of water through flexible pavements was modeled using the idealized cross section of a typical flexible pavement as shown in Figure 8-25a. A SEEP/W finite element model was developed based on this cross section (SEEP 2001). Figure 8-25b shows the resulting finite element mesh. The mesh included 11,422 quadrilateral and triangular elements.

Each sublayer of the asphalt mix was assigned a permeability value as given in Table 8-5. These permeability values were calculated using the following empirical formula (Masad 2005):

13. $$k = \frac{V_a^{\,m}}{c.S_{agg}^{t}} \frac{\gamma}{\mu} \tag{8.13}$$

where: k is the coefficient of permeability in m/sec.

γ is the unit weight of the fluid $\gamma = 9.79$ kN/m^3.

μ is fluid viscosity and is equal to 10^{-3} kg/(m.sec) for water.

V_a is the total percent air voids in an asphalt mix. The c, m and t values are obatined through statistical data fitting to the permeability values expressed in the units of 10^{-5} cm/sec.

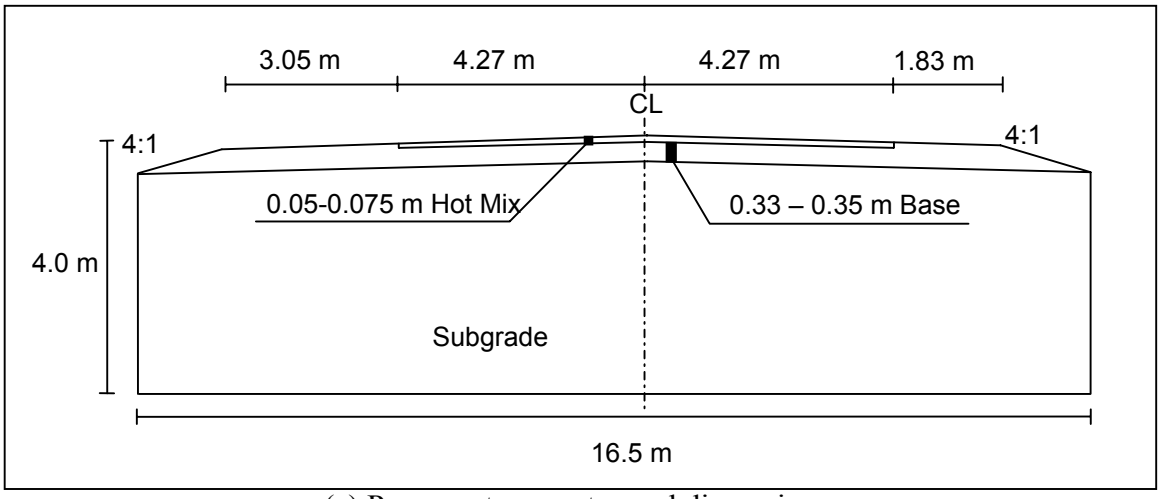

(a) Pavement geometry and dimensions

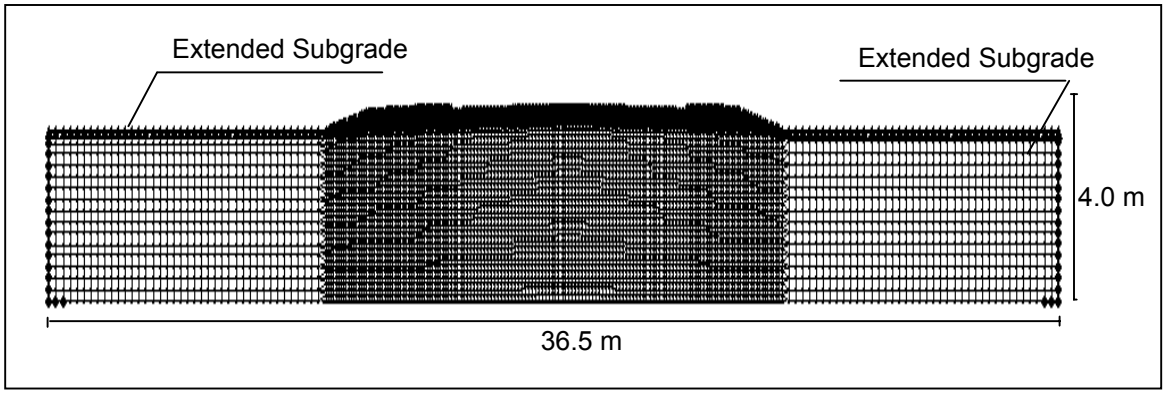

(b) Finite element model

Figure 8-25. Illustration of the finite element model.

Table 8-5. Average Sublayer Permeability for Finite Element Simulation

Project	Sublayer thickness (mm)	Permeability (10^{-5} cm/sec)
A	25	3837.69
	25	579.5
	25	547.95
	25	826.99
B	25	592.64
	25	544.87
	25	165.00
	25	328.55

The base course layer was represented with 3062 quadrilateral and triangular finite elements. The granular aggregate base material was assumed to have a saturated permeability of 15.4×10^{-5} cm/s. This value was selected to represent a dense graded crushed granite aggregate base (Ariza and Birgisson 2002). The subgrade soil permeability was taken as 0.275×10^{-5} cm/s to represent a sandy clayey silty soil (Ariza and Birgisson 2002). The subgrade was represented with a coarser mesh of finite element, consisting of 6120 quadrilateral and triangular elements. The subgrade was extended laterally 10 m beyond the area covered by the asphalt and base layer (Figure 8-25b), on each side, in order to represent real conditions more accurately, and provide continuity to the extension of the subgrade.

To adequately model the transient flow of water through the pavement system, a transient finite element analysis was performed. A pavement system at initial equilibrium, defined by a water table, was subjected to a transient "rain event," resulting in time-dependent changes in the volumetric moisture content throughout the pavement system. The water table was set at a depth of 0.76 m from the top of the pavement at the centerline cross section. The precipitation events input into the numerical model correspond to real precipitation measurements gathered at the Mn/ROAD project site (Ariza and Birgisson 2002).

Figure 8-26 shows the variation in total heads for projects A and B at the peak of the rain event for the four HMA sub-layers. In order for water to flow under saturated conditions from one location to another, a positive difference in total heads has to be present. From Figure 8-26, it is clear that the total heads throughout the four asphalt layers analyzed do not differ significantly across the thickness of the HMA layer, meaning that only a small amount of water is flowing in the vertical direction. In contrast, a significant gradient in total heads away from the centerline is present for both cases, meaning that water is primarily flowing horizontally away

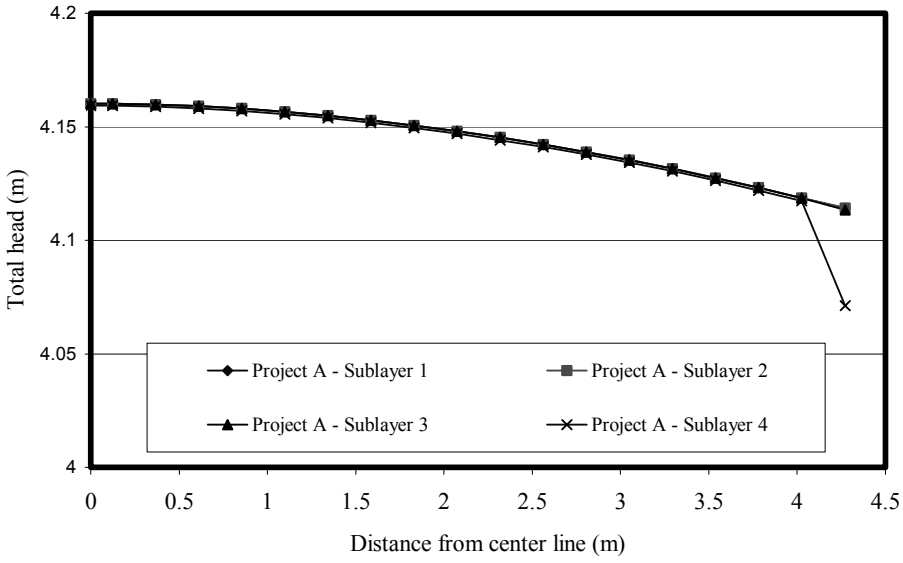

(a) Project A

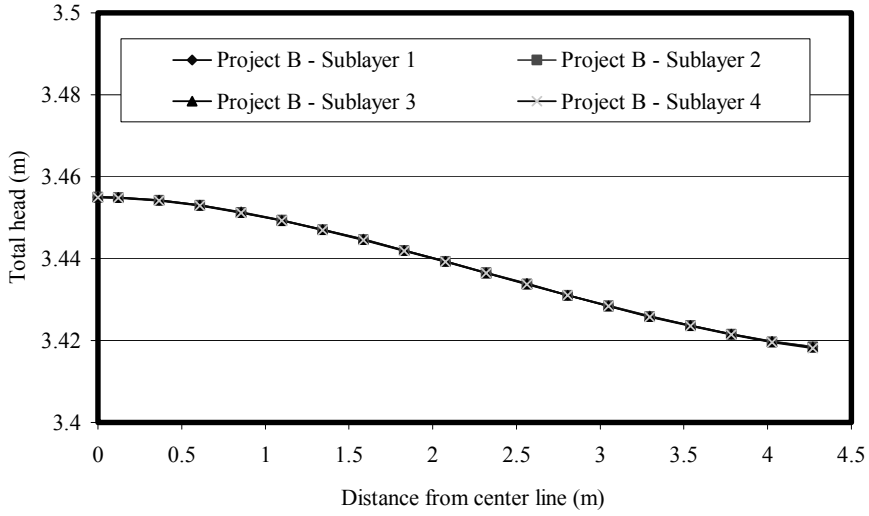

(b) Project B

Figure 8-26. Total head versus distance in HMA pavement layer.

from the centerline in the hot mix asphalt layer. It should be noted that Figure 8-26 is related to the flow over a large distance horizontally, and may therefore not depict the more detailed flow patterns over a smaller area in the HMA layer.

Figure 8-27 presents a closer look of the flow vectors in the area near the centerline of pavement. In Project A, which has the largest gradient in permeability from the top to the bottom of the HMA layer, the flow is primarily in the horizontal direction away from the centerline, with a small vertical flow component. In addition, most of the flow is concentrated in the top two HMA sub-layers. Similarly, in Project B, which has the smallest gradient in permeability from the top to the bottom of the HMA layer, the water flows primarily in the horizontal direction away from the centerline. However, the flow vectors for Project B (Figure 8-27b) have a slightly larger vertical component of flow, as compared to Project A. The lower two HMA sub-layers in Project B now show noticeable flow, even though the flow vectors are smaller than for the top two HMA sub-layers. It is noted that different scales are used in Figure 8-27 to illustrate the flow vectors for Projects A and B due to the difference in the measured permeability and flow amount in these two projects.

The fluid flow patterns for an idealized pavement layer with uniform air void distribution are simulated by assuming the permeability to be uniform throughout the HMA layer, with a saturated permeability (k_{sat}) of 500.0×10^{-5} cm/s, which is the average permeability of the samples from Projects A and B. Figure 8-28 shows the flow vectors for this case. As expected, the flow is mainly vertical which is different from the cases where non-uniform air void distribution is present in the HMA layer.

The effects of base permeability on the flow pattern through the HMA layer were evaluated, by increasing the saturated base permeability (k_{sat}) by 100 times to 1540.0×10^{-5} cm/s for project A. Figure 8-29 shows the flow vectors in the area near the centerline of pavement. The flow now has a stronger vertical gradient than in the case of a lower base permeability (Figure 8-27), meaning that more of the water is now flowing vertically through the pavement. However,

interestingly, Figure 8-29 shows that the high permeability top layer in the HMA layer still has a significant horizontal flow component, despite the high base permeability value.

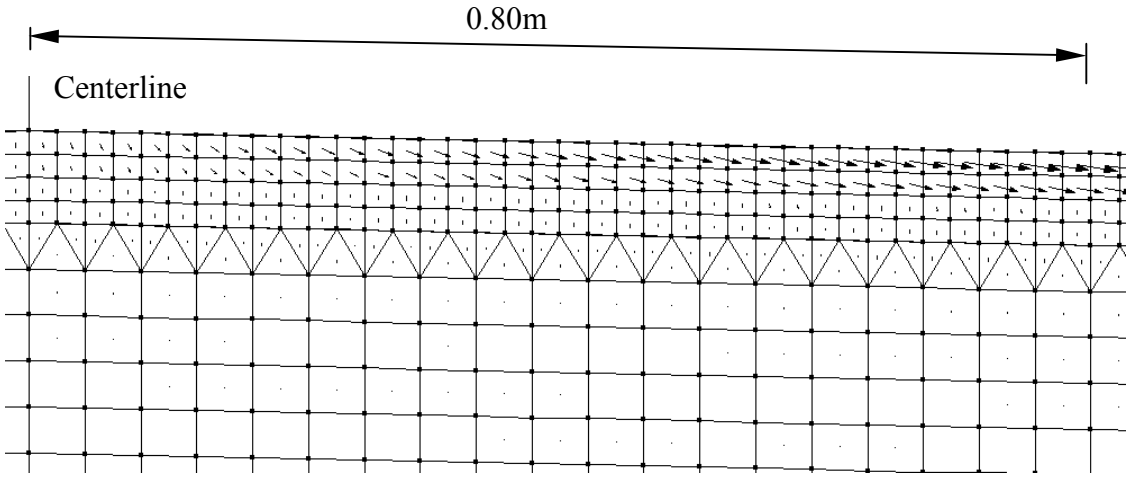

(a) Project A

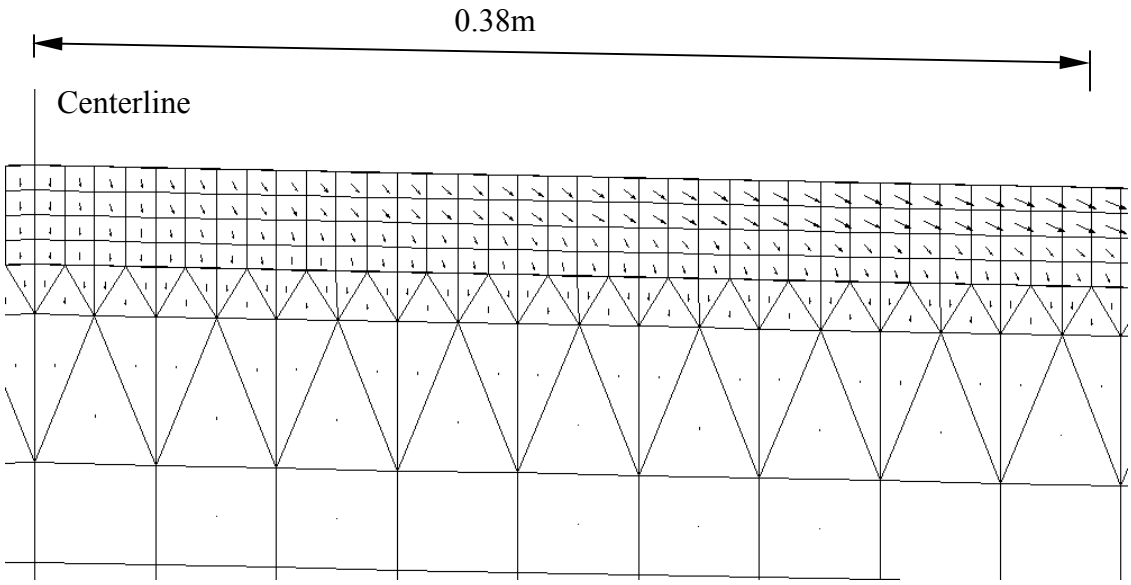

(b) Project B

Figure 8-27. Predicted flow vectors near centerline for Projects A and B.

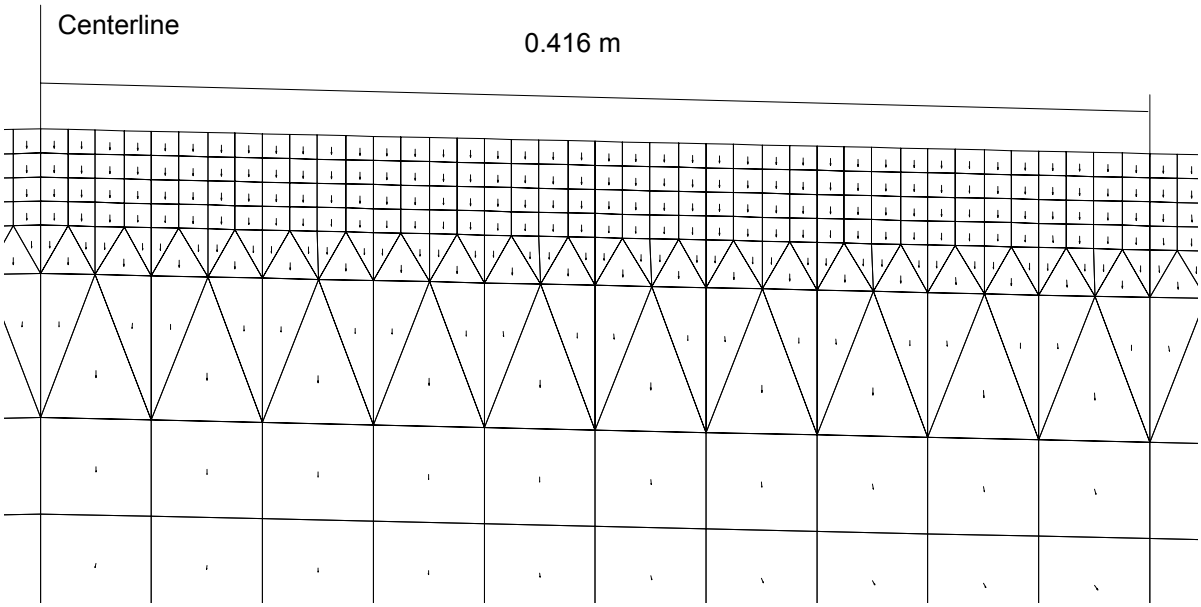

Figure 8-28. Predicted fluid flow for uniform hydraulic conductivity in asphalt concrete layers.

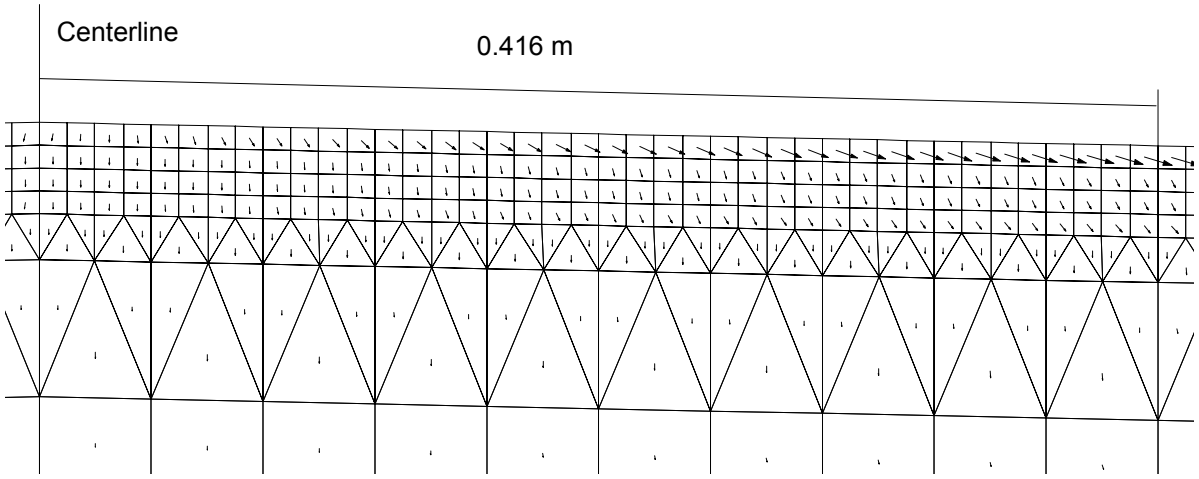

Figure 8-29. Predicted fluid flow for Project A with an increased base permeability.

The variation in permeability through typical HMA layers from higher at the surface to lower at the bottom of the HMA layer will encourage lateral flow in the more permeable part of the HMA layer, and discourage vertical flow into the underlying base course material. Conse-

quently, the associated moisture related damage would depend not only in the average permeability in an asphalt mix, but on the percent air voids and the direction of the developed flow patterns.

8.8 Summary of Findings

This chapter related moisture damage to air void distribution, permeability, and bond energies of mixtures. The resistance of HMA to moisture damage was evaluated using two parameters that were derived based on fracture mechanics principles. These parameters are the energy ratio (ER), and the number of cycles to failure (N_f). The ratio of these parameters calculated under wet and dry conditions was taken as indication of resistance to moisture damage.

The air void size distribution was found to follow the Lognormal distribution. A good correlation was found between permeability and the "pore size parameter" that reflects percent air voids and the expected value of the air void diameter squared.

The relation between the N and ER ratios and the mean air void size and permeability showed that there are "pessimum" air void size and permeability values at which the mix has the least resistance to moisture damage. This concept can be used to design mixtures outside the "pessimum" range in order to improve the resistance to moisture damage. This concept also implies that some mixtures consisting of the same aggregate type, may have a natural resistance to moisture damage, whereas other mixtures may be more susceptible to moisture damage. This means that even though on the average limestone mixtures may be less susceptible to moisture damage than granite mixtures, there may be gradations that make the limestone mixture more susceptible to moisture damage than the expected norm. The implications of this for conditioning are that mixtures should not be brought to a preset saturation level. Also, the use of short-term cyclic pore pressure conditioning is likely to be more appropriate than long-term

conditioning, since induced pore pressures and therefore damage are likely affected greatly by the void structure of mixtures.

The difference in moisture damage between limestone and granite specimens with similar gradations was related to the cohesive and adhesive bond energies under dry and wet conditions. The asphalt showed a better healing ability when water was present but a decrease in its fracture resistance. Also, the granite mix exhibited more susceptibility to moisture damage as it had less resistance to fracture and less ability to heal than the limestone mix under wet conditions. The current asphalt mix design methods need to account for the cohesive and adhesive properties of asphalt mixtures as well as for the air void structure which are highly related to moisture damage.

Finally, the air void distributions obtained from X-Ray CT analysis was used to predict the fluid flow in typical flexible pavements. The variation in permeability through typical HMA layers from higher at the surface to lower at the bottom of the HMA layer will generally encourage lateral flow in the more permeable part of the HMA layer, and discourage vertical flow into the underlying base course material. Consequently, the associated moisture related damage would depend not only on the average permeability in an asphalt mix, but on the direction of the developed flow patterns. A measure of permeability using the NCAT Field Permeameter may be more appropriate (Cooley and Brown 2000). Also, the critical near-surface area encompasses the locations of likely high pore pressures from vehicle tires. The results of the finite element analysis clearly show that this near-surface region is highly susceptible to saturation and therefore pore pressures are likely the main cause of premature moisture damage and raveling in this region.

8.9 References

Ariza, P., and Birgisson, B., "Evaluation of Water Flow Through Pavement Systems," Research Report, Minnesota Department of Transportation, St. Paul, MN, 2002.

Al-Omari, A., Tashman, L., Masad, E., Cooley, A., and Harman, T., "Proposed Methodology for Predicting HMA Permeability," *Journal of the Association of the Asphalt Paving Technologists*, Vol. 71. pp. 30-58, 2002.

Castelblanco, A., "Probabilistic Analysis of Air Void Structure and Its Relationship to Permeability and Moisture Damage of Hot Mix Asphalt," Master's Thesis, Texas A&M University, College Station, TX, 2004.

Cheng, D., Little, D., Lytton, R., and Holste, J., "Use of Surface Free Energy Properties of the Asphalt-Aggregate System to Predict Moisture Damage Potential," *Journal of the Association of Asphalt Paving Technologists*, Vol.71, pp. 59-88, 2002.

Choubane, B., Page, G.C., and Musselman, J.A., "Investigation of Water Permeability of Coarse Graded Superpave Pavements," *Proceedings*, Association of Asphalt Paving Technologists (AAPT), Vol. 67, 1998.

Choubane, B., Page, G.C., and Musselman, J.A., "Effects of Different Water Saturation Levels on the Resistance of Compacted HMA Samples to Moisture Induced Damage," presented at the 80th Annual Transportation Research Board (TRB) Meeting, Washington D.C., 2000.

Cooley, Jr., A.L., and Brown, E.R., "Selection and Evaluation of a Field Permeability Device for Asphalt Pavements," *Journal of the Transportation Research Board 1723*, TRB, National Research Council (NRC), Washington, D.C. pp. 73-82, 2000.

Curray, J. R., "Analysis of two dimensional orientation data," *Journal of Geology*, Vol. 64, p. 117–131, 1956.

Denison, C., Carlson, W. D., and Ketcham, R. A. "Three dimensional quantitative textural analysis of metamorphic rocks using high-resolution computed x-ray tomography: Part I. Methods and techniques," *Journal Metamorph. Geol.,* Washington, D.C., Vol. 15, p. 29-44, 1997.

Garcia-Bengochea, I, "The Relation between Permeability and Pore Size Distribution of Compacted Clayey Silts," Master's Thesis, Purdue University, 1978.

Huang, C.H., and Holtz, R.D., "A Probabilistic Permeability Model and the Pore Size density Function," *International Journal for Numerical and Analytical Methods in Geomaterials,*Vol. 10, pp. 543-553, 1986.

Image Pro Plus, Media Cybernetics, L.P, Version, 4.1, Maryland, 1999.

"ImageTools: Image analysis program," Department of Dental Diagnostic Science, University of Texas Health Science Center, San Antonio, TX, 1997.

Lytton, R.L., *Adhesive Fracture in Asphalt Concrete Mixtures*, Chapter in Book Edited by Youtcheff, J., In Press, 2004.

Maple, 9.01, Waterloo Maple Inc., 2004.

Minitab, 13.1, *Statistical Software for Windows*, Minitab, Inc, Pennsylvania, 2002.

Masad, E., Muhunthan, B., Shashidhar, N., and Harman, T., "Internal Structure Characterization of Asphalt Concrete Using Image Analysis," *Journal of Computing in Civil Engineering*, April 1999.

Masad, E., Jandhyala, V.K., Dasgupta, N., Somedavan, N., and Shashidhar, N., "Characterization of air void distribution in asphalt mixes using X-ray CT," *Journal of Materials in Civil Engineering*, 2001.

Masad, E., Tashman, L., Niranjanan, S., and Little, D. "Micromechanics Based Analysis of Stiffness Anisotropy in Asphalt Mixes," *Journal of Materials in Civil Engineering*, ASCE, Vol. 14, No. 5, 2002.

Masad, E., Birgisson, B., Al-Omari, A., and Cooley, A., "Analysis of Permeability and Fluid Flow in Asphalt Mixes," *ASCE Journal of Materials in Civil Engineering*, 2005.

Maupin, Jr., G.W., "Asphalt permeability Testing: Specimen Preparation and Testing Variability," *Journal of the Transportation Research Board 1767*, TRB, NRC, Washington, D.C., pp. 33-39, 2001.

Roque, R., Birgisson, B, Sangpetgnam, B., and Zhang, Z., "Hot Mix Asphalt Fracture Mechanics: A Fundamental Crack Growth Law for Asphalt Mixtures," *Journal of the Association of Asphalt Paving Technologists*, Vol. 71, pp. 816-827, 2002.

Roque, R., Birgisson, B., Drakos, C., and Dietrich, B., "Development and Field Evaluation of Energy-Based Criteria for Top-Down Cracking Performance of Hot Mix Asphalt," *Journal of the Association of Asphalt Paving Technologists*, Vol. 73, 2004.

SEEP /W Users Manual. Version 4.24. GEO-SLOPE International Ltd. Calgary, 2001.

Tashman, L., Masad, E., D'Angelo, J., Bukowski, J., and Harman, T., "X-ray Tomography to Characterize Air Void Distribution in Superpave Gyratory Compacted Specimens," *The International Journal of Pavement Engineering,* Vol. 3, pp. 19-28, 2002.

Tashman, L., Masad, E., Peterson, B., and Saleh, H., "Internal Structure Analysis of Asphalt Mixes to Improve the Simulation of Superpave Gyratory Compaction to Field Conditions," *Journal of the Association of Asphalt Paving Technologists*, Vol. 70, 2001.

Terrel, R.L., and Al-Swailmi, S., "The Role of Pessimum Voids Concept in Understanding Moisture Damage to Asphalt Concrete Mixtures," *Transportation Research Record*. *No. 1386*, TRB, NRC, Washington, D.C., pp. 31-37, 1993.

Wang, L.B., and Lai, J.S., "Quantify Specific Surface Area of Aggregates Using an Imaging Technique," *Journal of the Transportation Research Board,* TRB, NRC, Washington, D.C., 1998.

CHAPTER 9
FUNDAMENTAL CONSIDERATIONS II - EFFECTS OF PERMEABILITY AND VEHICLE SPEED ON PORE PRESSURES IN HOT MIX ASPHALT PAVEMENTS

9.1 Background

Based on the micromechanical analysis in Chapter 8 and the laboratory test results in Chapter 5, it is now established that most asphalt mixtures have an open enough air void structure to allow water to infiltrate and cause pore pressures during loading. The finite element analysis of water flow through typical pavement sections showed that most of the moisture during and after a rain event will tend to stay in the near-surface region where pore pressures are likely to be significant. These pore pressures in the pavement during and immediately after rain events likely play a significant role in premature moisture damage, including both stripping and cohesive softening. It would be desirable to develop a laboratory-based conditioning procedure that more closely simulates actual mechanism of moisture damage in the field, including the presence of pore pressures. This means that it is also necessary to determine the range of magnitudes of pore pressures that are associated with a typical flexible pavement configuration.

In the following, predicted pore pressures for typical ranges of mixture properties, pavement configurations, and vehicle tire loads will be evaluated. The goal is to determine reasonable ranges of pore pressures for use in a laboratory-based conditioning procedure. However, first recent work on the determination of asphalt mixture permeability will be reviewed briefly.

9.1.1 Mixture Permeability

The problem of moisture damage in HMA pavements occurs when water can infiltrate the pavement system and prematurely deteriorate the pavement. A key factor in the ability of the water to infiltrate is the permeability of the asphalt layer.

It was acknowledged early on that Superpave coarse-graded mixtures are not impermeable, since they don't contain a large portion of fines. In fact, work by Choubane et al. showed that Superpave mixtures tend to be more permeable than conventional Marshall dense-graded mixtures (Choubane et al. 1998). The latter has lead researchers to investigate the factors that influence permeability. Others have tied permeability with the in-place air void level. Work performed by Kandhal (1994) suggests that there is a range of air voids between six and fourteen percent that allows the water to infiltrate the pavement but will not drain freely. Kandhal named this range of air voids as the pessimum range. Pessimum means the opposite of optimum. Therefore, damage is more likely to occur within the pessimum range. Based on the work presented in Chapter 6, this concept of pessimum air voids has been extended with the aid of micromechanics, where it was shown that there is an average air void diameter size or a "pessimum size" at which moisture damage is maximum. A possible interpretation of this behavior is that small air void sizes reduce the infiltration of water to the mix, while large air voids make it easier for the water to drain out of the mix. Hence, good resistance to moisture damage is obtained at these two levels of air void sizes.

Other work performed by various researchers suggests that the air void level is not the only factor that affects the permeability (Mallick et al. 2001; Cooley et al. 2001). Mixtures with the same percent air voids can have very different permeabilities. The factor that causes this may be the interconnectivity of the voids. Very coarse-graded mixtures do not contain large quantities of fine materials, which would fill the voids within the mixtures and decrease the amount of interconnected voids. Another factor that will affect the interconnectivity of the voids is the nominal maximum aggregate size (NMAS) of the mixture. As the NMAS increases then the void size within the mixture increases, thus increasing the possibility of interconnected voids.

Cooley et al. (2001) found that the void range where the permeability increases with small changes in the air voids vary depending on the NMAS. Listed in Table 9-1 are the critical permeabilities and air void levels for various NMAS as found by Cooley et al. (2001). The permeabilities of laboratory compacted specimens compare very well to the permeabilities found in the field. Kanipong et al. (2001) and Maupin (2001) both found that the permeabilities of laboratory specimens were between $30 - 150 \times 10^{-5}$ cm/sec for an approximate air void level of 7 percent. Note that the permeabilities of these mixtures are very comparable to a fine sand or silty sand.

Table 9-1. Critical Field Permeabilities and Air Voids for Various NMAS (Cooley et al. 2000)

NMAS	Air Void Level (%)	Permeability (10-5 cm/sec)
9.5	7.7	100
12.5	7.7	100
19.0	5.5	120
25.0	4.4	150

The permeability is also a factor in the design of pavements. Mallick et al. (2001) suggest using a very dense-graded mixture 75-100 mm below the surface. This dense layer will act as an impermeable barrier so that any water/water vapor from the subgrade will not infiltrate into the asphalt layer. Others suggest using a free-draining system that will drain the water into a longitudinal edge drain (Kandhal 1994).

Another aspect of the pavement, which impacts its permeability, is its construction. For instance, Mallick et. al. (2001) found that the lift thickness of the pavement greatly influences the permeability. The thicker a lift becomes, then the chance of interconnected voids decrease and the permeability will also decrease. The work presented in Chapter 8 also showed that the permeability of a field mixture is variable throughout the compacted layer. The permeability at the top and bottom of the layer is higher than for the middle part of the layer.

The significance of permeability in a new Superpave mix design on a major Interstate was recently identified by the Florida Department of Transportation (FDOT) (Musselman et al. 1998). Visual observations of the pavement showed water exiting the pavement onto the surrounding shoulders. Further investigation revealed that the pavement was saturated and that the water was flowing through the pavement and up and over the shoulder. The FDOT concluded that the permeability of coarse-graded Superpave mixtures are greater than previously used dense-graded mixtures at the same air void levels (Musselman et al. 1998).

It is generally accepted that newly placed HMA pavements are placed at a higher than designed air void content (6-7 percent) with the assumption that traffic loadings will decrease the air void content over time. The voids may be interconnected and then can allow water to move through the pavement. Once the pavement starts to consolidate due to traffic, the interconnected voids close and trap water in the voids.

The authors believe that some degree of saturation is possible in all pavements. In particular, the finite element modeling presented in Chapter 8 using the distribution of air voids from actual field cores to establish permeability, clearly showed that the top portion of mixtures in the field is likely to become saturated during a rain event. Moreover, based on identified permeabilities and field observations of coarse-graded Superpave mixes, the potential of achieving saturation is realistic. In the following, the potential pore pressures will be examined which can be generated in a typical coarse-graded Superpave mix subject to moving wheel loads at different speeds assuming that the pavement is saturated.

9.1.2 Influence of Pore Pressure

Increases in pore pressure takes place when the void volume in the HMA pavement is reduced due to loading. The magnitude of pore pressure is a function of both compressibility

and permeability of the asphalt skeleton. High levels of pore pressure have the potential of rupturing the asphalt film on the aggregate. Such breaks in the asphalt film may provide pathways for water infiltration onto the surface of the aggregate, resulting in stripping.

In addition, moving traffic loads are dynamic in nature and may have rates of loading greater than fluid velocities (controlled by permeability), which result in fluid pressures varying with time at a given point. Moreover, due to the dynamic nature of the loading, the response, i.e., pore pressure has wave characteristics. An example of the latter is shown in Figure 9-1. Water is compressed in the voids in front of the tire as it rolls towards a point (positive pore water pressure). As the tire passes the point, the water is sucked out of the voids (negative pore water pressure). Consequently, the movement of the water creates a compression/tension cycle in the voids. It is proposed that this cycling of pore pressure may act as a mechanism for rupturing the asphalt film and result in stripping. Moreover, the cyclic movement of the water may result in migration of fines and asphalt binder to the surface of the pavement.

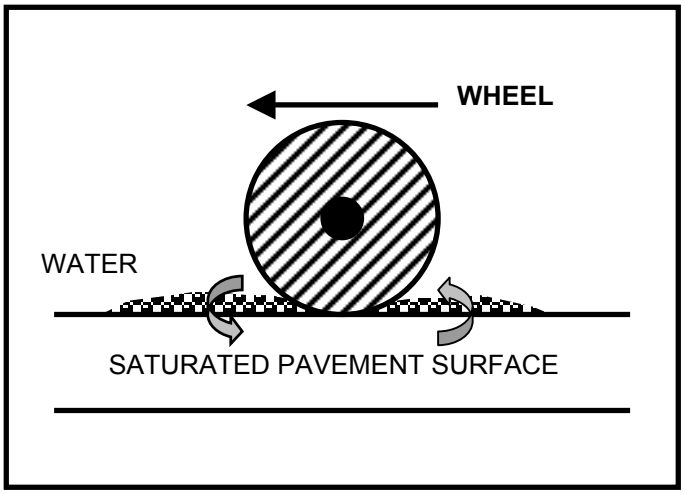

Figure 9-1. Depiction of scour

9.1.3 Mathematical Modeling

In order to establish likely pore pressure ranges for typical mixture properties, pavement configuration, and vehicle tire loads, it is necessary to account for the void structure in the HMA mixture. The theory of mixtures provides a link between the void structure (microstructure) of materials and a continuum description that is suitable for finite element formulations. A finite element formulation based on the theory of mixtures was employed which captures dynamic pore water pressure effects. The asphalt pavement is treated as a two-phase material, consisting of a solid skeleton and liquid filled voids. The solid skeleton (HMA) was assumed to be linear elastic while the liquid (water), filling the voids, was assumed to be incompressible. The pavement response was evaluated using a two-dimensional plane strain model.

9.2 Finite Element Formulation for the Theory of Mixtures

In saturated pavement analysis, the HMA, base, and subgrade are composed of two phases: 1) the solid phase or skeleton and 2) the fluid phase occupying the void volume. A theory which treats each separately and together is the theory of mixtures. Using the concept of volume fractions, the microscopic quantities (i.e., density, porosity, etc.) are transitioned to macroscopic quantities, which are subject to continuum balance laws. The three continuum laws, which apply at a point, are the conservation of linear momentum for both the solid and fluid phase and the conservation of mass of the total system. These three partial differential equations, known as the strong form, can be solved under simple boundary and initial conditions. For more complex and realistic geometry (boundary conditions) and initial conditions, no closed form solution exists. Because of this a numerical methods such as finite difference or finite elements must be employed. One such finite element code is PlasFEM developed at the University of Florida. A brief description follows.

To solve the coupled differential equations through finite elements, they are transformed from point expressions to volume expressions through integration. The latter is referred to as a weak form involves the introduction of approximations (i.e., shape functions) describing fluid and skeleton displacements, velocities and accelerations. The volume quantities are referred to as finite elements. The resulting equations are given as

$$\begin{bmatrix} M^{ss} & 0 & 0 \\ 0 & M^{ff} & 0 \\ 0 & 0 & 0 \end{bmatrix} \begin{Bmatrix} \ddot{u}^s \\ \ddot{u}^f \\ \ddot{p} \end{Bmatrix} + \begin{bmatrix} C^{ss} & -C^{sf} & 0 \\ -C^{fs} & C^{ff} & 0 \\ 0 & 0 & 0 \end{bmatrix} \begin{Bmatrix} \dot{u}^s \\ \dot{u}^f \\ \dot{p} \end{Bmatrix} + \begin{bmatrix} K & 0 & -G^{sp} \\ 0 & 0 & -G^{fp} \\ -G^{ps} & -G^{pf} & -P \end{bmatrix} \begin{Bmatrix} u^s \\ u^f \\ p \end{Bmatrix} = \begin{Bmatrix} F^s \\ F^f \\ F^p \end{Bmatrix} \qquad (9.1)$$

or as

$$Ma + Cv + Kd = F(t) \qquad (9.2)$$

where each of the matrix terms are given in Table 9-2. This is often referred to as a u^s-u^f-p formulation since these variables (skeleton displacements, fluid velocities, and fluid pore pressures) are solved directly. To solve the above expression a time integration procedure is required. There are both implicit and explicit methods. PlasFEM uses the Newmark Implicit method due to its stability. Moreover, since PlasFEM is a fully implicit code, i.e., recovering stress, stiffness, etc., it guarantees a quadratic rate of convergence. PlasFEM is capable of analyzing both two and three dimensional pavement cross-sections (Pinto 1998).

9.3 Finite Element Modeling

Next, a description of the finite element mesh, elements, and boundary conditions will be given followed by a discussion of the loading function.

9.3.1 Finite Element Mesh, Elements, and Boundary Conditions

The plane-strain finite element mesh used in this study is shown in Figure 9-2. The mesh consists of 943 nine-node elements with 3,901 nodes. The nodes, when analyzed in a dynamic

Table 9-2. Summary of Matrices for $u^s - u^f - p$ Formulation

Element Array	Definition
Solid Phase Mass (consistent)	$M^{ss} = \int_{\Omega_e} N_k^s (1-n) \rho_s N_l^s \, d\Omega$
Fluid Phase Mass (consistent)	$M^{ff} = \int_{\Omega_e} N_k^f n \rho_f N_l^f \, d\Omega$
Viscous Damping	$C^{ss} = \int_{\Omega_e} N_k^s n^2 \rho_f g \left(K_{ij}\right)^{-1} N_l^s \, d\Omega \;\; C^{sf} = (C^{fs})^T = \int_{\Omega_e} N_k^s n^2 \rho_f g \left(K_{ij}\right)^{-1} N_l^f \, d\Omega$
	$C^{ff} = \int_{\Omega_e} N_k^f n^2 \rho_f g \left(K_{ij}\right)^{-1} N_l^f \, d\Omega$
Stiffness of Solid Skeleton	$K = \int_{\Omega_e} N_{k,j}^s \sigma'^s_{ij} \, d\Omega$
Coupling terms	$G^{sp} = \int_{\Omega_e} N_{k,i}^s \; (1-n) \; N_l^p \, d\Omega$
	$= \int_{\Omega_e} B_k^s \; (1-n) \; m \; N_l^p \, d\Omega$
	$G^{ps} = \int_{\Omega_e} N_k^p \; (1-n) \; N_{l,i}^s \, d\Omega$
	$G^{fp} = \int_{\Omega_e} N_{k,i}^f \; n \; N_l^p \, d\Omega$
	$G^{pf} = \int_{\Omega_e} N_k^p \; n \; N_{l,i}^f \, d\Omega \; m^T = \begin{bmatrix} 1 & 1 & 1 & 0 & 0 & 0 \end{bmatrix}$
Fluid Volumetric Stiffness	$P = \int_{\Omega_e} N_k^p \frac{n}{K_f} N_l^p \, d\Omega$
External terms	$F^s = F^{sb} + F^{st} - F^{sp} = \int_{\Omega_e} N_k^s (1-n) \; \rho_s b_i \; d\Omega + \int_{\Gamma_e} N_k^s \left(\sigma'^s_{ij} - (1-n)p\right) \; n_j \, d\Gamma$
	$F^f = F^{fb} - F^{fp} = \int_{\Omega_e} N_k^f n \rho_f b_i \; d\Omega - \int_{\Gamma_e} N_k^f \; n \; p \; n_j \, d\Gamma$
	$F^p = 0$
	where N^f is the shape functions describing fluid displacements N^s is the shape functions describing the skeleton displacements N^p is the shape functions describing the fluid pore pressures

saturated state, have five degrees of freedom corresponding to fluid and solid displacements in the X and Y direction as well as pore pressure. Only the four corner nodes of each element have the pore pressure degrees of freedom.

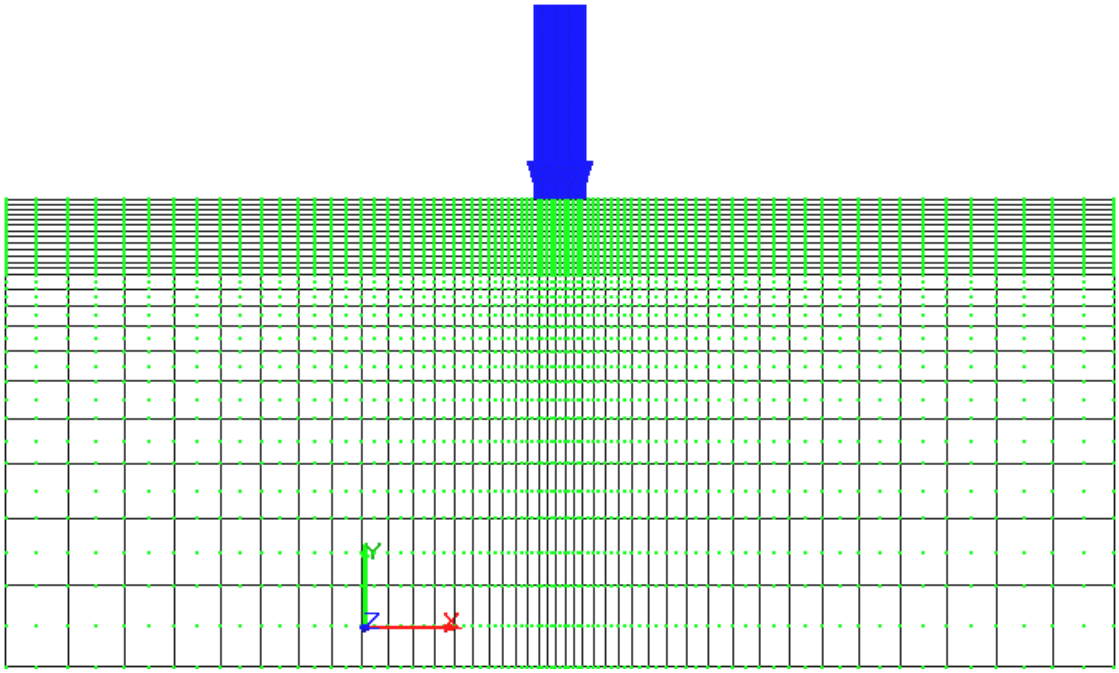

Figure 9-2. Finite element mesh with 943 nodes used to evaluate pore pressures.

The total horizontal and vertical dimensions of the mesh are 635cm by 305cm. Elements are finer near the top and middle (where the wheel load will be applied) of the mesh and gradually grow coarser toward the sides and bottom of the pavement cross-section.

The pavement cross-section consists of three different materials. An upper HMA layer, which is 20.26cm thick, overlies a 30.48cm base course and a 254cm thick subgrade. There are 6 rows of elements in the asphalt layer, with the top three rows (10.16cm) corresponding to higher permeable material and the bottom three rows (10.16cm) corresponding to the lower permeable material. The base layer consists of 7 rows (30.48cm) and the subgrade is composed of 10 rows (254cm). Each row contains 41 elements. A description of the material properties can be found in Table 9-3. It should be noted that the permeabilities studied are typical for many dense graded hot mix asphalt pavements (Choubane et al. 1998).

Table 9-3. Material Properties of Pavement Layers

Properties	Upper asphalt layer	Lower asphalt layer	Base	Subgrade
Elastic Modulus (kPa)	1379000.0	1379000.0	310275.0	103425.0
Poisson's Ratio	0.35	0.45	0.30	0.45
Porosity	0.07	0.05	0.30	0.10
Solid Density (Mg/m^3)	2.28	2.28	2.12	1.90
Fluid Density (Mg/m^3)	1.0	1.0	1.0	1.0
Fluid Bulk Modulus (kPa)	1.00E+11	1.00E+11	1.00E+11	1.00E+11
Permeability (cm/sec)	1.00E-04 (and variable)	1.00E-06	1.00E-04	1.00E-06

For the solid phase, the left and right boundaries were free to move vertically but not horizontally, the lower boundary was fixed both horizontally and vertically, and the upper boundary was free to move both horizontally and vertically. For the fluid phase, the left and right boundaries and the upper boundary, except for the loaded portion, were pervious while the lower boundary was impervious. Under the loaded area, the impermeability was achieved by constraining the vertical displacements of the solid and liquid phases to be the same. In PlasFEM, the latter is achieved by "slaving" those degrees of freedom, i.e., by assigning the same equation number to both degrees of freedom (Pinto 1998; Arduino 1996).

9.3.2 Loading Function

The wheel load was assumed to be 12.7cm wide with a contact pressure of 792 kPa. To simulate an assumed smoothly varying tire loading, a time dependent haversine function (Huang 1993) is employed. If the load peak is F_{max}, and d is the total duration of the loading, the applied loading function at any time t is represented by:

$$F(t) = F_{max} \sin(\pi t/d) \tag{9.3}$$

The duration of the load is based upon the vehicle speed, s, and the assumption that the tire, with radius a, has no effect at a distance of 6a. The duration is then equal to

$$D = 12a/s \tag{9.4}$$

The imposed load peaks at time d/2, simulating the time when the tire is directly above the point of interest. After t = d the wheel load has no effect. The limitation in using the haversine load is that the load never moves, just the intensity changes. Note, this is not an accurate simulation of the shear stresses due to rotation of principle planes that the pavement experiences with an approaching wheel. However the latter was assumed acceptable for the study of permeability effects. This paper looked at a wheel load traveling at 72, 96, and 128 kilometers per hour (kph), or a haversine load duration of 0.07620, 0.5715, and 0.04286 seconds, respectively.

9.4 Discussion of Results

9.4.1 Effect of Permeability

Figure 9-3 shows the time history response of pore pressures on surface of the Asphalt layer under the center of the tire load. In this case, the permeability of the lower asphalt layer was kept constant at 10^{-6} cm/s, whereas the permeability of the upper asphalt layer was varied from 10^{-4} cm/s to 10^{-6} cm/s. The results show that the pore pressures at the top of the asphalt layer increase from 300 kPa to 615 kPa as the permeability of the upper asphalt layer decreases from 10^{-4} cm/s to 10^{-6} cm/s.

Figure 9-4 shows the time history of pore pressures at the centerline of the applied tire load at the interface between the upper and lower asphalt layers. Interestingly, in this case as the permeability decreases from 10^{-4} cm/s to 10^{-6} cm/s, the pore pressures decrease from approximately 200 kPa to 100 kPa. Evidently, at the interface between the two asphalt layers, the higher the permeability, the higher the pore pressure. This means that even though lower permeability in

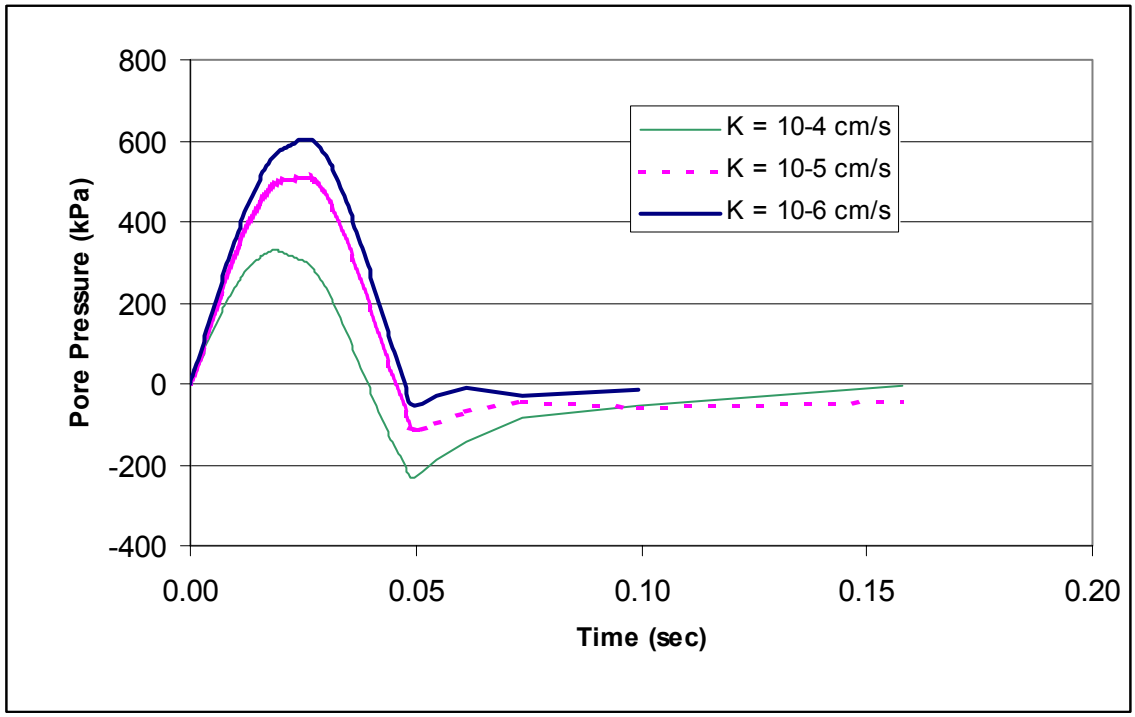

Figure 9-3. Pore pressure histories on the surface for different values of permeability.

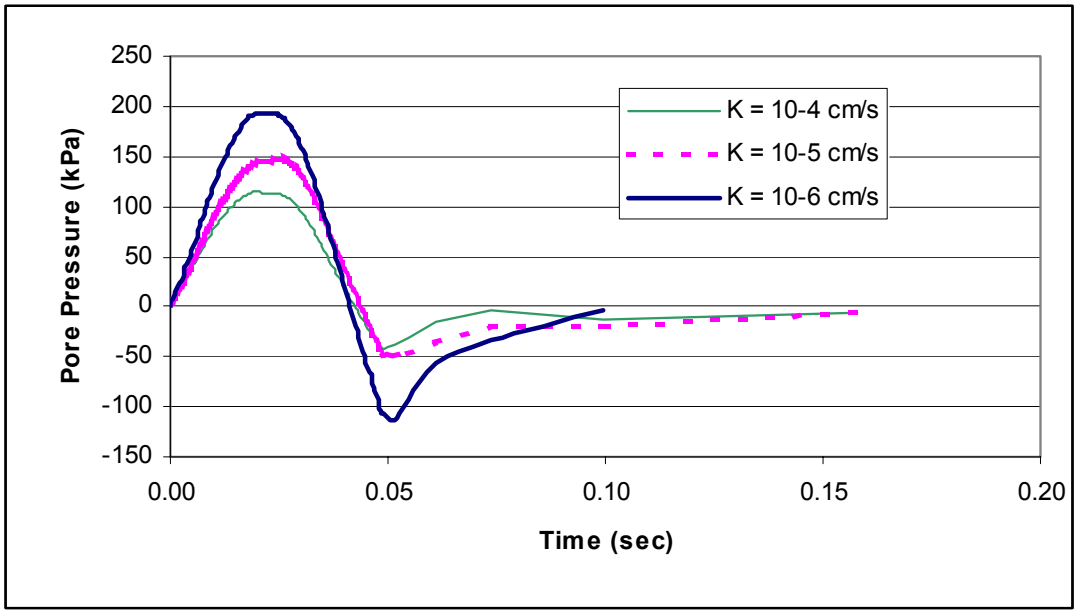

Figure 9-4. Pore pressure histories at the interface for different values of permeability.

the top asphalt layer may result in higher pore pressures close to the surface, the pore pressures dissipate rapidly with depth in the lower permeability material.

Another interesting trend observed in both Figures 9-3 and 9-4 is that for the early portion of the loading, the pore pressures increase very rapidly as the applied tire load is transferred to the pore fluid, since the fluid cannot escape the skeleton in a short time. Subsequently, the pore water pressures decrease after the peak of the haversine loading function is reached. Before reaching equilibrium, after the wheel load is almost gone, the positive pore pressures change to negative suction pressures, as the surrounding material skeleton recovers from the load and sucks the water back into the voids in between the aggregates. This reversal from very large positive pore pressures (around 600 kPa) to sizable suction (up to –200 kPa) as the wheel load is applied may result in hydraulic scouring and stripping, where fines and asphalt film are broken off and migrated out of the mixture. Similarly, this is seen at the interface between the upper and lower HMA layer interface from +200 kPa to –125 kPa. The interface has been observed historically, e.g., by Kandhal (1994), to be a location of observed moisture damage.

9.5 Effect of Vehicle Speed

Figure 9-5 shows the pore pressure at the interface between the two asphalt layers, the upper asphalt layer had a permeability of 10^{-4} cm/s while the lower asphalt layer had a permeability of 10^{-6} cm/sec. As the vehicle speed decreases, the duration of the loading increases, resulting in smaller pore water pressure increases. This is expected, since at higher speeds a greater proportion of the load is transferred to the pore fluid versus the solid skeleton as a result of the reduced time for the pore fluid to escape. The results show only slight differences, a maximum of 190 kPa at 128 kph compared to 170 kPa at 72 kph, and –100 kPa at 128 kph

compared to –120 kPa at 72 kph. The latter suggests that higher speeds are similar to decreasing permeability.

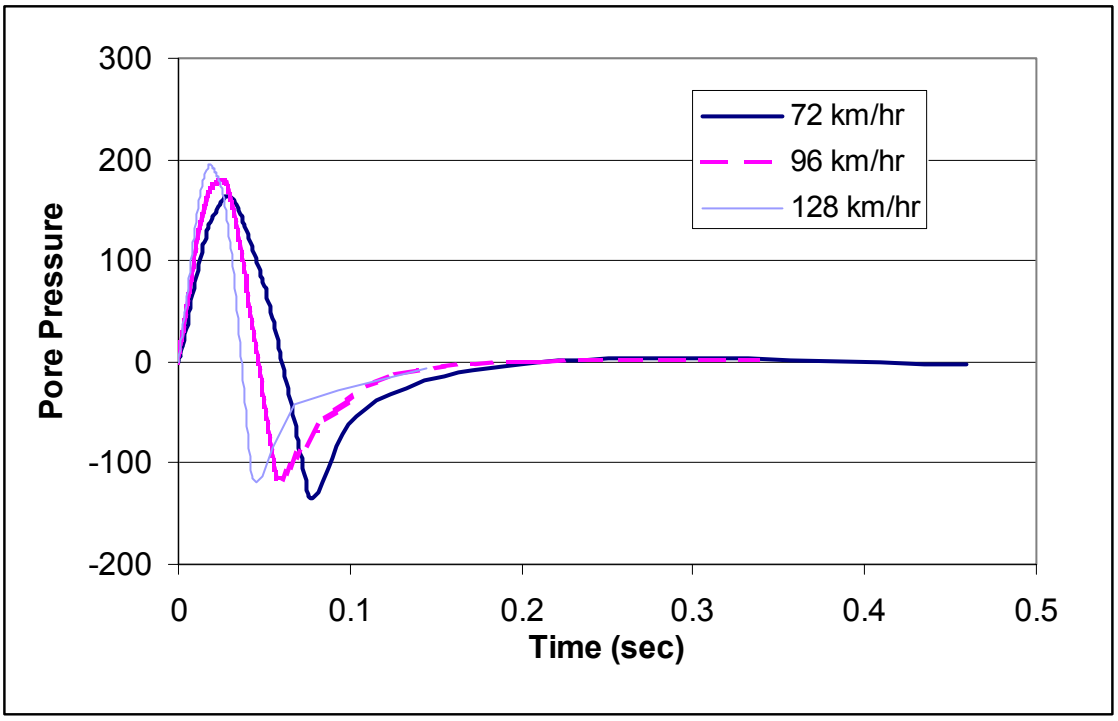

Figure 9-5. Pore pressure histories at the interface for different vehicle speeds.

9.6 Summary and Conclusions

Finite element analysis is an effective tool for the numerical solution of complex boundary problems where analytical solutions are not practical. One case is the study of a moving wheel load over a saturated pavement system. This chapter presents the coupled solution of pore pressures and deformations in a pavement system subject to dynamic wheel loads. This chapter looked at the effects of permeability and vehicle speed on pore pressures in the asphalt layer. Some key observations from this analysis were

1. Large reversal of pore pressures occurs as the wheel travels over a point in the pavement. For instance, large positive values (+600 kPa) as the wheel approaches to large negative

values, i.e., suctions (-200 kPa) occur as the wheel passes. Note such large pore pressure cycling may cause asphalt stripping and scouring.

2. The distribution of pore pressure underneath the wheel is proportional to the asphalt permeability. The lower the permeability the higher magnitude at the surface and the faster the attenuation with depth.
3. Higher vehicle speeds result in higher pore pressures along the interface between the upper and lower asphalt layers. This is due to the faster rate of loading versus time the pore pressure has to decay.
4. Due to the sign reversals and large magnitudes of pore pressure, asphalt skeleton stresses may be significantly impacted. In addition, the large positive pore pressures may result in bonding problems between the upper and lower asphalt boundaries.

In conclusion the study shows that there exist significant pore pressures (compression and suction) along with cycling in an asphalt layers due to dynamic loading. These pore pressures may range in value from about 100 kPa (14.6 psi) to about 600 kPa (88 psi). However, in the critical interface zone between upper and lower layers, pore pressure values of –100 kPa to +200 kPa were predicted. Dynamic wheel loads and their effects on pore pressure generation should not be ignored when analyzing and designing flexible pavements. These pore pressure effects should also be considered in the development of an appropriate laboratory-based conditioning procedure for mixtures.

9.7 References

Arduino, P., "Multiphase description of Deforming Porous media by the Finite Element Method," Ph.D. Dissertation, Georgia Institute of Technology, Atlanta, 1996.

Choubane, B., Page, G.C., and Musselman, J.A., "Investigation of Water Permeability of Coarse Graded Superpave Pavements," *Proceedings*, Association of Asphalt Paving Technologists (AAPT), Vol. 67, 1998.

Cooley, Jr., L.A., Brown, E.R., and Maghsoodloo, S., "Development of Critical Field Permeability and Pavement Density Values for Coarse-Graded Superpave Pavements," *Transportation Research Record*, Transportation Research Board (TRB), National Research Council (NRC), Washington, D.C., 2001.

Huang, Y.H., *Pavement Analysis and Design*, Prentice-Hall, Englewood Cliffs, NJ, 1993.

Kandhal, P.S., "Field and Laboratory Investigation of Stripping in Asphalt Pavement: State of the Art Report," *Transportation Research Record 1454*, TRB, NRC, Washington, D.C., 1994.

Kanitpong, K., Benson, C.H., and Bahia, H.U., "Hydraulic Conductivity (Permeability) of Laboratory Compacted Asphalt Mixtures," *Transportation Research Record*, TRB, NRC, Washington, D.C., 2001.

Mallick, R.B., Cooley, Jr., L.A., Teto, M.R., Bradbury, R.L., and Peabody, D., "An Evaluation of Factors Affecting Permeability of Superpave Designed Pavements," *Transportation Research Record*, TRB, NRC, Washington, D.C., 2001.

Maupin, Jr., G.W., "Asphalt Permeability Testing: Specimen Preparation and Testing Variability," *Transportation Research Record*, TRB, NRC, Washington, D.C., 2001.

Musselman, J.A., Choubane, B., Page, G.C., and Upshaw, P.B., "Superpave Field Implementation: Florida's Early Experience," *Transportation Research Record 1609*, TRB, NRC, Washington, D.C., pp. 51-60, 1998.

Pinto, P., "Coupled Finite Element Formulations for Dynamic Soil-Structure Interaction," Ph.D. Dissertation, University of Florida, Gainesville, 1998.

CHAPTER 10
PROPOSED CONDITIONING SYSTEM

10.1 Introduction

Chapters 3, 4, 5, 8, and 9 have shown the potential importance of the effect pore pressures may have on mixture moisture damage. Chapters 6 and 7 focused on the identification of a consistent testing and analysis framework for quantifying the effects of moisture damage in mixtures. Chapter 8 dealt with fundamental aspects of how micromechanical distribution of air voids in mixtures as well as binder and aggregate type affect moisture damage in mixtures. The results from Chapter 8 show clearly that field mixtures located in the near-surface region of pavements where the vehicle loads are highest are permeable and will therefore likely develop significant pore pressures during and immediately after a rain event. Chapter 9 continued the evaluation of fundamental aspects of mixture behavior by providing a finite element analysis of typical flexible pavement sections, using permeabilities and percent air voids consistent with those determined in Chapter 8. The results showed that mixtures are likely to develop pore pressures that may range from about 100 kPa (14.6 psi) to 600 kPa (88 psi). These magnitudes of pore pressures are likely high enough to cause premature cohesive softening and stripping in mixtures that have a combination of permeabilities in the pessimum range, as identified in Chapter 8. The effect of aggregate type may either enhance or reduce the effect of pore pressures on moisture damage, as discussed in Chapter 8. Similarly, the presence of anti-stripping additives will generally decrease moisture damage, as discussed in Chapter 7.

In summary, the framework for the consistent evaluation of moisture damage has been established, and pore pressures have been identified as a likely major mechanism of premature moisture damage in mixtures. However, there is still a need to develop a moisture conditioning system that more closely simulates the primary mechanism of moisture damage in the field,

namely cyclic pore pressures. In this chapter, a new cyclic pore pressure conditioning system based on a modified triaxial chamber will be developed. The basic idea behind this system is to be able to both apply cyclic pore pressure and loads at the same time, if needed. If only pore pressures are desired for conditioning of mixtures, the current system could be greatly simplified into a self-contained table-top system that would not require an external loading frame.

In the following, the basis for the development of this new system will be discussed, followed by a discussion on the design of the system, as well as basic plumbing and environmental control considerations.

10.2 Background

The Cyclic Loading and Pore Pressure Conditioning System is a modified triaxial system designed specifically for the cyclic pore pressure conditioning of asphalt specimens. The concept of the Cyclic Loading and Pore Pressure Conditioning System was prompted by the need to analyze better the effects of water-induced damage to an asphalt mixture. Conditioning a specimen in the triaxial environment allows for precise application of stress in three different directions, if needed. If a specimen is thought of as a cube, these directions can be represented in the familiar x-y-z coordinate system. The laboratory created specimens are cylindrically shaped, thereby reducing the coordinate system to an axial vector (y) and a sum of radial vectors (x). These vectors, acting normal to the surface of the specimen, can be increased or decreased in a multitude of combinations allowing control of axial and confining stresses onto the specimen.

For years, the triaxial cell has been used by the geotechnical engineering community to assimilate insitu stresses on the specimen of interest and then, through deviation of the confining and axial stresses, quantify the material's reaction to an anticipated load. The advantage of soil testing in a controlled environment is of significant value and allows the engineer greater control

than could be acquired in the field. At present, there are several systems in different stages of development that attempt to simulate field conditions while, at the same time, producing a testing sequence that is simpler and more accurate than systems presently used. The Cyclic Loading and Pore Pressure Conditioning System is unique amongst other systems used today in that the system is designed to be versatile and comprehensive with respect to specimen testing and conditioning.

As with soil, asphalt concrete specimens have long been tested in a triaxial cell. Tests such as hydraulic conductivity (permeability), resilient modulus, complex modulus, shear strength, and creep are common in asphalt test laboratories using a triaxial device. A distinct limitation to the triaxial cells constructed today as compared with the Cyclic Loading and Pore Pressure Conditioning System is the design of the force application piston and how it transfers stress onto the specimen. Traditionally, these platens are no more than a disk of rigid material that acts as a medium between the force from a shaft and the specimen itself. The limitation occurs when stress is applied to the circumferential surface as occurs when confining stress is applied. As the confining stress increases, so too does the axial stress onto the specimen. This relationship limits the stress combinations and stress paths that can be applied onto the specimen. The initial design of the Cyclic Loading and Pore Pressure Conditioning System addressed this problem by designing a top platen (piston) encased within a sleeve. This piston-sleeve design relieves the researcher of the limitation of stress paths by allowing the axial and confining stresses to be independent of one another, thereby allowing for greater control and flexibility with applied stresses. In addition, the system is designed to allow for in-place conditioning with the support of an external water temperature conditioner as well as the ability to perform both constant and falling head permeability testing without removing the specimen from the test cell.

These added benefits allow for a sequence of testing and/or conditioning to be performed without the risk of damage to the specimen during transportation from one test setup to another. Also, the additional integral capabilities of the Cyclic Loading and Pore Pressure Conditioning System diminish the need for auxiliary equipment required to perform testing of conditioned specimens.

10.3 Design Considerations

Prior to the commencement of the system design, a full understanding of the end purpose of the system needed to be defined. The system needed to be capable of performing tests in compression and tension, as well as applying pore pressures both independent and in conjunction with loading. As a result, the structural frame of the cell needed to be designed to allow for the corresponding forces. The tests would all be performed in effective stress state conditions, thereby creating the need to develop a saturation procedure. And lastly, the system needed to be capable of getting a specimen to a stabilized temperature rapidly and maintain that temperature throughout the duration of the test.

Saturation of specimens, particularly those composed of soil, in triaxial cells is typically achieved by pulling permeant through the specimen's structure using vacuum techniques. For the design of the Cyclic Loading and Pore Pressure Conditioning System, allowance was made so that the system would be capable of applying a vacuum as well as forcing the permeant through the specimen from the influent end.

The variation in test data, as a result of inconsistent specimen temperature during testing, is well known and of foremost concern for a test requiring a high degree of precision. Hot mix asphalt is extremely temperature susceptible (e.g., Roberts et al. 1996). Repeatability of tests such as resilient modulus (M_r) determination is very unlikely if specimen groups are tested at varying temperatures. For this reason, the creation of a system that would be capable of

achieving target temperature rapidly and continue to maintain that temperature throughout testing was a criterion for design.

The achievement of heating and cooling of water used in existing triaxial testing systems used at the University of Florida and in many systems are through indirect methods. Heating is achieved via conduction from thermo probes onto the base plate. The base plate would, in turn, heat the confining water. Thermo probes are commercially available and operate much like the surface heating coil on an electric stove. As electricity is passed through the probe, resistance is developed that transforms the electrical energy to heat. Typically, two probes, approximately ⅜ inches in diameter and 8 inches long, fit into the base plate of the cell via smooth borings that run parallel to one another. The main disadvantage of this design is that the cell acts as a heat sink, requiring that it be heated prior to the confining water. The specimen is then reliant upon the conduction of heat from the confining water in order to arrive at the test temperature. The combined mass of steel and water requires a large amount of time and energy to arrive at the test temperature. Additionally, cooling of the confining water is achieved via indirect methods. Chilled water is circulated through a copper coil that travels around the exterior surface of the confining cylinder. To minimize the absorption of thermal energy from the atmosphere, the cell was wrapped with a plastic-encased sheet of fiberglass insulation. Although the insulation impedes the absorption of unwanted thermal energy, it is not completely effective and the achievement of low temperatures is not possible due to the inefficiency of the system. As with the method of heating, this configuration must condition the temperature of the cell prior to the confining water, thereby creating a lengthy conditioning period.

It was recognized early in this process that a direct method of water conditioning would need to be developed that would be capable of readying a specimen in a reasonable amount of

time as to make the system useful in production testing. The rapid achievement of test temperature was largely based upon three factors:

1. The selection of properly sized cooling and heating devices.
2. Reduction of the length of transmission lines in order to minimize thermal losses or gains.
3. The minimization of the volume of confining water space within the cell thereby minimizing the amount of energy required by the temperature conditioner to be either removed or added to the water.

The overall appearance of the cell is very typical of other existing triaxial cells. The structural core consists of two round plates separated by posts or what are referred to in this report as struts. The structural core is encased with a cylinder and the entire package is sealed which creates an enclosed cavity capable of being pressurized. The variable of the cell's design is the proportionality of these components. The dimensions of the test specimen dictated much of the subsequent design of cell components. The diameter of specimens used with this cell was decided as 4 inches (100 millimeters). This system was developed as a prototype and it was deemed prudent to ensure it could operate properly before designing a cell capable of testing larger specimens (6 inches or 150 mm). Additionally, as the diameter of the specimen increases, the overall size of the cell increases in a near proportional manner. Therefore, in an attempt to balance overall size and cost to manufacture a device for this research project, the smaller specimen size was chosen.

The system was designed as a self-contained testing device. In order to achieve a saturated specimen, backpressure saturation techniques would be required. The integration of a vacuum device capable of relieving at least one atmosphere of pressure to assist with the liberation of air trapped in the specimen was required.

Although a prototype, the system was intended for use in production testing. The process for specimen installation was examined as the cell design progressed. Owing to the complexity of the installation of instrumentation used to monitor the specimen, AutoCAD generated schematics were used to ensure that these instruments could be installed in conjunction with the specimen. Traditional triaxial tests, M_r tests, and Complex Modulus tests also required that a latex membrane be placed over the specimen and overlapped over the end platens. This step is critical for ensuring the isolation of the saturated specimen from the confining water. Therefore, consideration was given to the allowances required to enable the operator to successfully position this membrane in a limited space in order that the overall size of the cell be minimized as greatly as possible. For this, several mockups were made to determine which combination of configuration and spacing provided the optimum balance of size and function.

As discussed in research for a modified Environmental Conditioning System (ECS) developed at the University of Texas, El Paso (Alam et al. 1998), one of the problems experienced was the lack of rigidity with the system as a whole. This lack of rigidity could contribute to erroneous data as a result of linear displacement of the specimen during dynamic testing since the system will deform slightly when induced by high-pressure loads. To avoid such a problem with this system, connectivity of components of the cell was examined prior to the construction. Where components interfaced with an o-ring incorporated to act as a seal, allowance was made to ensure that the groove in which the o-ring was seated provided proper volume to contain the compressed seal. This would allow the mating components to achieve surface-to-surface contact thereby producing a rigid connection. The center vertical core of the cell is configured to allow for all forces from the piston to be directed normal to the base plate without rotation or movement from an inclusive component. The base platen and piston employ

both end bearing and thread bearing from a threaded rod and piston shaft respectively. This compliment of connectivity creates an extremely stable union of components.

Finally, a great effort was made to produce a system that not only would be simple to manufacture and operate, but would also be as cost effective as requirements would allow. Utilizing available raw metal shapes and specifying proper tolerances of machining constructed a relatively inexpensive cell. Components that required a high degree of machining effort, such as the top and base platen, were specified only after being investigated for alternative design and necessity for the desired function of the cell.

10.4 Construction and Design

The Cyclic Loading and Pore Pressure Conditioning System is composed of six sub systems:

1. Modified triaxial cell
2. High-pressure water distribution system
3. Data acquisition system (Material Testing Systems (MTS) Model 810)
4. Hydraulic load frame (MTS 22 kip)
5. Low temperature water conditioner
6. High temperature water conditioner

Part of the objective of this research was the design and manufacture of the former two (1 and 2) sub systems and subsequent integration with the latter four (3 through 6) support sub systems. A schematic of the system components is shown in Figure 10-1.

10.4.1 Cyclic Loading and Pore Pressure Conditioning System Design

The design for the modified triaxial cell was approached in the following order:

1. Determination of parameters of targeted testing that dictated design elements of the cell (e.g., size of specimens to be tested, instrumentation to be integrated with the cell, and system pressure)
2. Piston assembly design
3. Top and base plate design
4. Strut design and bearing capacity calculation
5. End platen design
6. Confining cylinder selection
7. Confining ring design
8. Seal selection and placement
9. Component tolerance specification
10. Radial LVDT holder design

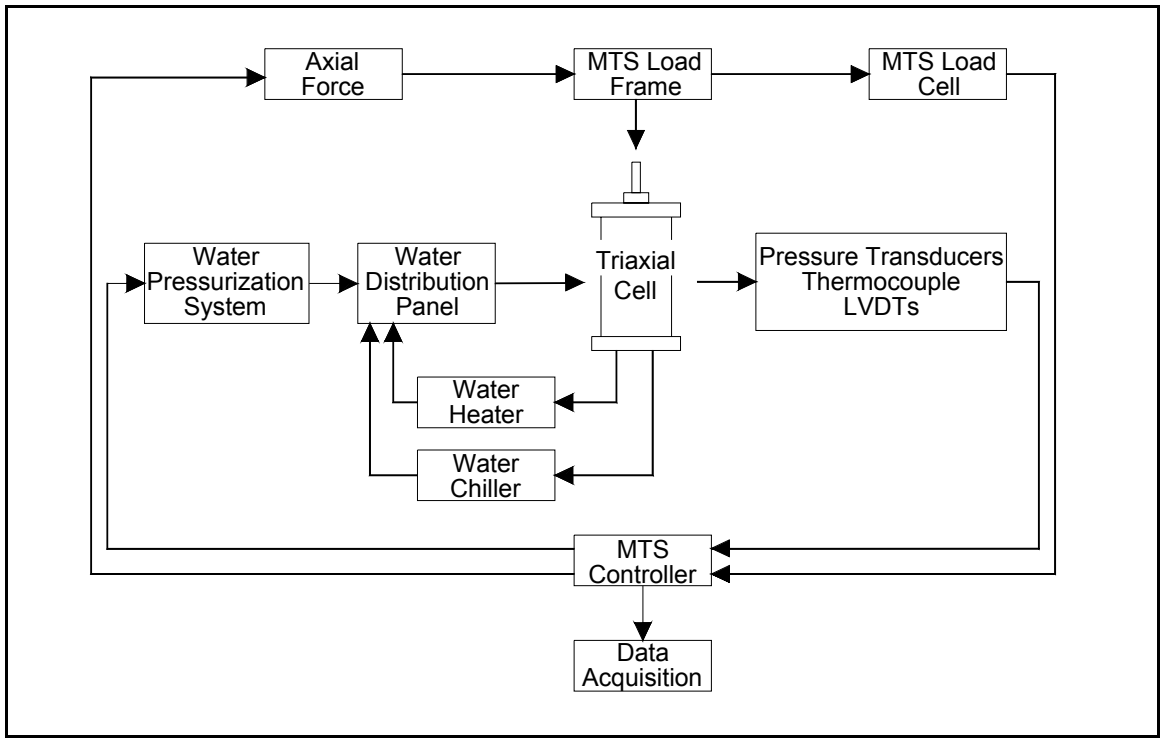

Figure 10-1. Cyclic loading and pore pressure conditioning system component schematic.

Design parameters determination

The design specimen height was arrived at as a compromise between recommended aspect ratios for the two primary tests of the system, hydraulic conductivity (permeability) and resilient modulus. During the literature review of permeability testing, an aspect ratio recommendation was found to be from 0.5 to 1.0 (Carpenter and Stephenson 1986). This translates into a specimen height of 2-4 inches (50-100 millimeters). The recommended aspect ratio of a specimen for resilient modulus testing is 1.50, which translated into a specimen 6 inches (150 millimeters) high. A compromised design specimen height of 5.5 inches (137.5 millimeters) was decided upon in order to facilitate both of these tests into one device.

The cell was also designed for the development of a new test in which large confining pressures would be placed onto the specimen to induce a failure in tension. This meant that the cell would be expected to contain larger pressures than those in typical triaxial cells. Based upon the mechanics of the anticipated failure, the cell was designed to contain 400 psi of fluid pressure.

At this point in the design process, as with all new equipment development, reasonable engineering judgment needed to be applied for certain parameters. One of these parameters is the length of piston stroke required for the desired test. As will be discussed later, the design of the top platen assembly required that the maximum stroke length be minimized to maintain sealing integrity. Based on review of previous compression to failure testing, the maximum stroke length was concluded to be 0.75 inches.

Another issue of design was how large the cell needed to be made in order to minimize structural stresses and facilitate specimen installation. A thorough effort was made to limit the overall size of the cell without making it so compact as to interfere with specimen installation and subsequent data acquisition instrumentation such as linear variable displacement transducers

(LVDTs). This effort was made out of structural concerns with regards to the sizing of the supporting struts (vertical support members) compared to the end area of the cell. As the interior diameter of the cell increased, so too did the diameter of the four supporting struts required to restrain the resulting force on the top and bottom plates of the cell. The four struts that maintain the position of the base and top plates are analogous to the columns of a building. However, unlike columns, the struts must maintain forces in tension since the interior of the cell is pressurized. Therefore, as the end area of the cell (top and base plates) increases, so too does the resulting tension forces acting on the struts. An optimization of end area versus strut diameter was performed to produce an interior cell cavity that was adequately sized to install instrumentation, yet compact enough for reasonable structural component sizing. The cell is intended for 4 inch (100 millimeter) diameter specimens with an aspect ratio of 1.25-1.50. Side views of the cell components are shown in Figures 10-2 and 10-3. All components are fabricated of 303 stainless steel with the exception of the piston, end platens, and the confining cylinder, which were made from 6061-T6 aluminum. Stainless steel was chosen for four reasons: 1) availability, 2) high strength to unit area ratio, 3) ease of machining, and 4) corrosion resistance. Aluminum was the logical choice for components such as the confining cylinder where weight was an issue and the end platens and piston where intricate design details precluded the use of hardened steel.

Throughout the design process, corrosion control of components was a factor of material selection. Owing to the aggressive environment that these components operate in, the potential for reaction between dissimilar metals was an issue for design. Aluminum and stainless steel are considered “compatible,” as shown in galvanic series charts, when one material is finished with

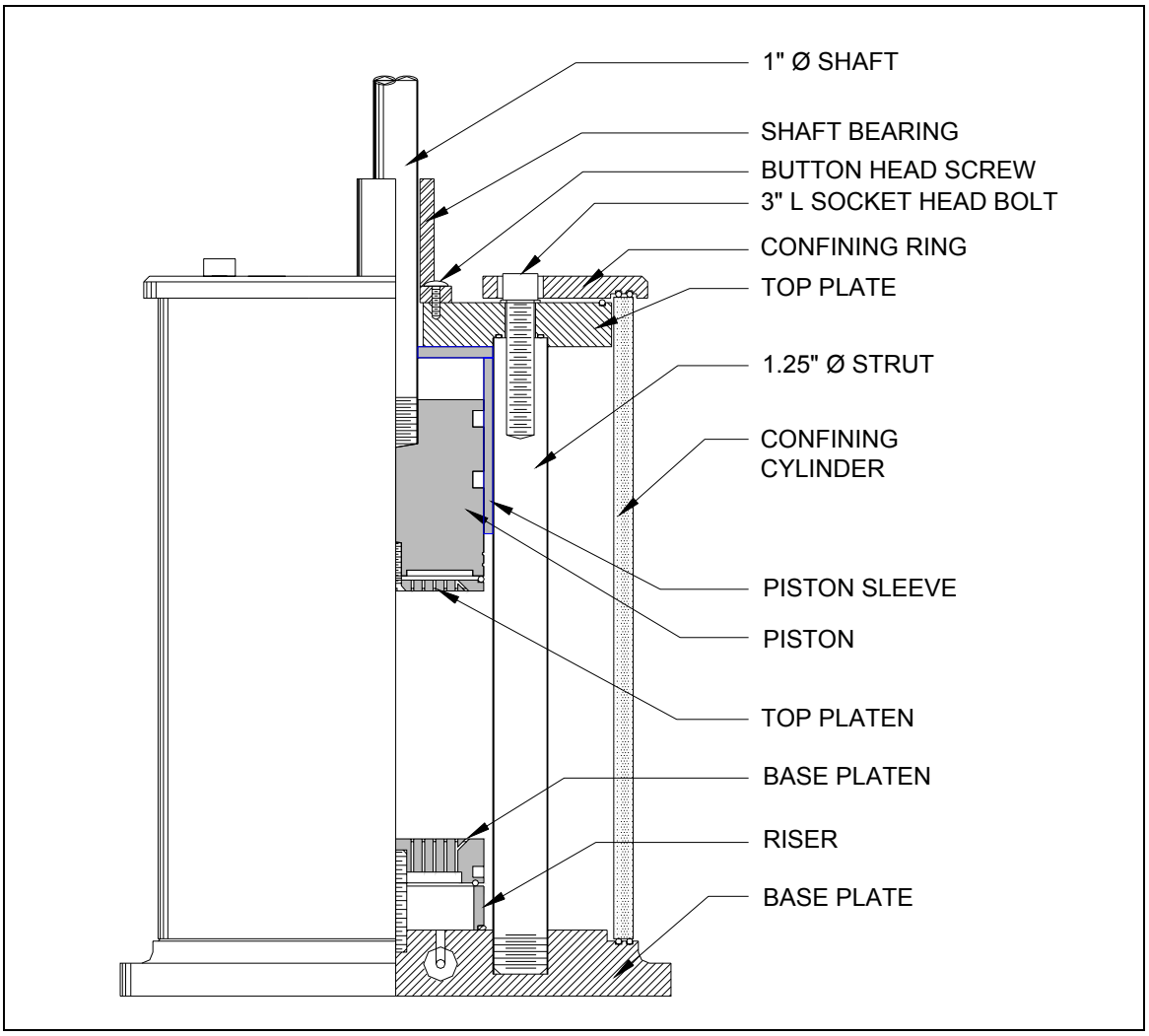

Figure 10-2. Triaxial cell through drawing–front view.

at least one coat of anodizing primer (Juvinall 1983). Where aluminum was used, these components were anodized to retard the corrosion process. Anodizing of aluminum alloys produces a stable aluminum oxide film that provides substantial corrosion resistance (Juvinall 1983). Additionally, separation between aluminum and stainless steel components was provided via buna-N o-rings, which further assisted with the dampening of electrical current flow through the dissimilar metal interface.

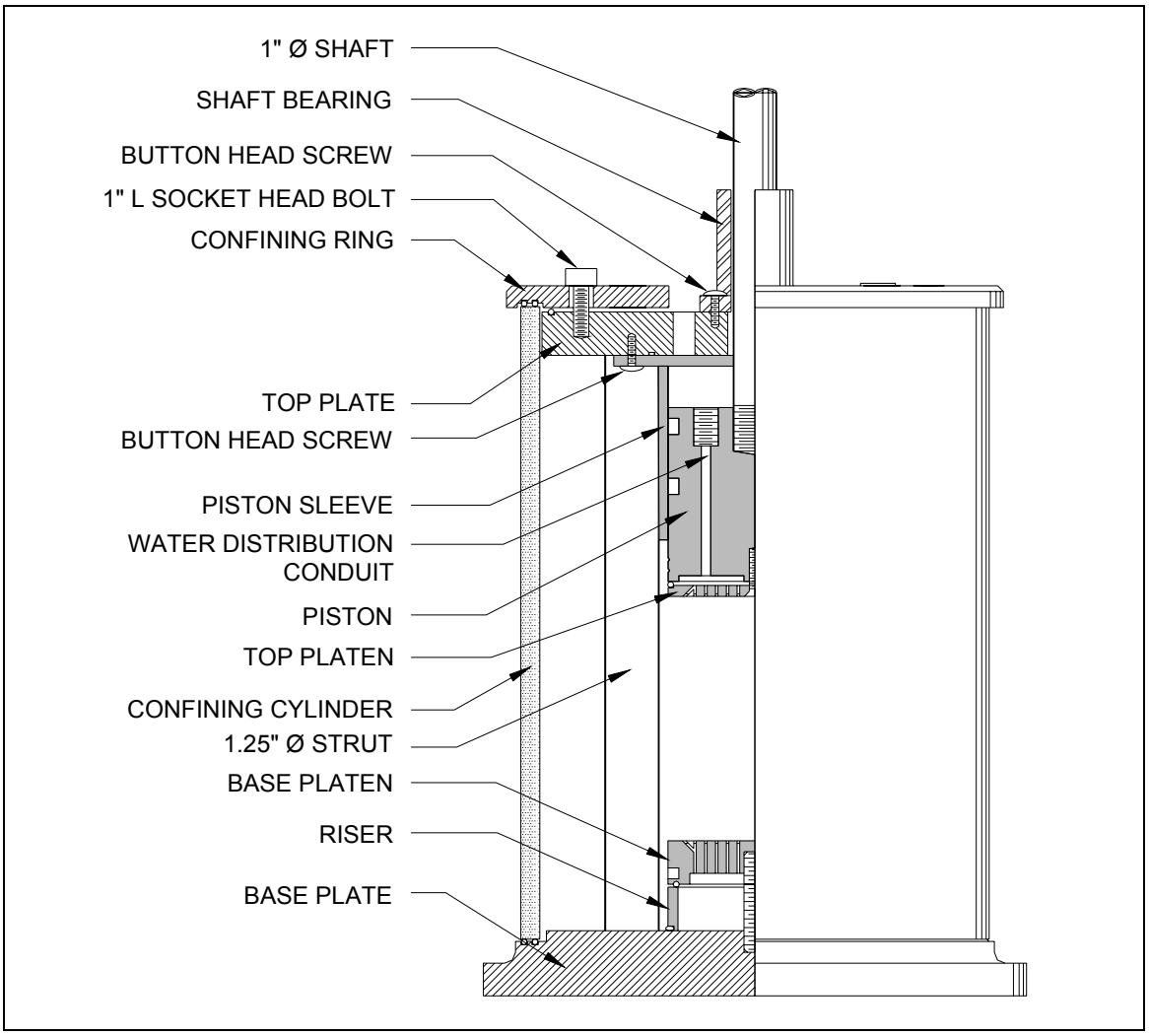

Figure 10-3. Triaxial cell through drawing–rotated 45° from front view.

With the major design parameters defined, efforts were directed to the design of the individual components.

Piston assembly design

The piston assembly was a logical place to begin the design process in that it dictated many of the subsequent component designs. It was imperative that the sizing and function of the piston assembly be determined prior to the design and manufacture of the remaining cell components. As was previously mentioned, the most prominent distinction between the Cyclic Loading and Pore Pressure Conditioning System and traditionally manufactured cells is the

piston-sleeve assembly. The challenge of design was to create an assembly that would yield low frictional contributions while simultaneously providing a leak-proof barrier between the interface of the cell and the atmosphere. The initial piston-sleeve assembly design consisted of a Frelon® bearing for a sleeve and a custom fabricated stainless steel cylinder for a piston. A Frelon® bearing is a commonly used bearing constructed of a hollow, aluminum cylinder that is lined with a sheet of the low-friction material Frelon®. The opinion at the time was that the Frelon® bearing would act as a low friction surface for the cylinder to cycle on while, at the same time, preventing water from emigrating from the triaxial cell interior, past the Frelon® bearing, and to the exterior of the cell. The foremost advantage to this design was the immediate availability of the bearing from several suppliers with bore diameters of 4 inch and 6 inch common. After procuring a bearing for a determination of suitability, several weaknesses were discovered. First, the sheet of Frelon® that lines the bore is glued to the inside of the aluminum cylinder and results in a poor quality seam where the two ends of the sheet union. After consideration, it was decided that this seam would not be capable of restraining the increasing water pressure from within the cell during a typical testing sequence. Secondly, the roundness from true of the interior of the bearing (bore) varied in excess of .003 inches in diameter that would make the complimentary mating of a piston difficult. After consulting with several area machinists, it was concluded that even if a matching piston could be manufactured, the precision required between the piston and the Frelon® bearing to accomplish the aforementioned goals is too high and not practical nor cost effective for the project.

The next consideration for a piston assembly was more tolerant of geometric imperfections and proved easier and less costly to fabricate. The piston assembly is composed of two main components: a piston sleeve and a piston. The piston sleeve is affixed to the top plate of

the cell and acts as a fixed member for the piston to travel within. As is illustrated in Figure 10-4, the piston sleeve was constructed using stainless steel. This material was selected for its ability to be machined to very high tolerances and polished for low frictional contributions of seals in contact with the interior surface. Additionally, this component required welding as part of its manufacture thereby dismissing aluminum as a viable candidate. As can be seen in Figure 10-4, the piston contains a flanged ring allowing for the passage of bolts to secure it to the top plate. This flanged ring was welded to the tubular portion of the piston, which made fabrication costs lower than if the piston were to be machined from a solid piece of material. The utilization of available geometric shapes and sizes from material suppliers not only expedited the construction process, but also aided with the creation of a cost-effective cell.

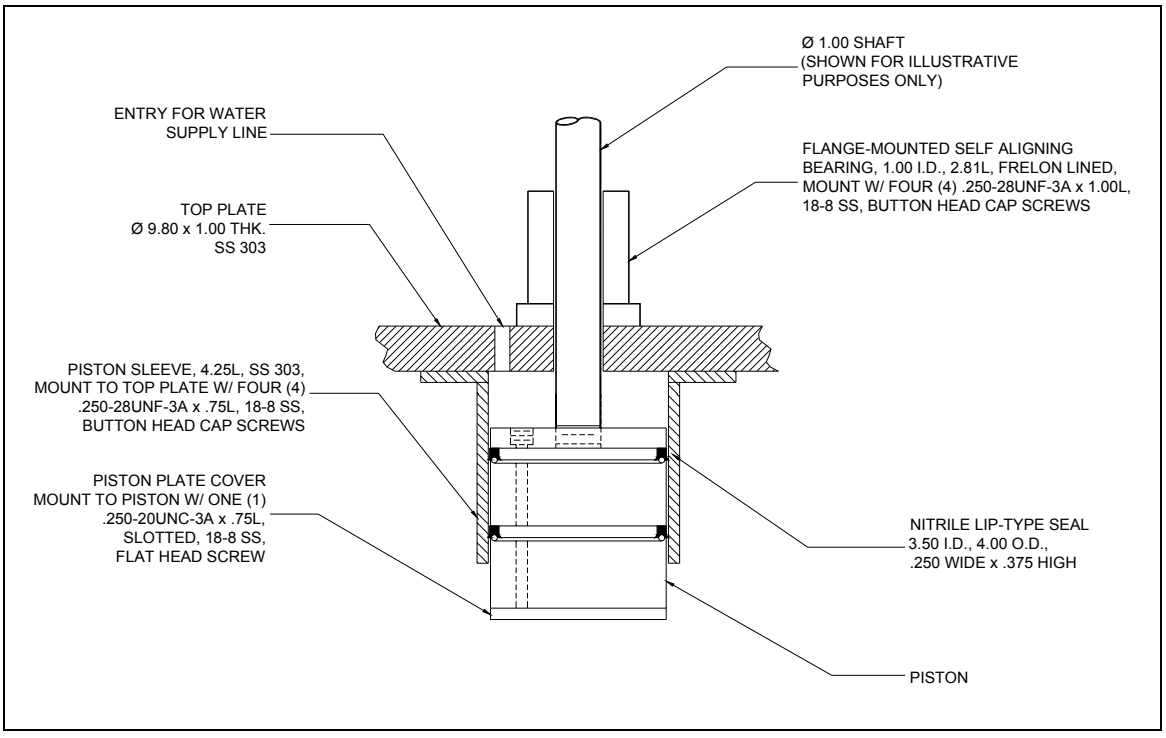

Figure 10-4. Piston assembly detail.

Conversely, the piston is machined from a billet of aluminum to provide the strength necessary for compression-based tests. The piston contains two inscribed grooves about its circumference designed to receive flexible seals. Although one seal would have been adequate for this application, duplicity was chosen to further steady the piston inside of the sleeve and act as a backup if the primary seal were to fail. Due to the critical role these seals play in the successful operation of the cell, the grooves were designed to compliment the component specifications of the seals. These seals are made of wear-resistant Nitrile lip seals and resemble a flared "U". They are installed into the grooves of the piston cupped in the downward direction, which forces any increase in water pressure to act within and outwardly through the seal. This change of pressure increases the "squeeze" of the seal onto the interior surface of the piston sleeve. These seals are appropriate for this application in that as they wear at the contact surface, the downward cup design compensates by allowing the seal to open to a greater degree, thereby assuring a tight seal against the piston sleeve. This attribute provides a much longer service life than could be expected from other seals having a more symmetrically shaped profile. Seals with a symmetrical profile such as o-rings, are less forgiving of an uneven wear pattern and are not appropriate to dynamic applications.

This configuration has performed extremely well in proof testing and throughout several production tests, having successfully prevented any bypass of water from the cell's interior. For the purpose of design, the seals are considered to be consumable components of the test system and will eventually require replacement. After many sequences of testing, the seals have performed up to the design goal and indicate no visible signs of wear.

Top and base plate design

The thickness of the base and top plate is a function of the bearing capacity required from the struts onto the plate and was calculated with a factor of safety of 2 at the maximum safe

operating pressure of 800 psi. It was anticipated that the cell would operate in the range of 0-400 psi for the types of tests the system was being designed for.

The base plate performs three basic functions. First, it acts as a staging platform for other components of the system. Secondly, it contains the watertight entrances for instrumentation cables entering the cell, and thirdly, it includes the conduits for pressurized water entry both through and around the specimen.

There are four ports (through holes) that were specified for use with plug-in type fittings available from Geotechnical Consulting & Testing Systems (GCTS), Tempe, Arizona. These fittings consist of hollow cored, threaded male and female pieces that, when tightened together, compress a confined o-ring, thereby sealing the interface. The cables for instrumentation used for the system can be chased through these assemblies, allowing for easy installation of any combination of instruments into the cell. These cables exit the cell's interior and are neatly chased via grooves in the bottom of the plate to the data acquisition system.

The protocols for testing require that the system be capable of circulating water both through and around the specimen. The ability to transport water through the specimen is essential for achieving saturation and also is essential for permeability testing. In order to apply fluid pressure around the specimen and condition it to the testing temperature, it was required to have an entrance for fluid coming from the water distribution panel. With these requirements in mind, the base plate has two 1/8-in diameter conduits that run through the center of the base plate terminating at the specimen location and the cell cavity location.

The thickness of material chosen for the base plate was dependent upon the required bearing surface area of the threaded struts that fastened into the plate. An optimization was conducted to size the struts versus the thickness of the plate (see strut design for further discussion).

The primary function of the top plate is to act as a platform for the piston assembly. The plate is fastened to the four struts via socket head screws that pass through the plate. At this point in the design process, a block shear type of failure about the socket head screw had not been investigated. This analysis was conducted in the following component phase therefore, at this point, the thickness of the plate was assumed to be 1 inch. The piston assembly is fastened to the lower face of the top plate with four (4) stainless steel button head cap screws. A 1 inch inside diameter flange-mounted self-aligning bearing is fastened to the upper face of the plate to guide the travel of the rod attached to the piston. The incorporation of a self-aligning bearing eliminates the potential for damage to the piston sleeve from a misaligned piston. Both the piston assembly and the self-aligning bearing are capable of being adjusted about the vertical axis of the cell to ensure proper alignment of the end platens on either end of the specimen.

The top plate contains two 0.500 inch diameter holes that allow the exiting of fluid from within the cell. One hole is located such that it falls over the piston. This hole allows for the placement of copper tubing for the transport of water from the top of the specimen. The second hole is positioned outside of the piston assembly profile providing an outlet for temperature-conditioned water or an inlet for pressurized air.

Strut design

By this time in the design process, the diameter of the struts was already determined during the optimization process within the base plate design stage. The connectivity of the struts to the plates was determined based upon methodology of construction. As can be derived from the connection detail shown in Figure 10-5, the success of an adequate seal at all o-ring points is dependent upon the uniform compression of these seals along the length of the o-ring. To ensure uniformity, the separation between the top and bottom plates must be tolerable within a fraction

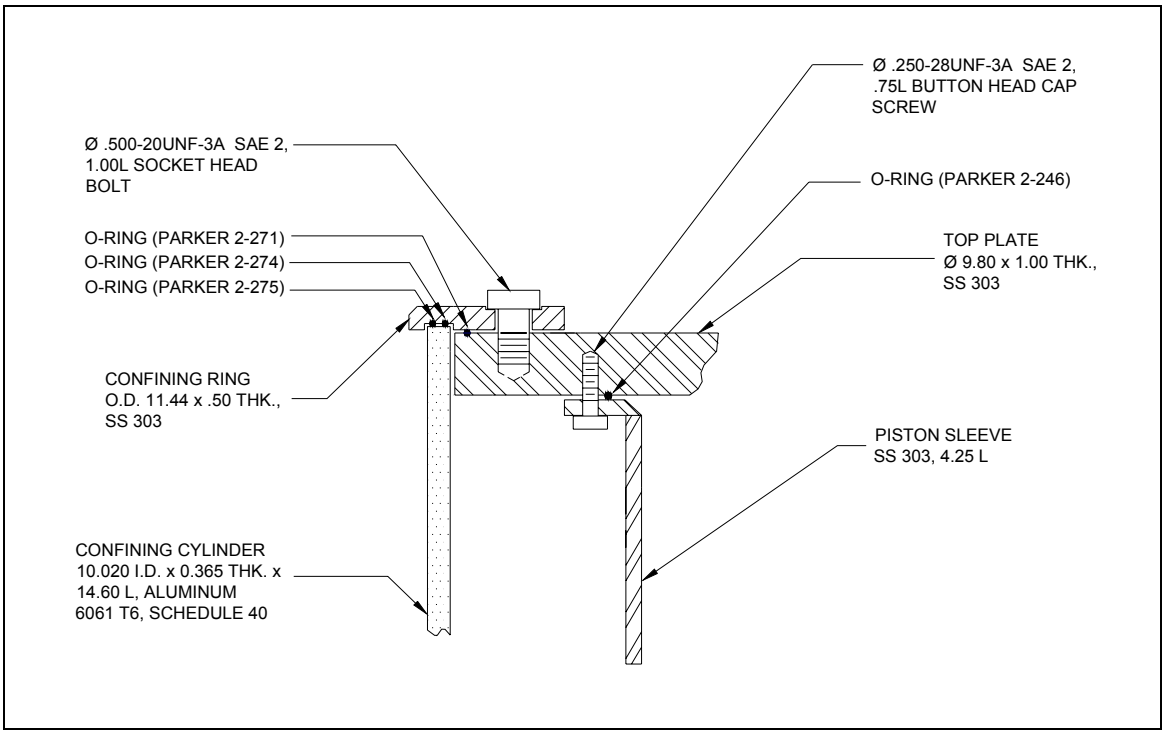

Figure 10-5. Top plate to confining ring connection detail.

of the o-ring's diameter. If, for example, the distance of separation were too far out of tolerance, one portion of the o-ring would contact before the opposing side, creating an inadequate seal. Designing a strut that would be capable of adjustment was therefore necessary to ensure uniformity of seal compression.

All four struts are typical and are a combination of exterior (male) threading on the end that interfaces with the base plate, and interior (female) threading on the end interfacing with the top plate. This combination allows for the struts to be adjusted for equidistant separation prior to the top plate being installed. Subsequently, as shown in Figure 10-5, the top plate is secured using the high-strength socket head bolts.

The design of the threaded ends of the struts had to be specified. Since the struts were to be designed as tension members, the end bearing capacity of the struts were not considered and the design approach turned to the bearing ability of the threads. Bolts (as is the assimilation of

the male strut end) can fail in tension four different ways: 1) thread stripping of the bolt if it is a weaker material than the nut, 2) thread stripping of the nut if it is a weaker material than the bolt, 3) stripping of the bolt and nut if both are of similar material, and 4) shearing of the bolt if thread bearing strength surpasses the bolt's tensile strength (Juvinall 1983). In the case of the base plate connection, where the strut (bolt) and the base plate (nut) are of the same material and limited engagement depth precludes shearing of the strut, failure mode 3 controlled the design.

Based upon the geometry of the cell, an applied factor of safety of 2, and the pressures it is designed to contain, the resulting tension force anticipated for each strut was calculated as 15.7 kips. The bolt tensile force required to yield the entire threaded cross section is defined as:

$$F = A_t S_y \approx \frac{\pi}{4}(0.9d)^2 S_y \tag{10.1}$$

where: F = bolt tensile load required to yield the entire thread-stripping failure surface of the strut (kips)

A_t = total surface area of threads resisting tensile force (in^2)

S_y = yield strength of strut (0.2% offset) (ksi)

d = major diameter of the strut (in)

The bolt tensile load required to yield the entire thread-stripping failure surface of the base plate is defined as:

$$F = \pi d(0.75t)(0.58S_y) \tag{10.2}$$

where: F = bolt tensile load required to yield the entire thread-stripping failure surface of the base plate (kips)

d = major diameter of the strut (in)

t = depth of engagement into the base plate (in)

S_y = yield strength of strut (0.2% offset) (ksi)

Equating the former two expressions for F yields balanced tensile and thread-stripping strengths when the depth of engagement is approximately:

$$t = 0.47d \tag{10.3}$$

The process for calculating the design of the strut to base plate connection was as follows:

1. Calculate depth of engagement using Equation 10.3
2. Arbitrarily choose a thread designation and, by using the depth of engagement t solved for in step 1, determine the corresponding bolt tensile load required to yield the entire thread-stripping failure surface of the base plate, F, as defined in Equation 10.1
3. Continue with iterations of differing thread designations until F, as defined in Equation 10.2 approximates the design resistance force of 15.7 kips as defined for design.

The design of the strut to top plate connection utilized the same methodology as the previous connection with the primary exception being that it has inside threads and utilizes a socket head bolt (see Figure 10-6). The socket head bolts are Society of Automotive Engineers (SAE) Grade 5, with yield strength, S_y, of 92 ksi. For all sense and purpose, this level of strength far exceeds the requirement of this application. However, the cost of these bolts was reasonably low and the added level of strength is of value when considering this added strength effectively removes a failure mode from probability. The additional failure modes that needed to be checked were:

1. Shearing at the reduced-area cross section
2. Shearing of the bolt
3. Block failure (pullout) of the top plate about the socket head: bolt interface

With the design of these connections accomplished, the structural core of the system was complete. The following components would be designed to compliment this structure.

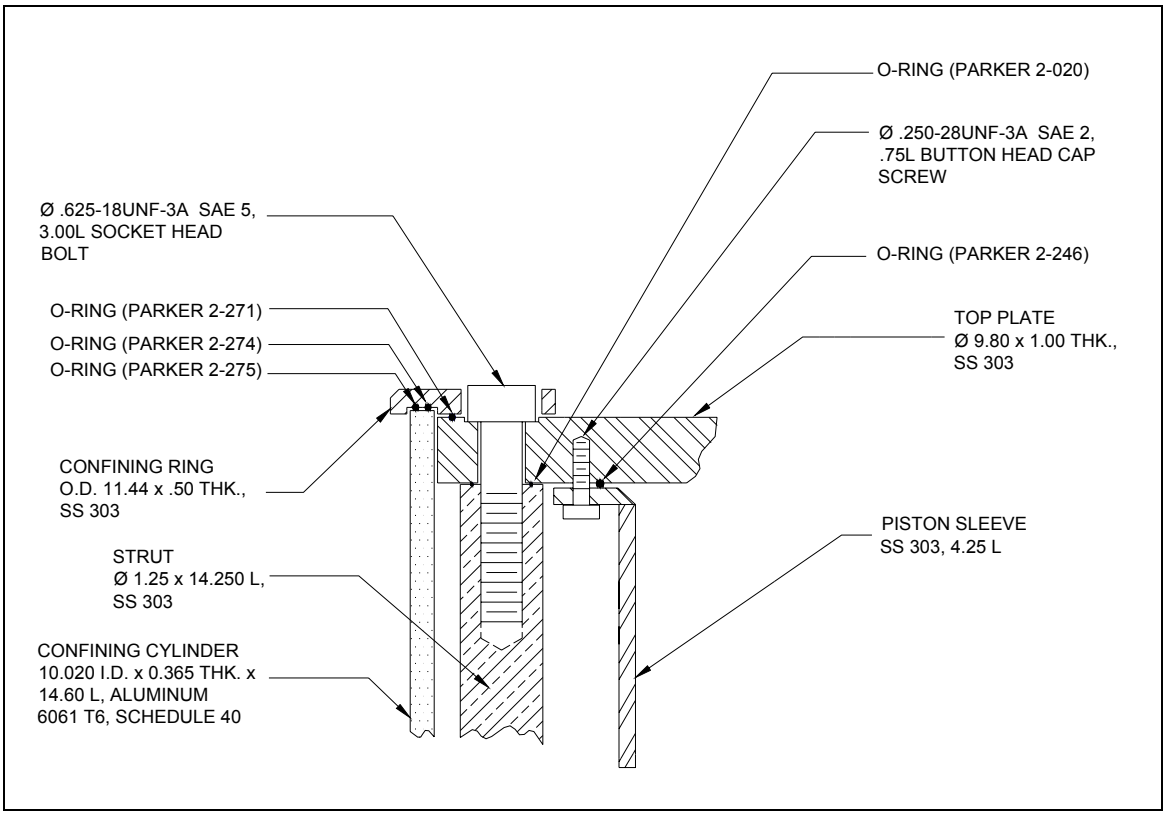

Figure 10-6. Top plate to strut connection detail.

End platen design

The approach for the design of the end platens began with a review of needs for this component from each test. Depending upon the test, these platens needed to perform different tasks. For example, tests such as resilient modulus and drained and undrained compression, required that the platens resist induced compressive stresses. Additionally, any contributory end effects resulting from friction between the platens and the specimen's ends needed to be minimized as much as design would allow. Other tests such as constant and falling head hydraulic conductivity (permeability) placed a greater emphasis on the ability of the platens to conduct and distribute water with a minimal amount of interference. It is the opinion of this researcher that existing designs do not efficiently allow the transport of fluid through the

specimen but rather force the fluid through specific and limited paths, thereby introducing error into the test. This becomes evident when an inventory of losses due to constrictions, expansions, and bends along the fluid's path is made. After consideration of the requirements it was concluded that different platens would be required for different tests.

Unlike more commonly used end platens, which distribute water via one hole and conducting grooves or dimples, those in the Cyclic Loading and Pore Pressure Conditioning System contain many orifices across its surface. This allowed water to be transported through the test specimen uniformly and without concern for isolated piping or excessive pressure gradient development. Additionally, these platens are fabricated with concentric grooves to better distribute the water across the face of the specimen. This configuration is also advantageous in the initial specimen saturation phase since it allows for a front of fluid to pass through the specimen, which more effectively liberates entrapped air bubbles. The presence of conducting channels across the entire profile of the platens diminishes the likelihood of entrapped air bubbles between the platens and the specimen.

The complexity of the profile coupled with the relatively small conducting orifices specified dismissed stainless steel as a material candidate. Aluminum was chosen due to its relative ease of machining and ability to harden to a level required for use by anodizing the part. Both the top and the bottom platen have identical profiles. This similarity ensures conservation of volume in and out of the specimen and decreases production costs since only one profile had to be identified for machining.

The top platen is basically a plate that caps the end of the piston. It is fastened via a screw into the piston which when tightened, compresses an o-ring placed between the two mating parts that prevents water from being conducted through the mated seam. The base platen

is attached to the base plate via a threaded stud that also assists with the proper, concentric alignment of the platen about the cell. A concentric, half-round groove is machined into the mating face of the platen for installation of an o-ring serving the same purpose, as does the aforementioned o-ring. Machined into the circumference of the platen are two half-round grooves that are used to "seat" the o-rings that hold the latex membrane to it. Additionally, a 1.0 inch high hollow riser was manufactured that can be placed between the base plate and platen. The option of using a riser allows a specimen height range of 5-6 inches (127.0-152.4 millimeters).

For compression-based testing it was necessary to protect the faces of the platens from marring and increased damage. Additionally, the concentric grooving in the face of the platens introduced an unfavorable end constraint of the specimen. To lessen these end effects, several sets of low friction, high-strength Duron® platens were fabricated to fit between the aluminum platens and the specimen. These Duron® platens are mechanically fastened to the aluminum end platens to prevent any shifting during testing. Additionally, they contain concentrically positioned holes that compliment the location of the grooves contained in the aluminum platens, thereby still allowing a method to saturate a specimen and determine its hydraulic conductivity prior to compressive testing.

Confining cylinder design

Due to the large diameter of the cell, the availability of cylindrically shaped material was limited. Early in the design process, it was understood that the larger the cell's diameter became, the less number of incremental diameters of confining cylinder would be available. With this in mind, the selection of a suitable material/diameter combination was researched. Since the cell would be operating at much higher pressures than typical triaxial cells, plastics, such as the

commonly used material Lucite® with a maximum allowable wall pressure of 150 psi, would not be adequate.

The finished length of the confining cylinder, considering cumulative compression of o-rings, was calculated as 14.60 inches with a required diameter of approximately 9.5 inches or larger to accommodate the struts, specimen, and instrumentation within the cylinder. Since this component would require constant removal and reinstallation for testing, the overall weight was a concern for two reasons: 1) physical requirements for any future operators (i.e., strength) were not reasonable to assume, and 2) as the weight of the cylinder increases and becomes more unwieldy, so too does the potential for damage attributed to mishandled or colliding parts. Therefore, relatively dense materials such as stainless steel were excluded from consideration. Aluminum alloys were researched for adequacy and availability. Aluminum 6061-T6 weighs approximately 0.10 lb/in^3, which is roughly one-third the weight of a stainless steel material. A 10" nominal diameter, schedule 40 pipe was located which has yield strength of 40 ksi. The anticipated maximum hoop stress was calculated as (Beer and Johnston 1992):

$$\sigma_{hoop} = (\text{factor of safety})\left(\frac{Pr}{t}\right) \tag{10.4}$$

where: P = maximum operating pressure (psi)

r = inside radius of cylinder (in)

t = cylinder wall thickness (in)

With a factor of safety of 2, the hoop stress was calculated as 10.98 ksi, far below the allowable stress of the material. Although thinner walled material was available, it would not have been adequate since this narrower dimension would have created difficulties mating with the o-ring seals at the ends of the cylinder. It is of value to note that pipe of this dimension and

material type is difficult to locate. This type and size pipe is used in specialized applications such as electric generation plants and is manufactured in lengths exceeding 10 feet. The procurement of a 15 inch long piece of these segments entailed a special cutting fee. The cylinder, while being structurally adequate, does raise a concern with similarly designed cells that may be constructed in the future. Owing to the fabrication method and subsequent storage of the material at the manufacturer, the material is slightly out of round when purchased. This distortion makes the mating of the cylinder to the o-rings contained in the lower and upper portions of the cell more difficult than if the cylinder were truly round. If additional cells are manufactured in the future, thicker walled cylinders are recommended followed by a center-less ground method of machining to create a cylinder that is truly round.

Confining ring design

The confining ring is one of the most critical of all the components. The ring compresses the seals in contact with the confining cylinder and the seal inset into the exterior face of the top plate that prevents the migration of pressurized fluid from the interior of the cell. The ring is attached to the top plate via four 1 inch long socket head bolts. These bolts resist the force applied to the ring through a gap between the confining cylinder and the top plate. The force against the ring is relatively small compared to forces exerted onto other components. For this reason, the nominal thickness of the ring is 0.50 inches. The socket head bolts employ flat washers between them and the surface of the confining ring to increase the contact area with the ring. The ring was analyzed for block shear about the bolts as well as stripping type failures of the bolt to top plate connection.

The confining ring has a recessed, concentrically located channel machined into the face that contacts the confining cylinder. This channel helps to align the top of the confining cylinder

within the ring thereby "locking" the two components together. Two semi circular grooves are placed into the channel for the placement of o-rings where the confining ring interfaces with the confining cylinder. Four through holes are positioned into the ring that complement the locations of the bolt heads from the top plate to strut connections. An additional through hole is provided which fits over a quick disconnect fitting installed into the top plate allowing fluid to be cycled through the cell's interior.

Radial LVDT holder design

The use of LVDTs is necessary for the computation of the variation of the cross sectional area of the specimen during failure testing in compression. These LVDTs are positioned such that they are normal to the cylindrical surface of the specimen in 90° increments. A holder was designed that allows for the installation of four LVDTs in this configuration. Machined from aluminum and anodized for corrosion resistance, the holder contains four through holes that allow the holder to be integrated with the struts of the cell. Slightly oversized, these through holes enable the holder to travel to any position along the length of the struts. Once positioned, the holder is affixed to the struts via eight nylon-tipped, stainless steel setscrews. The nylon tip prevents marring of the strut and is intended for applications where the setscrew is continuously reengaged. The LVDTs are placed into the holder via through holes and restrained with stainless steel set screws. This simple configuration allows for rapid positioning of the devices at any position along the length of the specimen.

Seal selection and placement

With the exception of the u-cup seals used for the piston, all other seals were accomplished with buna-N o-rings supplied by Parker Seals, Inc. Buna-N (nitrile) is a commonly used o-ring material that is available in a wide range of diameters and cross sectional thickness. Table 10-1 lists the technical specification details related to the o-rings. This material is resistant to

Table 10-1. Nitrile O-ring Schedule

Component	Parker Part Number	Number Required	Application Description
Base Plate	10-341	1	Interface between confining cylinder and base plate
	2-008	4	Sealant for cables exiting through base plate
Top Plate	2-272	1	Interface between top plate and confining ring
	2-160	1	Interface between top plate and Frelon bearing
Strut	2-118	4	Interface between top of strut and top plate
Confining Ring	2-275	1	Interface between confining ring and confining cylinder
Piston Plate	2-044	2	Restraining rings for membrane to piston plate
Piston Plate Cover	2-044	1	Interface between piston plate cover and piston plate
Base Platen #1	2-044	2	Restraining rings for membrane to piston platen
	2-042	1	Interface between base platen and base plate
Base Platen #2	2-044	2	Restraining rings for membrane to piston platen
	2-042	1	Interface between base platen and base plate

petroleum-based fluids and maintains its shape and pliability after a high number of compression cycles. The combination of these factors was necessary for the anticipated use of these o-rings. The design of all components relying on these seals was performed simultaneously with the o-ring selection process. This coordination ensured that specially sized o-rings would not have to be manufactured.

As shown in Figures 10-5 and 10-6, the o-rings are placed such that as the cell is assembled, the proper alignment of the o-rings with the corresponding component can be achieved easily. The cross sectional diameter of the o-rings was chosen such that an equivalent degree of compression of all the o-rings is accomplished following the tightening of the cap head bolts about the confining ring. The consideration of group-dependent compression of the o-rings is critical to ensure that each individual seal is properly compressed to maintain the confinement pressure.

The grooves that accept the o-rings are predominately square in profile and of adequate cross sectional area to allow for the total inclusion of the o-ring upon compression. As was previously discussed in the design considerations section, this provision allows for proper sealing while simultaneously facilitating rigidity at the interface developed from the surface-to-surface contact. Where the aluminum base platen interfaces with the base plate, a semi-circular groove profile was specified. This shape allows for the inclusion of only half of the cross section with the remaining half being reserved for compressed deformation in the area between the two components. This configuration is intentional to prevent galvanic corrosion between these two components. Where contact occurs between aluminum alloy and stainless steel, corrosion will be accelerated (Juvinall 1983). Aluminum is more anodic than steel and therefore will have the greater tendency to ionize and develop a greater negative charge (electrode potential). The aluminum component acts as an anode and the steel a cathode, thereby allowing for the development of an electrical current flowing from the aluminum to the steel. This continuous discharge of aluminum ions will eventually corrode that part. Another type of corrosion, electrochemical corrosion, can occur if these parts are placed in an electrolytic solution such as fresh water or water with a high salt content. An electrolytic solution acts as an ion carrier with positively charged aluminum ions going into solution leaving an excess of negatively charged electrons on the component (electrode). This action will continue until a condition of equilibrium is reached (Halliday et al. 1992). Since these components function in an environment where water is repeatedly drained from and refilled into the cell, equilibrium would not occur and continued corrosion could be expected.

The combined use of an insulator (nitrile o-ring) and de-ionized water as a confining fluid helps to lesson the potential for corrosion of these components. Additionally, the aluminum base platen and riser was anodized to fill in the porous surface of the material, making it more

resistant to the effects of corrosion and hardening it to protect the surface from abrasion. Compared to the cost of machining the intricate platen, the relatively small cost to anodize the part is prudent for maintaining its integrity.

Instrumentation ports

With these components designed, attention then turned towards the requirements for instrumentation incorporated with the cell. As a minimum, it was decided that a total of five sealed "ports" were needed to analyze the specimen during testing. Of these ports, two are designated for axial LVDTs, two for radial LVDTs, and one for temperature monitoring by way of a thermistor probe. With the exception of the thermistor probe which is connected to an outlet conduit at the top of the cell, the remaining instruments exit the cell through the base plate and are chased neatly to the back of the cell. In order to ensure there are no leaks when the LVDT cables penetrate through the base plate, special two-piece fittings were procured. These fittings were designed such that as the two parts are screwed together an o-ring compresses against the cable that is passed through the two parts, thereby effectively sealing the penetration. Additionally, the two-part assembly contains an outer o-ring that seals against a bore made through the base plate. This configuration makes instrument installation of the cell rapid and flexible with regards to configuration.

Component tolerance specification

As with any machine design, the specification of dimensional tolerance was required as part of the design process. Since two different materials, aluminum alloy, and stainless steel, were used in the cell thermal expansion effects needed to be considered.

The only moveable component in the cell is the piston. As a result, this component and the tolerance of the sleeve it oscillates within, warranted special consideration. Calculation of

dimensional tolerance was accomplished using tables published by the American National Standard Index (ANSI 1978). The piston sleeve assembly was considered as a running clearance fit, which is typical for applications requiring lubricant between the piston and sleeve (Earle 1994). Although no lubricant was intended to be used, the gap created between the two components ensured that there would not be any abrasion due to contact. Any contact could cause unrecoverable damage to the surface of the piston and diminishing the effectiveness of the u-cup lip seals. The calculated tolerances were then checked versus the anticipated expansion of the piston and sleeve to ensure that a gap would still exist at high testing temperatures. For calculation, the high test temperature was taken as 140°F. Coefficients of thermal expansion were taken as $12x10^{-6}$ in/°F for aluminum alloy and $8x10^{-6}$ in/°F for stainless steel (Juvinall 1983). As can be seen from these values, the higher coefficient of thermal expansion for the aluminum alloy piston validated the design considerations. If the gap between the piston and the sleeve were too small, the piston could become engaged with the sleeve at high operating temperatures. Since the piston was to be anodized, the diameter and tolerance were defined as post-coating.

All through hole locations were specified using rectangular coordinates. Over-sizing of holes, in locations where bolts would be used, was specified with common drill diameters. This relieved the fabricator from the needless effort of obtaining an over-prescribed tolerance. This over-sizing made all the mechanical connection points flexible with regards to orientation of the mating parts. This flexibility allowed for mild adjustments, which created optimal sealing conditions for the structural components.

The length of the confining cylinder was defined to the hundredth of an inch. Although a more stringent overall length could have been specified, doing so would have placed an undue

burden on the fabricator and resulted in higher than necessary cost. The ability for the struts to be lowered or raised meant that the clear distance of the top and bottom plate controlled with the struts could correct any error in the overall length of the confining cylinder.

Square-profiled grooves for o-rings were specified a tolerance as recommended by the manufacturer. These tolerances represent the manufactured tolerance of the o-rings, which, due to their elastic property, can adjust to minor dimensional intolerance.

10.4.2 Fluid Distribution System

The fluid distribution system is critical for effective stress state tests and cyclic pore pressure conditioning without any other application of stresses. The system is composed of four basic components: 1) a hydraulically driven volume changer, 2) a 50 mL capacity graduated burette/annulus, 3) a manually controlled fluid routing board, and 4) a vacuum/pressurized air control panel.

The water delivery and pressurization system is separate and free standing from the cell. All fittings and conduits are high-pressure capacity with the minimum pressure fitting having a capacity of 1200 psi. This surplus of capacity over and beyond the maximum test pressure is owed to the availability of fittings from common suppliers. Valves are manufactured from carbon steel and are gate valve typed.

In determining the layout of the distribution lines, an effort was made to limit the length of each respective line. In long conduits, a phenomenon referred to as a dynamic front can occur where pressure exerted at one end of the conduit is delayed from developing at the opposite end of the line. This is attributed to a retardance of the pressure transmittance due to sidewall friction. The valves were positioned such that they limit the length of conduit between the area of interest and the pressure transducer monitoring that line.

The system is pressure-driven via a servo-controlled, hydraulically actuated volume changer. This volume changer acts similarly to a syringe in that it draws and "plunges" water from a bore-type reservoir. Through a network of unidirectional valves, the volume changer is capable of refilling with de-aired water from an inline storage reservoir without allowing a decrease in pressure in the network beyond it. From the volume changer, pressurized water can be distributed through one or any combination of three conduits: bottom of specimen, top of specimen, or cell interior (confining space around the specimen). Each of these three lines is monitored with a pressure transducer that communicates to the volume changer through a system controller, thereby allowing for the control of exerted pressures within and around the specimen. This closed loop control allows for precise measurement and rapid monitoring of pressure. Additionally, the volume changer is monitored by an LVDT, which reports the displacement of the piston within it. As with the pressure transducers, this LVDT acts in a closed loop with the system controller allowing for rapid monitoring and command of positioning. By calibrating the volume of water discharged from the volume changer per linear displacement, the quantity of fluid forced through the specimen can be determined. This is a critical design element in that this quantity allows for the verification of saturation of the specimen.

In order to protect the cell against damage due to an accidental over-pressure, a blow-off valve was installed in the distribution system that is gauged to open if line pressure exceeds 400 psi. This valve is located in the distribution line that supplies water around the specimen. This position was logical since the test with the greatest anticipated pressure is the indirect tension (extension) test wherein the pressure around the specimen is increased until failure occurs. Since the volume changer is rated at 1200 psi, far exceeding the capability of the cell, it was believed prudent to allow for the safe release of unwanted pressure if a system malfunction occurred.

Measures such as this are essential in designing a safe system considering that the relative incompressibility of water can yield compounding values of pressure with very little displacement of the volume changer.

The basis for designing this system is for the testing of specimens in effective stress conditions. Therefore, it is necessary to ensure that the specimen is saturated and that the fluid used for saturation is free from dissolved air. The water used for all testing is first de-aired using a 2-liter capacity vortex de-airer. This fluid is then stored in a large volume until testing. For the initial filling of the cell to begin a testing sequence, the large volume is drawn on directly via a filling line that utilizes elevation head to expedite filling. For the distribution of fluid through the specimen, the water is first conveyed to a smaller storage tank where, through a network of check valves, the fluid can be introduced into the volume changer or burette.

Backpressure saturation is possible from a water volume storage tank and vacuum line integrated to the water distribution system. This allows for a specimen to be installed into the cell and saturated and conditioned in-place prior to testing.

For flow measurements through the specimen, the system is outfitted with a calibrated 50 mL burette that is designed specifically for use when performing permeability testing.

10.4.3 Water Temperature Conditioning Systems

For temperature control, the water delivery system can be connected to either a heater or chiller unit. The heater and chiller are each capable of pumping water through the water delivery system and into and out of the cell cavity prior to returning in a closed-loop path. Temperature conditioning in this manner utilizes the principle of conduction as the mode of energy transference.

The combination of the heating and chiller units allows the test specimen to be controlled within the range of 2-75ºC. Unlike other systems which use indirect conditioning methods (e.g., a closed conduit running through a temperature bath), this configuration has proven very responsive and capable of conditioning a specimen from room temperature to the aforementioned range limits in less than 90 minutes. A discussion on conditioning confirmation with this system is presented later.

10.5 Targeted Testing

The compilation of systems was designed to provide a more efficient manner in which to perform a multitude of tests in one workstation. The Cyclic Loading and Pore Pressure Conditioning System is designed to test asphalt specimens in both effective and total stress conditions, as well as moisture condition specimens with or without any other stresses present. Protocols were developed which allowed the system to perform:

- In-place saturation and conditioning.
- Constant head permeability determination.
- Falling head permeability determination.
- Compression testing.
- Resilient modulus testing.
- Complex modulus testing.

Future development will allow the system to perform other tests such as:

- Creep testing.
- Tension testing.

The successful development of these protocols will allow the user to perform a multitude of tests without relocating or damaging the specimen. The improvements incorporated into this new system also makes the excitation of pore water pressure more easily controlled, thereby allowing for a better assessment of specimen response to these pressures.

10.5.1 Cyclic Loading and Pore Pressure Conditioning System Specifications

Overall Dimensions ..... 18.95 inches high x 12.50 inches Diameter

Maximum Operating Pressure ..... 400 psi

Maximum Design Pressure ..... 800 psi

Maximum Piston Travel Length ..... 0.75 inches

Specimen Diameter ..... 4 inches (100 millimeters)

Specimen Aspect Ratio ..... 1.25 – 1.50

Accessory Ports ..... 4 Through Base Plate, 1 Through Top Plate

LVDT Orientation Capability ..... 2 Axial, 4 Radial

Volume of Water to Fill Cell ..... 3.6 gal (825in3)

Structural Frame Material ..... Stainless Steel 303

Confining Cylinder Material ..... Aluminum 6061-T6

Piston & End Platen Material ..... Aluminum 6061-T6

Soft Seal Material ..... Buna-N O-rings

Piston Seal Material ..... 2-Nitrile U-cup Lip Seals

Water Conditioning Range 2-75ºC

10.6 Temperature Control System

Fluid was used for temperature control. This required the specimen to be sealed with a 3.048×10^{-4}-m (0.012-in.) thick latex membrane during testing. For temperatures above 2° C,

circulating water was used for temperature control. The water delivery system can be connected to either a heater or chiller unit. The heater and chiller are each capable of pumping water through the water delivery system and into and out of the cell cavity prior to returning in a closed-loop path. Conditioning in this manner utilizes the principle of conduction as the mode of energy transference. Figure 10-7 depicts a schematic of the heating/cooling system used.

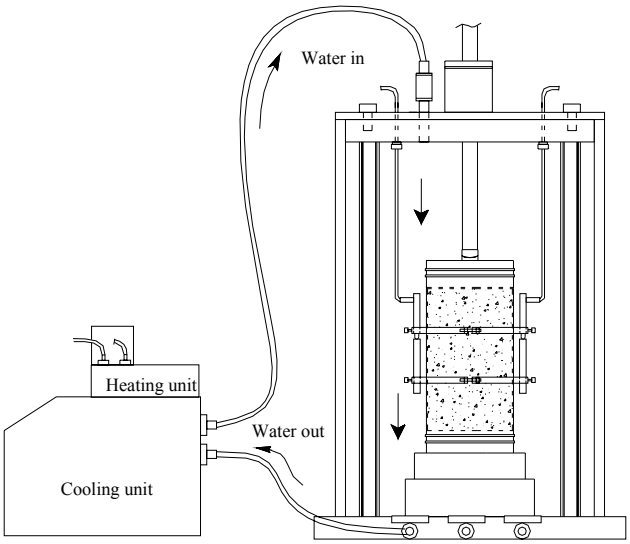

Figure 10-7. Temperature control by circulating water.

The combination of the heating and chiller units allows the test specimen to be controlled within the range of 2º C to 75º C. Unlike other systems, which use indirect conditioning methods (e.g., a closed conduit running through a temperature bath), this configuration has proven very responsive and capable of conditioning a specimen from room temperature to the aforementioned range limits in less than 90 minutes.

At the time the specimen is first placed into the system, it is stabilized at room temperature. The specimen is surrounded about its circumferential perimeter by confining water. This

water acts as a medium for temperature conditioning of the specimen. As the temperature-conditioned water surrounding the membrane-encased specimen is cycled through the system, thermal energy is either drawn from the specimen, as occurs during cooling, or added to it, as occurs during heating. During the cooling process, heat is conducted from the specimen to the "colder" confining water; the opposite is true for the heating process. As this process continues, concentric layers of the cylindrically shaped specimen reach thermal equilibrium starting from the outer layer and migrating towards the central core (Çengal 1997).

The transfer of energy from more energetic particles to less energetic adjacent particles through interactions is the thermodynamic process of conduction. The equation for the rate of heat conduction is defined as:

$$Q_{cond} = kA \frac{\Delta T}{\Delta x} \tag{10.5}$$

where Q_{cond} = rate of heat conduction, (W);

k = thermal conductivity of the layer, (W/(m·K));

A = area normal to the direction of heat transfer, (m^2);

ΔT = temperature difference across the layer, (K); and

Δx = thickness of layer, (m).

The "layer" referenced in the variable definition, Δx, is the latex membrane that encapsulates the specimen. Thermal conductivity of the latex membrane is approximately 0.13 W/m · K with a thickness, Δx, of 3.048×10^{-4} m (0.012 in.). A circumferential surface area of approximately 0.045 m^2 simplifies Eq. 10.5 to:

$$Q_{cond} = 19.19 \cdot \Delta T \text{ (W)} \tag{10.6}$$

As can be seen from Eq. 10.6, the larger the difference in temperature across the layer, the greater the rate of heat conduction. Additionally, it can be inferred that, as the temperature on either side of the layer approaches equilibrium, the rate of heat conduction decreases. Therefore, to achieve a specimen target temperature rapidly, the temperature difference between the specimen and the circulating water must be as large as possible to maximize the rate of heat conduction without surpassing the target temperature.

10.6.1 Specimen Set-up for Temperature Calibration

The final portion of the specimen to reach temperature equilibrium is the central core. Therefore, it is this region of the specimen that controls the length of conditioning time prior to the establishment of thermal equilibrium. Since the testing protocol for specimen temperature conditioning relies upon conductance for specimen heating or cooling, it was necessary to plot the change in temperature of the confining water and the core of the specimen versus time.

Although both the heater and chiller units used with the system digitally report the water temperature within their fluid reservoirs, thermal losses or gains that occur along the fluid distribution panel can vary from the reported temperature by several degrees. A series of trials were conducted for both cooling and heating to determine the most time conservative sequence to rapidly achieve the target temperature. Since the rate of heat conduction is directly proportional to the temperature difference across the layer (latex membrane), initially set temperatures were significantly lower (in the case of cooling) or higher (in the case of heating) than the target temperature to expedite thermal equilibrium. The large combined mass of the triaxial cell, water, and components of the distribution panel required a large rate of energy exchange be implemented in order to achieve the target temperature.

Two type-K thermocouple probes connected to digital gages were used to report the temperature of the confining water and the core of the specimen throughout a series of heating and cooling sequences. The thermocouples used were bare-tip and were connected to digital gages that had a recording tolerance of ±0.1° C. Prior to implementation, the thermocouples were calibrated using a certified laboratory grade mercury thermometer. From these calibrations, offsets were determined across the anticipated range of temperatures. These offsets were applied to the raw recorded data to derive a time versus temperature relationship.

The calibration of the specimen in conditions as close as is possible to those anticipated during testing is extremely important to fully account for variables of energy transference. These variables are present due to thermal sources and sinks (metal cell components), as well as insulators (latex membrane). Thermocouple 1, used to monitor the confining water temperature, was installed through one of the accessory ports located at the base of the triaxial cell. In order to avoid false readings that may have occurred by contact between the probe and metal components of the cell, the end of the probe was suspended within the volume of the cell with cotton thread. Thermocouple 2, which was required to be inside of the specimen, was more difficult to install. To simulate testing conditions, the specimen was required to be wrapped in the latex membrane thereby preventing routing of the thermocouple into the cell like that of the formerly discussed probe. Routing of the thermocouple wire through the cell's piston was eventually decided as the only viable option to achieve placement of the probe even though it required dismantling of active components of the system. The specimen used for calibration was prepared by first cutting the ends to facilitate contact between the specimen and the end platens. To allow for the installation of the probe into the specimen, a 0.25-inch diameter hole was drilled into the specimen, parallel with the longitudinal axis, starting centered on the end of the specimen and

terminating at a depth equal to ½ the length of the specimen. The thermocouple was then inserted through the cell's piston and into the void in the specimen. In order to affix the thermocouple in its position and prevent energy transfer from the air-filled void to the end of the piston, the end of the specimen was sealed with silicone. The specimen was then set aside for 24 hours to allow the silicone to cure. Following the 24-hour cure time, the specimen was positioned between the end platens, wrapped with latex membrane, and secured to the end platens with O-rings.

As previously discussed, the installation of the thermocouple into the specimen required partial dismantling of the piston assembly. The removal of components used to conduct water through the specimen prevented a saturation sequence as is typical with test specimens. Therefore, it was decided to calibrate the heating and cooling times of the specimen in a dry condition. Water is a more efficient conductor of thermal energy than is air, 0.613 W/(m · K) and 0.026 W/(m · K), respectively, therefore testing with a dry specimen yields conservative calibration times for thermal equilibrium.

10.6.2 Method of Cooling and Heating Calibration

At the commencement of the cooling conditioning process, both the specimen and the conditioning water were approximately 25° C which was the typical ambient temperature of the room in which testing occurred. A multitude of chiller set temperature combinations were run to determine the most expedient sequence for equilibrium with a target end temperature of 10° C ± 0.1° C for the specimen. Owing to the efficiency of the chiller unit, care was taken not to allow the chiller to run lower than the target temperature for too long. Once the specimen temperature is achieved in the cooling process, any increase in temperature can only occur due to thermal conduction from the surrounding warmer environment.

The heating conditioning sequence began with the specimen at approximately the target temperature of the cooling process (10 °C). This was done in order to allow for future non-destructive testing of specimens at low and high temperatures progressively. As with the temperature combination iterations with the cooling process, those for the heating process followed the same logic. The target end temperature was set at 40 °C ± 0.1 °C for the specimen.

Initially, 60 minutes of conditioning time was the target for achievement of thermal equilibrium within the specimen. This target conditioning time was used as a basis for sizing of the heater and chiller used with the system. After several calibration sequences, it was validated that this limited conditioning time was sufficient to achieve the target temperature but that an additional 30 minutes would allow for further stabilization. Although the specimen may be at the target temperature, the entire mass of the system may not. Therefore, the additional energy exchange can help to bring more of the system to the target temperature, which acts as a thermal blanket around the specimen.

10.6.3 Cooling Calibration Results

For the target temperature of 10° C, the chiller was initially set at 7° C. Initial conditions for the specimen and circulating water were 27.1° C and 25.0° C, respectively. The chiller set temperature was held for 40 minutes at which time the set temperature was increased to 8° C and maintained for an additional 50 minutes. The specimen reached the target temperature of 10° C after a total of 61 minutes of conditioning time. Further conditioning was conducted for 29 minutes at which time the specimen stabilized to 10.0° C. The chiller was then turned off thereby terminating the flow of conditioned water through the system. The specimen core temperature was monitored for an additional 30 minutes wherein the end temperature of the

specimen was 10.1° C. This range of temperature (10° C ± 0.1° C) was considered acceptable for the anticipated testing. Water circulation was maintained throughout testing.

As is shown in Figure 10-8, the chilled circulating water achieved the set temperature very rapidly. Prior to stabilizing at the initial set temperature of 7° C, the water temperature is shown to drop to a temperature lower than the set temperature. This is attributed to the response sensitivity of the chiller itself. In order to rapidly lower the temperature of the circulating water, the chiller maximizes the amount of energy that it can draw from the fluid. As the circulating water approaches the set temperature, the chiller decreases the rate of energy transference, thereby decreasing the change in temperature per time. As was observed in all cooling sequences conducted, a ΔT of 18° C (initial temperature of 25° C to a set temperature of 7° C) was large enough that the efficiency of the chiller exceeded its ability to decrease the rate of heat conduction. As a result, the chiller "overshot" its target temperature. Additionally, it is shown that for the maintenance of the target temperature inside of the specimen, the chiller must be set

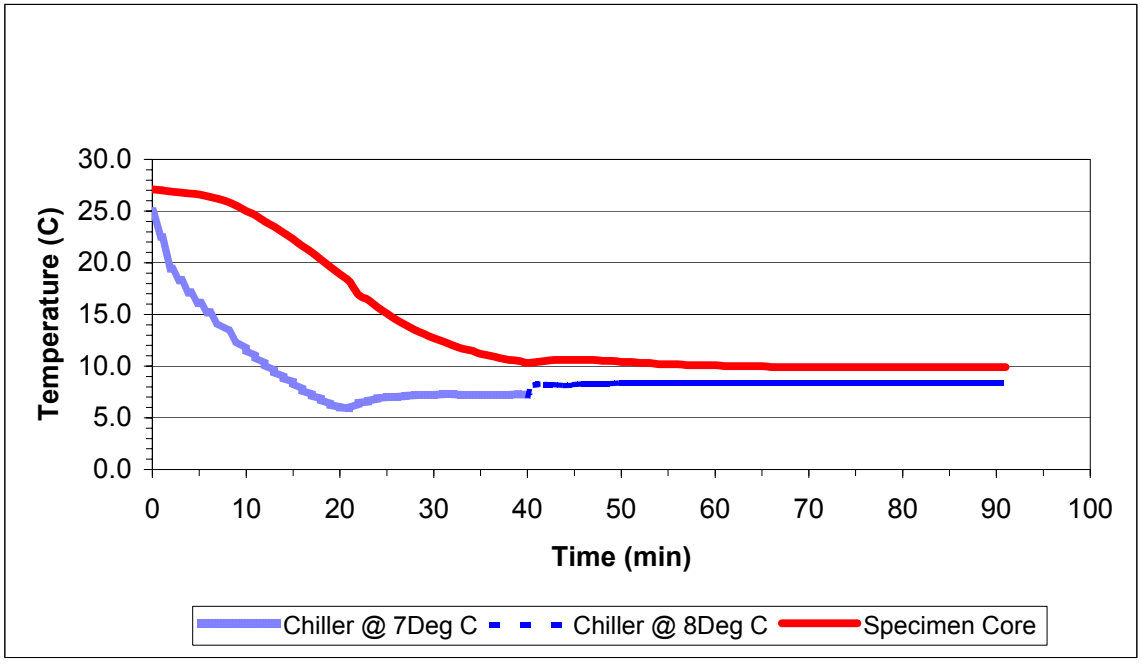

Figure 10-8. Typical time vs. temperature-specimen to 10° C (GA-C1)

to a lower temperature. For a specimen target temperature of 10° C, the chiller is required to be set to 8° C. This loss of 2° C from the time the fluid left the chiller to reaching the interior of the cell is attributed to the conditioning water gaining energy from the ambient temperature room as the fluid is conducted through the distribution lines and the cell itself.

The prescribed protocol for cooling the specimen to 10° C is summarized as:

1. Set chiller to 7° C and run for 40 minutes;
2. Change chiller set temperature to 8° C and run for 50 minutes; and
3. Perform complex modulus testing.

10.6.4 Heating Calibration Results

Initial conditions for the specimen and circulating water at the commencement of the heating process was 10.2° C and 26.5° C, respectively. For the target temperature of 40° C, the heater was initially set at 45° C. The heater set temperature was held for 55 minutes at which time the set temperature was decreased to 40° C and maintained for an additional 35 minutes. At the end of the total 90 minutes of conditioning, the specimen core temperature had reached 40.0° C. The heater was then turned off thereby terminating the flow of conditioned water through the system. The specimen core temperature was monitored for an additional 30 minutes wherein the end temperature of the specimen was 39.9° C. This range of temperature (40° C ± 0.1° C) was considered acceptable for the anticipated testing. During anticipated testing, the heated water circulation is maintained throughout testing.

As is shown in Figure 10-9, the circulating water achieved the set temperature very rapidly at which it was allowed to stabilize while the specimen core temperature increased. Also notable is the near parallelism of the rate of temperature increase in specimen and heater from 0 to 35 minutes of test time. This parallelism is consistent with the equation for the rate of heat conduction.

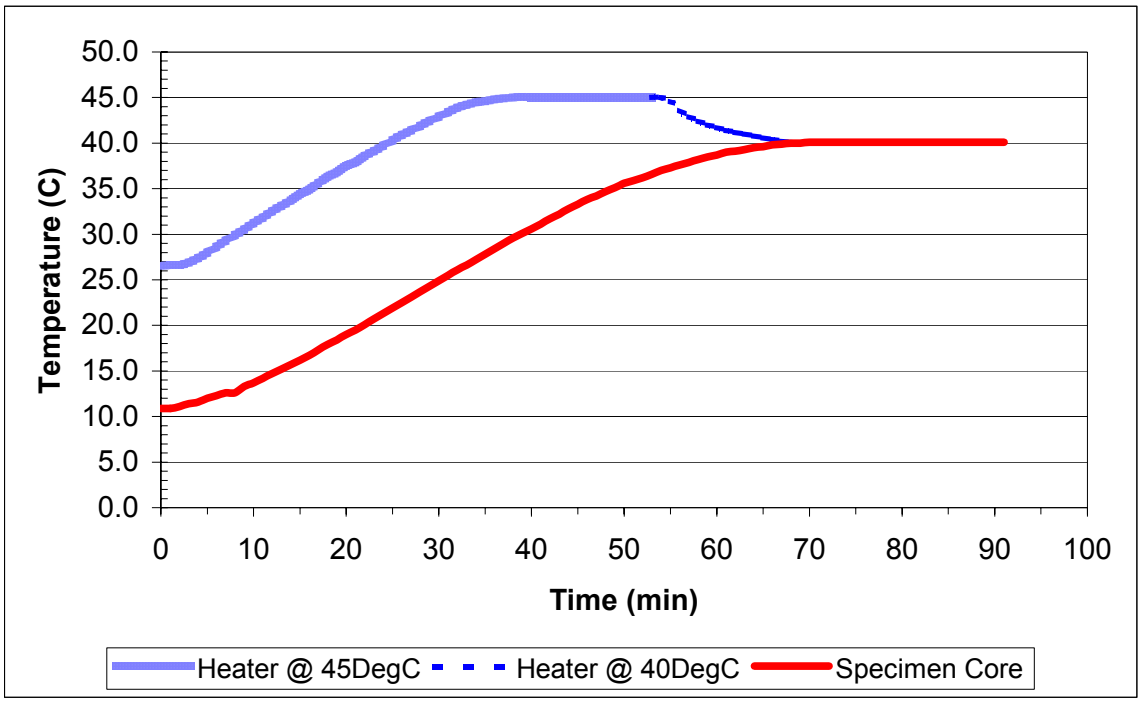

Figure 10-9. Time vs. temperature-specimen to 40° C (WR-C1)

The prescribed protocol for cooling the specimen to 40° C is summarized as:

1. Set heater to 45° C and run for 55 minutes;
2. Change heater set temperature to 40° C and run for 35 minutes; and
3. Perform complex modulus testing.

The protocols for cooling and heating were initially developed using both the GA-C1 and WR-C1 mixes with percent voids of 7.0% ± 0.5%. It is recommended that this protocol be used with the mixes used in this research and other coarse mixes with approximately similar air void percentage. For other mixes, a baseline should be developed using the same methodology as presented herein to ensure the amount of time and temperature to stabilize the core of the specimen.

10.7 Summary

In this chapter, the development and design of the Cyclic Loading and Pore Pressure Conditioning System were described, followed by a description of the pore pressure control system. The heating and cooling system is also described.

10.8 References

Alam, M.M., Vemuri, N., Tandon, V., Nazarian, S., and M. Picornell, M., "A Test Method for Identifying Moisture Susceptible Asphalt Concrete Mixes," University of Texas at El Paso, El Paso, Texas, 1998.

ANSI, *Preferred Hole Basis Clearance Fits*, ANSI B4.2, 1978.

Beer, F.P., and Johnston, Jr, E.R., *Mechanics of Materials,* 2nd Edition. McGraw-Hill, Inc., New York, 1992.

Carpenter, G.W., and Stephenson, R., "Permeability Testing in the Triaxial Cell," *Geotechnical Testing Journal* Vol. 9, No. 1, pp. 3-9, 1986.

Çengal, Y.A., *Thermodynamics and Heat Transfer*, Irwin/McGraw-Hill, Boston, 1997.

Earle, J.H., *Engineering Design Graphics*, 8th Edition, Addison-Wesley Publishing Company, New York, 1994.

Halliday, D., Resnick, R., and Krane, K., *Physics*, 4th Edition, John Wiley & Sons, Inc., New York, 1992.

Juvinall, R.C., *Fundamentals of Machine Component Design*, John Wiley & Sons, Inc., New York, 1983.

Roberts, F.L., Kandhal, P.S., Brown, E.R., Lee, D., and Kennedy, T.W., *Hot Mix Asphalt Materials, Mixture Design, and Construction*, 2nd Edition. NAPA Research and Education Foundation, Lanham, 1996.

CHAPTER 11
EVALUATION OF A NEW CONDITIONING PROCEDURE USING CYCLIC PORE PRESSURE TO INDUCE MOISTURE DAMAGE OF ASPHALT MIXTURES

11.1 Introduction

In this chapter, the moisture conditioning system described Chapter 10 is evaluated for use in asphalt mixtures. Five mixtures – two limestone mixtures and three granite mixtures will be subjected to cyclic pore pressure conditioning. The granite aggregate used is a known stripping aggregate. The limestone mixtures are known to have a high resistance to stripping. The limestone mixture used has been widely used by the Florida Department of Transportation. The conditioned mixtures will be tested with the Superpave IDT test for fracture properties and the results will be compared to unconditioned mixtures. Finally, the results will be compared to average calculated dynamic pore pressures within the voids of the mixtures, as obtained from micromechanical analysis.

The results of presented, show that cyclic pore pressure conditioning of mixtures results in accelerated moisture damage and stripping of the granite mixtures. In comparison, the limestone mixtures are shown to be resistant to pore pressure induced moisture damage. The Energy Ratio (ER), discussed previously in Chapter 7, is again shown to be a useful parameter for detecting a range of moisture damage in mixtures. Using results from X-Ray Tomographic Imaging of the mixtures tested, the moisture damage as quantified by the ER is shown to rank mixtures in accordance with the calculated dynamic pore pressures obtained from the micromechanical analysis.

Based on the results presented, cyclic pore pressure conditioning of mixtures, followed by Superpave IDT testing of fracture parameters with the ER may form the basis of promising combined performance-based specification and testing criteria for evaluating the effects of moisture damage in mixtures as well as the overall resistance to fracture.

11.2 Objectives

Using five mixtures with aggregates of known moisture damage susceptibility, the primary objective of this research was to evaluate the use of a new cyclic pore pressure-based moisture conditioning system, along with a fracture mechanics-based criterion, the ER, for inducing and quantifying the effects of moisture damage in mixtures. A secondary objective was to evaluate the relationship between: 1) the amount of damage as quantified by the ER, and 2) predicted pore pressures obtained from micromechanical analysis of mixtures. Finally, appropriate recommendations will be made regarding the conditioning and determination of moisture damage in mixtures, including the effects of relevant mixture properties.

11.3 Scope

This chapter deals with the use of the new cyclic pore pressure moisture conditioning system discussed in Chapter 10 along with a Supepave IDT-based fracture performance-based criterion, the ER, for the conditioning and subsequent evaluation of moisture damage on mixtures containing aggregates of known stripping performance. Below, a description is provided of the materials and methodologies used, followed by the cyclic pore pressure protocol used. The ER for conditioned and unconditioned mixtures is compared. In addition to the Energy Ratio, the key Superpave IDT fracture parameters monitored include creep properties, resilient modulus, tensile strength, fracture energy limit, and dissipated creep strain energy limit.

11.4 Materials and Methodology

11.4.1 Aggregates, Gradations, and Binder Used

Two groups of aggregates were used. The first consisted of crushed granite from Georgia that has shown potential for stripping. The second consisted of an oolitic limestone aggregate

that has in the past not shown significant stripping potential. Both aggregate groups are used extensively in Florida and are considered to be excellent materials resulting in well-performing mixtures.

The granite mixtures were made up of four components: coarse aggregate, fine aggregate, screenings, and mineral filler. They were blended together in different proportions to provide three 12.5-mm nominal maximum aggregate size mixtures of coarse and fine gradations. These mixtures are denoted as: GA-C1, GA-F1, GA-F3, with the letters C and F denoting coarse-graded and fine-graded mixtures according to whether the gradation passes below or above the SuperPave^{TM} restricted zone. The limestone mixtures consisted of two previously designed limestone SuperPave^{TM} mixtures (WR-C1 and WR-F1) prepared by the Florida Department of Transportation (FDOT). The two limestone mixtures were known to be highly resistant to stripping. The purpose of selecting granite and limestone mixtures of varying gradation was to ensure that the mixtures tested were of different aggregate type, permeability, and other volumetric properties. The resulting gradations are shown in Table 11-1. The mixtures ranged from what could be described as fine uniformly-graded and fine dense-graded to coarse uniformly-graded and coarse gap-graded.

Design asphalt contents for all the mixtures were determined such that each mixture had 4 percent air voids at N_{design} = 109 gyrations. Finally, PG 67-22 (AC-30) asphalt was used for all limestone and granite mixtures in this study. Table 11-2 shows the volumetric properties for the mixtures used.

11.4.2 Mixture Preparation

All mixtures were produced in the laboratory following Superpave mixture design protocols. First, the aggregates and asphalt binder were heated to 150 °C (300 °F) for three

Table 11-1. Gradations for Granite and Limestone Mixtures

Sieve Size (mm)	Percent Material Passing each Sieve Size				
	GA-C1	GA-F1	GA-F3	WR-C1	WR-F1
19.0	100.0	100.0	100.0	100.0	100.0
12.5	97.4	94.7	94.6	97.0	96.0
9.5	89.0	84.0	85.1	90.0	85.0
4.75	55.5	66.4	65.1	60.0	69.0
2.36	29.6	49.2	34.8	33.0	53.0
1.18	19.2	32.7	26.0	20.0	34.0
0.60	13.3	21.0	18.1	15.0	23.0
0.30	9.3	12.9	12.5	11.0	15.0
0.15	5.4	5.9	7.7	7.6	9.6
0.075	3.5	3.3	5.8	4.8	4.8

Table 11-2. Volumetric Properties of Granite and Limestone Mixtures

Properties	Mixture				
	GA-C1	GA-F1	GA-F3	WR-C1	WR-F1
Asphalt Content (%)	6.63	5.68	5.14	6.50	6.30
Specific Gravity of Asphalt	1.035	1.035	1.035	1.035	1.035
Bulk Specific Gravity	2.345	2.374	2.404	2.235	2.244
Theoretical Max. Specific Gravity	2.442	2.473	2.505	2.328	2.338
Air Voids (%)	4.0	4.0	4.0	4.0	4.03
Voids in Mineral Aggregate (%)	18.5	16.6	15.1	15.4	15.6
Voids filled with Asphalt (%)	78.5	75.9	73.3	74.16	74.17
Effective Specific Gravity of Aggregate	2.710	2.706	2.720	2.549	2.554
Absorbed Asphalt (%)	0.3	0.3	0.5	1.3	1.074
Effective Asphalt (%)	6.3	5.4	4.7	5.3	5.293
Dust to Asphalt Ratio	0.6	0.6	1.2	0.7	0.761
Surface Area (m^2/kg)	3.3	4.1	4.9	4.9	6.05
Film Thickness theoretical, microns	19.9	13.4	9.9	11.2	9.0

hours prior to mixing. After mixing, the mixtures were reheated to 135 °C (275 °F) for two hours before compaction. The specimens were then compacted on the IPC Servopac Superpave gyratory compactor to 7± 0.5 percent air voids. For each pore pressure and temperature combination, three samples of each mix were prepared. In addition, three unconditioned specimens for each mixture were prepared.

11.4.3 Specimen Pore Pressure Conditioning

Using the conditioning system described in Chapter 10, the conditioning of the asphalt specimens takes place by exerting cyclic pore pressure on all water accessible voids of the specimen. First, each specimen was subjected to vacuum saturation, in which the chamber was filled with enough water to cover all sides of the specimen and a vacuum of 25 in-Hg was applied to the conditioning chamber for 15 minutes. After 15 minutes, the vacuum was removed from the chamber and the specimen was allowed to rest for another 15 minutes. Based on the micromechanical characterization of mixtures in Chapter 8, no specific saturation levels were targeted, since each mix has a unique void structure that may enhance or reduce the saturation capacity of the mixture. It was felt by the researchers that forcing a target saturation level might cloud the effective differences between mixtures in resisting moisture ingress and therefore possibly moisture damage.

Next, the water in the cell was heated by to the prescribed temperature (25 °C or 40 °C) using the environmental conditioning system and protocols described in Chapter 10. Once the specimen was determined to be at the prescribed temperature, a temperature controlled heating pad was wrapped around the chamber wall. An insulation blanket was then placed around the heating pad. At that point the tubes of the hydraulic setup were purged of air by pushing water through them using the volume changer. The chamber was connected to the hydraulic volume changer. Water pre-heated to the desired conditioning temperature was then pushed into the bottom of the chamber with the upper part of the chamber connected to the annulus tubes with their vent open. This allowed any chamber air to be forced out. Next, the vent at the top of the chamber was switched to the connection leading to the vacuum control panel. The pressure was decreased by 10.2 in-Hg (5.0 psi) in order to remove any remaining air in the system and sample.

This decrease in pressure was maintained for 15 minutes. The valve to the vacuum tube was closed and water was allowed to recede back into the chamber to replace the air that had just been removed. The sample was allowed to sit for another 15 minutes before this final air removal process was completed. At this point in the conditioning procedure, a saturated sample had been enclosed in an airtight environmental chamber completely filled with water at normal pressure. The valves to the top and bottom of the environmental chamber had been closed and the valve connecting the hydraulic volume changer to the water source was opened.

Finally, the computer program controlling the conditioning procedure was turned on. The program started by drawing water from the source into the volume changer. The water source valve was then closed and the valve to the bottom of the environmental chamber was opened. The program was instructed to continue and did so by signaling the hydraulic volume changer to push water into the chamber until the pressure transducer, which was connected to the top of the chamber, read a change of 5.0 psi (10.2 in Hg). Next, the bottom chamber valve was closed and the water source valve reopened. The water source valve was again closed and the bottom chamber valve reopened. The hydraulic volume changer then continued to the main stage of the conditioning where it would apply cyclic pressure into the chamber. Four different combinations of cyclic pore pressure and temperature were evaluated:

- 5-15 psi and 25 °C,
- 5-25 psi and 25 °C,
- 5-30 psi and 25 °C,
- 5-15 psi and 40 °C.

The conditioning cycle was repeated once every three seconds (0.33 Hz), following a sine waveform, for a total of 5800 cycles. Once these cycles were completed, the pressure was

released. Lastly, the heating blanket was removed (if used) and the chamber was emptied. The sample was now considered conditioned.

Mixture performance testing

Once the moisture conditioning was completed, the conditioned mixtures were allowed to drain for 36 hours. Then, conditioned and unconditioned specimens were cut, by a wet saw, into 50-mm (2-inch) thick specimens. The specimens were placed in a dehumidifier chamber for 48 hours to dry them of any remaining moisture and bring them to a constant humidity level. The Superpave IDT test was used to perform Resilient Modulus (M_R), Creep Compliance, and Strength tests (Buttlar and Roque 1994; Roque et al. 1997; Sedwick 1998) from which the following properties were determined: tensile strength, resilient modulus, fracture energy limit (FE), dissipated creep strain energy limit (DCSE), and creep properties. Using these mixture properties and the fracture mechanics-based Energy Ratio fracture performance specification criterion developed at the University of Florida, the effects of moisture damage on the fracture resistance of the mixtures were calculated. All Superpave IDT tests were performed at a constant testing temperature of 10 °C.

11.5 Evaluation of Cyclic Pore Pressure Induced Moisture Damage Using the Energy Ratio

In the following, the effects of moisture damage on the fracture resistance of mixtures are evaluated. Table 11-3 shows a summary of the mixture fracture properties obtained from the Superpave IDT fracture properties testing for the mixtures tested. The ER for conditioned mixtures is lower for all granite mixtures, as expected. Figures 11-1a, 11-2a, 11-3a, and 11-4a show a comparison between the changes in ER for conditioned and unconditioned mixtures, testing pressures and temperatures. Similarly, Figures 11-1b, 11-2b, 11-3b, and 11-4b show the ratio of the conditioned versus unconditioned ER for all mixtures, pressure, and temperature conditions

Table 11-3. Summary of Mixture Properties for Mixtures Without an Antistripping Additive

Material	Resilient Modulus, M_R (GPa)	Creep Compliance at 1000 seconds (1/GPa)	Tensile Strength, S_t (MPa)	Fracture Energy (kJ/m^3)	Failure Strain (10^{-6})	m-value	D_1 (1/psi)	DCSE (kJ/m^3)	Energy Ratio, ER	ER_{cond}/ER_{uncond}
Unconditioned										
GA-C1	6.32	15.60	2.10	12.50	7343.9	0.65	1.12E-06	12.15	2.75	--
GA-F1	8.745	7.88	2.59	11.20	5434.8	0.57	1.10E-06	10.82	3.49	--
GA-F3	10.21	4.89	3.00	8.20	3581.4	0.54	8.19E-07	7.76	3.69	--
WR-C1	8.53	2.54	2.14	2.50	1939.0	0.53	9.51E-07	2.23	1.09	--
WR-F1	8.56	5.00	2.17	3.00	1923.2	0.51	1.01E-06	2.72	1.40	--
Conditioned at 5-15 psi and 25 °C										
GA-C1	7.695	12.74	2.03	8.40	5144.8	0.71	6.49E-07	8.13	2.46	0.89
GA-F1	8.54	9.48	1.71	2.45	1950.0	0.67	6.26E-07	2.28	0.89	0.25
GA-F3	9.46	7.60	1.78	2.65	2117.8	0.67	4.85E-07	2.48	1.22	0.33
WR-F1	8.683	12.00	2.09	5.10	3230.0	0.65	9.19E-07	4.85	1.35	0.97
Conditioned at 5-25 psi and 25 °C										
GA-C1	6.75	12.19	2.02	8.00	5083.4	0.71	6.13E-07	7.70	2.49	0.90
GA-F1	8.235	9.94	1.67	2.55	2051.2	0.61	1.03E-06	2.38	0.77	0.22
GA-F3	9.69	6.69	1.91	2.65	1891.7	0.63	5.87E-07	2.46	1.20	0.33
WR-F1	8.683	12.00	2.09	5.10	3230.0	0.65	9.19E-07	4.85	1.35	0.97
Conditioned at 5-30 psi and 25 °C										
GA-C1	6.76	21.67	2.17	8.20	7115.6	0.86	3.81E-07	7.85	2.23	0.81
GA-F1	7.94	11.92	1.77	3.60	2677.4	0.72	5.57E-07	3.40	1.19	0.34
GA-F3	10.03	5.98	3.60	3.60	2345.9	0.51	1.24E-06	2.95	0.98	0.27
WR-F1	8.683	12.00	2.09	5.10	3230.0	0.65	9.19E-07	4.85	1.35	0.97
Conditioned at 5-30 psi and 25 °C										
GA-C1	7.68	11.51	1.59	3.60	2853.8	0.63	1.10E-06	3.44	0.94	0.34
GA-F1	7.3	8.44	1.59	2.90	2458.3	0.53	2.33E-06	2.73	0.59	0.17
GA-F3	9.89	5.88	1.69	1.90	1561.3	0.54	9.38E-07	1.76	0.86	0.23
WR-C1	8.53	5.59	2.45	2.25	2017.0	0.44	1.45E-06	1.90	1.01	0.93
WR-F1	8.683	12.00	2.09	5.10	3230.0	0.65	9.19E-07	4.85	1.37	0.98

tested. The granite mixtures (GA-1, GA-F1, GA-F3) all showed a decrease in ER with cyclic pore pressure conditioning, whereas the limestone mixtures (WR-C1 and WR-F1) showed only a slight drop in ER. Visual observations confirmed that all the granite mixtures showed stripping, whereas the limestone mixtures showed little or no evidence of stripping. Based on the previous testing of the granite mixtures (Chapter 5) the GA-C1 mixture was expected to show a greater change in ER than observed for all pressures at the testing temperature of 25 °C. However, cyclic pore pressure conditioning at an elevated temperature of 40 °C resulted in the expected drop in the ER for the GA-C1 mixture. Hence, based on these limited results, it appears that in addition to the application of pressure, elevated conditioning temperatures may be required to produce a consistent response in conditioned mixtures, as determined by the energy ratio parameter, ER.

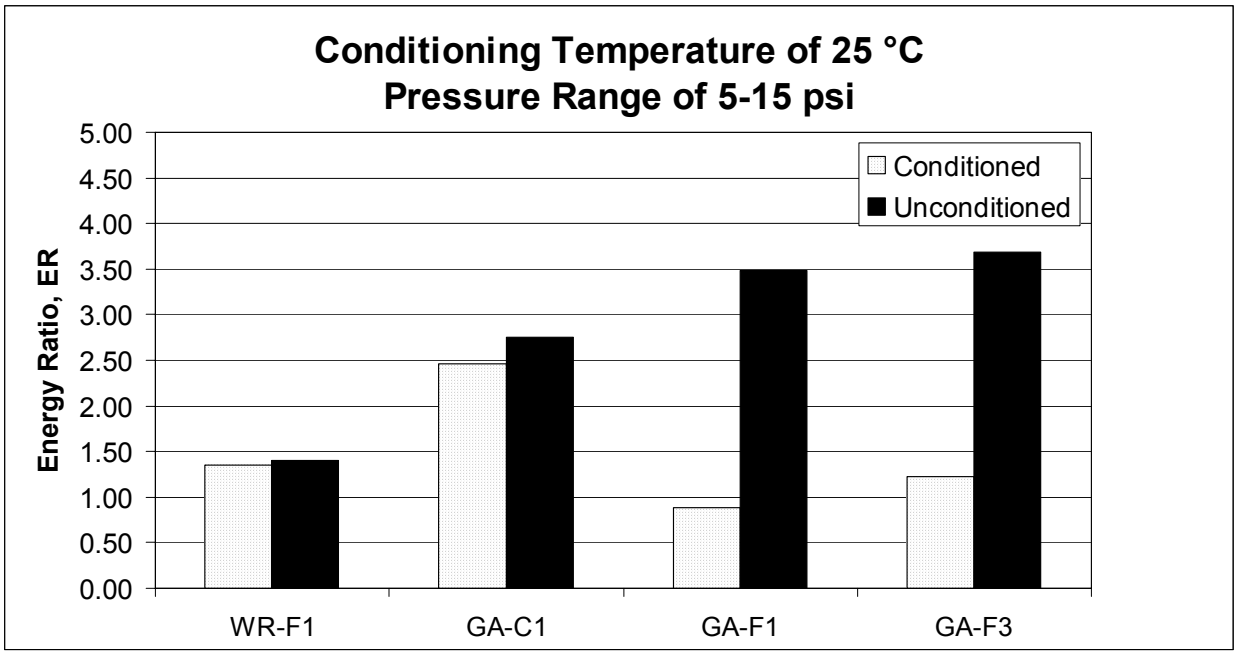

(a) Energy Ratio, ER

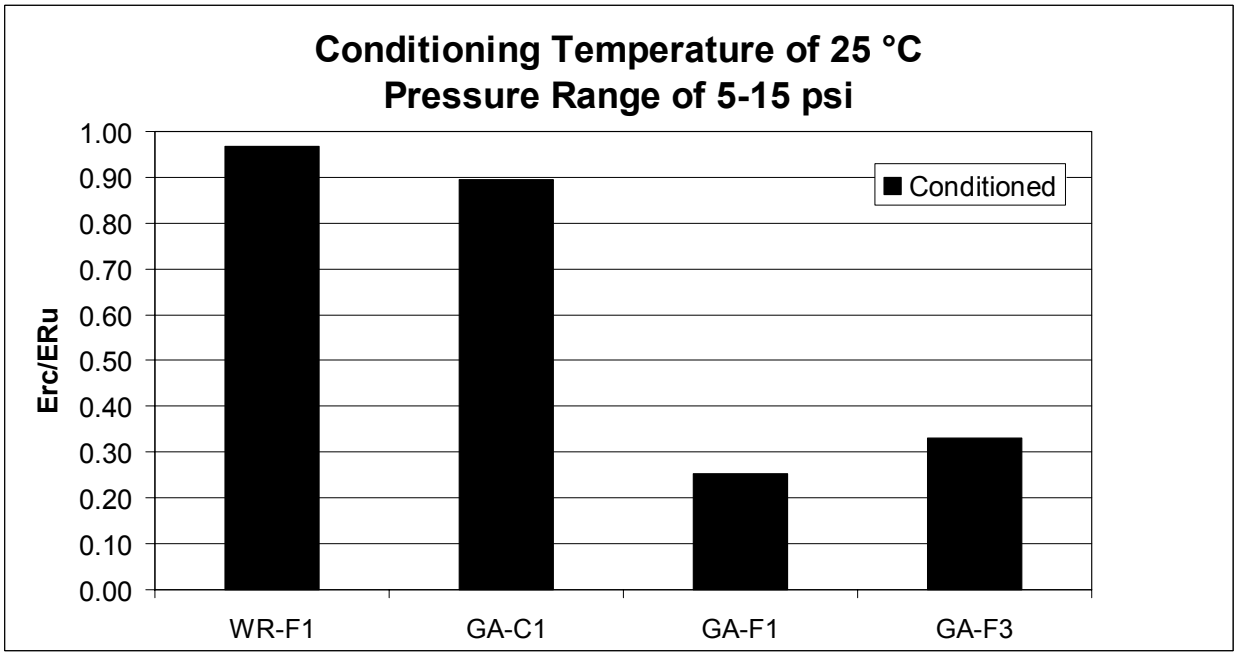

(b) Ratio of Conditioned versus Unconditioned Energy Ratio

Figure 11-1. Comparison of energy ratio values between unconditioned mixtures and mixtures conditioned at cyclic pore pressures of 5-15 psi and temperature of 25 °C.

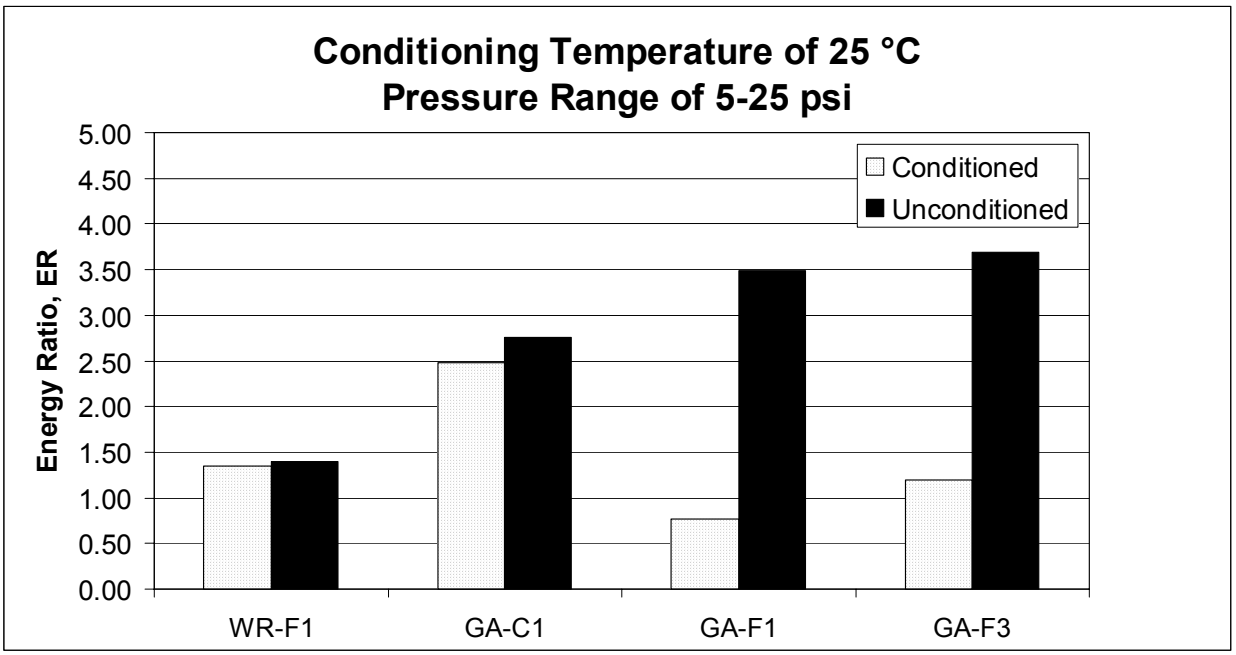

(a) Energy Ratio, ER

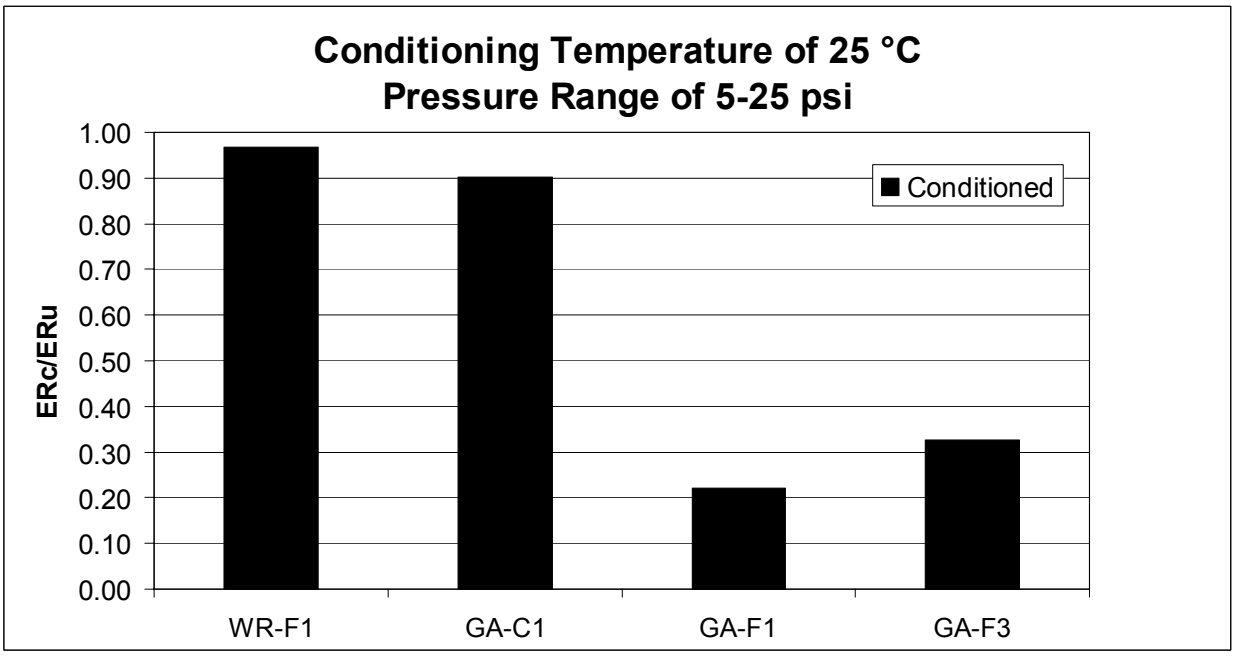

(b) Ratio of Conditioned versus Unconditioned Energy Ratio

Figure 11-2. Comparison of energy ratio values between unconditioned mixtures and mixtures conditioned at cyclic pore pressures of 5-25 psi and temperature of 25 °C.

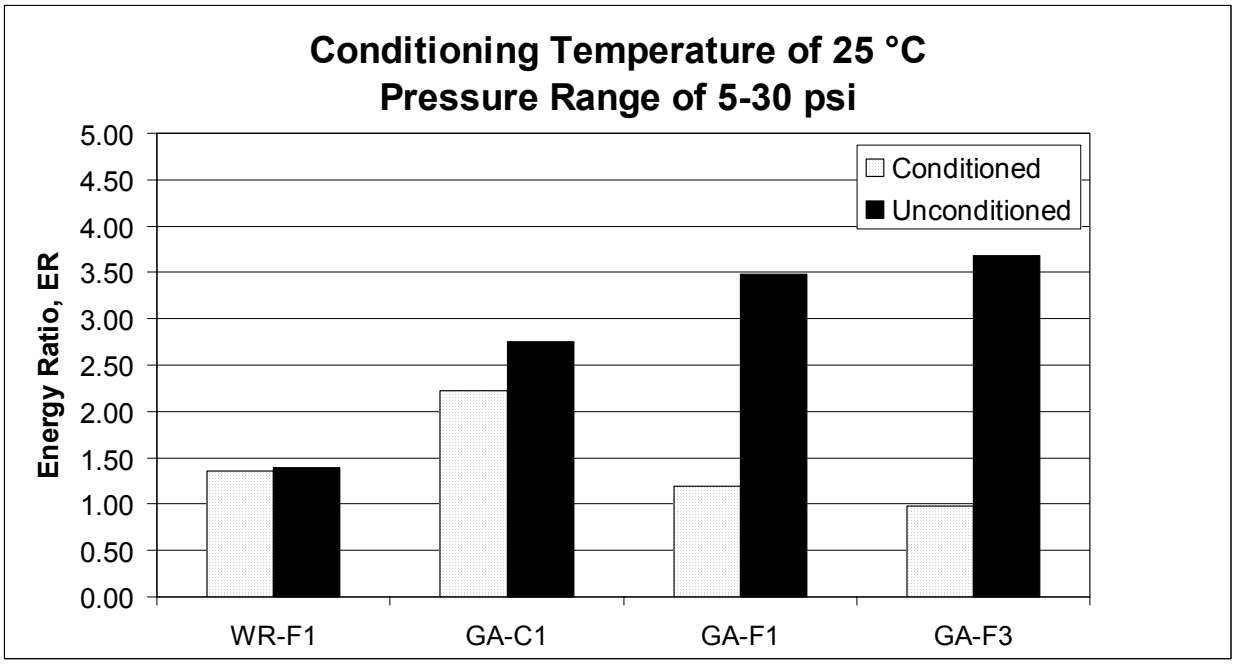

(a) Energy Ratio, ER

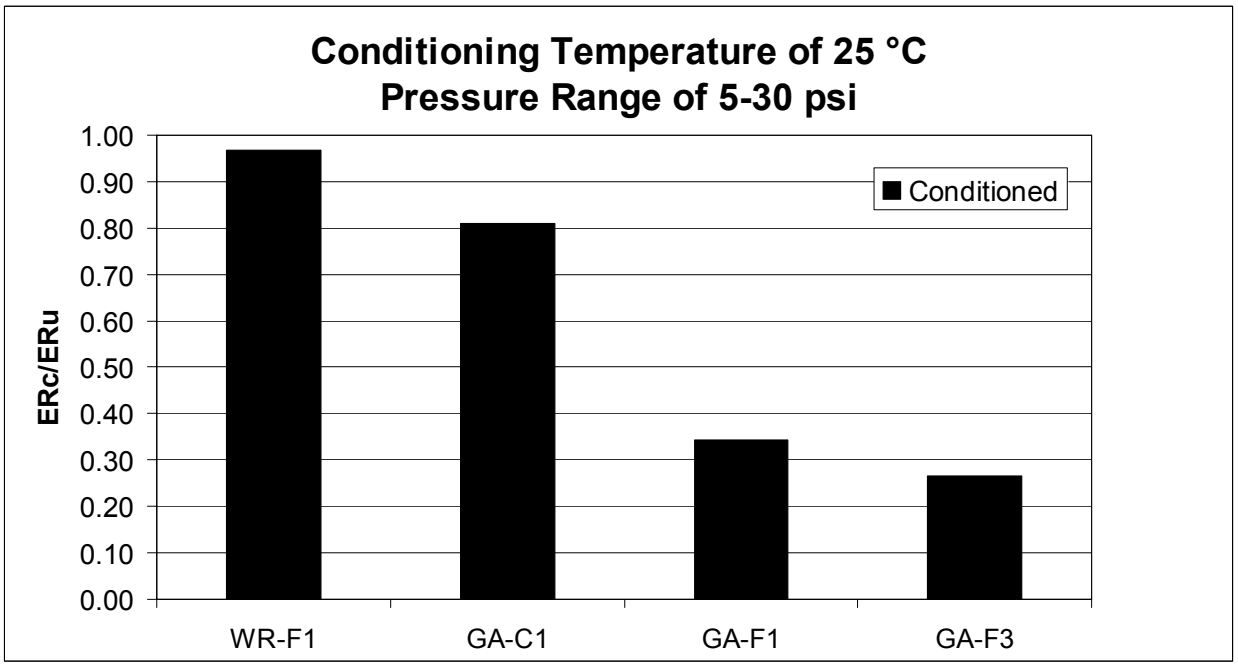

(b) Ratio of Conditioned versus Unconditioned Energy Ratio

Figure 11-3. Comparison of energy ratio values between unconditioned mixtures and mixtures conditioned at cyclic pore pressures of 5-30 psi and temperature of 25 °C.

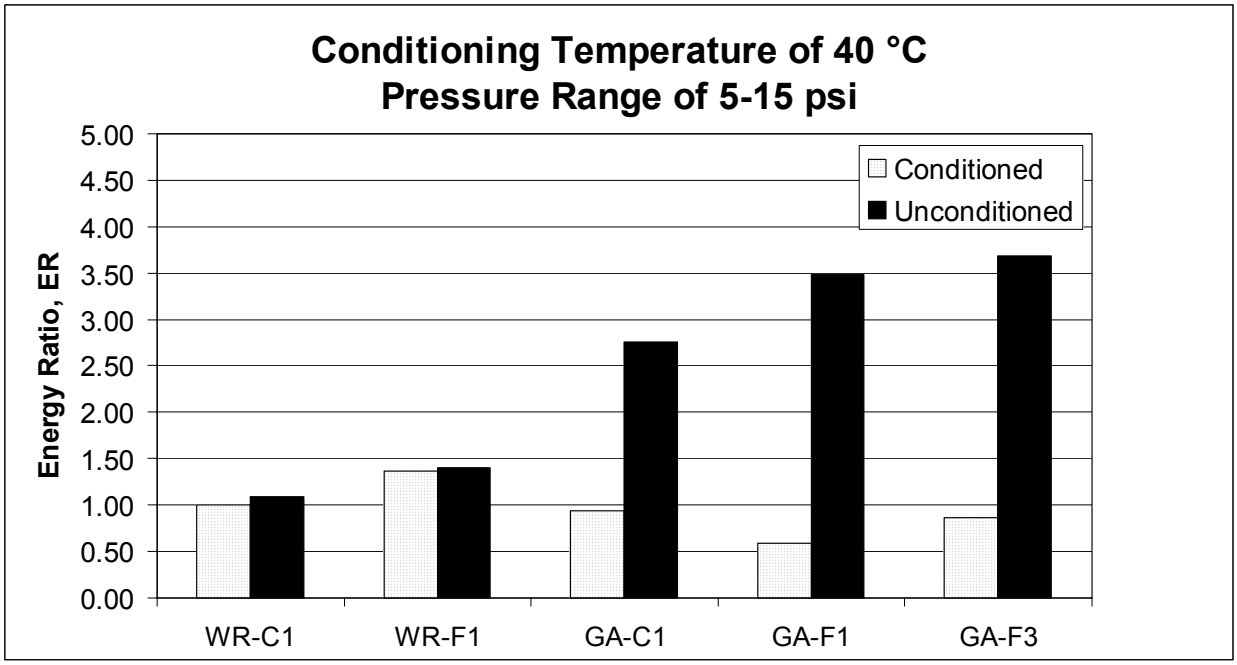

(a) Energy Ratio, ER

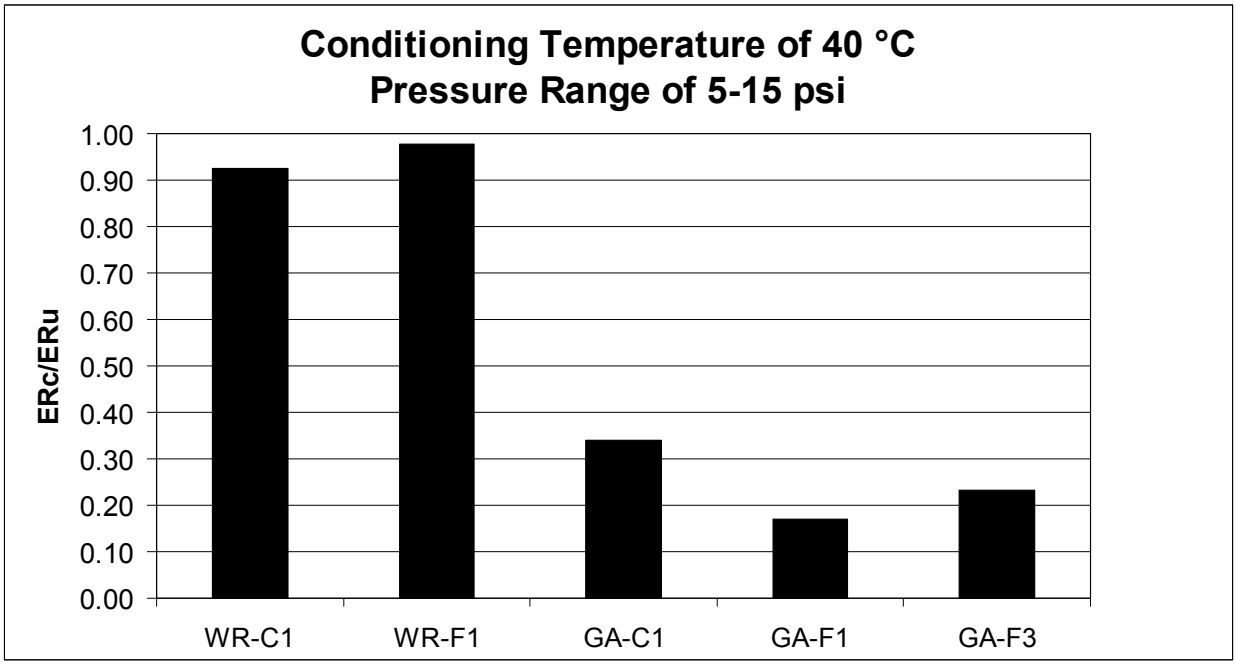

(b) Ratio of Conditioned versus Unconditioned Energy Ratio

Figure 11-4. Comparison of energy ratio values between unconditioned mixtures and mixtures conditioned at cyclic pore pressures of 5-15 psi and temperature of 40 °C.

11.6 Modeling of Mixture Pore Pressure Distribution Within Air Voids

Pressure distributions were calculated through the use of a three dimensional micro-structural fluid flow model developed by Al-Omari and Masad (2004). A model of the mixture microstructure was constructed from digital x-ray tomographic images. The main purpose of the fluid flow model is to determine the fluid flow characteristics and permeability when a fixed stress is applied to the specimen in a particular direction under saturated conditions. The pressure at each point of the microstructure due to flowing water was also calculated. The inputs into the model include the bitmap images obtained from an image analysis of square sections that are taken from digital x-ray computed tomographic original images. The use of square sections is simply due to convenience, because they work with a finite difference numerical scheme in which the control volume is chosen to have square images (Al-Omari and Masad 2004). Also, a hydraulic gradient is introduced so that water could flow from the inlet to the outlet of the microstructure.

Table 11-4 lists the predicted average interstitial air void pore pressures for each mixture. The results show that different pore pressure distributions can result due to the difference in mixes in terms of aggregate size distribution and aggregate type. Figure 11-5 shows a comparison of the ratio of the ER for conditioned and unconditioned mixtures for conditioning pressures

Table 11-4. Predicted Average Interstitial Air Void Pore Pressures

Mixture	Average Predicted Pore Pressure (N/m^2)
WR-C1	0.056
WR-F1	0.048
GA-C1	0.055
GA-F1	0.058
GA-F3	0.051

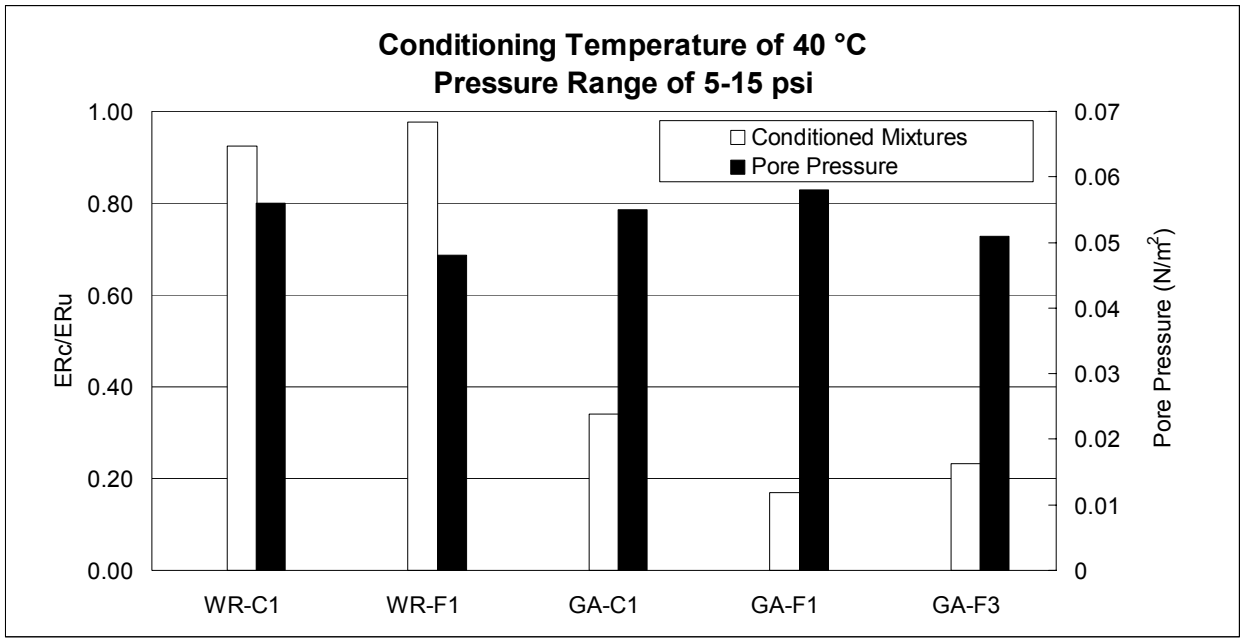

Figure 11-5. Comparison of energy ratio values between unconditioned mixtures and mixtures conditioned at cyclic pore pressures of 5-15 psi and temperature of 40 °C.

of 5-15 psi and temperature of 40 °C. Interestingly, for each aggregate type the results indicate that the relative damage, as measured by the ratio of the ER for conditioned and unconditioned mixtures, is inversely proportional to the average predicted interstitial air void pore pressure for each mixture. For example, the WR-C1 mixture shows slightly higher predicted interstitial pore pressures than the WR-F1 mixture, which is confirmed by the WR-C1 mixture showing slightly greater drop in ER than the WR-F1 mixture. The GA-F1 mixture shows the highest interstitial pore pressures and consequently also the greatest decrease in ER, followed by the GA-C1 and GA-F3 mixtures. Interestingly, even though the GA-C1 mixture has slightly higher interstitial pore pressures than the GA-F3 mixture, it shows a slightly lower drop in the ER than the GA-F3 mixture. This may be due to the differences in microstructure between coarse- and fine-graded

mixtures discussed in Chapter 5. Coarse-graded mixtures with a good coarse-aggregate contact structure may act to retard the ingress of water into protected pockets of mastic lying between the coarse aggregate contact structure.

11.7 Summary and Conclusions

The HMA fracture mechanics framework developed at the University of Florida has been shown previously in Chapter 6 to provide a rational framework for the evaluation of the effects of moisture damage on the fracture resistance of mixtures. Consequently, this allows mixture designers a way to rationally evaluate the effects of damage on mixture performance, thus forming the basis for mixture specification criteria for the effects of moisture damage on mixtures. In addition, the results from this Chapter show that cyclic pore pressure conditioning at an elevated temperature of 40 °C results in moisture damage patterns that are consistent with expected behavior. Limestone mixtures with proven field performance track records showed little or no moisture damage. The Georgia granite mixtures, which are known from to exhibit moisture damage without the presence of antistripping agents, showed moisture damage. The paper also evaluated three different cyclic pressure/temperature conditions. The findings indicated that conditioning at an elevated temperature (40 °C) resulted in moisture damage patterns that were consistent with expectations. Finally, the change in energy ratio with cyclic pore pressure conditioning was shown to be related to the predicted interstitial air void pressures developed in the mixtures tested.

The Energy Ratio (ER) can be used to evaluate the effects of moisture damage, independent of the conditioning procedure. Using a consistent framework for evaluating the detrimental effects of moisture damage, the effects of various different conditioning procedures

can also be evaluated more thoroughly. Similarly, cyclic pore pressures to condition mixtures can be used with or without ER testing.

The results presented in this chapter show that the use of cyclic pore pressure conditioning of mixtures accelerates the moisture damage induced in laboratory mixtures. Further research is needed to determine the correspondence between the equivalent "field" and "laboratory" damage levels and times.

11.8 References

Al-Omari, A., and Masad, E., "Three Dimensional Simulation of Fluid Flow in X-ray CT Images of Porous Media," *International Journal for Numerical and Analytical Methods in Geomechanics*, Vol. 28, Issue 13, pp. 1327-1360, 2004.

Buttlar, W.G., and Roque, R., "Development and Evaluation of the Strategic Highway Research Program Measurement and Analysis System for Indirect Tensile Testing at Low Temperatures," *Transportation Research Record No. 1454*, Transportation Research Board (TRB), National Research Council (NRC), Washington, D.C., pp. 163-171, 1994.

Roque, R., Buttlar, W.G., Ruth, B.E., Tia, M., Dickison, S.W., and Reid, B., Evaluation of SHRP "Indirect Tension Tester to Mitigate Cracking in Asphalt Pavements and Overlays," *Final Report* of the Florida Department of Transportation, University of Florida, Gainesville, FL, August 1997.

Sedwick, S.C., "Effect of Asphalt Mixture Properties and Characteristics on Surface Initiated Longitudinal Wheel Path Cracking," Master's Thesis, University of Florida, Gainesville, FL, 1998.